Silicon Carbide and Diamond Radiation Detectors

Thesis submitted for the degree of

Doctor of Philosophy

Colin Stuart Bodie

Space Research Group

School of Mathematical and Physical Sciences

University of Sussex

November 2021

Abstract

A commercial off the shelf (COTS) 4H-SiC photodiode and a custom made chemical vapour deposition (CVD) single crystal (SC) diamond detector were investigated, through experiments and computer modelling, as uncooled spectroscopic radiation detectors for high temperature ($\geq$ 20 °C) applications.

Each detector was connected to a low noise charge sensitive preamplifier (CSP) and a standard onwards readout electronics chain consisting of a shaping amplifier, a multichannel analyser, and a personal computer. In each case, the CSP was operated at the same temperature as the detector; the rest of the readout chain was kept at laboratory temperature.

Both detectors were electrically characterised at temperatures $\leq$ 100 °C before being illuminated by X-rays of energy, E, 5.9 keV $\leq E \lessapprox$ 25 keV and γ-rays ($E \leq$ 59.5 keV (COTS 4H-SiC detector); $E \leq$ 88.03 keV (diamond detector)). Both detectors were operated in spectroscopic photon counting mode at temperatures $\leq$ 100 °C; however, for the diamond detector, electronic noise prevented the spectroscopic photon counting detection of soft X-rays (E = 5.9 keV) at temperatures $\geq$ 80 °C. Analysis of the noise sources suggested that the capacitance and leakage current from the detectors' packages was responsible for much of the noise that degraded the resolution of both the 4H-SiC and the diamond detector spectrometers. Prior to the results presented in this thesis, the hard X-ray (E > 10 keV) response of this type of COTS 4H-SiC detector had not been investigated at high temperatures (> 20 °C) and soft (E = 5.9 keV) X-ray photon counting spectroscopy had not been demonstrated with a diamond detector.

The custom made CVD SC diamond detector was investigated as a detector for soft ($E \leq$ 66 keV) electron (β^- particle) particle counting spectroscopy. The electron spectrometer was successfully operated in particle counting spectroscopic mode without cooling at temperatures, T, -20 °C $\leq T \leq$ 80 °C. Monte Carlo computer modelling was used to energy calibrate the spectrometer; the simulations suggested that a thin (4.5 μm) deadlayer was present at the front of the diamond detector. This work resulted in the first energy calibrated β^- particle spectrum accumulated by a particle counting diamond detector electron spectrometer.

To investigate the utility of the detectors for neutron detection when coupled with Gd layers, custom Monte Carlo computer code was developed to model neutron absorption and the associated X-ray, γ-ray, and conversion electron emissions from thin ($\leq$ 25 μm) natural Gd foils. The experimentally characterised responses of the detectors to X-rays, γ-rays, and β^- particles were used to model their responses to the neutron interaction products emitted from the Gd layers. The research suggested that when coupled with such Gd layers, the investigated COTS 4H-SiC

and CVD SC diamond detectors are likely to result in useful devices for the detection of thermal neutrons in high temperature (< 100 °C) environments.

Acknowledgements

I am, and will remain, enormously grateful to everyone who has supported me through this research journey. That it may now almost be complete is something I am yet to process fully.

First, I wish to acknowledge my PhD supervisor Professor Anna Barnett. I was and remain an unlikely PhD candidate. I am grateful beyond words for the opportunity Professor Anna Barnett gave me when she invited me to join the Space Research Group at Sussex. I also thank her for sharing invaluable support, knowledge, expertise, enlightening discussions, guidance, and her sense of humour as my PhD progressed.

Particular thanks go to Dr Gwen Lefeuvre, who fabricated and provided the diamond detectors used in the work reported in this thesis. I also want to thank Dr Gwen Lefeuvre and the entire team a Micron Semiconductor for providing quickly new detectors and repairing another after my first ham-fisted device characterisations experiments.

I also want to thank and acknowledge my friends and colleagues at the Space Research Group whose patience, support, friendship, and guidance have been vital in getting me to this stage. My particular thanks go to Dr Matina Lioliou, Dr Silvia Butera, Dr Nathan Gemmell, Dr Mike Whitaker, Dr Shifan Zhao, and Marco Tedeschi. Without their support, friendship, and generosity of spirit I would have stalled long ago. Our shared experience will be held in the annals of my most cherished memories.

I must also acknowledge and thank the Science and Technologies Facilities Council for my funding in the form of an iCASE studentship.

Special thanks go to the Open University. I thank the Open University for re-invigorating my love of science, technology, and mathematics to such a degree that I was able to pivot toward this enormously rewarding academic enterprise.

I must also thank all my friends and family who over the years have kept me grounded and mindful of what in life is truly important. For this, I thank my late parents Anne and Jack, my brothers, my relatives, and my cherished friends whose associations with me span 45 years and more. Finally, and most definitely not last nor least, I thank my dearest family. Our son and daughter-in-law Fraser and Nora, our son Michael, and my wife and long-suffering life partner Pauline. This life is full, colourful, brilliant, light, and amazing for you guys being part of it. Who would ever need more?

Contents

Publications

Publications from work reported in this thesis

Bodie, C. S., Lioliou, G., and Barnett, A. M., 2021, '*Hard X-ray and γ-ray spectroscopy at high temperatures using a COTS SiC photodiode*', Nuclear Instruments and Methods in Physics Research Section A, Vol. 985, Art. No. 164663.

Bodie, C. S., Lioliou, G., Lefeuvre, G., and, Barnett, A. M., 2021, *'A single crystal chemical vapour deposition diamond soft X-ray spectrometer'*, Nuclear Instruments and Methods in Physics Research Section A, Vol. 989, Art. No. 164950.

Bodie, C. S., Lioliou, G., Lefeuvre, G., and Barnett, A. M., 2021, *'Electron spectroscopy with a diamond detector'*, Applied Radiation and Isotopes, Vol. 180, Art. No. 110027.

Bodie, C. S., Lioliou, G., Lefeuvre, G., and Barnett, A. M., 2021, *'High temperature X-ray and γ-ray spectroscopy with a diamond detector'*, in preparation.

Bodie, C. S. and Barnett, A. M., 2021, '*Modelling Gd-diamond and Gd-SiC neutron detectors'*, in preparation.

Chapter 1. Introduction

1.1 Introduction to radiation detection

Prior to the middle of the twentieth century, ionising radiation was detected using either: photographic film (e.g. silver halide crystals dispersed in a gelatine emulsion); via the scintillation of light from a phosphor; or with gas-filled ionisation chambers (Miller et al., 1962). Gas filled detectors operate on the principle that charged particles interacting with the gaseous medium in the chamber ionise gas molecules. An electric field applied across the chamber moved the ions and electrons which were created by the radiation interaction, thus inducing a measurable current pulse on the electrodes of the chamber. The first detector to do this directly was built by Rutherford and Geiger in 1908 (Rutherford & Geiger, 1908). Rutherford and Geiger's gas-filled radiation detector was subsequently refined by Geiger and Müller in 1928 (Owens, 2012), and became the Geiger-Müller (GM) tube (Geiger & Müller, 1928). The products of the ionisations, namely the created charge carriers, in the gas of a GM tube are greatly amplified by avalanche multiplication when the radiation induced charge carriers are accelerated by the large electrical field that is applied across the gas. The fast-moving radiation induced charge carriers collide with gas molecules and cause a cascade of further ionisations. The larger current pulse so induced, is easier to measure. Such has been the utility and simplicity of the GM tube that it remains in widespread use today for relatively inexpensive radiation counting applications (Knoll, 2010). Gas-filled particle detectors remained a lively research field up to 1950 (Fraser, 1989) before the research was superseded by work on crystal scintillators, and then subsequently by semiconductor radiation detectors. However, gas proportional X-ray detectors remained a bastion of X-ray astronomy photon counting and imaging instruments into the mid-1980s and they persisted in deep space missions into the C.21st. The Near Earth Asteroid Rendezvous (NEAR) mission to 433 Eros (Trombka et al., 2001) and the MESSENGER (MErcury Surface, Space ENvironment, GEochemistry and Ranging) mission to Mercury (Goldsten et al., 2007) utilised gas proportional detectors for X-ray fluorescence spectroscopy.

Thermal neutrons, free neutrons in thermal equilibrium with their surroundings and possessing kinetic energy, $E_{neutron}$, ≈ 25 meV, are typically detected by ^{3}He gas proportional counters. In such a counter, the reaction

$$^3_2\mathrm{He} + \mathrm{n} \rightarrow {}^3_1\mathrm{H} + \mathrm{p} + 764\,\mathrm{keV} \qquad (1.1)$$

takes place. The energy released is divided between the ^{3}H ion (triton) and the proton (E_{proton} = 573 keV and E_{triton} = 191 keV) which ionise the proportional counting gas (mainly CF_4).

Gas proportional X-ray detecting instruments began to be superseded by microchannel plate (MCP) technology when the Western militaries declassified MCP research in the early 1970s (Ruggieri, 1972), thereafter MCPs became widely used as imaging and particle counting radiation detectors (Fraser, 1989), particularly in spaceborne astronomical X-ray detecting applications. A comprehensive review of X-ray gas proportional counters and microchannel plate detectors can be found in work by Fraser (1989).

The first solid state ionisation chambers used to detect radiation were alkali halide and diamond crystals (Hofstadter, 1949) (Van Heerden & Milatz, 1950) (Chynoweth, 1952). Solid state detectors offered the promise of lower ionisation energies, greater stopping power for higher energy radiation, and more compact design. The crystals selected for radiation detection were insulators to facilitate the application of an electric field across the detector. The radiation induced charge could then be swept without large leakage currents from the crystals adding noise to the induced charge pulse. Early attempts at developing crystal radiation detectors were hampered by inefficiencies in charge collection caused by chemical impurities and defects in the crystals. The impurities and defects caused charge carriers to become trapped and to recombine before the induced charge could be fully collected by the detector's contacts. Large differences in charge collection efficiency were also often observed between different crystals as well as different areas of the same crystal.

The birth of the semiconductor industry in the 1960s ushered in the rapid development of solid state Si radiation detectors (McKenzie, 1979). The new Si semiconductor devices, based around reverse biased diodes, quickly superseded other types of detectors in many applications. The depletion region of a reverse biased diode gave rise to a zone where there was a dearth of free charge carriers and where the chemical impurities from the diode's doping promoted a built-in electric field. This depletion or space charge region, with its in-built electric field is, to a first approximation, the active layer of the radiation detector; here charge induced by radiation interactions is swept through the space charge region towards the detector's contacts; it is the movement of the charge carriers which induces charge on the contacts of the detector (Ramo, 1939) (Shockley, 1938). Each induced charge pulse is proportional to the detected energy of the quantum of radiation. The reverse biased diode also provides a high resistivity across the space charge region, consequently electronic noise caused by leakage current is less than an intrinsic crystal.

1.1.1 Si semiconductor radiation detectors

Si based detectors are the most prolific type of X-ray and γ-ray detector presently in use. Detectors made from Si have become the mainstay of solid-state radiation detection largely because of the microelectronics revolution improving access to high quality material and providing extensive material growth and device fabrication expertise (Lowe & Sareen, 2014). Today, Si detectors are available in a variety of formats which can be broadly classified as: charge-coupled devices (CCDs) (Boyle & Smith, 1970); Si drift detectors (SDDs) (Gatti & Rehak, 1984) and depleted field effect transistors (DEPFETs) (Kemmer & Lutz, 1987); and photodiodes (Shive, 1953).

The Si photodiode detector is a p-n structure of p type acceptor doped Si (with excess holes in the valance band) and n type donor doped Si (with excess electrons in the conduction band). The detector operates on the photovoltaic principle; upon exposure to light electron-hole pairs are created and swept by the in-built or applied electric field to generate photocurrent.

DEPFETs are a combined detector and amplifier structure (Kemmer & Lutz, 1987) (Lutz et al., 2016) that is particularly useful for X-ray detection. In essence, a DEPFET is a field effect transistor (FET) with source, drain, and gate located on the front side of a semiconductor structure with a fully depleted large area diode on the back. With a suitable (deep) doping arrangement, a potential minimum called the 'internal gate' is created below the transistor channel. Photon induced electrons rapidly collect at the internal gate, just below the transistor gate. The elections held at the internal gate are a 'mirror charge' that increases the FET current. The internal gate electrons can be shifted in and out of the internal gate repeatedly to give a non-destructive readout and first stage charge amplification. When the electrons at the internal gate are shifted in or out the transistor current changes; the difference in transistor current is proportional to the charge signal.

SDDs employ a volume of high purity n type Si material with a strong component of the electric field applied parallel to the surface of the detector. The electric field is generated by increasingly reverse biased field strips that cover the back face of the detector. The structure is fully depleted based on the sideward depletion principle (Gatti & Rehak, 1984). To keep capacitance low, the front end FET is integrated into the detector structure and is connected to the collecting anode. Near Fano-limited energy resolutions have been obtained with SDDs see **Section 2.3.1**. For example, the energy resolution of the alpha particle X-ray spectrometer, on-board the Mars Exploration Rovers Spirit and Opportunity, was ≈ 160 eV Full Width at Half Maximum (*FWHM*) at 5.9 keV when operated at -20 °C (Rieder et al., 2003).

CCDs, originally developed to replace photographic film, are comprised of metal-oxide-semiconductor (MOS) capacitors arranged in a two-dimensional array (columns and rows) upon a Si substrate (Lowe and Sareen, 2014). Localised potential wells (termed pixels or picture elements), below the metal electrodes, are produced when the capacitors are biased. Charge generated by photon interactions in the depletion region of the MOS structure are stored in the potential wells. By controlling the bias of the MOS capacitors in a sequence, the charge in a potential well is transferred (termed 'clocking') from one potential well to the next along a column or row of the array.

Despite the ubiquity of Si, some properties of the semiconductor material impose operating restrictions when Si is used for radiation detection (Hansson et al., 2014). Si has a relatively narrow bandgap (E_g = 1.12 eV) (Bludau et al., 1974), so Si detectors must be cooled, typically to ≤ 20 °C, to control the bandgap dependent thermally generated leakage current which can degrade the energy resolution of a radiation spectrometer (Strüder et al., 1999) (Bertuccio, 2005), this is particularly important for detectors of relatively low energy radiation quanta. Commercially available SDDs can provide energy resolutions of 125 eV *FWHM* at 5.9 keV (Amptec Inc N.D.). However, despite being able to operate with energy resolutions near to the Fano limit (see **Section 2.3.1**), Si based radiation detectors are not a panacea for radiation detection and measurement in all situations, see **Section 1.2**.

When Si detectors are operated at temperatures ≳ 20 °C thermally stimulated leakage current will substantially degrade the energy resolving capability of the spectroscopic system. This is an important performance-limiting factor, particularly if the detector is required in an application that encompasses a broad high temperature operating environment yet a resolved and closely spaced energy spectrum needs to be acquired. An example of such an application is machine condition monitoring (Lees, Bassford, & Barnett, 2016). In addition, even relatively benign radiation environments can cause radiation damage in Si devices (Hall & Holland, 2010). Such radiation damage will be evidenced by larger leakage current, lower charge collection efficiency (Koyama et al., 2007), and poorer energy resolutions as damage increases (Wiącek & Dąbrowski, 2016). The general consequence is that detector cooling and often radiation shielding are prerequisites for Si radiation detectors required to operate in harsh environments, yet not all situations are able to support the cooling and shielding required. Furthermore, the inclusion of cooling apparatuses and shielding increase the mass, volume, and power requirements of the complete radiation detection system. This increases the costs and complexity of the instrumentation, and in situations where the requirements cannot be supported, may prevent the use of it at all. The mass, volume, and power consumption budget of a radiation detection system

are all premiums that have to be minimised, without impacting negatively the performance of the system. It should be noted that an uncooled Si photodiode coupled to a charge sensitive preamplifier of substantially similar design to that used in the work reported in this thesis has recently been reported to function as a detector for photon counting X-ray spectroscopy at temperatures ≤ 80 °C (Lioliou et al., 2021). This is the first time such high temperature operation has been achieved with a Si photodiode and operating Si detectors under such conditions is far from common practice.

As such, significant research attention has been focused upon the development of alternative semiconductor materials for radiation detection which do not have the limitations of Si detectors; this has been driven by researchers working to address the use of radiation detectors in future space science research (Hansson et al., 2014), nuclear power generation (Pilotti et al., 2015), fundamental physics research (Sellin & Vaitkus, 2006), and industrial applications (Lees, Bassford, & Barnett, 2016).

1.1.2 Wide bandgap semiconductor detectors

GaAs (Barnett et al., 2011) (E_g = 1.42 eV (Bertuccio & Maiocchi, 2002)), CdZnTe (Zhang et al., 2005) (E_g = 1.54 eV (Siffert et al., 1976)), $In_{0.5}Ga_{0.5}P$ (Butera et al., 2017) (E_g = 1.9 eV (Kuo et al., 1998)), $Al_{0.52}In_{0.48}P$ (Whitaker et al., 2021) ((E_g = 2.31 eV (Cheong et al., 2014)) $Al_{0.8}Ga_{0.2}As$ (Barnett et al., 2010) (E_g = 2.09 eV (Saxena, 1981)), and 4H-SiC (Bertuccio & Casiraghi, 2003) (E_g = 3.27 eV (Madelung, 1982)) are among many wide bandgap semiconductors that are more temperature tolerant than Si and capable of spectroscopic photon counting response at elevated temperatures (≥ 20 °C). Many wide bandgap semiconductor detectors are also considered to be more radiation tolerant than Si in most circumstances (Owens & Peacock, 2004), (Moll, 2006) and (Bertuccio et al., 2013).

Before SiC was proposed as a useful material for radiation detection it had been shown to be a useful material for high frequency/high power/high temperature, and radiation resistant electronic devices (Ivanov & Chelnokov, 1992). In addition, the large electron saturation drift velocity (≈ 2×10^7 cm s^{-1}) (Harris 1995)) and the large breakdown field (≈ 4×10^6 V cm^{-1} (Weitzel et al., 1996)) of the 4H-SiC polytype guided the research of the material towards radiation detection (Rogalla, Runge, & Söldner-Rembold, 1999).

Early results with semi insulating 4H-SiC detectors (310 μm thick) illuminated with a ^{90}Sr radioisotope β^- particle source (endpoint E = 2.2 MeV) pointed to the advantages of wide bandgap material such as 4H-SiC for β^- particle spectrometry at room temperature (Rogalla, Runge, & Söldner-Rembold, 1999), although the relatively low quality of the semi insulating 4H-SiC used

by Rogalla et al. meant that the charge collection efficiency (CCE) was limited (≈ 12 %). Defects and material impurities within the semi insulating 4H-SiC acted as trapping centres which caused the response of the detector to decay after 20 minutes. The imperfect (sputtered) ohmic Al contacts were suggested as the likely principle cause of the decay of the detector's β^- particle response with time. It was reported that the applied electric field's distribution close to the detector's Al contacts varied as charge carriers were emitted from deep traps underneath the Al contacts.

Work with an epitaxial 4H-SiC detector (maximum active layer thickness ≈ 21 μm) with a 100 nm Au Schottky barrier contact illuminated by a ^{90}Sr radioisotope β^- particle source showed that a CCE of 100 % was possible (Bruzzi et al., 2003). The leakage current of the detector was ≲ 100 nA cm^{-2} at up to an applied reverse bias of 600 V. The detector did not polarise when it was illuminated (verified by constant charge collection at constant applied reverse bias) and priming (pre-irradiation to stabilise the detector's response) was not required.

The spectroscopic detection of β^- particles from a ^{90}Sr radioisotope β^- particle source with an epitaxial 4H-SiC detector with a thicker active layer (40 μm) and a 200 nm thick, circular (1.5 mm diameter) Ni_2Si Schottky contact was also reported (Nava et al., 2004). In that work a β^- particle spectrum was fully separated from the so called 'zero' energy noise peak for the first time, although the ^{90}Sr β^- particle pulse height spectrum was not calibrated to the energy of β^- particles. The detector and the associated readout electronics were operated at room temperature, the CCE of the detector was 100 %, and polarisation and priming effects were absent. The detector's depletion region (40 μm) saturated at an applied reverse bias of ≈ 50 V at which point the leakage current density of the detector was ≈ 1 pA cm^{-2}. The combination of low leakage current and minimum detector capacitance at 50 V reverse bias realised the short amplifier shaping time constant (0.5 μs) selected for the spectroscopic detection of β^- particles (see **Section 2.3.2**).

A commercial-off-the-shelf (COTS) 4H-SiC UV photodiode (5.15 μm active layer) was used by Zhao et al. to collect low energy β^- particle spectra emitted from a ^{63}Ni β^- particle radioisotope source (endpoint energy E = 66 keV) (Zhao et al., 2018). The β^- particle spectra were accumulated between 20 °C ≤ T ≤ 100 °C and the collected spectra were calibrated after the β^- particle energy losses up to the face of the detector were computed. The detected endpoint energy was 57 keV.

Bertuccio et al. (2001) first reported spectroscopic X-ray detection with epitaxial 4H-SiC (Bertuccio et al., 2001). The detector's epilayer was a 30 μm n type layer with a net doping concentration of 1.8 × 10^{15} cm^{-3}. A 2 mm diameter and 100 nm thick Au Schottky contact was deposited onto the front face of the detector. The leakage current of the device was ≈ 18 pA cm^2

at a field strength of 170 kV cm^{-1} (100 V applied reverse bias). With 500 V reverse bias applied across the detector the active thickness of detector was 16 µm. When the 4H-SiC Schottky diode detector was attached to appropriate readout electronics to accumulate an ^{241}Am X-ray and γ-ray spectrum, the Np L X-ray photopeaks at 13.9 keV and 17.8 keV were resolved clearly. Electronic noise limited the detector's energy resolution (2.7 keV *FWHM* (an equivalent noise charge (ENC) of 136 e^- rms) measured from a pulser's precision charge input). A significant component of this noise was attributed to the detector's high capacitance (16 pF) caused by the thin depletion width (16 µm) and the relatively large junction area (3 mm^2). Later work reported 4H-SiC devices operating at temperatures up to 100 °C (Bertuccio et al., 2004). The n type epilayers of the devices were 70 µm thick with nominal net doping concentrations of 5.3×10^{14} cm^{-3}. The photon counting capability of the devices arose from their very low leakage current densities (20 pA cm^{-2} and 1 nA cm^{-2} at 24°C and 100 °C, respectively). When 300 V reverse bias was applied across the detectors the depletion regions were ≈ 25 µm and the detectors' capacitances were ≈ 1.3 pF. For photon counting spectroscopy only the front end of the preamplifier (which consisted of the input Junction Field Effect Transistor, JFET, the feedback capacitor, and the test capacitor) were subjected to the same elevated temperatures (≤ 100 °C) as the detectors. The charge sensitive preamplifier (connected to the detectors and the front-end components) was operated at lower temperatures (≤ 40 °C). At temperatures > 45 °C the parallel white noise component of electronic noise (see **Section 2.3.2**) was dominated by the gate-drain leakage current from the front-end JFET and not the leakage current from the 4H-SiC detectors. The leakage current from the detectors and hence the parallel white noise attributable to the detectors was shown to be negligible when compared with the leakage current from the preamplifier's JFET. An ENC of 44 e^- rms on a pulser line at 100 °C was achieved; the analysis of the various noise sources in the spectrometer showed that incomplete charge collection noise was not present in the detectors (**Section 2.3.2**).

A SiC photodiode with a semi-transparent 'ultra-thin' (18 nm) Ni/Ti front Schottky contact was reported by Lees et al. (2007). The epitaxial layer was 20 µm thick with net n type doping = 4×10^{14} cm^{-3}. The ultra-thin Ni/Ti front Schottky contact lowered the barrier height from what would have been expected had a thicker equivalent Schottky contact been formed onto the detector; the ultra-thin contact was a compromise between detecting low energy X-rays and lowering the electronic noise from the detector's leakage current (see **Section 2.3.2)**. The depleted width of the detector varied between 12.7 µm and 14.7 µm as reverse bias across the detector was varied between 60 V and 80 V to detect X-rays and γ-rays between 5.9 keV (^{55}Fe (Mn Kα)) and 59.54 keV (^{241}Am γ-ray). The optimal spectrometer operating settings were found

by applying a reverse bias voltage across the detector that sufficiently depleted the detector for the efficient detection of X-rays and γ-rays without causing the detector's leakage current to rise excessively and hence add electronic noise to the spectra. The 4H-SiC detector was spectroscopic and detected the 5.9 keV (Mn Kα) X-ray emission from an ^{55}Fe radioisotope X-ray source with an energy resolution of 1.5 keV *FWHM* (≈ 87 e^- rms) being achieved at room temperature (23 °C) (Lees et al., 2007). The spectrometer's response was not linear in the energy range (5.9 keV ^{55}Fe (Mn Kα) to 59.54 keV (^{241}Am γ-ray)). This was attributed to charge loss or charge trapping in the 370 µm thick SiC substrate from which the 4H-SiC detector was grown. Later a similar SiC photodiode of the same type (semi-transparent with an ultra-thin Ni/Ti Schottky front contact) achieved an energy resolution of 1.3 keV *FWHM* (≈ 78 e^- rms) at 5.9 keV (Mn Kα) (Lees et al., 2009). After the detector had been characterised for X-ray spectroscopy it was irradiated with ≈ 63 MeV protons until a dose of 10^{11} protons cm^{-2} had been received. The detector was undamaged by the proton fluence and continued to resolve the combined Mn Kα, Kβ X-ray photopeak from an ^{55}Fe radioisotope X-ray source with an energy resolution of 1.3 keV *FWHM* at 5.9 keV. A second irradiation with ≈ 50 MeV protons delivered an accumulated dose of ≈ 10^{13} protons cm^{-2} to the detector. This radiation dose damaged the detector. The detector could still resolve the combined Mn Kα, Kβ photopeak from the same ^{55}Fe radioisotope X-ray source at room temperature, but the energy resolution had degraded to 2.5 keV *FWHM* at 5.9 keV (Lees et al., 2009). The damage from the second proton irradiation was also apparent in the > ×10^2 increase in the detector's leakage current when reverse bias voltage was applied.

In other work, an array of 4H-SiC Schottky photodiode X-ray detectors of similar type were operated in current mode over a temperatures range 20 °C to 140 °C; and as uncooled photon counting X-ray detectors at 30 °C. The diodes were 20 µm thick n type 4H-SiC epilayer wafers (which depleted to ≈ 10 – 14 µm when 200 V of reverse bias was applied). The diode array was grown on a resistive n type 350 µm thick SiC substrate. The nominal doping concentration in the epilayers, extracted from capacitance-voltage measurements, was 16.7 × 10^{14} cm^{-3}. The diodes were operated in current and photon counting modes; photocurrent was measured to range between 4 pA and 8 pA when reverse biases up to 100 V were applied across the diodes. The measured energy resolutions of the detector array varied between 1.36 keV and 1.68 keV at 17.4 keV when spectra from a Mo target X-ray tube were accumulated (Lioliou et al., 2016). Noise analysis of the X-ray spectra found the dominant noise source to be stray capacitances and dielectric noise at the input of the preamplifier (≈ 73 e^- rms ± 6 e^- rms). Any charge trapping noise in the spectrometer was assumed to be negligible in the detectors when > 60 V reverse applied bias was applied. This was attributed to improved X-ray induced charge transport when the electric filed strength was ≥ 100 kV cm^{-1} across the diodes.

The best photon counting X-ray spectroscopic results obtained with 4H-SiC to date showed an ENC of 10.6 e^- rms (196 eV *FWHM*) at 5.9 keV (the Mn Kα photopeak from an ^{55}Fe radioisotope X-ray source) at 30 °C increasing to 12.7 e^- rms (233 eV *FWHM*) at 5.9 keV at 100 °C (Bertuccio et al., 2011). This result represents the cutting edge of 4H-SiC radiation detector development using the highest quality materials and with the detectors connected to state-of-the-art CMOS preamplifiers. Alongside demand for state-of-the-art devices, there is also demand for lower cost COTS SiC X-ray spectrometers for machine condition monitoring (Lees, Bassford, & Barnett 2016), marine exploration and engineering (Lioliou & Barnett, 2017), nuclear waste monitoring, and low-cost CubeSat space missions (Zhao et al., 2016) (Zhao et al., 2017) (Zhao et al., 2018) (Zhao et al., 2018b).

Another material with great potential for radiation detector applications is diamond (E_g = 5.47 eV) (Clark, Dean, & Harris, 1964). Previously, diamond radiation detectors have been shown to respond to X-ray photons. Thin film (15 – 20 μm thick) polycrystalline (PC) diamond detectors were shown to generate photocurrent that was linear with radiation dose when illuminated with 50 keV ≤ E ≤ 250 keV bremsstrahlung and 6 MeV X-rays (Manfredotti et al., 1998), and a diamond detector's X-ray responsivity had been measured in the energy range 51 eV < E < 100 eV (Han et al., 1996). A linear relationship of photocurrent with X-ray radiation dose rate had been demonstrated with an electronic grade polycrystalline chemical vapour deposition (CVD) diamond detector with C (3 nm), Pt (16 nm), and Au (200 nm) centrally located, sputtered contacts (Schirru et al., 2013). The detector's quasi ohmic leakage current was ≈ ± 2 pA, at room temperature, with an electric field of ± 10 kV cm^{-1} (500 V) applied across the detector. The leakage current measurements reported in that work were an average value recorded after ≈ 30 minutes once the leakage current had stabilised, at each of the applied potential difference measured. Stable photocurrent measurements (from a ^{60}Co γ-ray source) were made when the electrical potential across the detector was restricted to < ± 2 kV cm^{-1} (100 V).

Natural diamonds had also been shown to produce a photocurrent response when illuminated with 10 keV and 45 keV X-rays (Tromson et al., 2000). Although the photocurrent response was found to vary with time as trap filling mechanisms evolved which in turn modified the space charge in the material, which affected the applied field across the devices.

The photocurrent response and tissue equivalence of diamond detectors prompted the investigation of them for radiation dosimetry (Prosvirin et al., 2004) (natural diamond) (Lohstroh et al., 2007) (single crystal (SC) CVD diamonds). Lohstroh et al. used α particle spectroscopy and Ion Beam Induced Charge (IBIC) imaging techniques to study charge transport in single crystal CVD diamond detectors, grown by Element Six (Lohstroh et al., 2007). To study charge

trapping mechanisms of N defects in CVD SC diamond additional N atoms were introduced during the diamond crystal's growth phase. The mobility and lifetimes of electrons and holes generated by α particle and ion beam injections did not vary as a function of temperature, T, -70 C ≤ T ≤ 27 °C, and the de-trapping lifetime did not change when the applied electric potential was raised. However, electric field polarisation in the device was related to the growth directions of the crystal; and hole transport was strongly affected when the dose rate was changed, which caused the device to be primed.

The study that first reported a single crystal (SC) CVD diamond radiation detector's spectroscopic response to fast neutrons also showed the detector to be capable of detecting 22.16 keV Ag Kα photons emitted by a ^{109}Cd radioisotope X-ray and γ-ray source (Schmid et al., 2004) The noise threshold of the preamplifier was ≈ 14 keV, which would have prevented spectroscopic detection of X-rays of energy ≲ 20 keV. Calibration studies of the SC CVD detector revealed an electron trapping mechanism that polarised the device which degraded the α particle spectrum after ≈ 10 hours of illumination.

In other work, the current mode response of a 35 μm thick SC CVD diamond detector, placed in the beamline of a synchrotron, was used to study the X-ray beam intensity at two different X-ray energies (10.6 keV and 12.5 keV) (Tartoni et al., 2009). When the detector was exposed to a sequence of X-ray pulses the current response reduced; this was attributed to a changing population of charge carrier traps in the material which was based on the detector's illumination history. X-ray beam profile monitoring with a CVD PC diamond detector has also been successfully demonstrated at energies of 17.5 keV and 19.6 keV (Mo Kα and Kβ) (Girolami et al., 2012).

The β^- particle induced current response of a diamond detector to β^- particles at T >> 20 °C was first reported by Pilotti et al., (Pilotti et al., 2015). The commercially obtained 500 μm thick SC CVD diamond detector was operated with an applied field of 10 kV cm^{-1} and the β^- particles were provided by a 1 MBq ^{90}Sr radioisotope β^- particle source. The detector registered a current response under β^- particle illumination at T ≤ 175 °C; at T > 175 °C no clear current response from the detector was obtained. The β^- particle response of diamond (SC CVD and PC CVD) to a ^{90}Sr/^{90}Y radioisotope β^- particle source (endpoint energy ≈ 2.3 MeV (Hansen, 1983)) was investigated as part of a study on diamond detectors for the purpose of active interrogation of concealed special nuclear materials (SNM) (Hodgson et al., 2017). A pathway for collecting a low energy β^- particle energy spectrum with a SC CVD diamond detector at laboratory temperature had been reported (Tchouaso et al., 2018). In that work, β^- particles within the estimated energy range 50 keV < E ≤ 820 keV were used to illuminate a commercially obtained

SC CVD diamond and the spectra accumulated were roughly calibrated using the endpoint energy of each of the radioisotope β^- particle sources used.

Prior to the work reported in this thesis, the performance of photon counting X-ray spectroscopic diamond detectors had not been reported at temperatures >> 20 °C, and a spectroscopic photon counting response to X-rays with energies < 10 keV had not been reported. However, research had been conducted investigating the current mode response of a diamond detector illuminated by an ^{55}Fe radioisotope X-ray source and a ^{63}Ni radioisotope β^- particle source (Lioliou et al., 2021).

It should also be noted that many (e.g. GaAs, $In_{0.5}Ga_{0.5}P$, $Al_{0.52}In_{0.48}P$, $Al_{0.8}Ga_{0.2}As$, and CdZnTe), but not all (e.g. 4H-SiC and diamond), wide bandgap materials also have larger X-ray and γ-ray linear absorption coefficients than Si. As such, their development has also been motivated by the need for better quantum detection efficiency at hard photon energies (Cromer & Liberman, 1970). The different linear absorption coefficients as a function of photon energy for some wide bandgap materials are presented in **Figure 1.1**. The photon absorption coefficients were computed from the XCOM photon cross sections database (Berger et al., 2010).

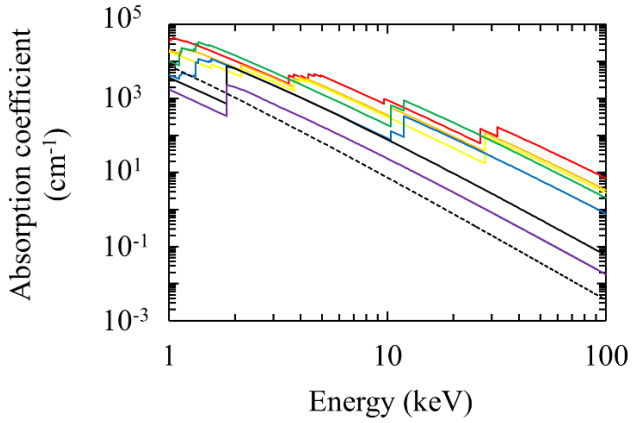

Figure 1.1. Linear absorption coefficient as a function of energy for CdZnTe (red line), $In_{0.5}Ga_{0.5}P$ (orange line), $Al_{0.52}In_{0.48}P$ (yellow line), GaAs (green line), $Al_{0.8}Ga_{0.2}As$ (blue line), Si (black line), SiC (purple line), and diamond (black dashed line). The discontinuities are the absorption edges associated with each material.

1.2 Motivation

In both nuclear science and space science, X-ray, γ-ray, electron (β^- particle), and neutron detectors are required that can operate in harsh (high temperature, intense radiation) environments for extended periods. Whilst Si radiation detectors can operate in some harsh environments if

systems for cooling and shielding the detectors are included, such additional equipment adds to the mass, volume, and power requirements of the instrumentation, and also increases complexity and decreases reliability since there are more components which could fail. Furthermore, in space applications, where mass, volume, and power are at a particular premium, the shielding and cooling apparatuses can decrease the overall science return of the mission, since they consume resources which could otherwise be used for additional scientific instrumentation. They also add cost; for example, the presently advertised specific cost to launch a payload to Geostationary Transfer Orbit (GTO) with SpaceX's Falcon 9 launch system is 11.3 US$ g^{-1} (Space Exploration Technologies Corp., N.D.). Although a significant premium, the launch costs today are less restrictive when compared with the specific cost for GTO insertion with the Ariane 5 ES in 2000 (24.3 US$ g^{-1}) (Sweeting & Underwood, 2014). Alternative detector technology that can be integrated into simpler, compact, temperature tolerant, and robust systems, with frugal power demands would be cause for photon and electron counting instrumentation to be deployed more frequently, thus returning more data, and potentially satisfying more scientific objectives at reduced cost.

As with many upscale technological systems designed for very specific applications, radiation detector technology can be adapted for alternative uses far removed from the original purpose. Tribological wear of lubricated machinery can be monitored by X-ray fluorescence spectroscopy (Lees, Bassford, & Barnett 2016) if X-ray detectors operable at high temperature are available. The assaying and decommissioning of nuclear installations could benefit from inexpensive detectors operable at high temperatures and in high radiation environments (Park et al., 2014). Portable X-ray fluorescence spectroscopy instrumentation could be deployed in harsh, remote, and rugged locations to assay industrial waste sites for hazardous waste deemed harmful to human health (Kennedy & Kelloway, 2021), or for spectrometry of archaeological or historical artefacts for example to reveal their composition (Williams-Thorpe, 2008). Neutron, γ-ray, and X-ray detectors, used for geochemical prospecting, for example oil well logging (Metcalfe et al., 2017) and ocean mining (Lioliou & Barnett, 2017), that are operable without stringent cooling requirements could prove particularly useful to their respective industries.

Until recently, thermal neutrons emitted from special nuclear materials (SNM) were almost exclusively detected using ^{3}He gas proportional counters. This type of detector is also used in a wide range of other applications, such as well logging (Glesius & Kniss, 1988), medical accelerators (Tosi et al., 1991), and fundamental research in nuclear and condensed matter physics (Kouzes et al., 2010) (Radulović et al., 2020). ^{3}He is extracted from the β^- decay of ^{3}H (tritium half-life, $t_{1/2}$, = 12.3 y) and it is separated from ^{3}H when nuclear warheads are periodically

refurbished (Kouzes et al., 2010). However, as a consequence of the reducing stockpile of nuclear warheads and demand for more ^{3}He gas proportional neutron detectors since the terrorist attacks on the New York World Trade Centre, the Pentagon Building, and the loss of United Airlines Flight 93 in 2001, the demand for ^{3}He has outstripped the supply. This has led to a rise in research and development of alternative thermal neutron detection technologies. Gas, liquid, plastic, and glass scintillators loaded with neutron reactive ^{6}Li, ^{10}B, ^{155}Gd, and ^{157}Gd are commercially available (Ihantola et al., 2018), and each type of detector has particular utility of purpose, although none alone completely match all the capabilities of ^{3}He gas proportional counters (Kouzes, 2009). The use of thermal neutron reactive natural Gd in conjunction with the detectors investigated in the thesis is the focus of **Chapter 7**.

1.3 Thesis organisation

This thesis presents experimental and Monte Carlo (MC) modelling results characterising a COTS 4H-SiC and a custom-made diamond detector for their response to X-rays, γ-rays, and electrons (β^- particles). The detectors were coupled to a custom-built low noise charge sensitive preamplifier of feedback resistor-less design and a standard onward readout electronics chain to accumulate spectra. X-rays, γ-rays, and β^- particles were provided by an ^{55}Fe radioisotope X-ray source, a ^{109}Cd radioisotope X-ray and γ-ray source, an ^{241}Am radioisotope γ-ray source, and a ^{63}Ni radioisotope β^- particle source.

Chapter 2 reviews the physics that underpins semiconductor radiation spectrometers. The noise sources that limit the energy resolution of a semiconductor radiation detector system are also reviewed. **Chapter 3** presents an investigation of the X-ray and γ-ray (E < 90 keV) response of a repurposed COTS 4H-SiC UV photodiode across the temperature range 20 °C ≥ T ≥ 100 °C. The electrical characterisation of the device and an analysis of electronic noise components impacting the energy resolution of the spectroscopic system are discussed. **Chapter 4** reports the electrical characterisation and soft X-ray (5.9 keV) spectroscopic response of the custom made SC CVD diamond photon counting spectrometer at 20 °C. **Chapter 5** presents results with the custom made SC CVD diamond configured as a temperature tolerant (-20 °C ≥ T ≥ 80 °C) β^- particle counting spectrometer. In **Chapter 6**, the work continues to detail investigation of a similar diamond detector to soft and hard X-rays (5.9 keV and 22.16 keV) and γ-rays (88.03 keV) at -20 °C ≥ T ≥ 100 °C. In **Chapter 7**, a MC model is presented which simulates thermal neutron absorption in, and the X-ray, γ-ray, and electron emissions from, natural Gd. The MC code also modelled the response of the SC CVD diamond and the COTS 4H-SiC detectors to the X-rays, γ-rays, and electrons emitted from natural Gd foils of different thicknesses. **Chapter 8** presents a summary of the work, draws conclusions, and suggests possible directions for future work.

Chapter 2. Radiation detector physics

2.1 Introduction

This chapter describes the physical principles relating to the spectroscopic photon and particle counting detection of X-ray, γ-ray, and β^- particles with semiconductor radiation detectors. The energy range is restricted to photons and β^- particles possessing energies of a few keV up to a maximum of 300 keV. Neutron interactions with matter are also discussed, in the context required for the Monte-Carlo simulations of thermal neutrons presented in **Chapter 7**. The physics of energy deposition, charge creation, and charge collection in solid state radiation detectors are reviewed before the various sources of noise that degrade the energy resolution of X-ray, γ-ray, and electron spectrometers are summarised. The instruments that constitute the readout electronics chain of radiation detection systems of the type used in the thesis are explained, and the sources of X-ray, γ-ray and β^- particle radiation used in the experimental work of the thesis are described.

2.2 Radiation interactions with matter

2.2.1 Photon interactions

The photon interaction of principle concern in this thesis is photoelectric absorption. Other important mechanisms of photon interactions in radiation detection are coherent (Rayleigh and Thompson) scattering, incoherent (Compton) scattering, and pair production. Pair production (the creation of an electron positron pair when a photon of sufficient energy interacts with the Coulomb field of the atomic nucleus) is the dominant interaction at photon energies > 10 MeV in absorbing materials of atomic number, Z, < 20 (Knoll, 2010); photons of such energies are outside the scope of this thesis. Compton scattering is the scattering of photons from atomic electrons, which are assumed to be at rest. The products of a Compton scattering interaction are a recoil electron and a scattered photon, which possesses less energy (and therefore a longer wavelength) than it had prior to the scattering. The scattered photons can continue to interact with nearby atoms through other (lower energy) interactions. In a detector, the lower energy photon interactions will give rise to a Compton continuum of energy. Compton scattering interactions are weakly dependant on photon energy, and are more probable in materials with more bound atomic electrons to scatter off (e.g., high Z atoms). At the photon energies considered in this thesis (< 90 keV) and for detectors fabricated from low Z materials, such as diamond (C) and silicon carbide (SiC) the Compton scattering probability is low (Lowe & Sareen, 2014). Rayleigh or coherent scattering and Thompson scattering relate to photons being elastically scattered from

an atom's bound electron cloud or a free electron respectively. In such scattering events, the energy of an incident photon is insufficient to ionise or excite an atom and the photon is scattered without an exchange of internal energy between photon and electron. Coherently scattered photons are scattered in a changed direction (Owens, 2012).

2.2.1.1 Photoelectric absorption

Photoelectric absorption is a process in which a photon incident upon an absorbing material transfers all of its energy to a bound atomic electron in the absorber, creating a photoelectron. About 80 % of photoelectric absorption occurs in the K shell of an atom, subject to the energy of an incident photon exceeding the K shell binging energy of the atom (Owens, 2012). Upon absorption the incident photon ceases to exist and a photoelectron is ejected from the electron shell with an energy equal to that of the incident photon minus the binding energy of the photoelectron. The vacancy in the ionised atom is quickly filled with the capture of a free electron from the material, or by the rearrangement of electrons from the outer shells of the atom. The result of atomic rearrangement is a competing process of characteristic X-ray and/or Auger electron emissions. In many cases, characteristic X-rays are reabsorbed by photoelectric absorption in less tightly bound electron shells. If the energy from all the photon interactions is contained within the detector then the sum of the kinetic energies of the excited electrons can be equated to the energy of the original incident photon. If the photoelectron, characteristic X-rays, and/or Auger electrons escape from the detector a fraction or possibly none of the energy of the original incident photon will be absorbed. A table of possible contributions to an energy spectrum from incident photon interactions is presented in **Table 2.1**. The probability of photoelectric absorption per atom varies ~ $Z^{4.5}$ (Knoll, 2010) (Lowe & Sareen, 2014), which accounts for the significantly higher photoelectric absorption coefficients in higher Z materials and detectors.

Absorbed in detector		Spectrum contribution
Photoelectron X-ray fluorescence/Auger electron	✓ ✓	Photopeak
Photoelectron X-ray fluorescence/Auger electron	✓ ×	Escape peak
Photoelectron X-ray fluorescence/Auger electron	× ✓	Fluorescence peak
Photoelectron X-ray fluorescence/Auger electron	× ×	No photon counting

Table 2.1. The contribution of photoelectron and X-ray fluorescence absorption to an energy spectrum.

2.2.2 The Beer-Lambert-Bouguer Law

The intensity, *I*, of monochromatic X-rays or γ-rays, exiting from an attenuating medium is given by the Beer-Lambert-Bouguer Law (Hubbell, 1999),

$$I(z) = \mathrm{I}_0 \exp(-\mu z) \tag{2.1}$$

where I_0 is the intensity of the light prior to entering the attenuating medium, μ is the linear attenuation coefficient of the absorbing medium, itself a function of photon energy, and z is the thickness of the attenuating medium. The linear attenuation coefficient accounts for all possible interactions (Rayleigh scattering, photoelectric absorption, Compton scattering, and pair production). To consider absorption alone, the absorption coefficient can be used. In this thesis all linear attenuation (and absorption) coefficients were obtained from mass attenuation (and absorption) coefficients, μ_m, given by the XCOM database (Berger et al., 2010). The linear attenuation (or absorption) coefficient is simply the product of the mass attenuation (or absorption) coefficient and the density of the medium, ρ, i.e.

$$\mu = \mu_m \rho \tag{2.2}$$

Plots of the linear attenuation and absorption coefficients for diamond and 4H-SiC are shown in **Figure 2.1**. At low energies, the linear attenuation (solid black line) and absorption (solid blue line) are near identical because the impacts of coherent (black dotted line) and incoherent (black dashed line) scattering are small. As photon energy increases, the linear attenuation and absorption coefficients diverge as the Rayleigh and Compton contributions to photon attenuation diminish and increase respectively.

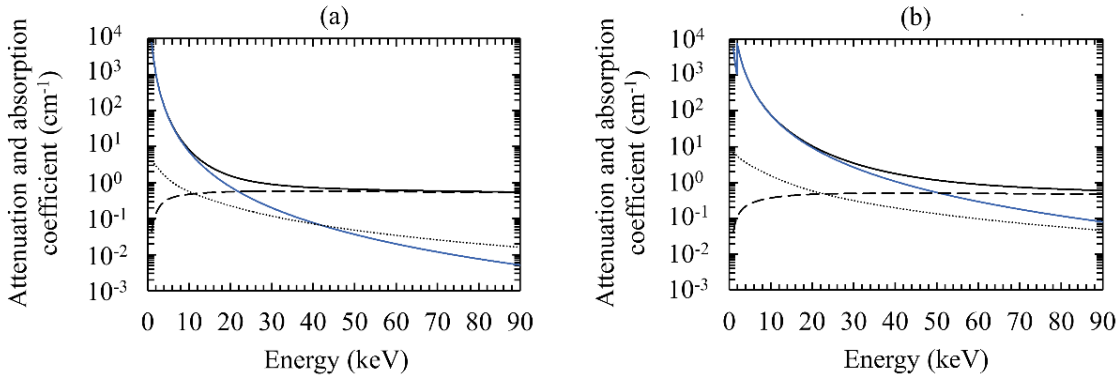

Figure 2.1. The energy dependence of linear attenuation coefficient (black line), linear absorption coefficient (blue line), Rayleigh (coherent) scattering (black dotted line), and Compton (incoherent) scattering (black dashed line) in (a) diamond and (b) 4H-SiC (Berger et al., 2010).

The discontinuity at 1.8 keV in **Figure 2.1 (b)** is the Si K absorption edge (Thompson et al., 2009). The K absorption edge for diamond (C atoms) occurs at 284 eV (Thompson et al., 2009) and is not seen in the figure, since only data for energies ≥ 1 keV is plotted for clarity.

2.2.3 β^- particle (electron) interactions

β^- particles (electrons) are not attenuated through matter identically to X-rays and γ-rays (Knoll, 2010); β^- particles can follow non-linear paths. Consequently, the path length of a β^- particle can be much greater than its penetration depth. Typically, the deposition of energy in matter by a β^- particle is a progressive process of many interactions, unlike a relatively low energy X-ray or γ-ray where only a single absorption event may occur.

Ionisation interaction occurs when a β^- particle causes the ejection of an atom's orbital electron. This interaction is governed by the incident β^- particle's energy and the binding energy of the ejected electron. If sufficient energy is imparted to the ejected electron a charge cascade of secondary and tertiary ionisations can occur. However, the probability that a β^- particle will cause an ionisation is governed by the particle's cross section, which is governed by its energy and the nature of the target atom (Ahmed, 2015). Vacancies from ionisations are quickly filled by the capture of free electrons in the material or by the atomic rearrangement of the atom's outer shell electrons. An atom will emit characteristic X-rays and/or Auger electrons when electrons from the outer shells fill the vacancies. An alternative to the ionising interaction is for a β^- particle to excite an orbital electron to a higher bound energy state. An X-ray photon will be emitted when the excited orbital electron relaxes to the ground state.

Another process where a β^- particle loses energy in a medium is where bremsstrahlung radiation is emitted as the β^- particle changes direction in response to the Coulomb interaction with an orbital electron or an atomic nucleus in the detector (Knoll, 2010). Bremsstrahlung radiative loses are governed by the β^- particle's energy and an absorbers atomic number, *Z*. Atoms of higher atomic number present a stronger electric field to a β^- particle which increase the radiative losses associated with a deceleration. The intensity of bremsstrahlung emissions are a function of Z^2 and more significant in high *Z* detectors (Knoll, 2010). A β^- particle (or any other charged particle) will emit bremsstrahlung radiation when accelerated by an electric field. It should be noted that bremsstrahlung radiation is not restricted to Coulomb interactions. Bremsstrahlung radiation is emitted when any charged particle is decelerated.

2.2.4 Neutron interactions

The absorption length of a neutron in a medium can be long. Neutrons do not interact via Coulomb repulsion; instead, neutrons either recoil from an atomic nucleus (scatter) or they react with atomic nuclei (absorption) (Rinard, 1991). If a neutron is scattered by an atomic nucleus, only its speed and direction are altered; the nucleus from which the neutron was scattered is substantially unchanged, although it can recoil or be left in an excited state from which some radiation will eventually be emitted. If a neutron is absorbed by a nuclide, nuclear fission can be induced or radiations such as γ-rays, charged particles, or neutral particles can be emitted.

The cross section, σ, quantifies the probability of a specific interaction occurring between a neutron of specific energy and an atomic nucleus; and the total cross section, σ_t, is the sum of all the scattering and absorption processes that can occur between the neutron and a nuclide (Knoll, 2010). The macroscopic cross section is therefore the total cross section multiplied by the number of nuclei per unit volume, *N*. For a beam of mono-energetic neutrons incident upon an absorber, the transmissivity of the medium is

$$F(z) = \mathrm{F}_0 \exp -(N\sigma_t z), \tag{2.3}$$

where F_0 is the intensity of a mono-energetic neutron beam prior to entering an absorbing medium, and the other symbols have been previously defined. As the total cross section of most atomic nuclei are $10^{-27} < \sigma_t < 10^{-21}$ cm^2, σ_t is more commonly expressed in units of barns [b], where 1 b = 10^{-24} cm^{-2}.

The neutron energies are, by convention, separated into three energy ranges, slow, intermediate, and fast (Knoll, 2010). The slow region encompasses neutrons with energies up to 0.4 eV, the so-called Cd cut-off (Pietropaolo et al., 2020). Within this energy region elastic collisions in an

absorber are probable, and neutrons are quickly brought into thermal equilibrium with the absorber. At room temperature neutrons in thermal equilibrium with an absorber, will possess an energy ≈ 25 meV, neutrons with such energies are called thermal neutrons. At such energy, neutron radiative capture reactions become the most probable (Knoll, 2010).

2.3 Semiconductor radiation detectors and spectrometers

2.3.1 Charge creation

Solid state detectors operate on the principle that the charge carriers (electrons and holes) created in the detector upon the absorption of a radiation quantum can move within the electric field of the detector and in doing so induce charge upon the contacts of the detector in an amount proportional to the energy of the incident radiation, in accordance with Shockley-Ramo theorem (Shockley, 1938) (Ramo, 1939).

The average number of electron hole pairs, N, generated by the absorption of a radiation quantum is,

$$N = E/\omega \tag{2.4}$$

where E is the energy possessed by the radiation quantum, and ω is the average electron-hole pair creation energy (the average amount of energy consumed in the creation of an electron-hole pair). Recent work has shown that the previously widely-used Klein relationship (Klein, 1968) between semiconductor bandgap, E_g, and ω is flawed, and that the Bertuccio-Maiocchi-Barnett relationship provides a better, albeit still semi-empirical, model for the relationship between the two parameters (Barnett et al., 2012a) (Barnett et al., 2013) (Whitaker et al., 2020). Rigorously measured and reliable values for ω_{SiC} *and* $\omega_{diamond}$ have not yet been reported. However, commonly cited values for ω_{SiC} and $\omega_{diamond}$ at laboratory temperature are 7.28 eV (Chaudhuri et al., 2013) and 12.82 eV (Keister et al., 2018), respectively. Because of the challenges in measuring reliable values for the electron-hole pair creation energy, particularly in materials with large ω, these values must be considered strictly upper limits of the parameter in each material rather than definite measurements. The ω_{SiC} reported by Chaudhuri et al. (2013) was obtained with 5.48 MeV alpha particles and $\omega_{diamond}$ reported by Keister et al. (2018) was obtained with soft X-rays (≤ 10 keV). Measurements of the electron-hole pair creation energy for a particular material can vary with different types and energies of initiating radiation quanta.

If the processes by which the electron-hole pairs were created were Poissonian, the standard deviation, σ, would be $\sqrt{N}$ (Lowe & Sareen, 2014), and since the number of carriers created is

typically large, the distribution would be Gaussian (full width at half maximum = 2.355σ). As such, the charge resolution, *R*, of the distribution would be $R = \left(\frac{FWHM\ of\ N\ distribution}{Model\ N}\right)$. However, it has long been known that the charge carriers created in a single absorption event are not independent of each other, and that the distribution is tightened compared to the Poissonian case, such that *R* becomes

$$R = 2.355\sqrt{F/N} \tag{2.5}$$

where *F* is the Fano factor (Fano, 1947) which is defined as the ratio of the observed variance in *N* to the Poisson predicted variance in *N*; for most modern semiconductor materials $F \approx 0.1$. Therefore, in energy terms, the *FWHM* of the distribution, and the energy resolution of the spectrometer in the Fano-limited case, becomes,

$$FWHM\ [\text{eV}] = 2.355\omega\sqrt{\frac{FE}{\omega}}. \tag{2.6}$$

Equation 2.6 is the Fano-limited energy resolution of a radiation spectrometer; it is the ultimate energy resolution achievable with a non-avalanche semiconductor detector. Assuming $F = 0.128$ (Chaudhuri et al., 2013) and 0.08 (Alig et al., 1980), and $\omega = 7.28$ eV (Chaudhuri et al., 2013) and 12.82 eV (Keister et al., 2018) for 4H-SiC and diamond, respectively, the expected Fano-limited energy resolutions for detectors made of these materials are given in **Table 2.2** at key energies of interest in this thesis.

Energy (keV)	Fano-limited energy resolution (eV)	
	4H-SiC	Diamond (C)
5.9	180	190
22.16	340	360
59.54	560	590
88.03	680	710

Table 2.2. Fano-limited energy resolution for 4H-SiC and diamond radiation detectors at selected energies, given $F = 0.128$ (Chaudhuri et al., 2013) and 0.08 (Alig et al., 1980), and $\omega = 7.28$ eV (Chaudhuri et al., 2013) and 12.82 eV (Keister et al., 2018) for 4H-SiC and diamond, respectively.

2.3.2 Electronic noise sources in semiconductor radiation spectrometers

In practice the energy resolution of a radiation spectrometer is degraded beyond the Fano-limited case by electronic noise (a consequence of the detector and the readout electronics, and their interconnection) and incomplete charge collection noise (a consequence of imperfect charge

transport in the detector, see **Section 2.3.2.5**). Thus, **Equation 2.6** is modified to include the effects of electronic noise, *A*, and incomplete charge collection noise, R_{ICC}, such that,

$$FWHM\ [eV]\ =\ 2.355\omega\sqrt{\frac{FE}{\omega}+A^2+{R_{ICC}}^2} \tag{2.7}$$

where *A* and R_{ICC} are in units of equivalent noise charge (*ENC*) (e^- rms). The electronic noise is not a single noise, rather it is composed of several separate but related noise components: parallel white noise, series white noise, induced gate current noise, dielectric noise, and $1/f$ noise. Comprehensive expositions of these sources are provided by (Bertuccio et al., 1996) and (Lioliou & Barnett, 2015), however, for the convenience of the reader a summary is provided for each component in the following subsections.

2.3.2.1 Parallel white noise

The origin of parallel white noise is the quantised nature of electric charge (Vasilescu, 2005). The current flowing in the gate of the input transistor of the preamplifier, I_{JFET}, and the leakage current of the detector, I_D, feeding into the channel of the JFET are not macroscopic continua of steady state charge flows, but rather distributions of charge varied around mean values. The *ENC* of the parallel white noise is given by

$$ENC_{pw} = \frac{1}{\mathrm{q}_e}\sqrt{\frac{A_3}{2}S_{pw}\tau} \tag{2.8}$$

where $\mathrm{q_e}$ is elementary electron charge and A_3 is a constant related to the characteristics of the shaping amplifier (Bertuccio et al., 1996) (Gatti et al., 1990). The parallel white noise power spectral density, S_{pw}, is given by,

$$S_{pw} = 2\mathrm{q_e}\alpha'(I_D + I_{JFET}) \tag{2.9}$$

where $\alpha' = 1$ if full shot noise is present in the preamplifier (Bertuccio et al., 1996). The parallel white noise component of electronic noise is also proportional to the shaping amplifier time constant, τ.

2.3.2.2 Series white noise

Series white noise is primarily a consequence of thermal noise that affects the drain current at the input JFET (Bertuccio et al., 1996). Thermal noise arises from the random thermal motion of free electrons in a conductor which induce a random voltage over time (Vasilescu, 2005). The *ENC* of the series white noise is given by

$$ENC_{sw} = \frac{1}{q_e}\sqrt{\frac{A_1}{2}S_{sw}{C_T}^2\frac{1}{\tau}} \quad (2.10)$$

(Bertuccio et al., 1996) where A_1 is a constant, determined by the signal shaping function. Values of A_1 are $0.5 \leq A_1 \leq 4$ (Gatti et al., 1990). The series white noise spectral density, S_{sw}, is given by

$$S_{sw} = \gamma\,\frac{4kT}{g_m} \quad (2.11)$$

where $0.7 \leq \gamma \leq 1$ is a dimensionless product of noise resistance and transconductance, g_m, of the JFET (Lioliou & Barnett, 2015), k is the Boltzmann constant, and T is temperature in Kelvin. The total capacitance at the preamplifier input, C_T, is the sum of detector capacitance, C_d, input transistor capacitance, C_i, feedback capacitance, C_f, and stray capacitance, C_s, (Bertuccio et al., 1996). The series white noise becomes a more significant component of electronic noise when the shaping amplifier time constant is reduced.

2.3.2.2.1 Induced gate current noise

Fluctuation in the drain current from thermal noise (related to the series white noise above) induce charge fluctuations onto the JFET gate via the capacitance that exists between channel and the gate of the JFET. These charge fluctuations are the origin of the induced gate current noise which depends upon S_{sw} (**Equation 2.11**). Series white noise can be re-written to include induced gate current noise by applying an experimentally obtained induced gate correction factor, G_c, where $G_c \approx 0.64$ (Bertuccio et al., 1996). The ENC_{sw} corrected to include induced gate current noise, ENC_{swc}, is given by

$$ENC_{swc} = ENC_{sw}\sqrt{G_c}\,. \quad (2.12)$$

2.3.2.3 Dielectric noise

Dielectric noise arises from thermal fluctuations in dielectric materials close to or in contact with the input of the preamplifier's JFET (Bertuccio et al., 1996). When lossy dielectric components with a loss tangent, tanδ, $\lesssim 0.1$, are polarised the local electric charge density fluctuates; charge density fluctuations induce fields that draw current from the external circuit which add to the noise (Lowe & Sareen, 2014). The *ENC* of dielectric noise is given by

$$ENC_{die} = \frac{1}{q_e}\sqrt{A_2 2kTdC_{die}} \quad (2.13)$$

where A_2 is a constant ($0.64 \leq A_2 \leq 2$) dependent upon the signal shaping function (Gatti et al., 1990), d is the dielectric dissipation factor (Bertuccio et al., 1996) given by

$$d = \frac{G(\omega')}{\omega' C_{die}} \tag{2.14}$$

where $G(\omega')$ is the loss conductance at angular frequency, ω' (Lowe & Sareen, 2014), and C_{die} is the capacitance of the dielectrics. The other terms have previously been defined. Numerous dielectric materials, such as the printed circuit board (PCB), detector packaging, die bonding epoxies, JFET passivation, and other dielectric materials are brought together to form the detector/preamplifier front end. All contribute to the lossy dielectrics and introduce stray capacitance. Other dielectric sources are the feedback capacitance and the test capacitance (if any) of the preamplifier. To calculate directly the dielectric noise each and every source of capacitance must be considered separately with its own unique dissipation factor. Dielectrics that are considered to be low noise have $d \approx 10^{-5}$ (Lowe & Sareen, 2014), other materials with larger dissipation factors (e.g. for FR-4 PCB, $d \approx 10^{-2}$) are considered lossy or noisy (Edwards & Steer, 2016).

2.3.2.4 1/*f* series noise

The origin of 1/*f* series noise is carrier generation and recombination from impurities and lattice defects in the depleted regions of the preamplifier's JFET (Vasilescu, 2005). It is a flicker noise that varies inversely with frequency and is related to the drain current in the channel of the JFET. The *ENC* of 1/*f* series noise is given by

$$ENC_{1/f} = \frac{1}{q_e}\sqrt{A_2 \pi A_f {C_T}^2} \tag{2.15}$$

(Bertuccio et al., 1996) where A_f is a characteristic constant of the JFET (Gatti et al., 1990) and the other terms have previously been defined.

2.3.2.5 Charge transport and incomplete charge collection noise

The electrons and holes created upon the absorption of a radiation quantum in a detector are separated and swept towards the respective contacts of the detector by the electric field applied to the detector. The velocity of each charge carrier (v_e and v_h, respectively) when a uniform electric field, $E_{detector}$, is applied to the detector is given by

$$v_e = \mu_e E_{detector} \tag{2.16a}$$

$$v_h = \mu_h E_{detector} \tag{2.16b}$$

where μ_e and μ_h are the mobility of the electrons and holes, respectively. The mobility of each charge carrier is specific to the detector material (Ahmed, 2015); nevertheless, the transport of

charge carriers through a semiconductor is impeded by impurities and defects in the semiconductor material (Owens, 2012). Such impurities and defects are introduced into the material during crystal growth and device fabrication; in addition defects can also be introduced by radiation damage (Spieler, 2005). The impurities and defects act as trapping and recombination centres. Charge carriers may be immobilised in trapping centres for a period longer than the read-out time for the detector (Knoll, 2010); and immobilised charge, when released, can cause a second burst of charge to be recorded from the detector. At recombination centres, charge may be lost when electrons and holes recombine. The lifetime of electrons and holes, τ_e and τ_h, respectively are restricted by the recombination process, which in turn limits the average distance they travel. The average distance of electron or hole travel, before recombination occurs, is the carrier recombination length, r_e and r_h, respectively. **Equation 2.16** can be re-written in terms of recombination lengths and charge carrier lifetimes as

$$r_e = \mu_e \tau_e E_{detector} \tag{2.17a}$$

$$r_h = \mu_h \tau_h E_{detector}. \tag{2.17b}$$

The recombination lengths limit the useful thickness of a detector, as charge carriers generated beyond a recombination length from the detector's electrode do not contribute to the detected charge.

Noise due to incomplete charge collection, R_{ICC}, is not easily quantified as it is closely related to the distribution and density of charge trapping centres in the detector as well as the intrinsic properties of charge transport of the detector material (Owens, 2012). An empirical relation that describes R_{ICC} has been given as

$$R_{ICC} = \frac{aE^b}{(2.355\omega)^2} \tag{2.18}$$

where a and b are semiempirical constants determined by best fitting **Equation 2.7** (Owens, 2012).

2.4 X-ray, γ-ray, and β^- particle spectroscopy electronics chain

A block diagram of the components that make up a spectroscopic system incorporating a semiconductor detector is presented at **Figure 2.2**. A radiation quantum incident upon the detector interacts with the detector (**Section 2.3.1**). A burst of charge, proportional to the energy deposited in the detector, is liberated by the detector/radiation interaction. Because the charge liberated in the detector is generally too small to be measured directly, a charge sensitive preamplifier is introduced into the electronics processing chain (Knoll, 2010). The preamplifier

integrates the transient current pulse from the detector to produce a voltage step proportional to the original burst of charge. The output from the preamplifier, a voltage pulse, is sent to the shaping amplifier where the amplitude of the voltage pulse is preserved in a shaped voltage pulse proportional to the original burst of charge from the radiation interaction in the detector. The shaping amplifier also improves the signal to noise ratio, and provides other functions to improve signal processing, such as pile-up rejection, baseline restoration, and pole-zero cancellation. The shaped voltage pulses from the shaping amplifier are sent to the multi-channel analyser (MCA). The height of each voltage pulses is measured in the MCA, and via a digitisation process each voltage pulse is assigned to a channel representative of a range of voltage heights. The output from the MCA is a histogram of voltage pulse heights, commonly referred to as the pulse height spectrum. The pulse height spectrum can be calibrated to an energy spectrum by the identification of pulse heights of known energy.

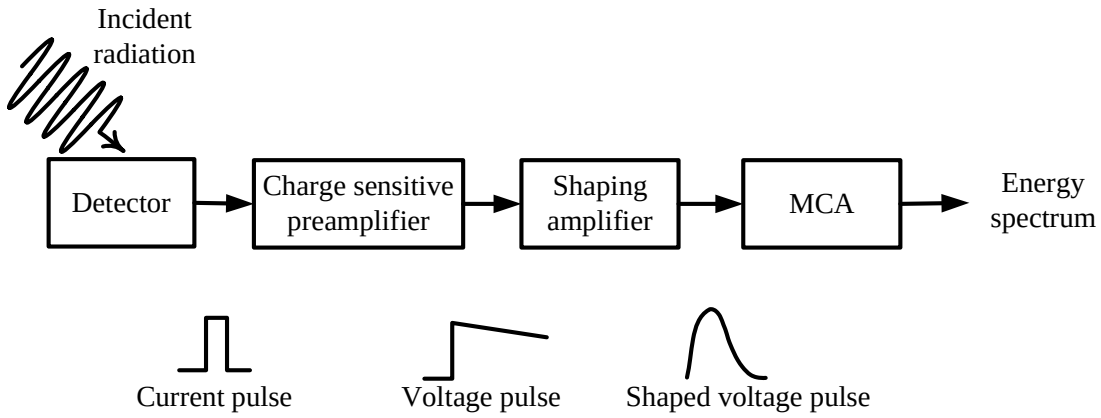

Figure 2.2. Block diagram of a spectroscopic system employing a semiconductor radiation detector.

For X-ray, γ-ray and β^- particle spectroscopy in this thesis, the detectors were connected to a custom built low noise charge sensitive preamplifier without feedback resistor of similar design to that reported by (Bertuccio et al., 1993). The preamplifier's input transistor was a Vishay 2N4416A Si Junction Field Effect Transistor (JFET) (Siliconix, 2001). The output signals from the preamplifier were shaped and amplified by an Ortec 572A shaping amplifier before being output to an Ortec EASY MCA 8k multi-channel analyser (MCA). The detector bias was applied using a Keithley 6487 voltage source.

2.5 Radiation sources used in this research

The X-rays and γ-ray photons used to study the detectors reported in this thesis were provided by three different radioisotope sources. Together they provided photon energies at characteristic energies from 5.9 keV to 88.03 keV. An ^{55}Fe radioisotope X-ray source provided Mn Kα (5.9 keV) and Mn Kβ (6.5 keV) X-rays (Schötzig, 2000). A ^{109}Cd radioisotope X-ray and γ-ray source provided Ag Kα (22.16 keV and 21.99 keV), Ag Kβ (24.94 keV, 24.99 keV, and 25.46 keV) X-rays and 88.03 keV γ-rays (Xiaolong et al., 2010). An ^{241}Am radioisotope γ-ray source provided γ-rays of characteristic energies up to 59.54 keV, as well as Np X-rays (Chu et al., 1996) (Verma, 2017) (Denecke, 1987). The electrons emitted from the ^{55}Fe and ^{109}Cd X-ray and X-ray and γ-ray sources, as well as the α particles emitted from the ^{241}Am radioisotope γ-ray source were entirely absorbed by a 250 μm Be X-ray window on each of the sources. The X-ray window of the ^{109}Cd radioisotope X-ray and γ-ray source attenuated the majority (> 99 %) of the Ag L X-rays emitted by that source.

The electrons (β^- particles) used to study the diamond detector reported in this thesis were provided by a ^{63}Ni radioisotope β^- particle source (endpoint energy = 66 keV; average energy 17.45 keV (Erjun & Junde, 2001)). The source was composed of an inactive Ni substrate onto which a 3 μm thick layer of ^{63}Ni had been electroplated. The active layer was then protected by a 1 μm thick inactive Ni electroplated layer to satisfy laboratory radiation safety protocols.

Chapter 3. Hard X-ray and γ-ray spectroscopy at high temperatures using a COTS 4H-SiC photodiode

3.1 Introduction

The work in this chapter has been published (see **Section Publications**). This chapter describes a commercial-off-the-shelf (COTS) silicon carbide (4H-SiC) UV photodiode that was electrically characterised and investigated as a low-cost spectroscopic photon counting detector of X-rays and γ-rays. The detector was coupled to a custom-built low noise charge sensitive preamplifier, and illuminated by ^{55}Fe and ^{109}Cd radioisotope X-ray sources and an ^{241}Am radioisotope γ-ray source, thus providing photon energies from 5.9 keV to 59.5 keV. The detector and preamplifier were operated uncooled at temperatures between 20 °C and 100 °C. At a temperature of 20 °C, the energy resolution (full width at half maximum, *FWHM*) of the spectrometer was found to be 1.66 keV ± 0.15 keV at 5.9 keV and 22.16 keV and 1.83 keV ± 0.15 keV at 59.5 keV. At a temperature of 100 °C, the *FWHM* were 2.69 keV ± 0.25 keV, 2.65 keV ± 0.25 keV, and 3.30 keV ± 0.30 keV, at the same energies. Shaping time noise analysis found dielectric noise to be the dominant noise source, except when long amplifier shaping times were used at high temperatures – under such conditions white parallel noise dominated. Noise associated with incomplete charge collection was found to be negligible at energies up to 22.16 keV and at temperatures ≤ 60 °C; however, incomplete charge collection noise could not be discounted when the spectrometer was operated at higher temperature (80 °C) and was detecting higher energy photons (59.5 keV). Although the detector was thin (and thus inefficient at high photon energies) the low cost and commercial availability of the 4H-SiC device make it an attractive prospect for use in cost-sensitive applications such as university-led CubeSat missions.

3.2 COTS 4H-SiC detector

The 4H-SiC detector used in this investigation was a randomly selected COTS UV p-n photodiode of geometry similar to that described by Prasai et al. (Prasai et al., 2012) and made by SG Lux GmbH, Berlin, Germany. The photodiode had an active area of 0.06 mm^2. The thickness of its n type and p type layers were 5 μm and 0.15 μm, respectively. The stated net donor and net acceptor concentrations were $N_D - N_A = 8 \times 10^{15}$ cm^{-3} and $N_A - N_D = 6 \times 10^{18}$ cm^{-3} (Prasai et al., 2012). The photodiode was purchased from a standard electronic components retailer. It was supplied packaged in a TO-18 can with a UV window. The UV window was removed prior to characterisation so that the photodiode could be illuminated directly by X-rays and γ-rays.

3.3 Experiments and results

3.3.1 Leakage current measurements

The 4H-SiC photodiode was placed in a custom-built electromagnetically-screened, and light-tight test harness located within a TAS Micro MT Climatic cabinet, and connected to a Keithley 6487 picoammeter/voltage source. The test harness was purged with dry N_2 (< 5 % relative humidity) before being sealed. Once the test harness was sealed, the climatic cabinet was continually purged with dry N_2 to ensure a dry environment and mitigate against any effects of humidity (Barnett et al., 2010). National Instruments LabVIEW software was used to automate the measurements. Leakage current as a function of reverse bias was measured at temperatures from 100 °C to 20 °C, in 20 °C intervals. To ensure that the 4H-SiC detector was at thermal equilibrium in the test harness during each measurement, 30 minutes waiting time was allowed at each test temperature before the bias was applied and the measurement made. The detector was reverse biased in 1 V increments up to a maximum of 175 V. The results are presented in **Figure 3.1**, where the diode's leakage current (including leakage current of the detector's packaging) is shown as a function of applied reverse bias. The maximum leakage current recorded was 78.4 pA ± 0.6 pA at 175 V reverse bias and 100 °C. The leakage current at 175 V and 60 °C was 2.1 pA ± 0.4 pA. At temperatures of 40 °C and below, the leakage current was within the noise floor of the picoammeter (± 0.4 pA) at all investigated reverse biases. At 100 V reverse bias, the leakage current was 42.7 pA ± 0.5 pA at 100 °C, and 1.1 pA ± 0.4 pA at 60 °C. As it is useful to compare these results with previous reports in the literature; leakage current densities were also considered. At 100 °C and at 60 °C respectively, the leakage current densities were 71.2 nA cm^{-2} ± 0.8 nA cm^{-2} and 1.8 nA cm^{-2} ± 0.7 nA cm^{-2}, respectively. These leakage current densities were greater than those reported by Bertuccio et al. (Bertuccio & Casiraghi, 2003) for a 30 μm thick 4H-SiC detector, where current densities of around 1 nA cm^{-2} were reported at 100 °C, at field strengths of 53 kV cm^{-1} and 103 kV cm^{-1}. At 104 kV cm^{-1} the COTS UV 4H-SiC photodiode had a leakage current density of 8.4 nA cm^{-2} ± 0.7 nA cm^{-2}, similar to that reported by Zhao et al. (Zhao et al., 2017) for a similar device from the same manufacturer (7.9 nA cm^{-2} ± 0.7 nA cm^{-2} at 101 kV cm^{-1}).

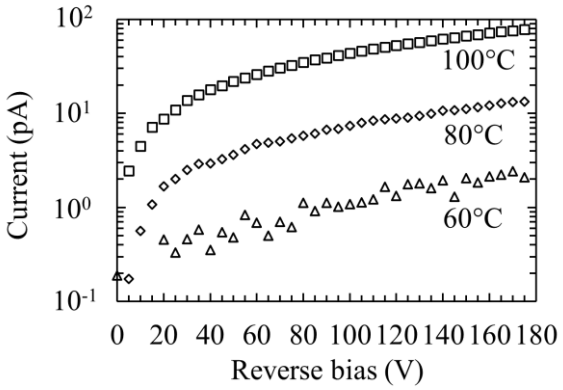

Figure 3.1. The 4H-SiC detector's leakage current as a function of reverse bias voltage; 100 °C (open squares), 80 °C (open diamonds), and 60 °C (open triangles). At an applied reverse bias of 175 V the leakage current measurement uncertainty was ± 0.6 pA and ± 0.4 pA at 100 °C and 60 °C, respectively.

3.3.2 Capacitance measurements

The capacitance of the detector was measured as a function of applied reverse bias and temperature. The photodiode was placed in another test harness, purged with dry N_2, and subjected to the same environmental regime in the same TAS Micro MT Climatic cabinet as had been used for the leakage current measurements. Capacitance measurements were recorded as a function of reverse bias from 0 V to 175 V, increasing in 1 V steps. Measurements were made from a temperature of 100 °C to 20 °C, in decrements of 20 °C. An HP 4275A multi frequency LCR meter, with a test signal of 50 mV rms magnitude and 1 MHz frequency, was used to measure the photodiode's capacitance as a function of applied reverse bias. The LCR meter was subject to an "open and short" correction in accordance with the manufacturers recommended procedure before measurement was commenced (Hewlett Packard, 1979). LabVIEW software was used to automate the process.

The detector's package and the bare-die detector each introduced capacitance when the assembly was reverse biased. The majority of package capacitance originated from the borosilicate glass insulation that insulated the TO package's isolated pin from the rest of the package. Other sources of stray capacitance included the silver loaded epoxy used to die attach the detector to the package. As the detector was wire bonded to its package in parallel with the packaging capacitance, a capacitance measurement of the packaged detector was followed by a capacitance measurement of a similarly prepared package with the detector's wire bonds removed. The capacitance of the packaged detector with bond-wires removed was subtracted from the capacitance of the detector

with wire bonds intact to estimate the capacitance of the detector's depleted width. The apparent depletion width was then calculated. The apparent depletion width as a function of applied reverse bias, $W(V_R)$, was calculated assuming that the diode may be approximated as a parallel plate capacitor (Sze & Ng, 2007), such that

$$W(V_R) = \frac{\varepsilon_0 \varepsilon A}{C_{DL}(V_R)} \tag{3.1}$$

where $C_{DL}(V_R)$ is the measured capacitance of the depletion layer, ε_0 is the permittivity of free space, ε is the relative permittivity (dielectric constant), and A is the effective area of the device. The diode's capacitance (with packaging capacitance subtracted) and its calculated apparent depletion width as a function of reverse bias at 100 °C and 20 °C are presented in **Figure 3.2**. The calculated depletion width of the detector at 100 V reverse bias was 2.47 µm ± 0.04 µm and 2.41 µm ± 0.03 µm at 100 °C and 20 °C, respectively. Within the uncertainties of the measurements, the apparent depletion width did not vary over the temperatures investigated. Despite an epitaxial layer width of 5.15 µm (Prasai et al., 2012), at face value the capacitance measurements suggest that only a portion of the epitaxial layer was depleted, reaching a maximum of 2.41 µm ± 0.03 µm at 100 V reverse bias. Given the manufacturer stated donor concentration (8×10^{15} cm^{-3}) (Prasai et al., 2012) and the abrupt junction approximation (Sze & Ng, 2007), a depletion width of 3.7 µm at 100 V would have been expected, although no uncertainty in the concentration was stated by the manufacturer.

The inverse of the capacitance per unit area squared, $1/C^2$, was plotted as a function of applied detector reverse bias **Figure 3.2 (c)** to calculate the donor concentration from the abrupt junction approximation. On the basis that the detector epitaxial layer depleted to 2.41 µm at 100 V reverse bias, the donor concentration of the n type layer was calculated to be 1.8×10^{16} cm^{-3} at 100 °C and 2.0×10^{16} cm^{-3} at 20 °C. The manufacturer's stated donor concentration (8×10^{15} cm^{-3}) being less than the calculated donor concentration suggested that the detector's depletion width was greater than the 2.41 µm ± 0.03 µm determined from **Equation 3.1**. The built-in potential of the 4H-SiC detector, calculated from **Figure 3.2 (c)**, was ≈ 10 V.

Also, despite the depletion region seemingly being only a portion of the epitaxial layer thickness, results previously reported for a detector of the same type (but in that case used as an electron spectrometer (Zhao et al., 2018)) suggested that the entire epitaxial width of the detector was active for radiation detection. It is possible that a significant portion of the epitaxial layer was not depleted and that despite this the whole of the epitaxial layer contributed to the detected signal since the electron and hole recombination lengths in $N_D - N_A = 8 \times 10^{15}$ cm^{-3} n type and $N_A - N_D = 6 \times 10^{18}$ cm^{-3} p type doped 4H-SiC are ≈ 1.1 µm (Liaugaudas et al., 2015) and ≈ 20 µm

(Grivickas et al., 1999), respectively. Nevertheless, care should be taken in interpreting the capacitance measurements since they were made using packaged devices rather than bare dice. Furthermore, the computation of the depletion width from measurements relies on approximation of the detector to a parallel plate capacitor. The sensitivity of the measurements to additional capacitances is also noted; an unaccounted 1.87 pF capacitance in series with the detector would result in a detector of capacitance ≈ 1 pF (i.e. depletion width of ≈ 5 μm) appearing to have the capacitance characteristics measured above. The reason for the discrepancy in depletion width between the measurement of capacitance as a function of reverse bias, the doping density calculation, and the epitaxial layer thickness are unknown. However, given that the electron spectroscopy measurements of Zhao et al. (Zhao et al., 2018) indicated that the whole of the epitaxial thickness was active, the full thickness of the epitaxial layer (5.15 μm) was assumed to be active and depleted for the quantum detection efficiency calculation below. Nevertheless, the simplicity of this assumption is recognized. Other effects may also reduce the active layer thickness of the detector; for example, if the detector had a recombination region close to the contact (as has been measured in other X-ray photodiodes (Lioliou et al., 2016)) this would reduce the thickness of the active layer, and the quantum detection efficiency of the device would be reduced both as a consequence of the reduction in active layer thickness and because of the introduction of a deadlayer ahead of the active layer.

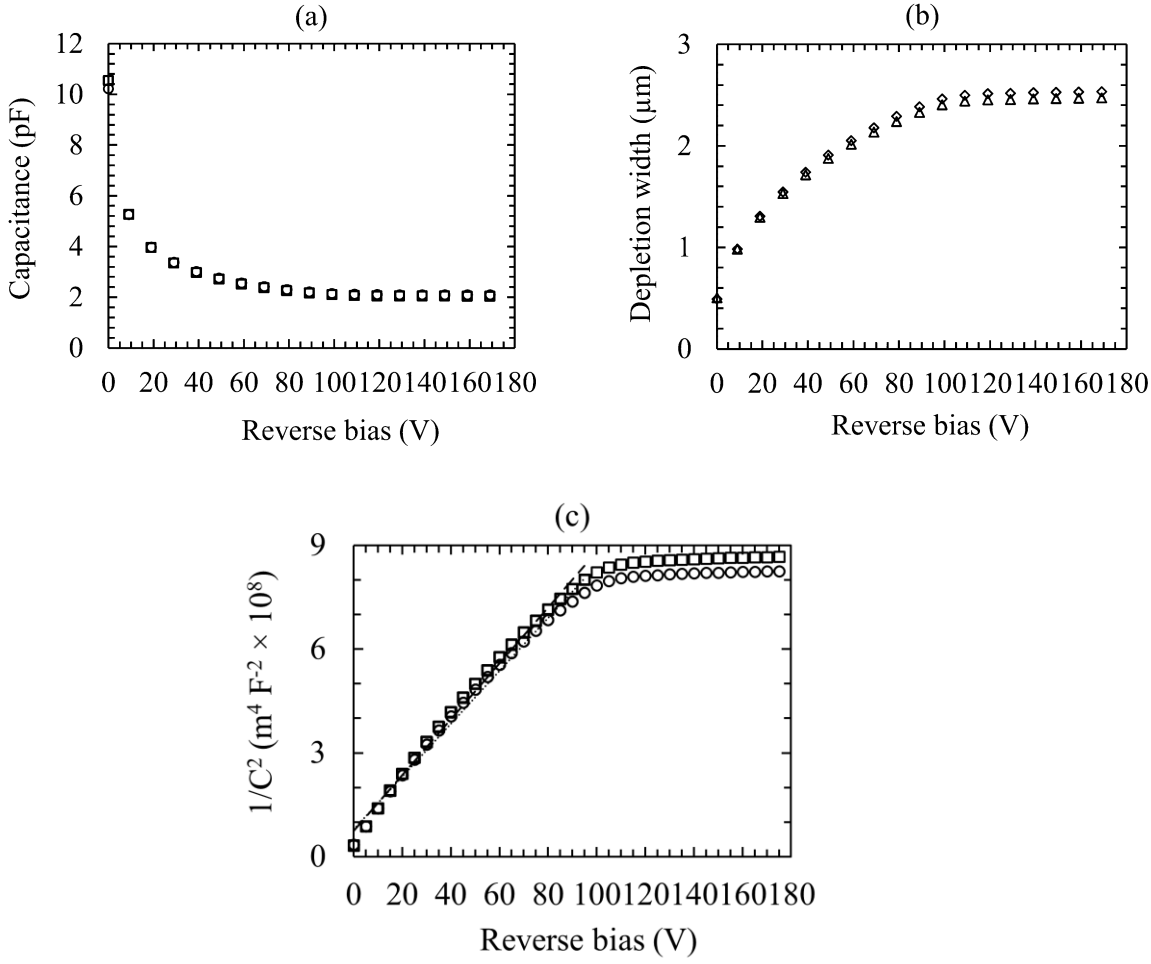

Figure 3.2. (a) The 4H-SiC diode's capacitance at 100 °C (open squares) and 20 °C (open circles) as a function of applied detector reverse bias; (b) the apparent depletion width implied by the measured capacitances at 100 °C (open diamonds) and 20 °C (open triangles) as a function of reverse bias and (c) $1/C^2$ at 100 °C (open squares) and 20 °C (open circles) as a function of reverse bias used to calculate the doping density of the n type epitaxial width of the 4H-SiC diode. Error bars are omitted for clarity; at 100 V depletion width, the uncertainties were ± 0.04 μm and ± 0.03 μm at 100 °C and 20 °C, respectively.

Assuming a 5.15 μm active region thickness, the quantum detection efficiency, *QE*, of the detector from 1 keV to 60 keV was calculated using the Beer-Lambert-Bouguer Law (**Equation 2.1**) for light attenuation and absorption,

$$QE = \prod_{i=1}^{i=n} \exp\left(\mu_i \rho_i t_i\right)\left(1 - \exp\left(\mu_{en} \rho t\right)\right), \tag{3.2}$$

where μ_i is the mass attenuation coefficient of inactive layers before the detecting medium, ρ_i is layer density, t_i is layer thickness, μ_{en} is the mass absorption coefficient of the detecting medium,

ρ is its density, and t is thickness of the detector's active layer (Hubbell, 1999). Mass absorption and attenuation coefficients were obtained from the NIST XCOM database (Berger et al., 2010).

The calculated quantum detection efficiency of the 4H-SiC detector is presented in **Figure 3.3**; the discontinuity shown at 1.8 keV is the Si K absorption edge. The 4H-SiC material's inherent properties, and the thickness of the diode's active layer, limited the *QE* of the photodiode, Si and C have relatively low linear X-ray attenuation coefficients when compared with many other wide bandgap compound semiconductor materials used for detectors. The *QE* of the energies of specific interest for the results reported presently were 0.167 at 5.9 keV, 3.52×10^{-3} at 22.16 keV, and 1.56×10^{-4} at 59.5 keV. For comparison, the *QE* of a GaAs detector of equal thickness would have been 0.349, 8.26×10^{-2}, and 5.02×10^{-3} at the same photon energies. It should be noted that the quantum detection efficiency calculations did not account for any carrier recombination region close to the front contact of the detector, which would have reduced the quantum detection efficiency of the detector, from that calculated (Lioliou et al., 2015)

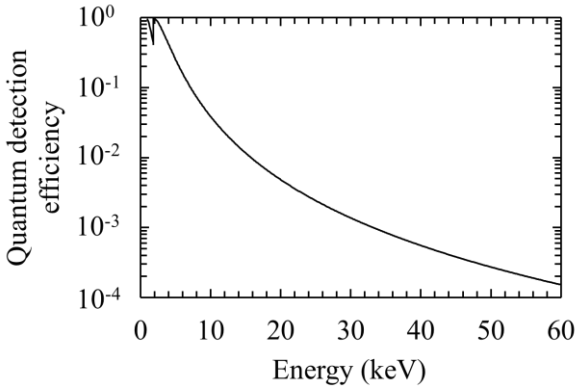

Figure 3.3. Quantum detection efficiency of the 4H-SiC diode reverse biased at 100 V. The discontinuity at 1.8 keV is the Si K absorption edge.

3.4 X-ray and γ-ray spectroscopy

The 4H-SiC photodiode was connected to a custom-built low noise feedback resistorless charge sensitive preamplifier (similar in design to that reported by Bertuccio et al. (1993). The input transistor was a Vishay 2N4416A Si Junction Field Effect Transistor (JFET) (Siliconix, 2001). Output signals from the preamplifier were shaped and amplified by an Ortec 572A shaping amplifier before being output to an Ortec EASY MCA 8k multi-channel analyser (MCA). The detector bias was applied using a Keithley 6487 voltage source. Each radioisotope X-ray/γ-ray source (^{55}Fe, ^{109}Cd, ^{241}Am) was placed ≈ 9 mm above the detector in turn.

The test harness containing the 4H-SiC detector, preamplifier, and each radioisotope X-ray/γ-ray source, was located inside a TAS Micro MT climatic cabinet for temperature control. The other equipment was located outside of the climatic cabinet and operated at ambient laboratory temperature. The temperature inside the climatic cabinet was raised to 100 °C, and then decreased in 20 °C steps to 20 °C; spectra were accumulated at each set temperature. The process was repeated using each radioisotope X-ray/γ-ray source. All spectra were accumulated with the detector reverse biased at 100 V.

3.4.1 ^{55}Fe and ^{109}Cd X-ray spectroscopy

First, spectra were accumulated with an ^{55}Fe radioisotope X-ray source (activity 121 MBq). The spectra were accumulated at all available amplifier shaping times (τ = 0.5 μs, 1 μs, 2 μs, 3 μs, 6 μs, and 10 μs). The live time for each spectrum was 360 s. The photopeak detected in response to illumination with the ^{55}Fe radioisotope X-ray source was a combination of the characteristic ^{55}Fe Mn Kα (5.9 keV) and Mn Kβ (6.49 keV) X-ray emissions (Schötzig, 2000). Gaussians that took account of the relative emission ratios, and the relative detection efficiency of the SiC X-ray detector, were fitted to the detected photopeaks to deconvolve the contributions of the closely spaced X-ray emissions (e.g. Mn Kα and Kβ lines). The spectrometer was then calibrated using the position of the spectrometer's zero energy noise peak and a fitted X-ray peak (in this case the Mn Kα line), assuming a linear variation of charge with energy on the MCA's charge scale. A representative ^{55}Fe X-ray spectrum is presented in **Figure 3.4 (a)**. The counts of the zero energy noise peak in this spectrum were eliminated by setting the MCA low energy cut-off at ≈ 2.5 keV after determination of the zero energy noise peak's position. However, a small portion of the right hand side of the zero energy noise peak can still be seen. The total corresponding photocurrent, calculated from the total counts in a spectrum, was ~ 0.03 pA at all temperatures and shaping times. The energy resolution of the spectrometer (as quantified by the *FWHM* of the fitted Mn Kα photopeak at the best available shaping time) as a function of temperature is shown in **Figure 3.5 (a)**. It should be noted that the shaping time at 20 °C could be further optimized if the shaping amplifier had shaping times longer than 10 μs. The *FWHM* of the Mn Kα photopeaks improved from 2.69 keV ± 0.25 keV at 100 °C (at 1 μs shaping time) to 1.66 keV ± 0.15 keV at 20 °C (at 10 μs shaping time).

A second group of spectra were collected with the ^{55}Fe radioisotope X-ray source replaced with a ^{109}Cd radioisotope X-ray source (activity 296 MBq). Each ^{109}Cd spectrum had a live time of 2100 s. The same shaping times were used as for the ^{55}Fe X-ray measurements. The 88.03 keV γ-rays from the ^{109}Cd radioisotope source were not detected by the spectrometer because of the photodiode's low *QE* at 88.03 keV, the relatively low emission probability of that γ-ray, and the

relatively short live time. A 0.23 mm PTFE attenuator was placed between the ^{109}Cd radioisotope X-ray source and the detector to limit the photon count rate at lower energies where an Fe (Kα = 6.4 keV) fluorescence peak from the ^{109}Cd radioisotope source's capsule would have otherwise overshadowed the accumulated spectrum. The PTFE attenuated 0.730 and 0.038 of the fluorescent Fe Kα (6.4 keV) and ^{109}Cd Ag $K\alpha_1$ (22.16 keV) X-ray photons respectively. The characteristic photopeaks detected from the ^{109}Cd radioisotope X-ray source were a combination of the five characteristic Ag Kα (21.99 keV and 22.16 keV) and Kβ (24.91 keV, 24.94 keV, and 25.45 keV) emission lines (Chu et al., 1996). To measure the *FWHM* of the detected Ag $K\alpha_1$ (22.16 keV) peak, five Gaussians were fitted to each accumulated spectrum. The spectrometer was calibrated in an analogous manner as for the ^{55}Fe X-ray spectra, using the fitted Ag $K\alpha_1$ (22.16 keV) emission peak. A representative ^{109}Cd X-ray spectrum accumulated with the spectrometer is presented in **Figure 3.4 (b)**. In this spectrum, the counts of the zero energy noise peak were eliminated by setting the MCA low energy cut-off at ≈ 4 keV after determination of the position of the zero energy noise peak as per the ^{55}Fe X-ray spectra. An Fe (Kα = 6.4 keV) X-ray fluorescence peak from the ^{109}Cd radioisotope X-ray source's capsule was still visible despite the inclusion of the attenuator to limit detection of such fluorescence photons. The low *QE* of the 4H-SiC detector at higher energy limited the photon count rate of the detector at higher energies. The average count rate in the Ag $K\alpha_1$ (22.16 keV) photopeak was 10.1 s^{-1} ± 0.2 s^{-1} and 9.2 s^{-1} ± 0.2 s^{-1} at 100 °C and 20 °C, respectively. The equivalent photocurrent created in the 4H-SiC photodiode, as calculated from the total counts in the detected ^{109}Cd spectrum was ≈ 0.009 pA, was thus negligible as a steady state current noise source. The measured *FWHM* of the Ag $K\alpha_1$ photopeak, at the best available shaping time, as a function of temperature is shown in **Figure 3.5 (b)**. The *FWHM* of the Ag $K\alpha_1$ photopeak reduced from 2.65 keV ± 0.25 keV at 100 °C (at 1 µs shaping time) to 1.66 keV ± 0.15 keV at 20 °C (at 2 µs shaping time). The low energy tailing seen in **Figure 3.4** (e.g. as the saddle between the Ag Kα peak and the Fe Kα peak in **Figure 3.4 (b)**) was attributed to partial collection of charge created outside of the active region of the detector (Barnett et al., 2015).

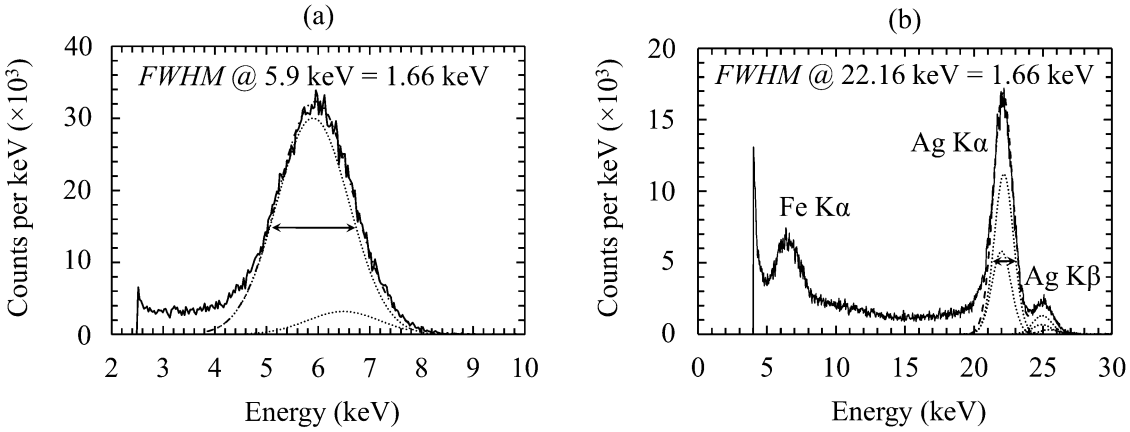

Figure 3.4. Representative (a) ^{55}Fe and (b) ^{109}Cd X-ray spectra accumulated using the 4H-SiC X-ray spectrometer (solid line) at 20 °C, with the detector reverse biased at 100 V, and using 10 μs and 2 μs shaping times, respectively. Dashed lines are the combined contributions of the fitted Gaussians; dotted lines are the respective contributions of the Mn and Ag Kα and Kβ emissions.

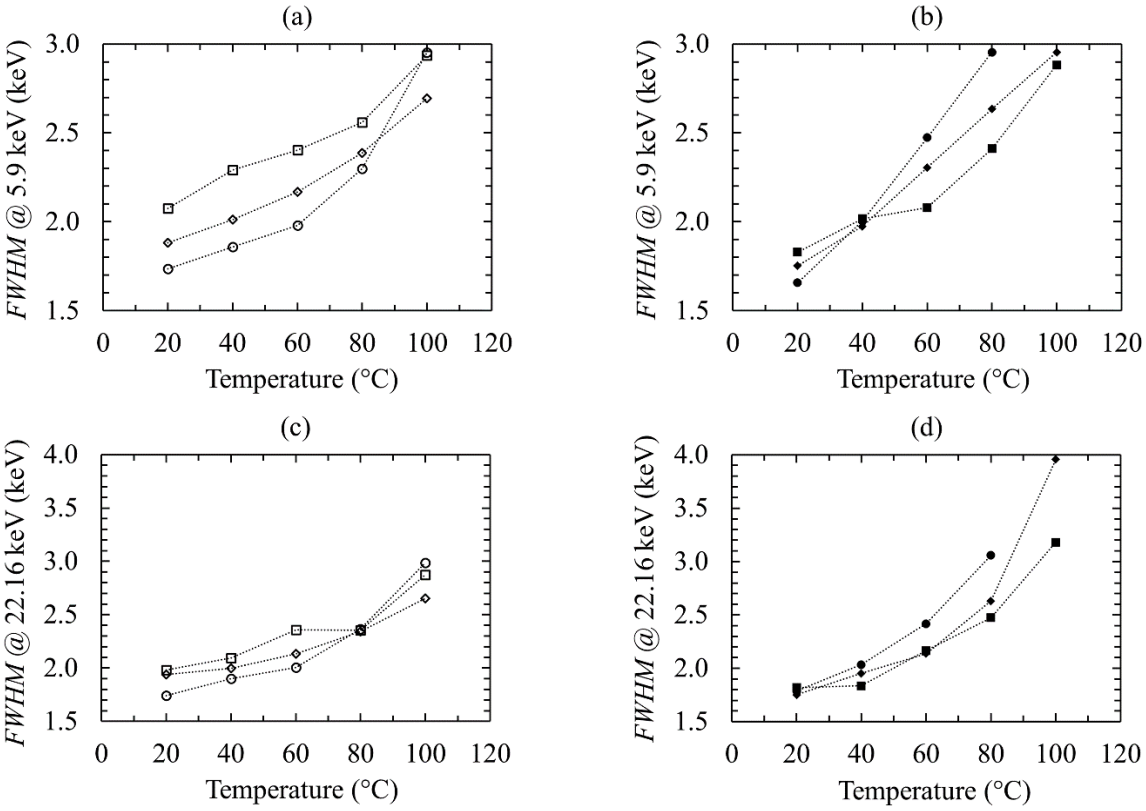

Figure 3.5. *FWHM* of the fitted Mn Kα (5.9 keV) and Ag Kα$_1$ (22.16 keV) photopeaks at all the shaping time constants available to the shaping amplifier as a function of temperature. Mn Kα (5.9 keV) photopeak *FWHM* at (a) 0.5 μs (open squares), 1 μs (open diamonds), 2 μs (open

circles), and (b) 3 μs (filled squares), 6 μs (filled diamonds), 10 μs (filled circles). Ag $K\alpha_1$ (22.16 keV) photopeak *FWHM* at (c) 0.5 μs (open squares), 1 μs (open diamonds), 2 μs (open circles), and (d) 3 μs (filled squares), 6 μs (filled diamonds), 10 μs (filled circles). Lines are a guide for the eye only.

Within the uncertainties of fitting the *FWHM* of the Mn Kα (5.9 keV) and Ag $K\alpha_1$ (22.16 keV) spectra broadened as temperature was increased. Best resolution (minimum *FWHM*) generally occurred with the shaping amplifier time constant ≈ 2 μs and the shaping times that yielded the best (lowest) *FWHM* at 5.9 keV and 22.16 keV were similar within the uncertainties of measurements. As an example, at 20 °C the *FWHM* of the 5.9 keV photopeak was 1.66 keV ± 0.15 keV at 10 μs shaping time and 1.74 ± 0.15 keV at 2 μs shaping time. At the same temperature, the *FWHM* of the 22.16 keV photopeak was 1.74 keV ± 0.15 keV at 10 μs shaping time and 1.66 ± 0.15 keV at 2 μs shaping time. It was therefore useful to select the shaping times that produced the best *FWHM* at both energies to compare the performance of the spectrometer at 5.9 keV and 22.16 keV. The *FWHM* of the 5.9 keV and the 22.16 keV photopeak at identical shaping times are presented in **Figure 3.6**.

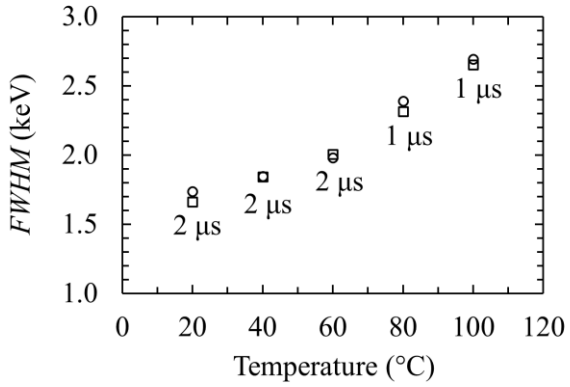

Figure 3.6. *FWHM* of the Mn Kα (open circles) and the Ag $K\alpha_1$ (open squares) X-ray photopeaks as a function of temperature at the same amplifier shaping times.

The *FWHM* of the Mn Kα (5.9 keV) and the Ag $K\alpha_1$ (22.16 keV) photopeaks were 2.69 keV ± 0.25 keV and 2.65 keV ± 0.25 keV respectively at 100 °C and 1 μs shaping time; at 20 °C and 2 μs shaping time the *FWHM* reduced to 1.74 keV ± 0.15 keV and 1.66 keV ± 0.15 keV, respectively. The optimum shaping time of the spectrometer and the different noise components associated with the photopeaks' broadening are discussed in **Section 3.5**.

3.4.2 ^{241}Am X-ray and γ-ray spectroscopy

The spectrometer was also investigated using an ^{241}Am X-ray/γ-ray source (activity 298 MBq) to illuminate the detector. The experimental set up and investigated temperature range for the ^{241}Am measurements was the same as was described for the ^{55}Fe and ^{109}Cd radioisotope X-ray source measurements. However, due to the lower quantum detection efficiency (1.56×10^{-4}) of the detector for the 59.5 keV γ-ray photons emitted by the ^{241}Am radioisotope γ-ray source, spectra were collected using only one shaping time at each investigated temperature. At temperatures ≥ 80 °C, spectra were accumulated at a shaping time of 1 μs; at temperatures < 80 °C, spectra were accumulated at a shaping time of 2 μs. Each spectrum had a live time of 6 days. Prior measurements were made to establish that the detector and preamplifier electronics were stable over durations of this length. To minimize disturbance to the detector and preamplifier front end electronics, the PTFE attenuator mentioned in **Section 3.4.1** was retained between the radioisotope radiation source and the detector; its attenuation of the 59.5 keV γ-rays was negligible (transmission = 0.991).

The spectrometer detected the characteristic ^{241}Am Np Lα (13.95 keV, 13.76 keV), Lβ (17.75 keV, 16.82 keV, 17.06 keV, 17.99 keV, and 17.51 keV), and Lγ (20.78 keV, 21.10 keV and 21.34 keV) X-ray emissions as well as the two ^{241}Am γ-ray emission lines (26.34 keV and 59.54 keV) (Chu et al., 1996). The sets of Np Lα, Lβ, and Lγ X-ray emissions formed three combined photopeaks since their individual components were not resolved by the spectrometer. Gaussians were fitted to the detected Np Lα, Np Lβ, ^{241}Am γ_1, and ^{241}Am γ_2 photopeaks. The spectrum accumulated at 20 °C is presented in **Figure 3.7 (a)**. An Fe (Kα = 6.4 keV) fluorescence peak from the capsule of the ^{241}Am radioisotope X-ray/γ-ray source is also visible. The measured *FWHM* of the fitted Np $L\alpha_1$, Np $L\beta_1$, ^{241}Am γ_1, and ^{241}Am γ_2 peaks are shown as functions of temperature in **Figure 3.7 (b)**. The *FWHM* at 59.5 keV was 3.38 keV ± 0.30 keV at 100 °C (1 μs shaping time), this improved to 1.83 keV ± 0.15 keV at 20 °C (2 μs shaping time). The MCA's charge scale was calibrated using the position of the detected ^{241}Am γ_1 (59.5 keV) peak and the position of the zero energy noise peak. At 20 °C, the Gaussian peak fitted to the ^{241}Am γ_1 photopeak contained a total of 23006 counts.

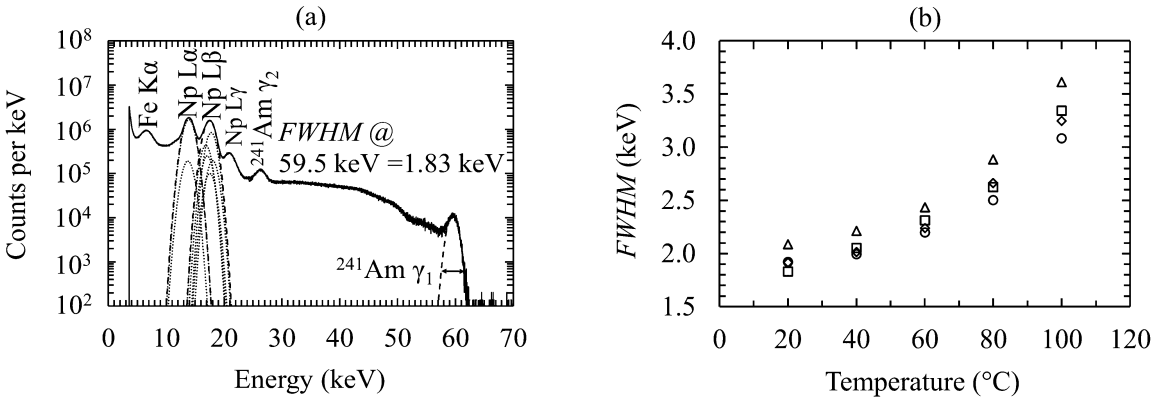

Figure 3.7. (a) ^{241}Am X-ray/γ-ray spectrum accumulated by the 4H-SiC spectrometer at 20 °C and using a 2 μs shaping time (solid line). Dashed lines are the combined contributions fitted Gaussians; the dotted lines are the Np Lα and Lβ emission lines respectively. (b) Measured *FWHM* of the ^{241}Am Np Lα_1 (13.95 keV) (open triangles), Np Lβ_1 (17.75 keV) (open diamonds), ^{241}Am γ_2 (26.34 keV) (open circles) and ^{241}Am γ_1 (59.5 keV) (open squares) emission lines, at 1 μs (≥ 80 °C) and 2 μs (< 80 °C) shaping times, as a function of temperature.

3.5 Noise analysis and discussion

The noise in a direct detection (i.e. without scintillator) non-avalanche photodiode photon counting X-ray or γ-ray spectrometer is commonly considered to be separated into three independent contributions: Fano noise, which is related to the stochastic nature of the charge creation processes in the detector (Fano, 1947); incomplete charge collection noise, which arises from any charge carrier trapping and recombination in the detector (Owens, 2012); and electronic noise, which can be further separated into four components, white parallel noise, white series noise including induced gate current noise, 1/*f* series noise, and dielectric noise. For a review of these electronic noise components, the reader is directed to refs. (Bertuccio & Pullia, 1993) (Barnett et al., 2012b) and **Section 2.3**. White parallel and white series noises vary with shaping time, whilst the other components are shaping time invariant. White parallel noise (driven by the total current at the input of the JFET (which arises from the leakage current in the drain-to-gate and the gate-to-source junctions of the input JFET and from the detector employed within the spectrometer)) increases as shaping time is increased; white series noise (driven by the total capacitance at the input of the JFET) decreases as shaping time is increased.

The combined contribution of the shaping time invariant noise components and shaping time variant noise contributions were extracted from the *FWHM* measurements made at 5.9 keV (^{55}Fe Mn Kα) and 22.16 keV (^{109}Cd Ag Kα_1), as functions of shaping time, by performing

multidimensional least squares fitting. Results of the multidimensional least squares fittings, at 20 °C and 80 °C, for the 5.9 keV data are presented in **Figure 3.8**. At 100 °C there were an insufficient number of data points (shaping times) to conduct the multidimensional least squares fitting; only four shaping times were collected because of increased noise. The multidimensional least squares fittings for the Ag $K\alpha_1$ (22.16 keV) data at 20 °C, 80 °C, and 100 °C are presented in **Figure 3.9**.

The best (narrowest) *FWHM* was achieved when the quadratic sum of white series and white parallel noise were a minimum. As an example, the best available shaping time to resolve the 5.9 keV (Mn Kα) photopeak at 20 °C was 10 μs in the present system (**Figure 3.5 (a)**). The quadratic sum of white series noise and white parallel noise were a minimum at 10 μs shaping time (**Figure 3.8 (a)**). For this X-ray energy (5.9 keV) and operating temperature (20 °C) the magnitude of the parallel white noise component was below the magnitude of the series white noise component at all the available shaping times.

In **Figure 3.8** and **Figure 3.9**, Fano noise and 1/*f* series noise were subtracted in quadrature from the combined shaping time invariant noise contributions, to show the quadratic sum of dielectric and incomplete charge collection noise.

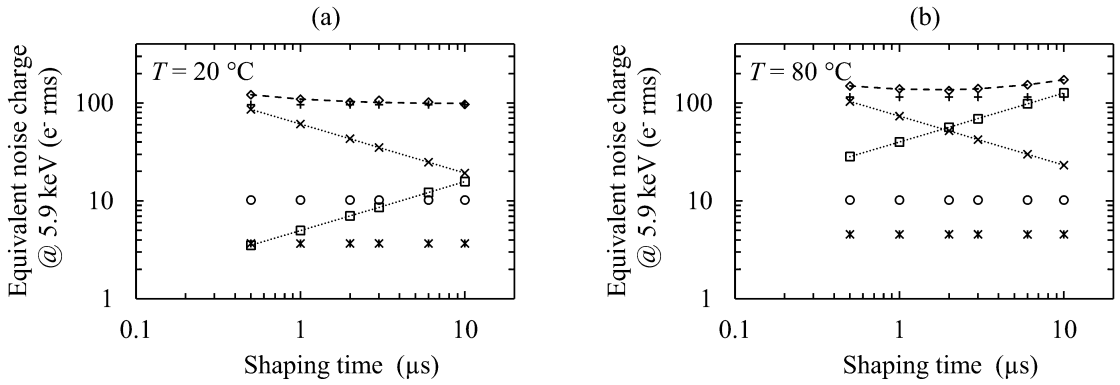

Figure 3.8. *FWHM* and noise contributions as a function of amplifier shaping time of the ^{55}Fe 5.9 keV Mn Kα X-ray photopeak (open diamonds) at (a) 20 °C and (b) 80 °C. Quadratic sum of dielectric and incomplete charge collection noise (+ symbols), white parallel noise (open squares), white series noise (× symbols), Fano noise (open circles), 1/*f* series noise (stars). Lines are a guide for the eye only.

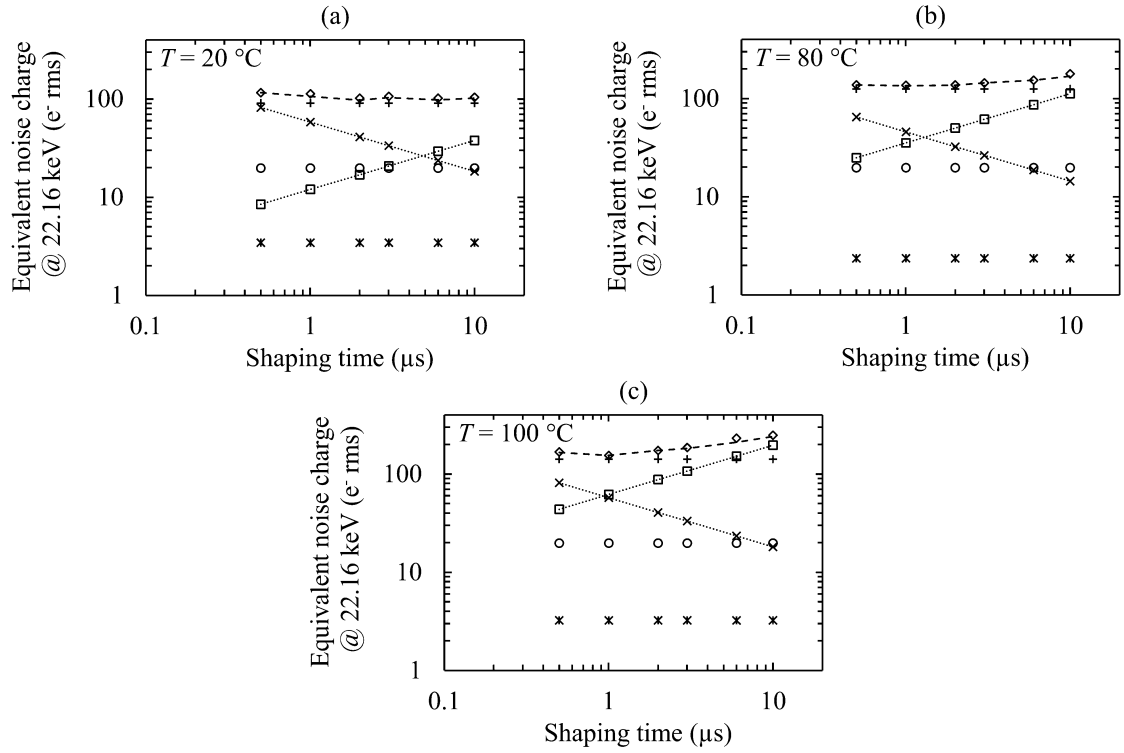

Figure 3.9. *FWHM* and noise contributions as a function of amplifier shaping time of the ^{109}Cd 22.16 keV Ag Kα_1 X-ray photopeaks (open diamonds) at (a) 20 °C, (b) 80 °C, and (c) 100 °C. Quadratic sum of combined dielectric and incomplete charge collection noise (+ symbols), white parallel noise (open squares), white series noise (× symbols), Fano noise (open circles), 1/*f* series noise (stars). Lines are a guide for the eye only.

The Fano noise was calculated assuming a Fano factor of 0.128 and electron-hole pair creation energy of 7.28 eV (Chaudhuri et al., 2013). Fano noise was calculated to be 10 e^- rms (175 eV *FWHM*), 20 e^- rms (338 eV *FWHM*), and 32 e^- rms (555 eV *FWHM*) at 5.9 keV, 22.16 keV, and 59.5 keV, respectively. 1/*f* series noise was calculated using the total capacitance at the input of the preamplifier derived from the multidimensional least squares fitting, with the capacitance of the preamplifier JFET estimated to be 2 pF (Siliconix, 2001) (Bertuccio & Pullia, 1993). Comparison between the quadratic sum of dielectric and incomplete charge collection noise at two energies, in this case 5.9 keV and 22.16 keV, can be used to infer the presence or absence of incomplete charge collection noise in the spectroscopic system. The quadratic combination of dielectric and incomplete charge collection noise can be computed by subtraction in quadrature of the other (known) components outlined above. Since the total dielectric noise was unknown, incomplete charge collection noise could not be computed directly by subtraction (in quadrature) of dielectric noise. However, since dielectric noise is photon energy invariant and incomplete charge collection noise is known to be photon energy dependent (Owens & Peacock, 2004) it was

possible to determine if incomplete charge collection noise was significant by consideration of the spectrometer's response to different photon energies.

At 5.9 keV, the quadratic sum of dielectric and incomplete charge collection noise decreased from 115 e^- rms ± 3 e^- rms (1.97 keV *FWHM*) at 80 °C to 96 e^- rms ± 5 e^- rms (1.65 keV *FWHM*) at 20 °C. At 22.16 keV, the quadratic sum of dielectric and incomplete charge collection noise decreased from 125 e^- rms ± 3 e^- rms at 80 °C (2.14 keV *FWHM*) to 91 e^- rms ± 5 e^- rms (1.55 keV *FWHM*) at 20 °C. The reduction of dielectric noise with temperature is well documented (Barnett et al., 2012b) (Lioliou & Barnett, 2015), but the specific quantitative reduction is impossible to predict without knowledge of the dielectric dissipation factors of each material contributing to the lossy dielectrics at the preamplifier's input. Although at each temperature, the quadratic sum of dielectric and incomplete charge collection noise, at each energy, were approximately equal, at 80 °C the difference (in quadrature) between dielectric noise and incomplete charge collection noise at 22.16 keV and 5.9 keV was significant (49 e^- rms ± 4 e^- rms). However, this difference in dielectric and incomplete charge collection noise between energies (5.9 keV and 22.16 keV) at 80 °C must be considered alongside other calculated noise contributions. For example, at 80 °C and at 1 μs shaping time the difference (in quadrature) of the white series noise at 5.9 keV and 22.16 keV was 57 e^- rms, and at longer shaping times similar differences in white parallel noise were recorded. Thus, it was not clear if any incomplete charge collection noise was present in the detector at 80 °C. Nevertheless, the dominant contributor to noise in the quadratic sum of dielectric and incomplete charge collection noise was dielectric noise.

It is useful to compare the capacitance and depleted width of this detector and hence the dielectric noise measured herein with other detectors previously reported in the literature. The capacitance of the COTS 4H-SiC detector was measured to be 2.7 pF when a reverse bias of 100 V was applied to the detector (**Figure3.2 (a)**); at this applied reverse bias the depleted width of the detector was reasoned to be ≈ 5 μm (**Section 3.3.2)**. A previous custom grown 4H-SiC wafer from which devices had been fabricated and employed as X-ray and γ-ray detectors had C_{DL} = 16 pF and a depleted width of 16 μm (**Section 1.1.1**) (Bertuccio et al., 2001). Low noise spectroscopic results with custom grown 4H-SiC wafers (44 e^- rms of noise found from precision charge injection) were first reported with 25 μm active widths with significantly lower capacitance (1.3 pF (**Section 1.1.2**) (Bertuccio et al., 2004). The best resolved X-ray and γ-ray spectra so far achieved with a custom made 4H-SiC device used a fully depleted n type epilayer (124 μm thick), with doping concentration = 5.2×10^{13} cm^{-3}. With a low and uniform doping concentration the capacitance of the wafer was 1.14 pA when fully depleted (Puglisi & Bertuccio 2019).

The known components of the dielectric noise (those that are readily calculable) are the noise contributions from the 4H-SiC detector and the Si JFET, whilst the unknown dielectric noise contributions are the detector's packaging and feedback, stray and test capacitances of the preamplifier (Lioliou & Barnett, 2015). The unknown dielectric noise contributions are not easily estimated given the lack of detailed knowledge of the dielectric dissipation factors and the dielectric constants of every source of capacitance within the preamplifier. The dielectric noise contribution from the 4H-SiC detector and the Si JFET can be estimated from capacitance measurements previously made on the 4H-SiC detector and attributing a nominal capacitance (2 pF (Siliconix, 2001)) to the Si JFET. The estimated dielectric noise contribution of the 4H-SiC detector and the Si JFET decreased from 5.6 e^- rms ± 0.3 e^- rms (95 eV ± 5 eV) to 5.2 e^- rms ± 0.3 e^- rms (90 eV ± 5 eV) and 28 e^- rms (480 eV) to 24 e^- rms (410 eV) from 80 °C to 20 °C respectively. Given that the dielectric noise contributions of the 4H-SiC detector and the Si JFET were low when compared with the quadratic sum of dielectric and incomplete charge collection noise calculated above there are opportunities to improve the resolution of the spectrometer by reducing or eliminating some of the stray capacitance (and the associated dielectric noise) acting at the input of the preamplifier. The preamplifier's JFET was packaged in a TO can, a simple noise reduction measure would be to locate the JFET and detector on a single package with the detector directly wire bonded to the JFET. Furthermore, the preamplifier's PCB was FR-4, replacing the FR-4 board with a PTFE or ceramic PCB would further reduce stray capacitance (and associated dielectric noise). A 4H-SiC JFET would also be beneficial (Lioliou & Barnett, 2015).

White parallel noise (driven, in part, by leakage current) increased in magnitude at all shaping times as the temperature was raised, this was expected since the effect of increased temperature was to increase the leakage current of the packaged detector and the preamplifier's Si input JFET. As an example, considering the noise at 22.16 keV, the white parallel noise component at a shaping time of 1 µs increased from 12 e^- rms to 62 e^- rms from 20 °C to 100 °C respectively. The combined leakage currents of the 4H-SiC detector and Si JFET at the front of the preamplifier calculated from the linear least squares fittings is presented as a function of temperature in **Figure 3.10**. The packaged detector's leakage current (**Section 3.3.1**) was a small component of this total leakage current. The total leakage current in **Figure 3.10** represents the leakage current of the detector, the reverse biased JFET drain-to-gate junction current, and the forward biased JFET gate-to-source junction current. When all the different leakage currents are independent of each other, the total system leakage current is equal to twice the sum of the detector's leakage current and the JFET's drain-to-gate leakage current (Bertuccio & Casiraghi, 2003) (Lioliou & Barnett, 2015). The source of an n type JFET such as that used in this preamplifier, is set to ground;

consequently, the JFET's drain-to-gate leakage current was controlled by the drain-to-source and drain-to-gate potential differences. When the detector's leakage current decreased, the JFET's gate-to-source voltage decreased which caused the JFET's drain-to-gate voltage to increase, which caused the JFET's drain-to-gate current to rise. Therefore, when the leakage current of the detector (which fed into the gate of the JFET) fell, the reduction in the total leakage current of the spectrometer was offset by a rise in the JFET drain-to-gate leakage current. This relationship between detector and JFET leakage current can be seen in the leakage current results shown in **Figure 3.1** and **Figure 3.10**. At 80 °C, the detector's leakage current was 7.37 pA ± 0.42 pA at 100 V reverse bias, the corresponding currents at the input to the preamplifier calculated from the multidimensional least squares fittings were 169 pA ± 18 pA and 136 pA ± 16 pA, when the 4H-SiC X-ray spectrometer was illuminated by the ^{55}Fe and ^{109}Cd radioisotope X-ray sources, respectively. At 60 °C, detector leakage current was 1.08 pA ± 0.40 pA, and the corresponding calculated currents at the input to the preamplifier were 108 pA ± 11 pA, and 72 pA ± 19 pA for the same X-ray sources. When the detector's leakage current reduced, the leakage current from the JFET's drain-to-gate junction was a proportionately larger part of the total system leakage current.

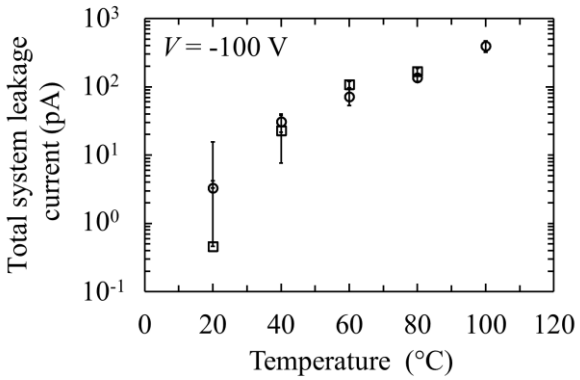

Figure 3.10. The total current contribution of the 4H-SiC diode and Vishay 2N4416A JFET (twice the sum of the detector's leakage current and the JFET's drain-to-gate leakage current) as a function of temperature as inferred from the multidimensional least squares fitting of the *FWHM* at 5.9 keV (open squares) and 22.16 keV (open circles) as a function of shaping time.

As the spectra collected with the ^{241}Am X-ray/γ-ray source were collected at a single shaping time, multidimensional least squares fittings could not be conducted. Nevertheless, noise in the spectrometer at higher energy can be estimated from these results. The quadratic sum of electronic and incomplete charge collection noise was calculated by subtracting Fano noise in quadrature from the *FWHM* of the ^{241}Am 59.5 keV γ-ray peak at each temperature. The quadratic

sum of electronic and incomplete charge collection noise from the ^{241}Am spectra were compared with the same noise contributions at 5.9 keV (^{55}Fe Kα) and 22.16 keV (^{109}Cd Kα$_1$), collected at the same shaping times. The results are presented in **Figure 3.11**. The quadratic sum of dielectric and incomplete charge collection noise at 5.9 keV, 22.16 keV and 59.5 keV were equal within the uncertainties at temperatures, T, 20 °C ≤ T ≤ 80 °C. This implied that incomplete charge collection noise, which is energy dependent, was negligible. However, at 100 °C the quadratic sum of electronic and incomplete charge collection noise at 59.5 keV exceeded that at 5.9 keV and 22.16 keV. As an example, at 20 °C, the quadratic sum of electronic and incomplete charge collection noise at 5.9 keV, 22.16 keV, and 59.5 keV was 103 e$^-$ rms ± 9 e$^-$ rms, 95 e$^-$ rms ± 9 e$^-$ rms, and 104 e$^-$ rms ± 9 e$^-$ rms respectively. At 100 °C the same noise contributions for the same energies were 157 e$^-$ rms ± 15 e$^-$ rms, 154 e$^-$ rms ± 15 e$^-$ rms, and 192 e$^-$ rms ± 18 e$^-$ rms respectively, suggesting that some additional noise was present in the ^{241}Am (59.5 keV) photopeak. At 100 °C, the difference (in quadrature) between the quadratic sum of electronic and incomplete charge collection noise at 22.16 keV and 59.5 keV was 114 e$^-$ rms ± 23 e$^-$ rms. The additional noise could have been a consequence of greater than expected parallel white noise if the leakage current of the detector (or JFET) had been unstable when the reverse bias of the detector was held constant at 100 V for 6 days whilst the ^{241}Am spectrum was collected; as such, further measurements were made to investigate this. Incomplete charge collection noise was also considered a possible source of the extra noise, even though the higher temperature (100 °C) might have assisted in releasing trapped charge.

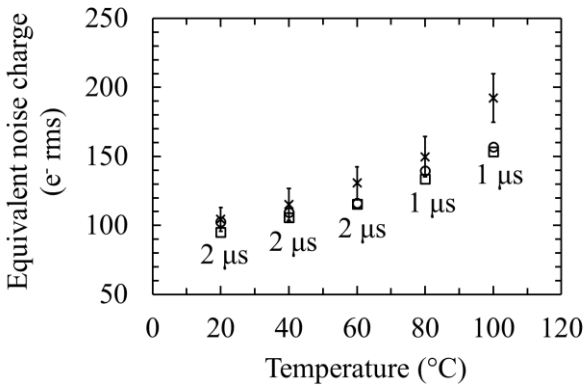

Figure 3.11. Equivalent noise charge of the quadratic sum of electronic noise and incomplete charge collection noise as a function of temperature for the ^{241}Am 59.5 keV γ-ray photopeak (crosses), ^{109}Cd 22.16 keV X-ray photopeak (open squares), and the ^{55}Fe 5.9 keV X-ray photopeak (open circles). For clarity, only error bars for the ^{241}Am 59.5 keV γ-ray photopeak have been

included. Errors bars for the ^{55}Fe Kα (5.9 keV) and ^{109}Cd Kα_1 (22.16 keV) X-ray photopeak ranged from ± 8.7 e^- rms to ± 14.6 e^- rms.

To test the long-term stability of the detector's leakage current, the detector was reversed biased for 6 days at 100 V and at 100 °C. The voltage burden of the Keithley 6487 picoammeter/voltage source meter was 200μV for current measurements up to 2 mA. The leakage current, which was measured at 60 second intervals using the procedures described in **Section 3.3.1**, is presented in **Figure 3.12**. At 100 V reverse bias the leakage current was initially 37.7 pA ± 0.5 pA (instrument uncertainty), which was less than previously measured in **Section 3.3.1** (42.7 pA ± 0.5 pA (instrument uncertainty)). After 24 hours, the leakage current had risen to 47.5 pA ± 0.5 pA (instrument uncertainty). After 48 hours, the leakage current rose linearly at less than 0.01 pA per hour, whilst it oscillated 0.3 pA root mean squared (rms) about an hourly mean value as it rose as a function of time. At the end of 6 days the leakage current was 49.0 pA ± 0.5 pA (instrument uncertainty), the average leakage current over the final five hours of measurement was 49.1 pA ± 0.5 pA (instrument uncertainty). Any leakage current rise in the detector should be considered in the context of its effect at the input to the preamplifier's JFET where the total system leakage current is equal to twice the sum of the detector's leakage current and the JFET's drain-to-gate leakage current (see previous paragraph). The extra detector leakage current (≈ 22 pA at the input of the preamplifier) would broaden the 59.5 keV γ-ray emission ≈ 11 e^- rms noise at 1 μs shaping time. This was insufficient to account for all of the extra noise at 100 °C. Therefore, the origin of the majority of the additional noise that broadened the 59.5 keV γ-ray emission, when the spectrometer was operated at 100 °C, is currently unknown. Nevertheless, a significant contribution to the total invariant noise in the FWHM of the 59.5 keV γ-ray photopeak was dielectric noise.

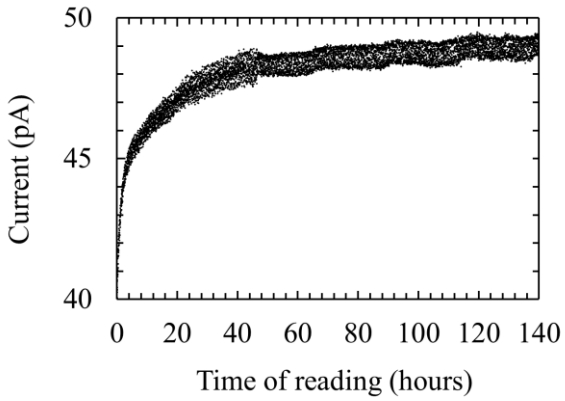

Figure 3.12. The packaged 4H-SiC detector's leakage current as a function of time, operating at 100 V reverse bias and at a temperature of 100 °C for 6 days. There are a total of 8640 leakage

current measurements, the measurement error was dominated by instrument uncertainty (3 % reading + 0.4 pA offset). The maximum recorded uncertainty was ± 0.55 pA and the minimum recorded uncertainty was ± 0.52 pA.

These results achieved with the detector need to be viewed in context with some other wide bandgap compound semiconductor radiation detectors. This detector was thin (5.15 μm) and the detector's performance was modest compared with the best results for many tailor-made detectors. A custom grown thick 4H-SiC strip X-ray detector depleted to a depth of 124 μm when reverse biased to 600 V has recently been reported (Puglisi & Bertuccio, 2019). This strip detector was used to accumulate an ^{241}Am spectrum at 200 V reverse bias with a pulser line width ENC of 11.6 e^- rms (214 eV *FWHM*) at 21 °C. A 40 μm thick, 200 μm by 200 μm area pixel GaAs detector operating at 23 °C achieved a resolution of 266 eV (≈ 26 e^- rms) *FWHM* at 5.9 keV (Owens et al., 2001). The results in reported by Puglisi & Bertuccio (2019) and Owens et al. (2001) were obtained from custom grown high quality materials attached to ultra-low noise preamplifier electronics and they benefitted from having the detectors directly wire bonded to the gate of the transistor at the front end of the preamplifier, rather than relying on packaged transistors as was the case for the results reported here with the COTS 4H-SiC photodiode. Nevertheless, it is remarkable that the COTS 4H-SiC detector reported here, which was intended as a UV detector, functions as well as it does as a spectroscopic detector of X-rays and γ-rays up to 60 keV, and that it can do so at high temperatures.

3.6 Conclusions

A COTS 4H-SiC UV photodiode has been characterized for its electrical and photon counting spectroscopic response across the temperature, T, range 20 °C ≤ T ≤ 100 °C, with X-ray and γ ray photons in the energy range 5.9 keV to 59.5 keV.

The leakage current of the packaged 4H-SiC detector at 100 V reverse bias was found to be 42.7 pA ± 0.5 pA at 100 °C, and 1.1 pA ± 0.4 pA at 60 °C. At 40 °C and below, the leakage current of the packaged 4H-SiC diode was below the noise floor of the picoammeter used (± 0.4 pA).

Measurements of capacitance as a function of reverse bias suggested that the detector could be depleted to 2.41 μm ± 0.03 μm at 20 °C, short of what was expected from the abrupt junction calculation (Sze & Ng, 2007) based on the manufacturer's specifications for the device (3.7 μm at 100 V). Notwithstanding this, a previous electron spectroscopy study suggested that most of the epitaxial width (5.15 μm) of the detector was depleted and active for radiation detection (Zhao et al., 2018). It was also noted that carrier recombination lengths in 4H-SiC are sufficiently large

to address the difference in depletion width calculated from capacitance measurements and the abrupt junction approximation with the full epitaxial depletion suggested by Zhao et al. (2018). Therefore, the *QE* of the detector was calculated using the full epitaxial width (5.15 μm) on the assumption that carriers were able either to diffuse to the depletion region prior to recombining or the full epitaxial width was depleted.

The detector was connected to a low noise charge sensitive preamplifier and operated as an X-ray and γ-ray spectrometer. The detector of the spectrometer was illuminated by ^{55}Fe, ^{109}Cd, and ^{241}Am radioisotope X-ray/γ-ray sources and was found to be responsive to, and capable of discriminating (subject to its energy resolution) photons of energy up to 59.5 keV (the highest energy investigated). The *FWHM* at 5.9 keV (^{55}Fe Mn Kα) improved from 2.69 keV ± 0.25 keV at 100 °C to 1.66 keV ± 0.15 keV at 20 °C. The *FWHM* at 22.16 keV (^{109}Cd Ag Kα_1) improved from 2.65 keV ± 0.25 keV at 100 °C to 1.66 keV ± 0.15 keV at 20 °C. Following this, the spectrometer was operated continuously for 6 days per temperature ranging from 100 °C to 20 °C, in 20°C decrements to accumulate ^{241}Am 59.5 keV γ-ray spectra. The *FWHM* at 59.5 keV (^{241}Am γ_1) improved from 3.38 keV ± 0.30 keV at 100 °C, to 1.83 keV ± 0.15 keV at 20 °C.

The noise components degrading the spectrometer's energy resolution, beyond that which would be expected in the Fano limited case, were analysed. A multidimensional least squares fitting of the measured *FWHM* as functions of shaping time for the accumulated ^{55}Fe and ^{109}Cd X-ray spectra showed that the dominant source of noise was dielectric noise at all the shaping times considered, up to temperatures of 40 °C. At higher temperatures (60 °C ≤ T ≤ 100 °C), the combined currents of the 4H-SiC detector and the preamplifier's Si JFET increased white parallel noise to such an extent that white parallel noise became the dominant noise component at the longest shaping times (6 μs and 10 μs) at 100 °C. When the quadratic sums of electronic noise and incomplete charge collection noise were compared at 5.9 keV and 22.16 keV, incomplete charge collection noise was found to be a negligible component of the total noise at lower temperatures (≤ 60 °C); however, at 80 °C, when the same comparison was made, the difference (in quadrature) in dielectric and incomplete charge collection noise was significant (≈ 49 e^- rms ± 4 e^- rms). At 59.5 keV and 100 °C, additional noise was also present when the quadratic sums of electronic noise and incomplete charge collection noise were compared at 5.9 keV and 22.16 keV. The detector's leakage current was measured again to determine if the detector was unstable when reverse biased for 6 days. Although the detector's leakage current rose by 11.3 pA ± 0.7 pA over the measurement period, this could not account for the broadening of the 59.5 keV ^{241}Am γ-ray photopeak observed at T =100 °C when compared with the noise

broadening at $T \leq 60$ °C. The source of the extra noise at 59.5 keV was unknown, but noise associated with incomplete charge collection at the higher energy could not be discounted.

The ready availability of these COTS devices, and the relative ease with which they can be repurposed from a UV photodiode to an uncooled spectroscopic soft and hard X-ray and γ-ray detector make them an attractive component for integration into an unshielded photon counting X-ray spectrometer on a low-cost low-mass CubeSat mission led by a University or a small entrepreneurial space-focused business. This COTS SiC radiation detector, could also find utility in terrestrial markets where the detector would be positioned uncooled, in a high radiation fluence background, without shielding, in difficult to access locations, and for extended periods. An oil well logging instrument may be one example application. The packaged detector and JFET would need to be appropriately paired with a commercial version of the low noise charge sensitive preamplifier used in the work reported here in order to minimise the dielectric losses that contributed to some of the photopeak broadening. Such an instrument, once built, would require further characterization and testing to determine its performance and optimum operating parameters and to identify definitively the source of the unknown noise component at 59.5 keV and 100 °C.

Future work on these COTS detectors should include radiation hardness characterisation, to investigate the effects of radiation damage to the detector and its degradation in performance over time when exposed to different types and doses of potentially damaging radiation; radiation types of interest in such studies may include neutrons, protons, electrons, helium nuclei, and heavy ions.

Chapter 4. Single crystal chemical vapour deposition (CVD) diamond soft X-ray detector

4.1 Introduction

The work in this chapter has been published (see **Section Publications**). A 2.0 mm width by 2.0 mm breadth by 0.5 mm thick electronic grade single crystal diamond grown via chemical vapour deposition was configured as a metal-semiconductor-metal X-ray detector. The detector was electrically characterised before it was connected to a bespoke charge sensitive preamplifier of low noise. An ^{55}Fe radioisotope X-ray source was used to illuminate the detector with soft (Mn Kα = 5.9 keV and Mn Kβ = 6.49 keV) X-rays. The detector and preamplifier were temperature controlled and operated at 20 °C. The energy resolution (full width at half maximum) of the diamond spectrometer was 2.48 keV at 5.9 keV. Shaping time noise analysis conducted on the X-ray spectra found dielectric noise to be the largest electronic noise contribution for all but the shortest of shaping times, when series white noise dominated. The work is the first report of a diamond detector's spectroscopic photon counting response to soft (< 10 keV) X-rays.

4.2 Diamond detector

An electronic grade CVD single crystal diamond (2.0 mm width by 2.0 mm breadth by 0.5 mm thickness) grown by Element 6 Ltd. (Element Six, N.D.) was cleaned in an acid bath to remove organic and non-organic surface contaminates. Square contacts (1.4 mm width by 1.4 mm breadth) were formed by sputtering both a Ti layer (50 nm thick) and an Ag layer (200 nm thick) on to the front and rear of the detector, in turn. After deposition of each contact, the detector was annealed at 400 °C. The detector was mounted in a TO-39 package using silver-loaded epoxy (Loctite, N.D.) and wire bonded. A schematic diagram of the diamond detector is shown in **Figure 4.1**.

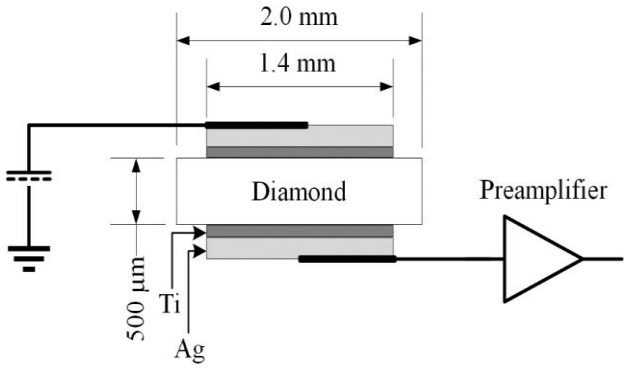

Figure 4.1. Schematic of the diamond X-ray detector showing its connections to the biasing power supply and the preamplifier (not to scale).

4.3 Detector characterisation and X-ray spectroscopy at room temperature (20 °C)

4.3.1 Leakage current measurements

The packaged detector's leakage current was investigated as a function of applied electrical potential difference. The detector was placed in an electromagnetically screened test harness in a TAS Micro MT Climatic Cabinet (kept at 20 °C). A Keithley 6487 picoammeter/voltage source was used to apply electrical potential and measure the leakage current. The detector was operated in a dry N_2 environment to mitigate against known effects of humidity on TO packages (Barnett et al., 2010). Electrical potential difference was applied across the detector in 5 V steps up to 100 V in both polarities with the leakage current recorded after a 5 second wait at each step. This process was automated with LabVIEW software. At applied potential differences up to 100 V, the leakage current of the packaged detector was less than the noise floor of the picoammeter (i.e. < 0.4 pA). This implied a leakage current density of < 20 pA cm^{-2} at an electric field strength of 2 kV cm^{-1}, assuming that the field was solely between the area of the two contacts, or < 10 pA cm^{-2} if the whole 2.0 mm by 2.0 mm area of the diamond was active. Such leakage current densities are lower than reported by other researchers using CVD diamond radiation detectors. For example, a single crystal CVD diamond detector grown by IIa Technologies Pte. Ltd., Singapore had a leakage current density of 400 pA cm^{-2} at the same electric field strength and at 25 °C (Kumar et al., 2017). Tsubota et al. reported two 0.5 mm thick single crystal CVD diamond detectors with leakage densities of 140 pA cm^{-2} and 30 pA cm^{-2} at an electric field strength of 2 kV cm^{-1} and at a temperature of 20 °C (Tsubota et al., 2015). Although the upper limit of the leakage current densities reported here for the present detector are lower than has been previously reported with diamond, they may be still be far greater than those reported for some other types

of wide bandgap semiconductor radiation detectors (only an upper limit to the leakage current density could be determined and that upper limit was greater than the leakage current densities measured for some detectors made of other materials). For example, a leakage current density of 1 pA cm^{-2} has been achieved with 4H-SiC detectors at a temperature of 27 °C and with an electric field strength of 104 kV cm^{-1} (Bertuccio et al., 2011). Low leakage currents are necessary to limit the parallel white noise component of X-ray spectrometers, particularly when longer amplifier shaping times are selected (Barnett et al., 2012b), see **Section 2.3** for further details.

4.3.2 Capacitance measurements

The capacitance of the packaged detector was measured with a HP 4275A Multi Frequency LCR meter as a function of applied potential difference. The packaged detector was placed in an electromagnetically screened test harness and after a 'zero open check' the LCR test signal was set to 1 MHz frequency and 50 mV rms magnitude. As per the leakage current measurements the test harness was located in a TAS Micro MT climatic cabinet at 20 °C with a dry N_2 environment. The capacitance of the detector was measured in 5 V steps up to a maximum applied potential difference of 100 V in each polarity. The capacitance was found to be independent of the applied potential difference; it was 870 fF ± 20 fF across the potential difference range measured. The capacitance contribution of the detector's packaging was also estimated (by measuring the capacitance of a similarly packaged diamond device with its wire bond removed) and found to be independent of applied potential difference; the capacitance of the detector's packaging was 520 fF ± 20 fF in parallel with the detector, thus implying a detector capacitance of 350 fF ± 30 fF. Given the relative permittivity of diamond (5.7) (Spear & Dismukes, 1994) (Sze & Ng, 2007), a detector thickness of 500 μm, contacts of 1.4 mm by 1.4 mm, (1.96 mm^2), and assuming that the capacitance characteristics of the detector could be approximated to those of a parallel plate capacitor, a capacitance of 200 fF was expected. The apparent capacitance of 350 fF ± 30 fF, implies a detector contact area of 3.47 mm^2 ± 0.30 mm^2, equivalent to an apparent square contact of 1.9 mm by 1.9 mm assuming a detector thickness of 500 μm, or alternatively assuming a contact area of 1.4 mm by 1.4 mm, a detector thickness of 280 μm ± 40 μm would be implied. It is possible that the greater than expected apparent capacitance was a result of edge effects around the detector's contacts. Capacitance sources associated with detector packaging and that were not included in the 520 fF ± 20 fF estimated, included the wire bond and the silver-loaded epoxy used in die attach; these sources may have also contributed to the measured capacitance.

4.3.3 X-ray spectroscopy at 20 °C

The quantum detection efficiency of the detector to X-rays was required to fit Gaussians to the accumulated X-ray spectra. The quantum efficiency of the detector was calculated using the Beer Lambert Bouguer Law (**Equation 2.1)** for light attenuation and absorption,

$$QE = \prod_{i=1}^{i=n} \exp\left(\mu_i \rho_i t_i\right)\ \left(1 - \exp\left(\mu_{en} \rho t\right)\right), \qquad (4.1)$$

where the first exponential term on the right side of **Equation 4.1** is the attenuation of photons in the i^{th} deadlayer in front of the detector's active region. μ_i is i^{th} layer's mass attenuation coefficient, ρ_i is that i^{th} layer's density, and t_i is that i^{th} layer's thickness. The second exponential term in **Equation 4.1** is the absorption of photons in the active region. Here, μ_{en} is the mass absorption coefficient of the active region (diamond), ρ is the density of the active region, and t is the thickness of the active region (Hubbell, 1999). The deadlayers were considered to be solely the Ag and Ti of the front contact, in the present case. The XCOM database (Berger et al., 2010) was accessed to obtain mass attenuation and absorption coefficients for X-ray photons in the relevant materials. The quantum detection efficiency of the detector is presented as a function of X-ray energy in **Figure 4.2**. The discontinuities between 3.35 keV and 3.81 keV and at 4.97 keV were caused by the Ag L and Ti K absorption edges of the detector's front contact.

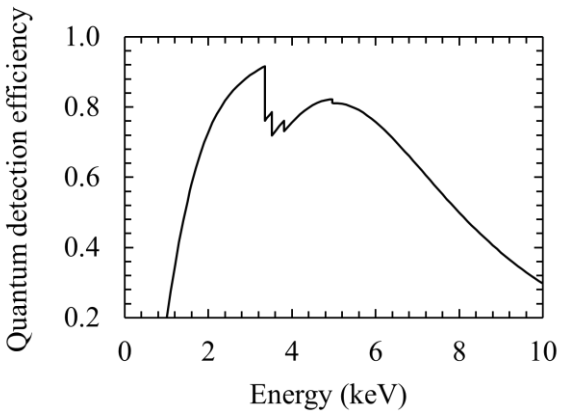

Figure 4.2. The diamond detector's calculated quantum detection efficiency at soft X-ray energies, (1 keV ≤ E ≤ 10 keV).

The detector was paired with a bespoke charge sensitive preamplifier of low noise; the preamplifier was of near identical design to that used in **Chapter 3**. A similar design of preamplifier was first reported by Bertuccio et al. (Bertuccio et al., 1993). The preamplifier was of feedback resistorless design – the leakage current of the detector was discharged through the preamplifier's input Junction Field Effect Transistor (JFET) which was slightly forward biased.

The JFET used in this preamplifier was a Vishay 2N4416A Si JFET (Siliconix, 2001). The detector and preamplifier were housed in an electromagnetically screened test harness. Output signals from the preamplifier were shaped and amplified by an Ortec 572A shaping amplifier before being fed to an Ortec EASY MCA 8k multi-channel analyser (MCA). The detector's potential difference was applied using a Keithley 6487 voltage source.

Soft (Mn Kα = 5.9 keV and Kβ = 6.49 keV) X-rays from an ^{55}Fe radioisotope X-ray source (106 MBq activity) were used to illuminate the detector; the source was placed inside the test harness, ≈ 6 mm above the detector. A 0.14 mm Al absorber (attenuating 99 % of the 5.9 keV photons) was positioned between the source and the detector to limit the photon flux incident on the detector. All spectra were accumulated with the test harness located inside a TAS Micro MT climatic cabinet at 20 °C. Spectra were accumulated at four applied potential differences (25 V, 50 V, 75 V, and 100 V) and the six shaping times available with the shaping amplifier used. The shaping times, τ, used to accumulate the spectra were 0.5 μs, 1 μs, 2 μs, 3 μs, 6 μs, and 10 μs. The live time limit of each spectrum was set to 90 s. In each case, the photopeak detected as a result of illumination with the ^{55}Fe radioisotope source was the combination of the characteristic ^{55}Fe X-ray emissions (Mn Kα = 5.9 keV) and Mn Kβ = 6.49 keV)) (Schötzig, 2000). Therefore, Gaussian fitting was required to detangle the detected Mn Kα and Kβ emissions. The fitted Gaussians took account of the relative X-ray emission ratios, and the detector's relative detection efficiency at the emitted X-ray energies. The spectrometer's charge scale was energy calibrated using the centroid of the fitted Mn Kα X-ray photopeak and the position of the spectrometer's zero energy noise peak. The relationship between energy and charge was then assumed to be linear. In the accumulation of each spectrum, a low energy threshold was set to limit MCA dead time once the position of the zero energy noise peak had been established. Once the low energy threshold was set, further counts from the zero energy noise peak were excluded from the spectrum. The ^{55}Fe X-ray spectrum accumulated with the spectrometer operated at 50 V applied potential difference and with a shaping time of 3 μs selected is presented in **Figure 4.3 (a)**. The fitted Gaussians that represent the detected Mn Kα and Kβ X-ray components are shown as dotted lines. The dependence of the full width at half maximum (*FWHM*) upon shaping time is shown in **Figure 4.3 (b)**. When 50 V and 75 V potential difference were applied across the detector, the energy resolutions (*FWHM* at 5.9 keV) achieved were identical (2.48 keV); at 25 V and 100 V applied potential difference the *FWHM* at 5.9 keV were 2.56 keV and 2.54 keV, respectively.

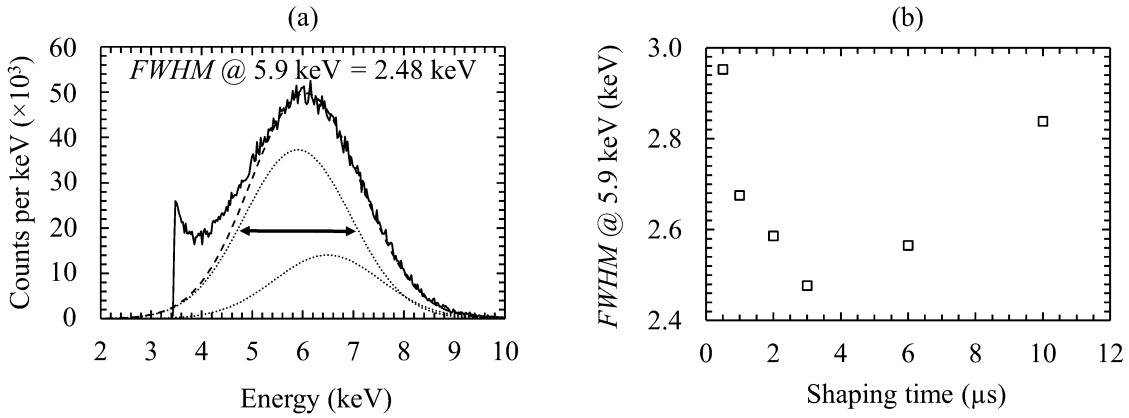

Figure 4.3. (a) The ^{55}Fe X-ray spectrum (solid line) accumulated with 50 V potential difference applied across the detector and the shaping time set to 3 μs. The fitted contributions of the Mn Kα and Kβ photons to the spectrum are shown as dotted lines; the dashed line shows the combination thereof. (b) The energy resolution (*FWHM*) achieved at 5.9 keV with the detector at a 50 V potential difference as a function of shaping time.

^{55}Fe X-ray spectra collected with the detector operated at four different applied potential differences (25 V, 50 V, 75 V, and 100 V) but with the same shaping time (3 μs) for the shaping amplifier are presented in **Figure 4.4**. To permit the reader to distinguish clearly each of the four ^{55}Fe X-ray spectra, in addition to displaying each spectrum superimposed on the others in **Figure 4.4 (a)**, each spectrum is also presented as a separate plot (25 V in **Figure 4.4 (b)**; 50 V in **Figure 4.4 (c)**; 75 V in **Figure 4.4 (d)**; 100 V in **Figure 4.4 (e)**. The photon count rate within the fitted Mn Kα (5.9 keV) peak (not shown for clarity in **Figure 4.4**), but similar to that in **Figure 4.3 (a)**, did not vary significantly with potential difference (or shaping time) thus suggesting that the detection efficiency of the detector was constant across the conditions investigated. The mean count rate in the Mn Kα photopeak over the four potential differences and the six shaping times investigated was 1110 s^{-1} ± 30 s^{-1} (rms error), where the rms error, *R*, was given by,

$$R = \sqrt{\frac{\Sigma(x_i - \bar{x})^2}{n}} \qquad (4.2)$$

where x_i is the value of the datum (in this case the count rate) of the i^{th} accumulated spectrum, $\bar{x}$ is the mean of the data (in this case the mean count rate in the fitted Mn Kα photopeak of all 24 accumulated spectra), and *n* is the number of data considered (24 in this case – four applied potential differences each with six shaping times). Background spectra of comparable duration to the accumulated X-ray spectra were accumulated before and after illumination of the detector with the ^{55}Fe radioisotope X-ray source. No background counts, beyond those of the zero energy

noise peak, were detected. The detected X-ray flux (both Mn Kα and Kβ) corresponded to a photocurrent of 0.131 pA ± 0.004 pA (rms error).

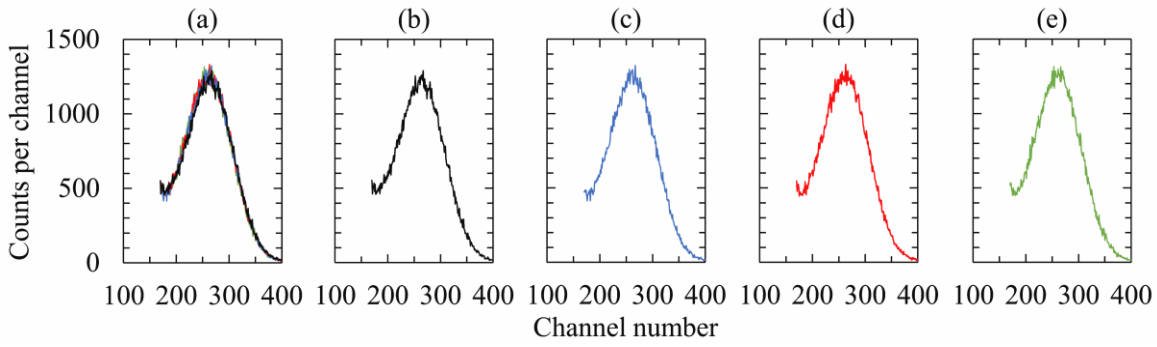

Figure 4.4. (a) The ^{55}Fe radioisotope X-ray spectra collected with the diamond detector operated at 25 V (black line), 50 V (blue line), 75 V (red line), and 100 V (green line) applied potential differences. Each spectrum is replicated in a separate plot using the same colour (b) 25 V, (c) 50 V, (d) 75 V, and (e) 100 V. The shaping time was 3 μs in each case.

4.4 Noise analysis

The three independent noise contributions in a direct detection photon counting X-ray spectrometer: Fano noise (related to ionisation processes in the detector (Fano, 1947)); electronic noise, *A*, (Lioliou & Barnett, 2015), and incomplete charge collection noise, R_{ICC}, (a consequence of carrier recombination and trapping (Owens, 2012)) were expressed in terms of energy resolution *FWHM* in **Equation 2.8**. For the convenience of the reader, the energy resolution expressed in units of equivalent noise charge (*ENC*) e^- rms is,

$$\Delta E\ (\mathrm{e^-\ rms}) = \sqrt{\frac{FE}{\omega} + A^2 + {R_{ICC}}^2}, \tag{4.3}$$

where ω is the electron-hole pair creation energy of diamond, E is the energy of an incident X-ray, and F is the Fano factor of diamond. Electronic noise can be further broken down into four components, i.e. parallel white noise, series white noise (including induced gate current noise), dielectric noise, and 1/*f* series noise (**Equation 2.9**, **Equation 2.13**, **Equation 2.14**, and **Equation 2.16**). For the reader's convenience the equations listed above from **Chapter 2** are reproduced below. White noise (series, ENC_{sw}, and parallel, ENC_{pw}) are related to amplifier shaping times, τ,

$$ENC_{sw} = \frac{\mathrm{B}}{\mathrm{q_e}} \sqrt{\frac{A_1}{2} 4kT \frac{\gamma}{\mathrm{g}_m} {C_T}^2 \frac{1}{\tau}} \quad , \tag{4.4a}$$

$$ENC_{pw} = \frac{1}{q_e}\sqrt{\frac{A_3}{2}2q_e(I_D + I_{JFET})\tau} \quad , \tag{4.4b}$$

where, **for Equation 4.4a**, B is a correction for induced gate current noise (0.8), A_1 is 1.85, γ is a dimensionless product of noise resistance and transconductance, g_m, of the preamplifier's input JFET, q_e is elementary electron charge, and C_T is the total capacitance at the input of the preamplifier's JFET. For **Equation 4.4b**, A_3 is 1.85, and I_D and I_{JFET} are the leakage currents of the detector and the Si JFET, respectively. In summary, parallel white noise is proportional to the shaping time, whilst series white noise has an inverse relationship with amplifier shaping time. Parallel white noise arises from the leakage currents of the detector and input JFET (Bertuccio & Pullia, 1993) (Barnett et al., 2012b) (Lioliou & Barnett, 2015); series white noise arises from the detector's capacitance, the preamplifier's input transistor capacitance, the feedback capacitance, the test capacitance (if present), and any other stray capacitances present at the input to the preamplifier.

Dielectric and 1/*f* series noise are shaping time independent. The *ENC* of 1/*f* and dielectric noise are given by **Equation 4.5a** and **Equation 4.5b**, respectively

$$ENC_{1/f} = \frac{1}{q_e}\sqrt{A_2\pi A_f {C_T}^2} \quad , \tag{4.5a}$$

$$ENC_{die} = \frac{1}{q_e}\sqrt{A_2 2kTdC_{die}}, \tag{4.5b}$$

where A_2 is 1.18, A_f is a characteristic constant of the JFET, C_{die} is a representative capacitance of the lossy dielectrics acting at the input JFET, and d is the respective dielectric dissipation factor.

The Fano noise of diamond at 5.9 keV was estimated to be 6 e^- rms (183 eV *FWHM*). In this calculation it was assumed that the electron-hole pair creation energy of diamond was 12.82 eV ± 0.13 eV (Keister et al., 2018) and its Fano factor was 0.08 (Alig et al., 1980). The electronic noise contributions were extracted using multidimensional least squares fitting from measurements of the experimental photopeak *FWHM* at 5.9 keV (Mn Kα) as a function of accumulated spectra shaping times. The difference between an experimentally measured and a multidimensional least squares fitted energy resolution was < 2 e^- rms (60 eV *FWHM*) for all 24 data points (four applied potential differences, six shaping times). The multidimensional least squares fittings derived the total capacitance at the input of the JFET; this capacitance was then used to calculate the 1/*f* series noise. The combined dielectric and incomplete charge collection noise component was derived by subtracting (in quadrature) series white noise (including induced

gate current noise), parallel white noise, Fano noise, and 1/*f* series noise, from the measured energy resolution. The extracted noise components are presented in **Figure 4.5**.

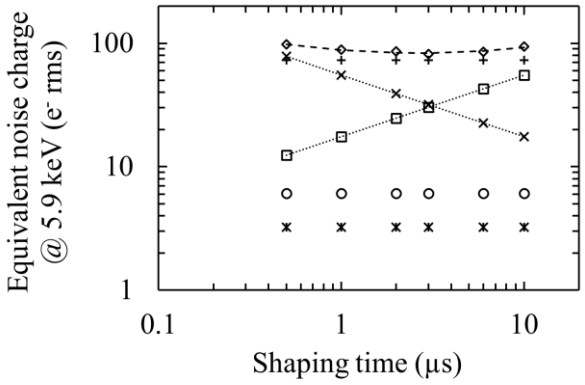

Figure 4.5. The noise components of the spectrometer expressed as a function of shaping time at 5.9 keV with 50 V potential difference applied across the detector. The noise contributions are total noise (open diamonds), quadratic sum of dielectric and incomplete charge collection noise (+ symbols), parallel white noise (open squares), series white noise (× symbols), Fano noise (open circles), and 1/*f* series noise (stars). The lines are included to guide the eye only; fitted *FWHM* (dashed line); fitted parallel and series white noises (dotted lines).

The series white noise dominated the noise contributions at 0.5 μs shaping time; here, series white noise contributed 78 e^- rms ± 26 e^- rms (2.4 keV ± 0.8 keV *FWHM*) and 78 e^- rms ± 23 e^- rms (2.4 keV ± 0.7 keV *FWHM*) at 50 V and 100 V applied potential difference, respectively. At 10 μs shaping time, series white noise reduced to 17 e^- rms ± 6 e^- rms (0.5 keV ± 0.2 keV *FWHM*) and 17 e^- rms ± 5 e^- rms (0.5 keV ± 0.2 keV *FWHM*) at 50 V and 100 V, respectively. At 0.5 μs shaping time, parallel white noise contributed 12 e^- rms ± 6 e^- rms (0.4 keV ± 0.2 keV *FWHM*) and 13 e^- rms ± 4 e^- rms (0.4 keV ± 0.2 keV *FWHM*) of noise at 50 V and 100 V applied potential difference, respectively. At 10 μs shaping time, parallel white noise had risen to 55 e^- rms ± 26 e^- rms (1.7 keV ± 0.8 keV *FWHM*) and 57 e^- rms ± 20 e^- rms (1.7 keV ± 0.6 keV *FWHM*) at 50 V and 100 V, respectively. A table summarising these results is presented as **Table 4.1**.

Amplifier shaping time (μs)	Series white noise (e^- rms)		Parallel white noise (e^- rms)	
	50 V	100 V	50 V	100 V
0.5	78 ± 26	78 ± 23	12 ± 6	13 ± 4
10	17 ± 6	17 ± 5	55 ± 26	57 ± 20

Table 4.1. Series and parallel white noise contributions at τ = 0.5 μs and τ = 10 μs with 50 V and 100 V potential difference applied across the detector.

The total leakage current at the input of the JFET was 27.5 pA ± 4 pA (uncertainty propagated from the nonlinear least squares fitting) at 25 V applied potential difference and 28.5 pA ± 3 pA at 100 V applied potential difference. Assuming that all leakage current contributions at the input of the JFET were independent of each other, the system leakage current was equal to $2(I_D + I_{JFET})$, where I_D was the leakage current of the packaged detector and I_{JFET} was the drain-to-gate leakage current in the Si JFET (Bertuccio & Casiraghi, 2003) (Lioliou & Barnett, 2015). The leakage current measured from the packaged detector at 20 °C and at applied potential difference ≤ 100 V was below the noise floor of the Keithley 6487 picoammeter (i.e. < 0.4 pA) **(Section 4.3.1**) which implied $I_{JFET} \approx 14$ pA in the forward biased Si JFET when the spectrometer was operating.

The total capacitance acting at the input of the preamplifier was inferred from the multidimensional least squares fitting. The capacitance was constant at 5.6 pF ± 0.1 pF (standard error) regardless of the potential difference applied across the detector. Here, the standard error, Q, is the standard error of the mean capacitance at the input of the JFET; Q is given by,

$$Q = \sqrt{\frac{\Sigma(x_i - \bar{x})^2/(n-1)}{n}} \tag{4.6}$$

where x_i, $\bar{x}$, and n have been previously defined, but in this case, x_i is the capacitance at an applied potential difference and $\bar{x}$ is the mean capacitance of n (four) spectrometer operating voltages. Having measured the capacitance of the packaged detector directly (870 fF ± 20 fF), it is clear that the series white noise was dominated by capacitances other than that of the detector. The dielectric noise of the detector, the Si JFET, and the detector's packaging can be estimated by considering the dielectric dissipation factors for these individual components and their associated capacitances. Assuming the dielectric dissipation factor of diamond was 6×10^{-4} (Spear & Dismukes, 1994) and the detector's capacitance was 350 fF ± 30 fF (**Section 4.3.2**) the detector itself contributed 9 e^- rms (267 eV *FWHM*) of dielectric noise. Some of this dielectric noise was likely also attributable to the silver-loaded epoxy (Loctite, 2014) used to attach the detector die to the TO-39 package (**Section 4.3.2**). The capacitance associated with the TO-39 package with the detector mounted on it, but with the wire bond removed, was 520 fF ± 20 fF (**Section 4.3.2**)

with the majority of this capacitance attributed to the borosilicate glass ceramic insulated leg on the TO-39 package. Using the borosilicate glass dielectric dissipation factor stated in the manufacturer's catalogue (0.0127 (Schott, 2014)), the TO-39 package was calculated to contribute 50 e^- rms (1.5 keV *FWHM*) of dielectric noise. The preamplifier's Si input JFET (nominal capacitance of 2 pF (Siliconix, 2001) (Barnett et al., 2012b) (Lioliou & Barnett, 2015), dissipation factor of 8×10^{-4}) contributed 24 e^- rms (737 eV *FWHM*) of dielectric noise.

Other sources of capacitance in a charge sensitive preamplifier for photon counting spectroscopy are the feedback, test, and stray capacitances (Lioliou & Barnett, 2015); although the preamplifier used in this report did not have a test capacitor installed. Feedback and stray capacitances are not easily calculated separately because the individual dielectric dissipation factors and dielectric constants of all those sources of capacitance (most notably the stray capacitance) within the preamplifier are unknown. However, the multidimensional least squares fitting implied that the quadratic sum of dielectric and incomplete charge collection noise was 73 e^- rms ± 1 e^- rms (rms error) (2.21 keV ± 0.04 *FWHM*) at 5.9 keV at all of the applied potential differences. The calculated known dielectric noise contributions were subtracted in quadrature from the quadratic sum of total incomplete charge collection noise and dielectric noise. This yielded a remaining noise of 46 e^- rms ± 2 e^- rms (rms error) (1.40 keV ± 0.07 *FWHM*) at 5.9 keV of dielectric noise and incomplete charge collection noise (if any) in the spectrometer.

Incomplete charge collection noise would be a consequence of the detector's charge collection efficiency (CCE) being less than unity. For detectors where CCE < 1, incomplete charge collection noise was expected to reduce when the potential difference applied across the detector was increased. For the detector presently reported, the quadratic sum of dielectric and incomplete charge collection noise (73 e^- rms ± 1 e^- rms (rms error)) at 5.9 keV did not change as the detector's applied potential difference was increased; this implied that incomplete charge collection noise was not a significant contributor to the noise measured. This is congruent with the observation that the count rate did not change when the potential difference applied across the detector was increased.

The total capacitance at the input of the JFET was 5.6 pF ± 0.1 pF (standard error). After subtracting the capacitance attributed to the packaged detector and the Si JFET, the remaining stray and feedback capacitance at the input of the preamplifier was 2.7 pF ± 0.1 pF (standard error). As previously discussed, the noise attributed to this combination of capacitances is not readily directly calculable given the lack of detailed knowledge of the dissipation factors of the individual dielectric components of which it is comprised, although previous (unreported) tests on earlier models of the preamplifier found feedback capacitance to be ~ 10 fF. Nevertheless, the

apparent noise contribution of these dielectrics (46 e^- rms ± 2 e^- rms (rms error)) and the unattributed, combined stray and feedback capacitance (2.7 pF ± 0.1 pF (standard error)) can be used to calculate an equivalent dielectric dissipation factor associated with the remaining capacitance. The effective dissipation factor for the entirety of the remaining capacitance was $2.1 \times 10^{-3} \pm 0.2 \times 10^{-3}$. This effective dissipation factor was compared with the dielectric dissipation factors of materials contained in the preamplifier to qualitatively assess the veracity of the effective dissipation factor.

The preamplifier's printed circuit board (PCB) was FR-4, which had a nominal dissipation factor of 1×10^{-2} (Edwards and Steer, 2016); Si components had a dissipation factor of 2×10^{-4} (Lowe and Sareen, 2014); and other dielectric components – considered to be low loss – had dissipation factors ~ 10^{-5} (Lowe and Sareen, 2014). The calculated effective dissipation factor in the previous paragraph ($2.1 \times 10^{-3} \pm 0.2 \times 10^{-3}$) is of reasonable order given the nominal dissipation factors of the preamplifier's materials and components. Given this, the earlier conclusion that incomplete charge collection noise was a minimal component of dielectric and incomplete charge collection noise was considered reasonable in this context. However, the simplicity and limitations of this analysis are acknowledged.

It is informative to compare the performance of the presently reported diamond X-ray spectrometer with similar studies undertaken using SiC X-ray detectors; SiC is another wide bandgap and relatively low atomic number material used in solid state detectors which are high temperature tolerant and radiation-hard. The best reported spectroscopic X-ray energy resolution obtained with a 4H-SiC detector stands at 196 eV *FWHM* at 5.9 keV (Bertuccio et al., 2011); that 4H-SiC detector was wire bonded to a custom built, state of the art, Complementary Metal Oxide Semiconductor preamplifier with an electronic noise contribution of 6.1 e^- rms (113 eV *FWHM*). However, 10 years earlier, the first reported spectroscopic response of a 4H-SiC detector was much more modest (2.7 keV *FWHM* obtained on a pulser line when illuminated with an ^{241}Am radioisotope) (Bertuccio et al., 2001). The new result presented here (energy resolution of 2.48 keV *FWHM* at 5.9 keV, with a diamond detector) emphasises the importance of a charge sensitive preamplifier with ultra-low noise at the start of the electronics chain, given that the electron hole pair creation energy in diamond is large (12.82 eV ± 0.13 eV (Keister et al., 2018)) compared with competing detector materials, e.g. 4H-SiC (7.28 eV) (Chaudhuri et al., 2013). Given the calculated dielectric noise contribution of the TO-39 package, the importance of low noise packaging is also significant.

The noise associated with the preamplifier's dielectric components used herein could be reduced by changing the FR-4 PCB to glass, ceramic, or polytetrafluoroethylene. Another beneficial

return in terms of dielectric noise reduction would be gained by mounting the detector and FET close together on a common package of low capacitance made from a low loss material. The use of different bonding epoxies to attach the detector to the TO-39 package could also reduce dielectric noise. Likewise, bump bonding the detector to the preamplifier (cf. die attach using silver-loaded epoxy and electrical connections made via wire bond) would also be beneficial for dielectric noise reduction.

4.5 Conclusions, discussion, and further work

A 2.0 mm by 2.0 mm by 0.5 mm electronic grade single crystal CVD diamond was configured as a metal-semiconductor-metal detector and coupled with a custom-built low noise preamplifier for X-ray photon counting. When the detector was illuminated by an ^{55}Fe radioisotope X-ray source at room temperature (20 °C) an energy resolution (*FWHM*) of 2.48 keV at 5.9 keV was achieved.

Shaping time noise analysis concluded that any incomplete charge collection noise in the detector was negligible when compared with other noise sources present in the spectrometer. The noise analysis also demonstrated that the majority of the noise (and thus degradation of the energy resolution beyond the Fano limit) was due to the detector's packaging, its connection to the preamplifier, and the preamplifier itself, rather than the diamond detector. The results reported are agenda setting in that they show for the first time that CVD diamond is a viable detector material for photon counting spectroscopic X-ray detection at photon energies < 10 keV.

The presently reported energy resolution with the diamond detector is modest, although it was shown that this was more a consequence of the detector's packaging and readout electronics rather than the detector itself. To improve the reported spectroscopic resolution the detector would need to be co-located alongside the JFET on a common package, made from a very low loss dielectric, of low capacitance, and of greater resistivity. A reduction of capacitance in the preamplifier by replacing its fibreglass reinforced epoxy laminate (FR-4) printed circuit board (PCB) with a low loss glass, ceramic, or polytetrafluoroethylene PCB would be an important evolutionary step to demonstrate a pathway to improving detector performance. Ultimately the preamplifier and detector will have to be collocated on a state-of-the-art circuit board with state-of-the-art components if the material (diamond) is to challenge more mature room and high temperature spectroscopic X-ray and γ-ray detectors. High temperature investigations of the CVD SC diamond detector are the subject of **Chapter 6** of this thesis.

The relatively low stopping power of C atoms to hard X-rays and γ-rays could see this type of detector find utility counting fast electrons, or other charged particles, in a mixed X-ray and γ-ray radiation field. Thermal neutrons could be detected if a neutron converter, such as Gd, were used

as a thermal neutron absorber; the prompt emission of internal converted atomic electrons could be counted by the diamond detector without significant intrusion from the competing concurrent prompt γ-ray cascade (Knoll, 2010). This hypothesis is explored with Monte-Carlo simulations in **Chapter 7.**

Chapter 5. Electron spectroscopy with a diamond detector

5.1 Introduction

The work is this chapter has been published (see **Section Publications**). The electronic grade single crystal (SC) chemical vapour deposition (CVD) diamond, previously investigated as a room temperature (20 °C) soft X-ray (< 10 keV) spectrometer (**Chapter 4**) was investigated as a prototype high temperature spectroscopic electron (β^- particle) detector. The diamond detector was coupled to the custom-built charge sensitive preamplifier of low noise (**Section 2.4**). A ^{63}Ni radioisotope β^- particle source (endpoint energy = 66 keV) was used to provide a spectrum of β^- particles incident on the detector. The operating temperature, T, of the detector/preamplifier assembly was controlled to allow its performance to be investigated between -20 °C ≤ T ≤ 100 °C, in 20 °C steps. Monte Carlo modelling was used to: a) calculate the β^- particle spectrum incident on the detector; b) calculate the fraction of β^- particle energy deposited into the detector; and c) predict the β^- particle spectrum accumulated by the instrument. Comparison between the model and experimental data suggested that there was a 4.5 μm thick recombination region at the front of the detector. The spectrometer was demonstrated to be fully operable at, -20 °C ≤ T ≤ 80 °C; the results suggested that some form of polarisation phenomenon occurred in the detector at >80 °C. This chapter presents the first energy calibrated low energy (≲ 50 keV) spectroscopic β^- particle diamond detector spectrometer.

5.2 Electrical characterisation and 63Ni β- spectroscopy

5.2.1 Diamond detector

The Element Six UK Ltd. electronic-grade CVD SC diamond (area 2.0 mm by 2.0 mm; thickness 0.5 mm) described in **Section 4.2** was used (Element Six, N.D.). The diamond had a square 1.4 mm × 1.4 mm contact (50 nm Ti, 200 nm Ag) was sputtered onto the centre of its front face and its rear face. The detector was mounted in a custom TO-39 style package with the detector's rear contact connected to the package by silver-loaded epoxy (Loctite, 2014) and the top contact connected to a pin of the package by wire bond, as per **Chapter 4**.

5.2.2 Leakage current and capacitance of the packaged detector

In **Chapter 4**, **Section 4.3.1** the leakage current of this detector was measured with the temperature controlled at room temperature (T = 20 °C); the measurements described here were made using the same packaged detector with the temperature controlled between -20 °C ≤ T ≤ 100 °C.

The leakage current of the detector was measured as a function of electrical potential difference and temperature. For this, the packaged detector was positioned inside a light shielded test harness. Once the detector was positioned, the test harness was sealed and purged with dry N_2 to displace environmental moisture. The test harness holding the packaged detector was then placed in a TAS Micro MT Climatic Cabinet. Once sealed inside, dry N_2 was continually fed into the climatic cabinet to ensure the test environment remained dry (relative humidity < 5 %) (Barnett et al., 2010). To commence measurement, the climatic cabinet's temperature was raised from ambient (≈ 20 °C) to 100 °C with a 30 minute pause in the temperature climb imposed every 20 °C. This allowed the test harness and the packaged detector to reach thermal equilibrium inside the cabinet without undue thermal stress. At 100 °C, the temperature inside the climatic cabinet was held constant for 1 hour before leakage current measurements were commenced. The electrical potential difference was applied across the detector in 5 V increments up to 100 V in both polarities. This procedure was repeated in 20 °C decrements until a temperature of -20 °C was reached; for the temperature descent, a 30 minute waiting time was imposed at each temperature to allow the test harness and detector to reach thermal equilibrium. A Keithley 6487 picoammeter/voltage source, controlled by National Instruments LabVIEW software, was used to apply the potential difference and measure the leakage current. The results of the measurements are presented in **Figure 5.1**.

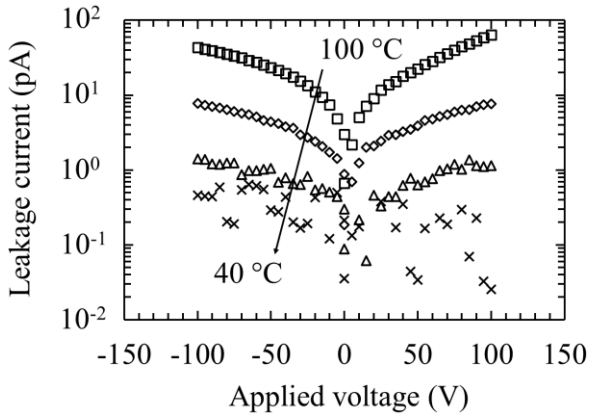

Figure 5.1. a) The leakage current of the packaged detector as a function of electrical potential, in both polarities, up to 100 V, and at temperatures, T, 40 °C ≤ T ≤ 100 °C. T = 100 °C (open squares), T = 80 °C (open diamonds), T = 60 ° C (open triangles), and T = 40 °C (crosses). At T < 40 °C, the detector's leakage current was below the noise floor of the picoammeter (± 0.4 pA). Error bars are omitted for clarity; at +100 V, the uncertainties in leakage currents were ± 0.6 pA and ± 0.4 pA at T = 100 °C and T = 60 °C, respectively.

The maximum packaged detector leakage currents recorded with +100 V of electrical potential applied across the detector were 63.4 pA ± 0.6 pA (T = 100 °C), 7.5 pA ± 0.4 pA (T = 80 °C), and 1.0 pA ± 0.4 pA (T = 60 °C). At $T \leq 40$ °C, the leakage current remained below the noise floor of the Keithley 6487 picoammeter (± 0.4 pA). A portion of the larger leakage current measured at higher temperatures was attributed to the thermal excitation of electrons into the diamond's conduction band (Ewan, 1979). A semiconductor's intrinsic carrier concentration is proportional to exp ($-E_g$ / 2kT), where E_g is the bandgap of the detector material and k is the Boltzmann constant. An Arrhenius plot of the detector's leakage current with ± 100 V potential difference applied across the detector, between 60 °C and 100 °C, was linear within the measurement uncertainty of the Keithley 6487 picoammeter/voltage source. This suggested that most of the leakage current came from the larger concentration of intrinsic carriers in the material at higher temperatures. The detector's leakage current density was 3.23 nA cm^{-2} ± 0.03 nA cm^{-2} at 100 °C and 100 V applied potential difference (field strength = 2 kV cm^{-1}); this assumed that the leakage current was constrained to the volume under the detector's electrical contacts and that surface leakage current pathways were negligible. Such a leakage current density is more than that reported by other researchers using CVD SC diamond. As an example, two electronic grade CVD SC diamond detectors, grown by Element Six UK Ltd (Element Six N.D.), had leakage current densities of 110 pA cm^{-2} and 220 pA cm^{-2} at 100 °C and a field strength of 2 kV cm^{-1} (Tsubota et al., 2015). However, Kumar et al. (Kumar et al., 2017) reported a much larger leakage current density (≈ 40 nA cm^{-2} at an electric field strength of 2 kV cm^{-1}) at 100 °C, for a CVD SC diamond detector grown by IIa Technologies Pte. Ltd., Singapore. The leakage currents reported by Tchouaso et al. for their β^- particle diamond detector (also grown by Element Six UK Ltd) were approximately 6.4 pA cm^{-2} and 12.7 pA cm^{-2} at an electric filed strength of ± 2 kV cm^{-1} (Tchouaso, et al., 2018). Those leakage current measurements were made at ambient laboratory temperature. The asymmetry of leakage current between polarities (**Figure 5.1**) for the presently reported detector have been reported for other CVD diamond detectors (Schirru et al., 2010) (Dueñas et al., 2014); asymmetric leakage currents and leakage current hysteresis in diamond detectors has been shown to depend upon the surface treatment employed prior to metallisation and the type of metallisation used (Pomorski et al., 2006).

The leakage current of the packaged detector at T > 40 °C and at an applied electrical potential difference of 100 V in both polarities reduced as a function of time (see **Figure 5.2)**. The maximum leakage current after 30 minutes with 100 V potential difference continuously applied across the packaged detector was 39.1 pA ± 0.5 pA, 6.3 pA ± 0.4 pA, and 0.6 pA ± 0.4 pA at T = 100 °C, T = 80 °C and T = 60 °C, respectively.

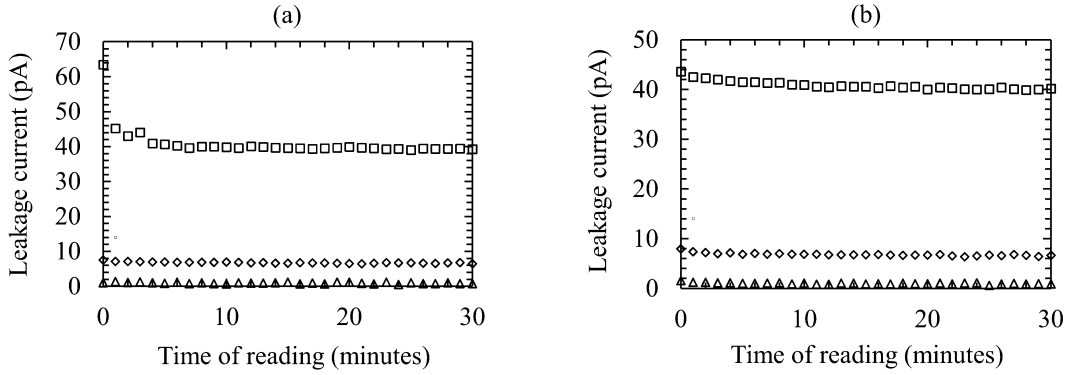

Figure 5.2. The leakage current of the packaged detector as a function of time at applied electrical potential differences of (a) +100 V and (b) -100 V, at temperatures of 100 °C (open squares), 80 °C open diamonds), and 60 °C (open triangles).

The capacitance of the packaged detector had been measured previously with the temperature controlled at room temperature, T = 20 °C (see **Section 4.3.2**). For this investigation the capacitance of the packaged detector was measured with the temperature controlled range -20 °C ≤ T ≤ 100 °C.

The capacitance of the packaged detector and an identical device with its bondwires removed, were measured as functions of applied potential difference, in 5 V steps up to 100 V in both polarities. The packaged detector and the device with bondwires removed were separately placed in a test harness, which was purged with dry N_2 and subjected to the same environmental regime as had been used for the leakage current measurements. A HP 4275A Multi Frequency LCR meter, with test signal set to 50 mV rms magnitude and 1 MHz frequency, was used to record the capacitance of the packaged detector and the device with bondwires removed. The packaged detector's capacitance was independent (within the LCR meter's uncertainties) of applied potential difference and temperature; it was 870 fF ± 20 fF and 840 fF ± 20 fF at 100 °C and -20 °C, respectively. The capacitance of the device with bondwires removed was 540 fF ± 20 fF and 520 fF ± 20 fF at the same temperatures. The capacitance of the bare die detector was therefore invariant and 320 fF ± 30 fF at all reported temperatures and electrical potential differences. Previously the capacitance of the detector was found to be 350 fF ± 30 fF at T = 20 °C (see **Section 4.3.2**).

5.2.3 ^{63}Ni β^- particle spectra

The packaged detector was connected to a custom-built low noise charge sensitive preamplifier with a Vishay 2N4416A Si input Junction Field Effect Transistor (JFET) (Siliconix, 2001) at its input (see **Section 2.4**). The detector and preamplifier were co-located in a light shielded test

harness. Charge pulses (in the form of voltage pulses) from the preamplifier's output were shaped and amplified by an Ortec 572A shaping amplifier. An Ortec EASY MCA 8k multi-channel analyser (MCA) subsequently sorted the voltage pulses from the shaping amplifier into appropriately distributed bins. The electrical potential difference across the detector was applied by a Keithley 6487 voltage source. The β^- particle spectrum was provided by a ^{63}Ni radioisotope β^- particle source (activity 179 MBq; endpoint energy 66 keV) (see **Section 2.5**). The ^{63}Ni β^- particle source was positioned ≈ 10.5 mm above the detector, inside the light shielded test harness.

As per the previously accumulated spectra in this thesis, the β^- particle spectra were collected with the test harness located in a TAS Micro MT climatic cabinet for temperature control. The shaping amplifier, MCA, and voltage source were located outside of the climatic cabinet and operated at ambient laboratory temperature. The test harness was purged with dry N_2 before it was placed in the climatic cabinet, and thereafter the climatic cabinet was continually fed with dry N_2 to ensure the test environment remained dry. The temperature inside the climatic cabinet was raised from laboratory temperature (≈ 20 °C) in 20 °C steps to 100 °C. At each 20 °C temperature step, a minimum 30 minutes waiting time was applied to allow the contents of the test harness to reach thermal equilibrium before the climatic cabinet temperature was raised further. ^{63}Ni β^- particle spectra were accumulated at 100 °C and then in 20 °C decrements, down to -20 °C. Each β^- particle spectrum was accumulated with a live time limit of 1800 s and with the MCA operated in 4096 channels mode. The detector was operated with an applied potential difference of 50 V and the shaping amplifier was set to a shaping time of 2 µs. The potential difference and shaping time were selected in light of preliminary measurements made with the detector and system: when the detector had been previously used as a prototype detector for X-ray spectroscopy (see **Section 4.3.3**), optimum energy resolution was achieved (as measured by the full width at half maximum of a Mn Kα (5.9 keV) photopeak from an ^{55}Fe radioisotope X-ray source) with similar settings. The optimum shaping time occurs when the quadratic sum of series and parallel white noise reach a minimum value (see **Section 4.4**). An exposition of the different electronic noise contributions of a non-avalanche X-ray spectrometer can be found in **Section 2.3.2**. At each temperature, a spectrum was collected without an electrical potential difference applied across the detector to check for the presence of any residual electric field sweeping charge in the detector. A characteristic shoulder attached to the so called zero energy noise peak without electrical potential applied externally would have been indicative of such polarisation. When the detector was confirmed to be unpolarised, the potential difference was applied (50 V) and β^- particle spectra were accumulated. Multiple β^- particle spectra were accumulated (at constant temperature, applied potential difference, and shaping time) to check that each set of conditions provided stable and repeatable results. The turn-around time (the time to save a spectrum and

start to acquire another) was < 2 minutes. To investigate any possible instability in performance, the turn-around procedure was repeated (i.e. spectra were collected repeatedly) until a second spectrum was obtained which was identical to that which had been acquired immediately previously. Thereafter, the applied potential difference was removed and the detector was checked for polarisation effects. If polarisation was detected (by the presence of a shoulder attached to the zero energy noise peak), the check was repeated until the apparent polarisation had dissipated.

The series of repeated spectra accumulated at 100 °C are presented in **Figure 5.3**. In **Figure 5.3**, most of the counts of the zero energy noise peak have been removed from the accumulated spectra; a low energy threshold was set on the MCA after establishing the noise peak's position, and for clarity, the counts accumulated below this threshold prior to its implementation are not presented.

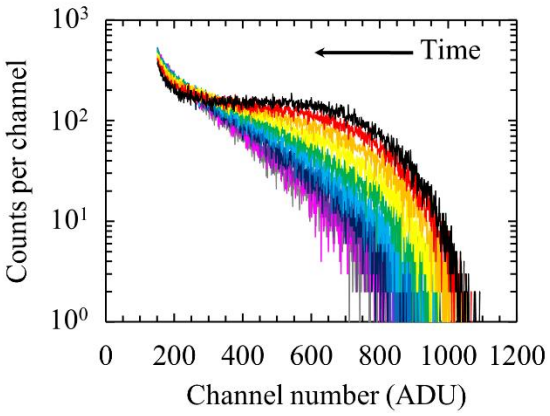

Figure 5.3. The ^{63}Ni β^- particle spectra repeatedly collected, 11 times, at 100 °C. Shown are the β^- particle spectra accumulated: initially (black line); at 32 minutes (red line), at 63 minutes (orange line), at 94 minutes (yellow line), at 126 minutes (green line), at 157 minutes (cyan line), at 189 minutes (blue line), at 224 minutes (indigo line), at 278 minutes (violet line), at 338 minutes (magenta line), and at 382 minutes (grey line). All spectra were collected with a live time of 1800 s.

The β^- particle spectra accumulated at 100 °C varied in morphology as a function of time. Two identical β^- particle spectra at 100 °C were first accumulated 382 minutes after the potential difference was first applied to the detector. In this time, the endpoint channel number had reduced from channel 1004 to channel 887, and the total number of counts had reduced and from 104400 to 54100. It was hypothesised that polarising effects in the detector were responsible for the

changing ^{63}Ni β^- spectrum. After the applied potential difference was removed from the detector, it was found that a residual electric field continued to sweep charge in the detector.

The reduction in MCA endpoint channel number and the reduction of counts collected when the spectrum was repeated, without changing the spectrometer's settings, was indicative of a progressively reducing electrical potential across the active region of the detector, as a function of time. This apparent polarisation of the detector is thought to have been caused by traps in the material's bandgap (Knoll, 2010) that created space charge regions acting in opposition to the applied field across the detector; such a phenomenon has been reported previously in both CVD PC (Manfredotti et al., 1996) and CVD SC (Lohstroh et al., 2007) diamond detectors. Polarisation phenomena have previously been shown to increase as a function of temperature, up to 55 °C, in CdTe radiation detectors (Siffert et al., 1976). Studies with SiC radiation detectors radiation damaged by 6.5 MeV protons and 1.0 MeV neutrons have suggested that high temperatures, up to 580 °C, can decrease the time taken to depopulate charge from deep traps and thus counter this polarisation effect (Ivanov et al., 2012).

The de-trapping lifetime, τ_d, can be expressed as (Bau et al., 1995) (Skidmore et al., 2009),

$$\tau_d = \frac{1}{N_c \sigma v_{th} exp\left(\frac{-E_t}{kT}\right)}, \qquad (5.1)$$

where N_c is the density of states, σ is the capture cross section of the trap, υ_{th} is the drift velocity in the applied potential difference, E_t is the activation energy of the trap, k is the Boltzmann constant, and T is the temperature of the detector in Kelvin. **Equation 5.1** implied that at higher temperatures the de-trapping lifetime increased and consequently trapping lifetime decreased. However, a shorter trapping lifetime implied that there would have been more free traps and that the rate of charge trapping would have been increased causing carrier mobility to decrease and consequently decreased charge collection efficiency. The consequence of the longer de-trapping lifetime explains the progressively more polarised spectrometer response seen in **Figure 5.3**. Intrinsic charge carrier concentration is also equal to $(4.83 \times 10^{21})\ T^{3/2} \exp(-E_G / kT)$ (Sze & Ng, 2007). At 100 °C, the greater intrinsic concentration of charge may have filled traps at a rate greater than the rate of any trap depopulation, this would have caused the polarisation to build up and disrupt the electrical field across the detector. This would have created a potential barrier for charge carriers transiting the affected regions of the detector. Deep traps also act as recombination centres eliminating charge carriers created in the detector; they are less affected by thermal activation so persist for long periods and are often not easily depopulated. Deep traps in diamond are emptied at 230 °C $\lesssim T \lesssim$ 280 °C (Bruzzi et al., 2002) (Bergonzo et al., 2007) and were thus

thought less likely to be responsible for the unstable performance exhibited by the presently reported detector at 100 °C. However, shallow traps are emptied at lower temperature ($T \lesssim 80$ °C) (Bergonzo et al., 2007); which would account for a continuously evolving trapping population polarizing the detector at 100 °C. At 100 °C the released charge from shallow traps could have collected under the detector's anode contact which would have caused a space charge region to form close to that contact. This could have transitioned the (approximately) Ohmic current-voltage characteristic of the detector to a space charge limited current-voltage characteristic (current proportional to the square of applied potential difference across the detector). Also, imperfections in the surfaces of CVD SC diamond wafers can be relatively deep (10 μm) (Zheng et al., 2020) which would make the CVD SC diamond surface/contact interface a likely region where space charge could have built up. Further characterisation of the spectrometer at 100 °C showed that the polarisation effect could be reversed by removing the applied potential difference from the detector for a short period (≈ 1 hour). After the detector was depolarised in this fashion, when the 50 V potential difference was reapplied the detector would repolarise as before. Further detailed study of the apparent polarisation phenomenon is warranted. A detailed study of the roles of the contact metallisation and diamond surface preparation in the observed behaviour may reveal that a key role is played by the detector fabrication process.

The β^- particle spectra collected at $T \leq 80$ °C are presented in **Figure 5.4**. The spectra are shown in their raw form with the MCA scale uncalibrated; the channel width (in energy and charge terms) of the spectra will have changed with temperature by virtue of variation in the preamplifier's conversion factor with temperature. At each temperature, the spectra were repeatable and the changing β^- particle spectra morphology, which was indicative of polarisation, was absent; however, a residual electric field remained in the detector when the applied potential difference was removed. This residual electric field dissipated in less than 30 minutes. The change in position of the apparent endpoint on the MCA's scale was primarily due to the change in performance of the preamplifier as a function of temperature. However, some contribution may have been from variation of the average electron-hole pair creation energy, which is known to vary as a function of temperature in other materials (Barnett et al., 2013) (Whitaker et al., 2017) (Butera et al., 2018). The number of counts in each spectrum decreased as a function of temperature. At 80 °C, the total number of counts collected in each spectrum was ≈ 78300 with an endpoint channel of 1080; at -20 °C the total number of counts collected were ≈ 50300 with the endpoint channel of 840. Some of the change in the position of the endpoint channel number will have been due to change in the conversion factor of the preamplifier with temperatures. However, given that the live time limit and shaping amplifier shaping time were unchanged between each spectrum; and given that the apparent endpoint of the lower temperature spectra

reduced towards lower channel numbers on the MCA scale, a corresponding increase in the number of counts per channel would have been expected, as each MCA channel would have had to encompass a larger range of β^- particle energies. However, the opposite was observed; the number of counts per channel remained either relatively constant or slightly reduced when the endpoint channel reduced with temperature (**Figure 5.3**). The reason for this is not fully understood at present; it may have been caused by the higher temperatures ionising trapping centres which removed space charge which was otherwise present at lower temperatures. In so doing, the effective volume of material available for electron-hole pair creation leading to detection of the incident radiation through the induction of charge on the contacts of the detector by virtue of the movement of the charge carriers within the detection medium may have been larger at the higher temperatures. Alternatively, or in addition, higher temperatures may have enabled collection of a greater portion of the charge created in the diamond outside of the volume defined by the contact metallisation. Based on the change in number of counts, the effective active volume of the diamond would have had to be 35 % greater at 80 °C than it was at -20 °C. Diffusion of charge from low field regions at higher temperatures may have contributed at least in part to a greater effective active volume under those conditions but the quantitative extent to which it did is presently unknown; more evidence would be required draw definitive conclusions as to the extent of this contribution. Furthermore, additional investigation of the phenomena reported here is essential if a complete understanding of the detector is to be achieved.

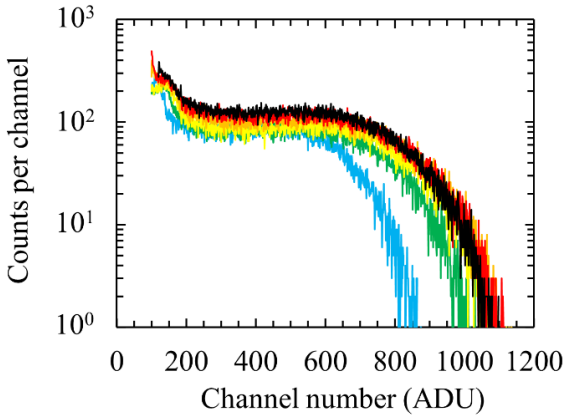

Figure 5.4. ^{63}Ni β^- particle spectra accumulated with the diamond detector from -20 °C ≤ *T* ≤ 80 °C. *T* = 80 °C (black line), *T* = 60 °C (red line), *T* = 40 °C (orange line), *T* = 20 °C (yellow line), *T* = 0 °C (green line), and *T* = -20 °C (cyan line). The spectrum live time limit was 1800 s in each case. It should be noted that the channel width in units of energy for each spectrum is not identical.

5.2.4 ^{63}Ni β$^-$ particle spectrum modelling

The CASINO (monte CArlo SImulation of electroN trajectory in sOlids) computer program (Drouin et al., 1997) (Hovington et al., 1997) was used to simulate the paths and the energy losses of the β$^-$ particles emitted from the ^{63}Ni β$^-$ particle source as they traversed the 1 µm Ni overlayer and the 10.5 mm dry N_2 atmosphere between the ^{63}Ni β$^-$ particle source and the top of the detector. Each simulated β$^-$ particle was allocated an energy between 1 keV and the ^{63}Ni endpoint energy of 66 keV, in 1 keV increments. The simulated spectrum of β$^-$ particles emitted from the ^{63}Ni β$^-$ particle source was dependent upon the emission probability of each β$^-$ particle's energy when emitted by ^{63}Ni and included the effects of self-absorption within the ^{63}Ni radioisotope source (Liu et al., 2015). A total of 18,549,380 β$^-$ particles across the 1 keV to 66 keV β$^-$ particle energy range were simulated. The total number of β$^-$ particles simulated was selected in order to provide good counting statistics across the whole of the energy range rather than to reflect the activity of any specific ^{63}Ni β$^-$ particle source. The density of the 1 µm Ni overlayer was modelled as 8.908 g cm^{-3} and the density of the N_2 atmosphere was modelled as 0.0012 g cm^{-3}. The physical model selected for the modelling was 'Mott'; the developers of CASINO have reported the associated backscattering coefficients to be in better agreement with experimental results at low electron energies (< 10 keV). The Mott model has also been found to be more accurate than the Rutherford cross section for low *Z* materials (Hovington et al., 1997). Of the three Mott models available to CASINO 'Mott by Interpolation' was selected as this model was computationally faster and known to be more accurate than the other selectable Mott models (Drouin et al., 1997). Other pertinent CASINO settings were: Ionisation Potential – Joy and Luo (Joy & Luo, 1989); Random Number Generator – the Press et al. (Press et al., 1986); Directing Cosine – Drouin et al (Hovington et al., 1997); and Effective Section Ionisation – Casnati et al. (Casnati et al., 1982). The computed trajectories of the simulated β$^-$ particles were used to calculate their residual energy after interacting with the 1 µm Ni overlayer and the dry N_2 atmosphere above the detector's face. The simulated β$^-$ particles at the face of the detector were analysed and the distribution of those energies produced the spectrum of β$^-$ particles incident upon the face of the detector. Both β$^-$ particle spectra (i.e. emitted from source and incident on detector) are presented in **Figure 5.5**. The endpoint β$^-$ particle energy emitted from the ^{63}Ni layer of the β$^-$ particle source was 66 keV, but after traversing the 1 µm Ni overlayer and the dry N_2 layer the endpoint energy of the spectrum reduced to 63 keV. It should also be noted that the temperature range reported here did not change the density of the Ni overlayer or the dry N_2 atmosphere sufficiently to alter the results of the CASINO modelling.

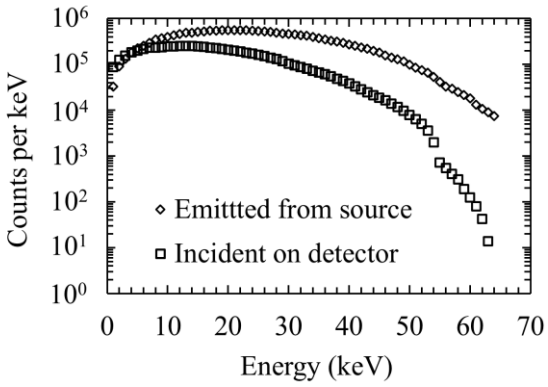

Figure 5.5. Simulated β^- particle spectrum emitted from the ^{63}Ni layer of the β^- particle source including the effects of self-absorption (open diamonds) and incident on the face of the detector having been attenuated by the 1 μm protective Ni overlayer and 10.5 mm of dry N_2 atmosphere (open squares).

The CASINO program was also used to calculate the quantum detection efficiency of the detector (i.e. the fraction of the energy deposited in the detector by β^- particles incident upon the face of the detector, as a function of energy up to 66 keV). To do this, 4000 β^- particles at each energy from 1 keV to 66 keV in 1 keV steps were simulated as incident upon a) the top metalized contact, and b) the non-metalized portion of the detector's top face, i.e. 8000 β^- particles were simulated at each energy. The number of β^- particles simulated was chosen in order to give good counting statistics rather than to reflect any specific individual case of illumination of the detector with β^- particles. At each energy, both simulations were combined in the ratio of the areas of the detector's face covered (49 %) and not covered (51 %) by the contact. As shown in **Figure 5.6**, the fraction of β^- particle energy deposited in the detector was 0.49 at 1 keV and this rose to 0.97 at 66 keV. However, it should be noted that this was calculated based on the assumption that the entire thickness (i.e. 500 μm) of the diamond usefully contributed to the quantum detection efficiency; this resulted in an overestimate of the detector's quantum detection efficiency since, as will be shown, the detector actually had a 4.5 μm deadlayer in the diamond at its top. Furthermore, it should be noted that the values stated and presented as part of the figure include backscattering losses.

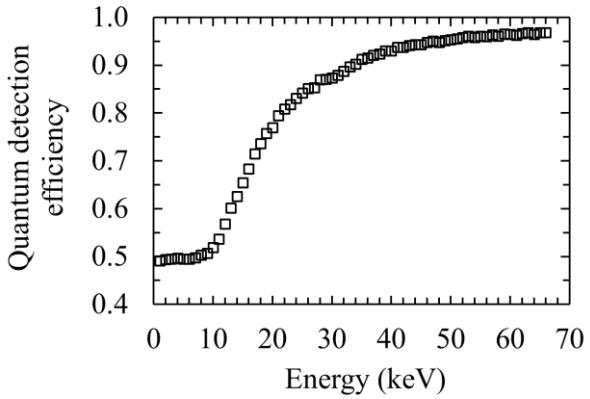

Figure 5.6. Quantum detection efficiency as a function of energy assuming that the whole thickness (500 μm) of the diamond contributed usefully to the quantum detection efficiency.

In order to predict the ^{63}Ni β^- particle spectrum that would be detected by the spectrometer, the CASINO simulations in **Figure 5.5** and **Figure 5.6** were combined. The resultant spectrum excluded any pulse pile up and detector edge effects, as well as the noise processes (Fano, electronic, and any incomplete charge collection noise) present in the spectrometer. The results for spectra at selected temperatures (80 °C, 20 °C, and -20 °C) are presented in **Figure 5.7**; similar results were obtained for all temperatures but three temperatures were selected for clarity of presentation. For comparison of the simulated spectrum and the experimentally detected spectra, the predicted spectrum and the experimentally detected spectra at each temperature were normalised. For this, the predicted spectrum was normalised to the mean number of counts in the generally constant region between 10 keV and 20 keV. The experimentally detected spectra were normalised to the mean number of counts in the generally constant region between 15 keV and 30 keV; this avoided counts from the zero noise energy peak adding to the averaged count. Experimental spectra were calibrated using the endpoint energy from the simulated spectrum, the position of the zero energy noise peak, and by taking account of the relative probability of detection as indicated by the number of counts that were detected.

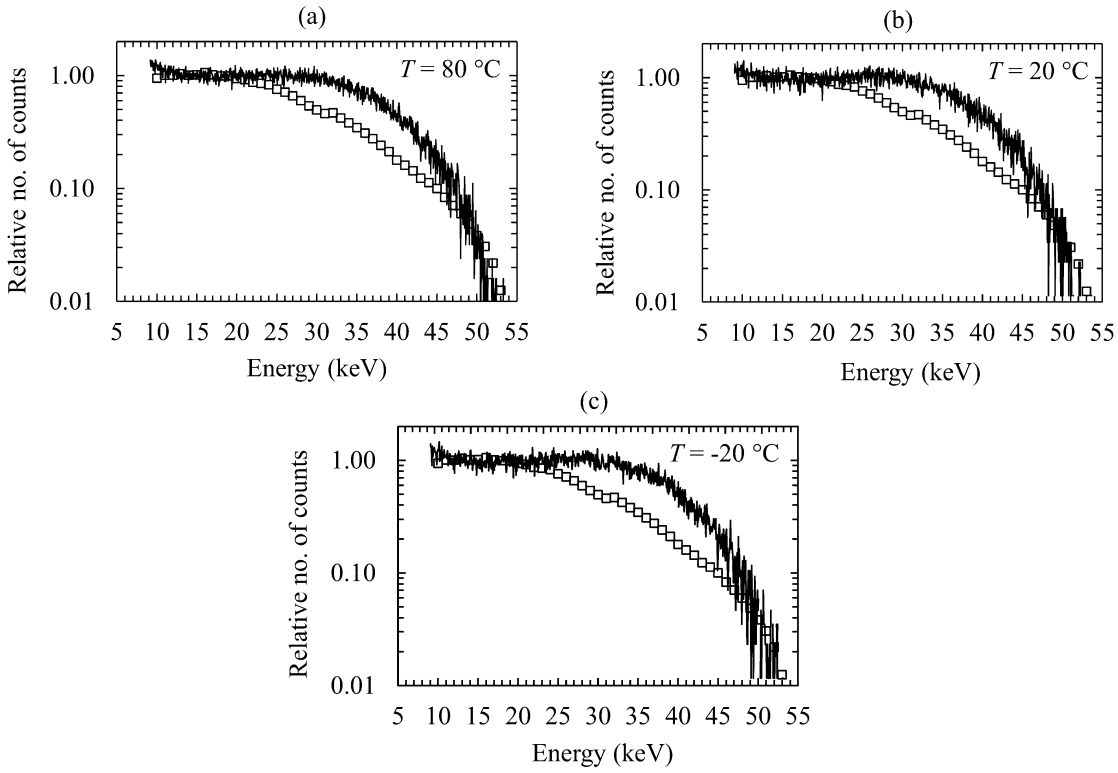

Figure 5.7. ^{63}Ni β^- particle spectra experimentally accumulated (black line) at (a) T = 80 °C, (b) T = 20 °C, and (c) T = -20 °C, as compared with that predicted by the simulation (open squares). To enable morphological comparison, the spectra are presented in terms of relative counts and the energy axis has been calibrated based on the position of the zero energy noise peak, the endpoint energy predicted by the simulation, and by taking account of the relative probability of detection as indicated by the number of counts that were detected.

As can be seen from **Figure 5.7**, the simulated and experimentally measured spectra had substantially different morphologies. The particular morphological difference shown is evidence of an inactive "dead" layer within the diamond at its front. Electron-hole pairs generated in a deadlayer are not able to move in the normal way so as to induce on the contacts of the detector the charge that they would have induced had they been created in an active region of the detector. Consequently, those charge carriers do not contribute to the accumulated spectrum. Such deadlayers (where generated charge is lost) have been reported at the detector/contact interface of other semiconductor radiation detectors (e.g. by Lioliou et al. (2016)). Further modelling in CASINO was used to compute the apparent thickness of the deadlayer in the present diamond detector.

The simulations which led to the production of **Figure 5.6** were rerun to include the presence of a deadlayer within the diamond immediately proximate to the front contact. The thickness of

deadlayer was varied from non-existent to 4.5 μm thick, in 0.5 μm increments. This produced new quantum detection efficiency predictions which included the effects of a deadlayer. Each simulation was then combined with the simulations of **Figure 5.5** to produce a number of predicted spectra for different deadlayer thicknesses.

A match between the predicted and experimentally detected spectra was accomplished when a 4.5 μm deadlayer at the top of the detector was included. The simulated spectrum (with 4.5 μm deadlayer) and the experimentally detected spectra was normalised to the mean number of counts in the generally constant region between 17 keV and 25 keV. The experimental spectra were then energy calibrated using the endpoint energy from the simulated spectrum and the position of the zero energy noise peak. In positioning the endpoint of the simulated spectrum, the relative probability of detection, indicated by the number of detected counts was also considered.

It was recognised that inclusion of a single deadlayer thickness across all temperatures was likely to be an oversimplification (the thickness of a recombination region is known to be temperature dependent in ultraviolet detectors (Blank et al., 2003)) but the approach employed here was considered adequate for present purposes. In future, synchrotron measurements could be employed to measure the profile and thickness of the dead region by measuring the X-ray quantum efficiency as a function of X-ray energy (Krumrey & Scholze, 2004). Alternatively, a measurement of the responsivity of the detector with ultraviolet, visible, and infrared wavelengths could determine deadlayer thickness (Lioliou et al., 2015). The calculated quantum detection efficiency for the detector, including the 4.5 μm deadlayer, is shown in **Figure 5.8**; for comparison, the quantum detection efficiencies which would have resulted had the deadlayer been 1.5 μm and 3.0 μm are also included. With a 4.5 μm deadlayer, the quantum detection efficiency (fraction of β^- particle energy usefully deposited in the active region of the detector) was 0.02 and 0.79 at 30 keV and 66 keV, respectively, cf. 0.87 and 0.97 without a deadlayer. The spectra predicted to be detected when the 4.5 μm deadlayer was included in the simulations are shown in **Figure 5.9** together with the experimentally detected ^{63}Ni β^- particle spectra; for clarity of presentation, only the spectra at temperatures of 80 °C, 20 °C, and -20 °C are shown. As was the case for **Figure 5.7**, the spectra are presented in terms of relative counts, based on the position of the zero energy noise peak, the endpoint energy predicted by the simulation, and by taking account of the relative probability of detection as indicated by the number of counts that were detected.

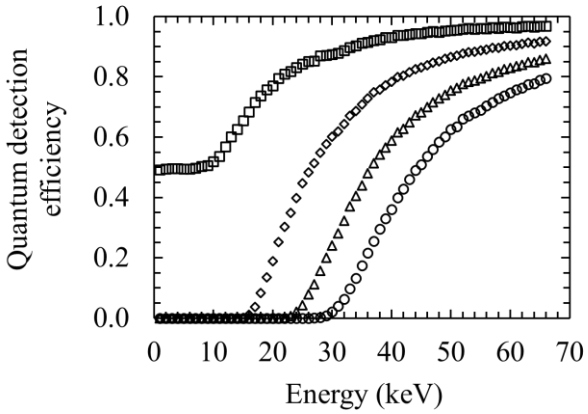

Figure 5.8. Quantum detection efficiency for the detector as a function of β^- particle energy when no deadlayer (open squares), and deadlayers of 1.5 µm (open diamonds), 3 µm (open triangles), and 4.5 µm (open circles) are included.

The apparent endpoint energy of the detected spectra (≈ 46 keV) was lower than the endpoint energy of the spectrum illuminating the detector (63 keV) because the detector's top contact and the 4.5 µm deadlayer attenuated the energy of the β^- particles before they could reach the active region of the detector. Electronic grade CVD SC diamond wafers are scaif polished (a mechanical process where diamond particles are used to abrasively polish the wafer's surface) (Lefeuvre, 2020). Imperfections caused by the polishing process can reach 10 µm below the polished surface (Zheng et al., 2020). It is hypothesised that this may have altered the electrical characteristics of the diamond resulting in the 4.5 µm thick deadlayer at the top of the detector.

Given that the front and rear of the detector were substantially similar, the presence of a similar deadlayer immediately proximate to the bottom contact was hypothesised but could not be concluded from the present data. The detector was sufficiently thick that the presence (or absence) of a comparable deadlayer at the bottom would not have changed the quantum detection efficiency within the energy range applicable for the present work; hence, regardless of the presence or absence of a 4.5 µm deadlayer at the bottom of the detector, the detected spectrum would be the same. Further CASINO simulations which included a deadlayer proximate to the bottom contact were performed and showed that the spectra predicted to be detected were identical regardless of the inclusion or exclusion of such a 4.5 µm thick bottom deadlayer.

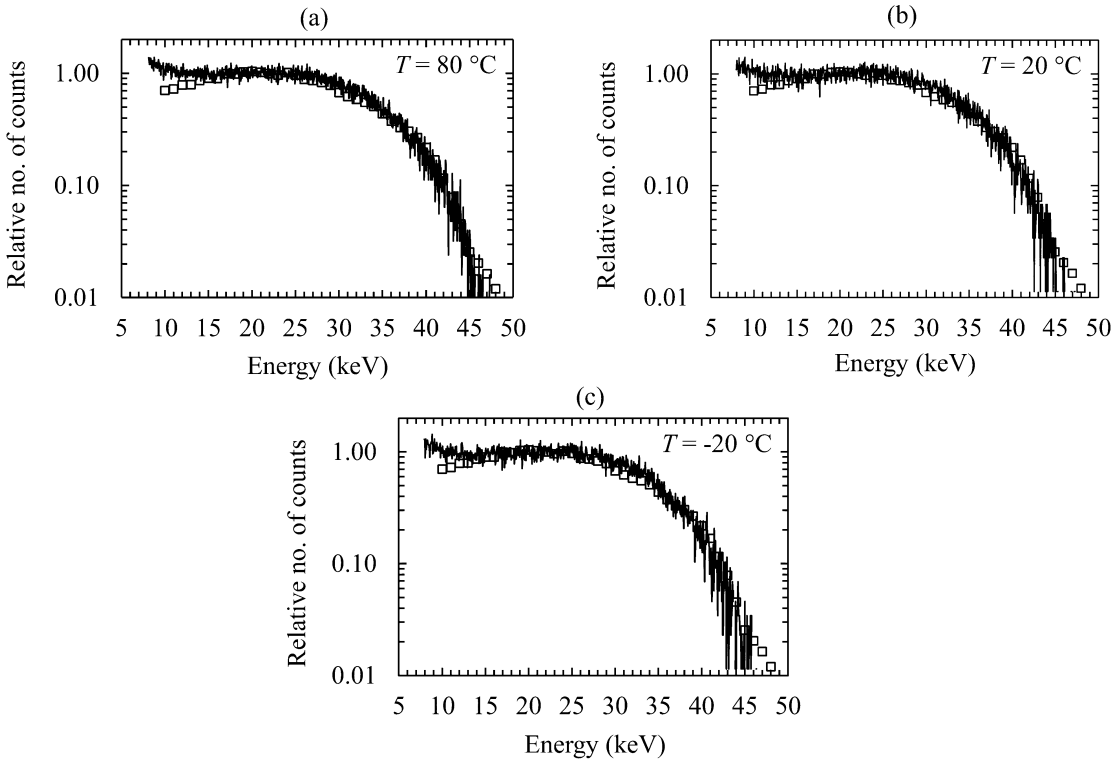

Figure 5.9. Comparison of ^{63}Ni β^- particle spectra predicted when a 4.5 μm deadlayer was included (open squares) and experimentally detected (black line) at temperatures of (a) 80 °C, (b) 20 °C, and (c) -20 °C, as compared with that predicted by the simulation (open squares). To enable morphological comparison, the spectra are presented in terms of relative counts and the energy axis has been calibrated based on the position of the zero energy noise peak, the endpoint energy predicted by the simulation, and by taking account of the relative probability of detection as indicated by the number of counts that were detected.

5.3 Discussion, conclusions, and further work

An electronic grade CVD SC diamond detector previously investigated as a room temperature (T = 20 °C) X-ray spectrometer (see **Section 4.3.3)**, was investigated for its performance as part of an electron (β^- particle) spectrometer. The detector was connected to a custom-built low noise charge sensitive preamplifier which was itself connected to a standard electronics chain. The detector was illuminated by a ^{63}Ni radioisotope β^- particle source. The spectrometer was investigated across the temperature range -20 °C $\leq T \leq$ 100 °C. At 100 °C, the detector experienced significant polarisation. Performance was stable at each of the lower investigated

temperatures (i.e. -20 °C ≤ T ≤ 80 °C) and polarisation did not impede the collection of spectra across this temperature range.

The detector's performance was modelled using CASINO. By comparison between the spectra predicted by the model and those experimentally accumulated, it was determined that the detector had a 4.5 μm thick deadlayer in the material in direct proximity with the front contact. It was hypothesized that imperfections were introduced into this region of material during a polishing process used by the supplier of the diamond from which the detector was fabricated.

These results show that spectroscopic detection of relatively soft (energy ≤ 63 keV) electrons (β^- particles) is possible at elevated temperatures (≤ 80 °C) using a CVD SC diamond detector. By virtue of being thick (500 μm), the presently reported detector had excellent quantum detection efficiency compared with most other prototype wide bandgap semiconductor detectors proposed for space-borne electron spectrometers (Lioliou et al., 2018) (Butera et al., 2019) (Whitaker et al., 2020) which are thin due to the difficulties inherent in producing high quality thick epitaxial structures in many of the materials investigated. Had the deadlayer been absent, with the presently reported contact configuration, the fraction of β^- particle energy deposited in the detector would have been 0.49 at 1 keV, and this would have risen to 0.97 at 66 keV. Even so, with the deadlayer being present, *QE* was 0.79 at 66 keV. Other wide bandgap detector materials have been reported as proof of concept or prototype β^- particle detectors that are temperature tolerant and radiation hard. A prototype GaAs p^+-i-n^+ mesa diode detector (10 μm active i layer) (Lioliou et al., 2018) was reported with a *QE* of 0.73 at 70 keV. In that case, the *QE* of this detector per unit thickness was bolstered by the greater stopping power of GaAs cf. diamond. However, the *QE* of the GaAs detector declined to 0.49 at 100 keV (100 keV β^- particles were less likely to fully deposit their energy in the active i layer). Other reported emergent semiconductor detectors considered as possibly suitable for deep space electron spectrometry are InGaP (Butera et al., 2019) and AlGaAs (Whitaker et al., 2020). The active i layers for both reported detectors were thin; 5 μm for InGaP and 3 μm for AlGaAs, consequently and despite the superior stopping power of the materials used in the detectors, the β^- particle *QE*s were lower than for the presently reported diamond detector. The *QE* of the InGaP detector was 0.45 at 62 keV and the AlGaAs detector's peak *QE* (0.53) occurred at 38 keV. Thicker i layers would be required for both of these detectors to improve their *QE*s.

Despite the specific limitations of the detector reported here, the results show that diamond is a promising candidate material for future solid state electron spectrometers which will be required for various terrestrial and space applications. Whilst polarisation limited operation of the detector at 100 °C, the wide bandgap of diamond (5.47 eV (Clark et al., 1964)) suggests that operation at

even higher temperatures is likely to be possible if the present polarisation problem can be eliminated. This potential for operation at extremely high temperatures and the expected radiation hardness of diamond detectors are key motivating factors for its study by researchers developing next generation instrumentation for space science. One key challenge to address is understanding the nature and mechanisms of the apparent polarisation phenomenon: detectors made from different CVD SC diamonds should be characterised and it may be advantageous to measure the change in performance of the present detector in detail at temperatures 80 °C < $T \leq 100$ °C in order to identify the transitionary behaviours between stable and polarised performance. Another potentially valuable avenue of exploration would be in seeking to understand how surface preparation changes the properties of the diamond detector close to its surface; a reduction in thickness (or preferably, elimination) of the deadlayer would improve the quantum detection efficiency at soft energies ($\lessapprox$ 25 keV). It is also informative to compare the diamond detector's response to β^- particles with that for photons of similar energies. The *QE* of the diamond detector for β^- particles is high because of its thickness. Despite the detector being thick, the detector's quantum detection efficiency for photons would be low, by virtue of carbon's low atomic number. For example, at 66 keV the detector's β^- particle detection efficiency was 0.79; however, its quantum detection efficiency for 66 keV photons was computed to be 0.71×10^{-5}. This suggests that this type of detector could find particular utility in detecting electrons or β^- particles in mixed electron/photon radiation environments as the need to discriminate or subtract the photon background would be reduced cf. for higher atomic number detectors.

Chapter 6. Hard X-ray and γ-ray detection using a chemical vapour deposited (CVD) single crystal (SC) diamond detector

6.1 Introduction

Following the initial characterisation of the diamond detector as an X-ray detector at 20 °C, as described in **Chapter 4**, further investigation of the detector's response was conducted at higher photon energies and operating temperatures. The responses of the detector to soft (5.9 keV) and hard (22.16 keV) X-rays and γ-rays (88.03 keV) as a function of temperature (-20 °C ≤ T ≤ 100 °C) were investigated. The X-rays and γ-rays, used to characterise the energy response of the detector, were emitted from an ^{55}Fe radioisotope X-ray source and a ^{109}Cd radioisotope X-ray and γ-ray source. The Mn Kα (5.9 keV) and Kβ (6.49 keV) X-ray emissions from the ^{55}Fe radioisotope X-ray source were detectable (i.e. separated from the zero energy noise peak) at temperatures of -20 °C ≤ T ≤ 60 °C; the Ag Kα (22.16 and 21.99 keV) and Kβ (24.94, 24.99 and 25.46 keV) X-ray emissions and 88.03 keV γ-ray emissions were detectable across the entire temperature range investigated (-20 °C ≤ T ≤ 100 °C). The detector and the preamplifier were operated without cooling. Noise analysis indicated that dielectric noise and possibly incomplete charge collection noise dominated the other noise sources at 5.9 keV. When the detector was illuminated with the ^{109}Cd radioisotope X-ray and γ-ray source, a high count rate introduced parasitic effects (possibly baseline shift) which reduced the optimum shaping time of the spectrometer. Leakage current measurements at 100 °C identified shallow traps in the detector.

After the measurements reported in **Chapter 4** and **Chapter 5**, the diamond was repackaged in the TO-39 package before work reported in this chapter was undertaken. Therefore, due to subtle differences which can arise in detector performance as a result of detector packaging, the repackaged detector was characterised afresh.

6.2 Detector characterisation, X-ray, and γ-ray spectroscopy at controlled temperatures (-20 °C ≤ T ≤ 100 °C)

6.2.1 Leakage current measurements

The detector's leakage current was measured with the packaged detector again installed inside an electromagnetically screened test harness that had been purged with dry N_2 before it was sealed.

The test harness was placed in a TAS Micro MT Climatic Cabinet, as per the initial measurements (see **Chapter 4** and **Chapter 5**), to control the temperature. The climatic cabinet was also continuously purged with dry N_2 to keep the test environment dry (< 5 % relative humidity) (Barnett et al., 2010). The temperature inside the climatic cabinet was raised from laboratory temperature (≈ 20 °C) to 100 °C in 20 °C steps. Every 20 °C step of the temperature climb was followed by a pause of 30 minutes to avoid thermal shocks and to enable the temperature of the test harness to equalise with the temperature inside the climatic cabinet. At 100 °C, a 60 minute pause was imposed before commencing measurements of leakage current as a function of applied potential difference across the detector at temperatures -20 °C ≤ T ≤ 100 °C in 20 °C decrements. For the temperature reductions, a 30 minute pause was imposed after the climatic cabinet stabilised at each temperature decrement before leakage current measurements were re-commenced.

A Keithley 2636B voltage source applied electrical potential difference to the detector and a Keysight B2980 femtoammeter measured the leakage current. The potential difference was applied in 5 V steps up to 100 V in both polarities. The potential difference was applied to the detector's top contact and the leakage current was measured from the lower contact. The application of the electrical potential difference and the measurement of leakage current was automated with National Instruments LabVIEW software. The leakage current was measured 5 s after the potential difference was applied; thereafter a further 5 s wait time was imposed before the applied potential difference was increased.

The measured leakage current of the packaged detector as a function of applied potential difference is presented in **Figure 6.1**. At +100 V applied potential difference, the leakage current was 40.6 pA ± 0.2 pA at 100 °C and 0.194 pA ± 0.005 pA at 40 °C. In the opposite polarity, at -100 V, the leakage current was 40.4 pA ± 0.2 pA at 100 °C and 0.294 pA ± 0.006 pA at 40 °C. At 20 °C and +100 V applied potential difference, the femptoammeter recorded a leakage current flow in the opposite direction to the applied potential difference, which was -0.017 pA ± 0.003 pA. At an applied potential difference of -100 V, the leakage current of the packaged detector was 0.121 pA ± 0.004 pA at 20 °C. At lower temperatures, the leakage current approached the noise floor of the Keysight B2980 femtoammeter (± 0.003 pA) and reduced to values which could not be measured reliably with the equipment employed. The uncertainties in the measurements were dominated by the accuracy of the Keysight B2980 femtoammeter (± 0.003 pA).

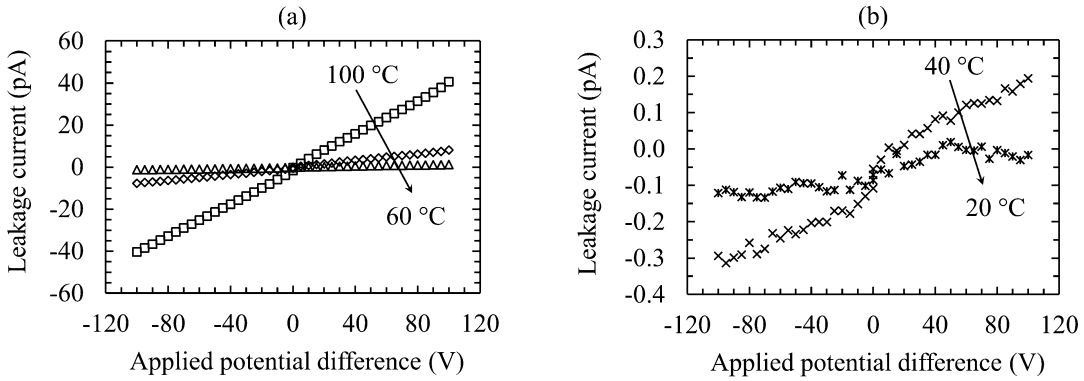

Figure 6.1. The leakage currents as a function of applied potential difference across the packaged detector, in both polarities, up to ±100 V, at (a) 100 °C (open squares), 80 °C (open diamonds), and 60 °C (open triangles) and (b) 40 °C (crosses) and 20 °C (stars). At temperatures below 20 °C the leakage current was below the noise floor of the Keysight B2980 femtoammeter (± 0.003 pA). Error bars have been omitted for clarity. At ±100 V the leakage current measurement uncertainty was ± 0.21 pA and ± 0.004 pA at 100 °C and 20 °C, respectively.

The leakage current arising from the detector's packaging was measured using a spare (i.e. unconnected) pin on the detector's TO-39 package. The package leakage current measurements were conducted immediately after the packaged detector's leakage current measurement, without disturbing the packaged detector in the climatic cabinet, using the procedures described above. The leakage current of the detector itself was calculated by subtracting the package leakage current from the packaged detector's leakage current; the results are presented in **Figure 6.2**. Discontinuities in leakage current at low applied potential difference, $V_{applied}$, were observed $+15\ V \leq V_{applied} \leq +25\ V$, at 100 °C and $+20\ V \leq V_{applied} \leq +45\ V$, at 80 °C. The uncertainties shown in **Figure 6.2** are the uncertainties of the measuring equipment and the relative measurement from one data point to the next. There would have been additional uncertainties (estimated to be ≈ ± 0.15 pA) from tribocharging as cables were moved between outputs on the test harness to measure leakage current from the packaged detector and the detector's packaging. The discontinuous measurement of leakage current could have been caused by fluctuations in leakage current as a function of time. Alternatively, the discontinuous leakage current measurement could have been caused by triboelectric charge being released. The broadly Ohmic behaviour of the detector's leakage current as a function of applied potential difference was observed to deviate at $V_{applied} \gtrapprox +80\ V$ at $T = 100$ °C and $T = 80$ °C. This was indicative of a transition from an ohmic conduction mechanism across the detector to a space charge limited leakage current conduction (SCLC) mechanism (see **Section 5.2.3**). At $V_{applied} \gtrapprox +80\ V$ (and at $T = 100$ °C and $T = 80$ °C) the leakage current across the detector transitioned to the Mott and

Gurney drift regime where the leakage current is proportional to the square of applied potential difference. The transition from Ohmic to SCLC at positive applied potential difference could have been caused by deeper imperfections, e.g. in the scaife polished surface of one face of the CVD SC diamond (see **Section 5.2.4**), alternatively asymmetry of the sputtered Ti/Au contacts on the face of the detector could have played a role in the detector's observed asymmetric leakage current.

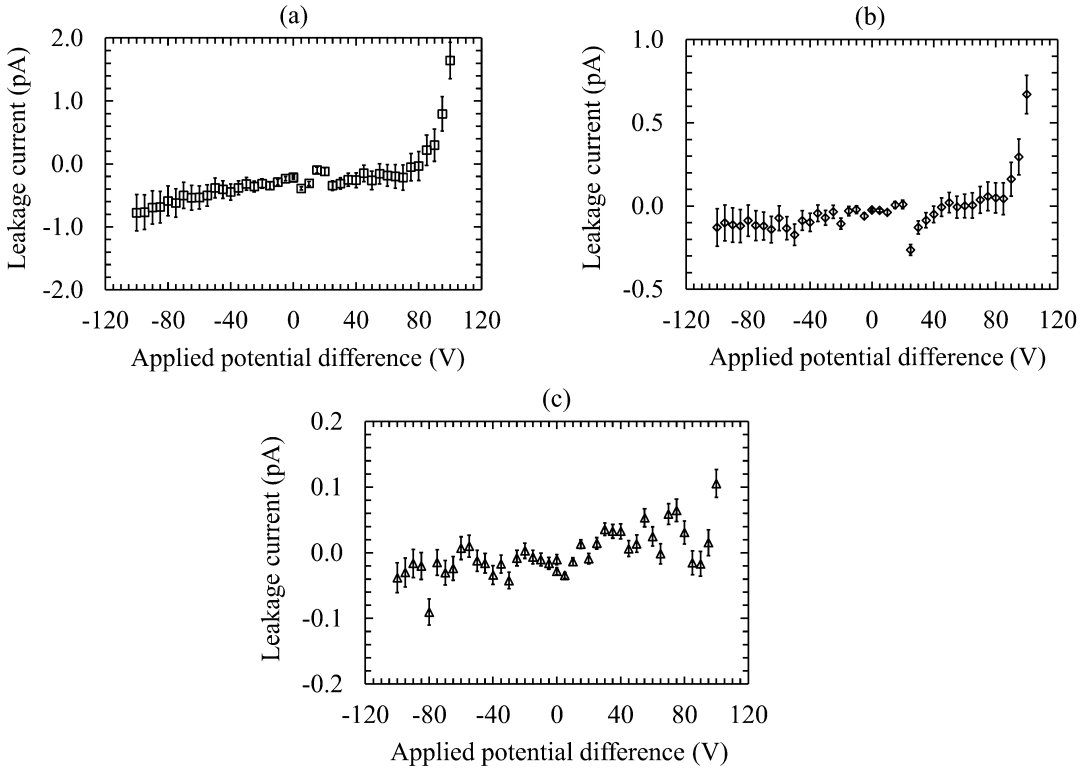

Figure. 6.2. The detector leakage current (i.e. the detector leakage current with the leakage current of the packaging subtracted) at (a) 100 °C (open squares), (b) 80 °C (open diamonds), and (c) 60 °C (open triangles). The error bars represent the uncertainties of the measuring equipment and uncertainty between one data point and the next. There was likely an additional uncertainty (estimated ≈ ± 0.15 pA), caused by triboelectric charge release, when cables were disconnected and reattached to the test harness to measure the packaged detector's leakage current and the leakage current of the detector's packaging.

The leakage current of the detector at an applied potential difference of +100 V was 1.64 pA ± 0.57 pA at 100 °C and 0.11 pA ± 0.02 pA at 60 °C. In the opposite polarity, at -100 V applied potential difference, the leakage current was 0.78 pA ± 0.29 pA at 100 °C and 0.04 pA ± 0.02pA at 60 °C. At T < 60 °C, the leakage current of the detector without the

packaging included could not be measured reliably. The maximum leakage current density, assuming the leakage current was constrained between the detector's 1.96 mm^2 square contacts, at an applied potential difference of +100 V (electric field strength 2 kV cm^{-1}) was 83.7 pA cm^{-2} ± 29.0 pA cm^{-2} at 100 °C, 34.2 pA cm^{-2} ± 5.86 pA cm^{-2} at 80 °C, and 5.38 pA cm^{-2} ± 1.08 pA cm^{-2} at 60 °C.

This leakage current density at 100 °C and field strength 2 kV cm^{-1} was less than that reported for another Element Six CVD SC diamond at the same electric field strength and temperature (Angelone et al., 2012), i.e. ≈ 420 pA cm^{-2} and ≈ 850 pA cm^{-2}, in forward and reverse polarity, respectively. That diamond detector also exhibited an opposite flow of leakage current with respect to the applied electric field up to ≈ 0.5 kV cm^{-1}. Leakage currents in diamond detectors that nominally flow in the opposite direction to the applied potential difference have also been reported at low (≤ 1 kV cm^{-1} (Tchouaso et al., 2018)) and high (≈ 5 keV cm^{-1} (Dueñas et al., 2014)) electric field strengths. It should also be noted that asymmetric and erratic dark/leakage currents have been previously reported in polycrystalline (CVD PC) diamond detectors (Edwards et al., 2005) (Alexopoulos et al., 2018). In high luminosity particle accelerators, erratic currents have been supressed by magnetic fields (0.1 T – 0.6 T) parallel to the CVD PC grain boundary or by lowering bias voltage below 3.3 kV cm^{-1} (Edwards et al., 2005). In the case of CVD SC detectors, leakage current has been shown to increase over time without exposure to ionising radiation (Pomorski et al., 2006). Such leakage current instability has been suppressed by demetallising the detector's contacts, which suggested that current instability was related to the metal diamond interface rather than the detecting medium (Pomorski et al., 2006). A diamond photodetector launched on the PROBA2 satellite exhibited a reduction in leakage current as a function of solar illumination time (5 years), possibly due to the desorption of water contaminants at the surface of the contacts (BenMoussa et al., 2015).

The leakage current stability of the packaged detector and the detector's packaging (empty package leakage current) were investigated as a function of temperature using the procedure described above. Leakage current was measured for two hours, at one-minute intervals, at 100 V applied potential difference across the packaged detector, in both polarities. The packaged detector's leakage current stability measurements are presented in **Figure 6.3**.

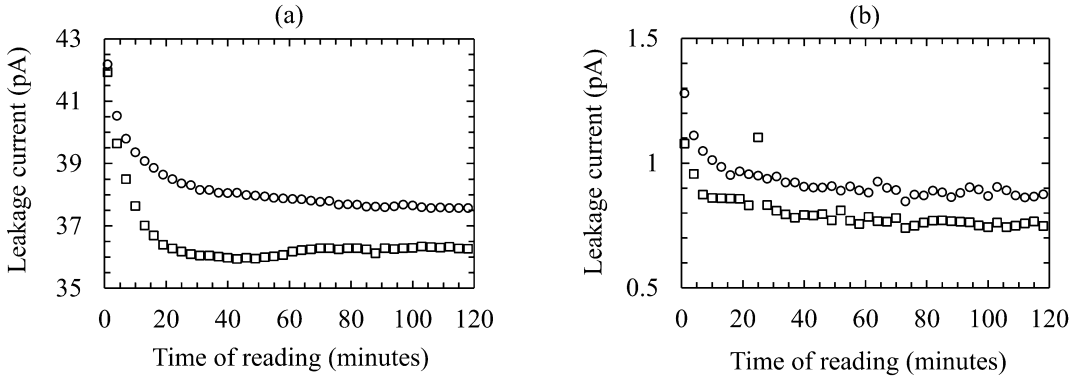

Figure 6.3. The stability of the packaged detector's leakage current as a function of time at an applied potential difference of 100 V in both polarities (+100 V open squares; -100 V open circles) at (a) 100 °C and (b) 60 °C. Error bars have been omitted for clarity. The uncertainties associated with the measurements of 42 pA and 0.87 pA were 0.2 pA and 0.02 pA, respectively.

At 100 °C, the packaged detector's initial leakage currents were 41.9 pA ± 0.2 pA and 42.2 pA ± 0.2 pA which reduced to 36.3 pA ± 0.2 pA and 37.6 pA ± 0.2 pA at +100 V and -100 V applied potential difference, respectively. The average leakage current of the packaged detector in the second hour of measurement, at 100 V in both polarities, along with the rms error, *R*, (**Equation 4.2)** where x_i is the value of the datum (in this case the leakage current) of the i^{th} measurement, $\bar{x}$ is the mean of the data (in this case the 60 leakage current measurements), and *n* is the number of data points considered (= 60), was calculated. At 100 °C, it was 36.3 pA ± 0.04 pA (rms error) and 37.7 pA ± 0.08 pA (rms error) at +100 V and -100 V, respectively. At 60 °C, the packaged detector's initial leakage currents were 1.08 pA ± 0.01 pA and 1.28 pA ± 0.02 pA which reduced after two hours to 0.75 pA ± 0.01 pA and 0.87 pA ± 0.01 pA at +100 V and -100 V, respectively. The average leakage current of the packaged detector in the second hour was 0.77 pA ± 0.03 pA (rms error) and 0.88 pA ± 0.01 pA (rms error) at +100 V and -100 V, respectively (see **Table 6.1**).

Reading	Leakage current at 100 °C (pA)		Leakage current at 60 °C (pA)	
	+100 V	-100 V	+100 V	-100 V
Initial	41.9 ± 0.2	42.2 ± 0.2	1.08 ± 0.01	1.28 ± 0.02
Final	36.3 ± 0.2	37.6 ± 0.2	0.75 ± 0.01	0.87 ± 0.01
Average (rms)	36.3 ± 0.04	37.7 ± 0.08	0.77 ± 0.03	0.88 ± 0.01

Table 6.1. The initial and final leakage current of the packaged detector with ±100 V potential difference applied across the detector at T = 100 °C and T = 60 °C, over 2 hours of measurement. The average leakage current in the second hour and the rms error is also given.

The leakage current of the detector with the leakage current attributed to the packaging subtracted, as a function of time, at an applied potential difference of 100 V in both polarities is presented in **Figure 6.4**. At 100 °C, the initial leakage current of the detector reduced to a steady state value, within the measurement uncertainties, after 20 minutes. At 100 °C, leakage currents were 4.81 pA ± 0.29 pA and 2.39 pA ± 0.30 pA which reduced to 1.08 pA ± 0.26 pA and 1.33 pA ± 0.26 pA at +100 V and -100 V, respectively. The average leakage current of the packaged detector in the second hour was 1.05 pA ± 0.04 pA (rms error) (+100 V) and 1.33 pA ± 0.08 pA (rms error) (-100 V). At T < 100 °C, the larger initial and subsequent reduction in leakage current as a function of time was absent. At 60 °C, the average leakage currents of the packaged detector were 0.04 pA ± 0.06 pA and 0.04 pA ± 0.03 pA at +100 V and -100 V applied potential difference, respectively. At T < 60 °C, the leakage current of the detector could not be distinguished from the noise.

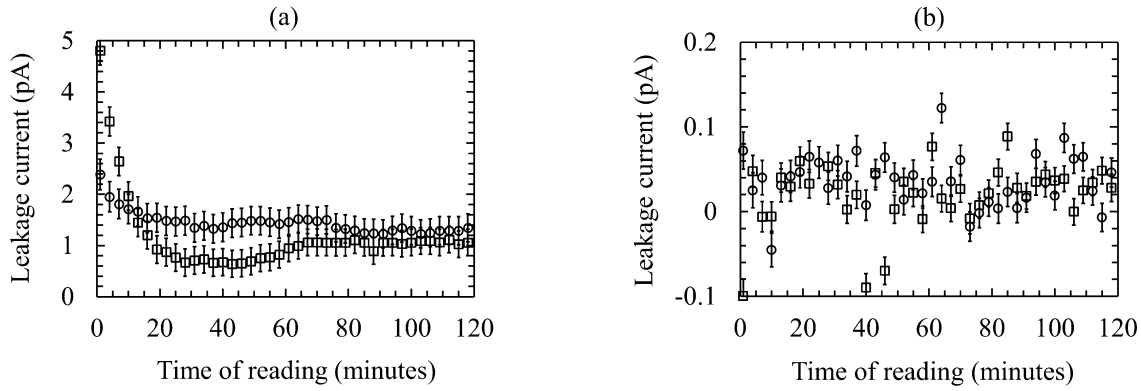

Figure 6.4. The stability of the diamond detector's leakage current (leakage current of the packaging separated) as a function of time at an applied potential difference of 100 V in both polarities (+100 V open squares; -100 V open circles) at (a) 100 °C and (b) 60 °C.

The high initial and subsequently stable thermally stimulated leakage current after 20 minutes, as seen in **Figure 6.3** and **Figure 6.4**, has been described in other X-ray and γ-ray studies with natural type IIa diamond, CVD PC diamond (Bergonzo et al., 2007) (Guerrero et al., 2006) and CVD SC diamond (Angelone et al., 2019) detectors; where deep and shallow trapping centres have been identified as the source of the initial (larger) leakage current. In diamond, deep level traps are released at high temperatures (≈ 230 °C – 280 °C) (Bruzzi et al., 2002) (Bergonzo et al., 2007) and are unlikely to play a significant role in the initially high leakage current seen here; however shallow traps are activated at lower temperatures (≈ 80 °C). At this temperature, the shallow trap population is gradually emptied, as indicated by the larger initial leakage current and subsequent lower stable leakage current measurement at 100 °C. This initially high leakage current was not observed when the empty package leakage current was subtracted from the packaged detector's leakage current, at 60 °C ≤ T < 100 °C. The detector's leakage current with the empty package leakage current subtracted could not be reliably measured at T < 60 °C.

6.2.2 Capacitance measurements

The capacitance of the packaged detector and the detector's packaging were measured, in turn, as a function of applied potential difference and temperature with a HP 4275A Multi Frequency LCR meter. A 'zero open' check was made with the packaged detector located in an electromagnetically screened test harness, before it was purged with dry N_2 and relocated to the same climatic cabinet as per the leakage current measurements. The climatic cabinet was continually purged with dry N_2 to keep the test environment dry. The LCR meter's test signal was set to 50 mV rms magnitude and 1 MHz frequency and the capacitance of the packaged detector was measured as a function of applied potential difference in both polarities up to 100 V. The potential difference was increased in 5 V increments and the capacitance was measured 5 s after the potential difference was reached. The climatic cabinet's temperature was raised to 100 °C as per the leakage current measurements. Capacitance as a function of voltage and temperature was measured from 100 °C to -20 °C in 20 °C decrements. The capacitance of the detector's packaging was measured after the packaged detector's capacitance was measured using the procedures described above.

The capacitance of the packaged detector as a function of temperature is presented in **Figure 6.5 (a)**. The capacitance was independent of the applied potential difference and temperature, within the investigated ranges; it was 910 fF ± 20 fF at 100 °C and 880 fF ± 20 fF at -20 °C. The capacitance of the packaging was also independent of the applied potential difference and temperature; it was 550 fF ± 15 fF at 100 °C and 525 fF ± 15 fF at -20 °C in parallel with the

detector. The capacitance of the detector is presented in **Figure 6.5 (b)**. The capacitance of the detector without the packaging included was invariant with applied potential difference and temperature; it was calculated by linear least squares fitting, to be 360 fF ± 5 fF within the investigated temperature range. A low detector capacitance will minimize the series white noise in a spectroscopic detector, particularly when short time constants are selected at the shaping amplifier (Barnett et al., 2012b).

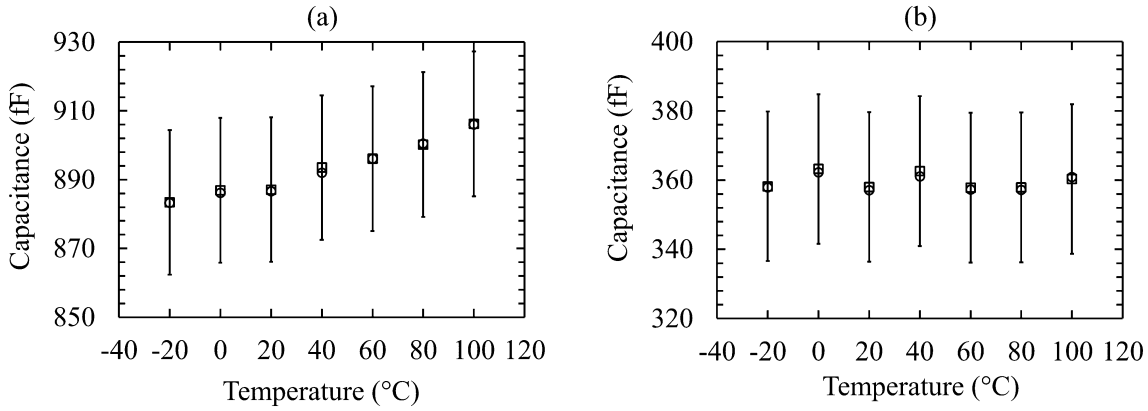

Figure 6.5. The detector capacitance at +100 V applied potential difference (open squares) and -100 V applied potential difference (open circles) as a function of temperature across the (a) packaged detector and (b) the detector with the capacitance of the packaging subtracted.

6.2.3 X-ray and γ-ray spectroscopy at -20 °C ≤ *T* ≤ 100 °C

The *QE* of the detector was calculated for photon energies up to 90 keV assuming that the active region of the detector was constrained within the thickness of the detector between the 1.96 mm^2 centrally located square contacts (see **Chapter 4)**. The attenuation of photons through the top electrical contact (200 nm thick Ag and 50 nm thick Ti) and a 4.5 μm layer that was electrically dead close to the contact at the top face of the detector (see **Chapter 5**) were included in the *QE* calculation. Deadlayers adjacent to electrical contacts have previously been observed in X-ray photodiodes (Lioliou et al., 2016). The calculated quantum detection efficiency of the detector is presented in **Figure 6.6**. The discontinuities shown in **Figure 6.6** between 3.35 keV and 3.81 keV, are caused by the abrupt change in linear attenuation coefficients from the detector's Ag contact at the Ag L shell absorption edge. The *QE* of the detector was considered when Gaussians were fitted to X-ray and γ-ray photopeaks in the spectra accumulated with the detector. The mass attenuation and absorption coefficients in Ag, Ti, and diamond were obtained from Berger et al. (2010).

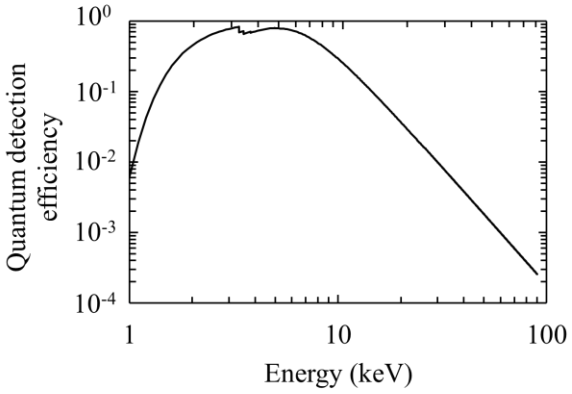

Figure 6.6. The calculated quantum detector efficiency of the diamond detector for photon illumination up to 90 keV. The discontinuity between 3.35 keV and 3.81 keV is the Ag L absorption edge.

As per previous experiments reported in this thesis, the packaged detector was connected to a custom-made low noise charge sensitive preamplifier, similar in design to ref. (Bertuccio et al., 1993). The input transistor was a Vishay 2N4416A Si Junction Field Effect Transistor (JFET) (Siliconix, 2001). Output pulses from the preamplifier were shaped and amplified by an Ortec 572A shaping amplifier before being output to an Ortec EASY MCA 8k multi-channel analyser (MCA) for digitization. The potential difference was applied across the detector using a Keithley 6487 voltage source. Spectra from an ^{55}Fe radioisotope X-ray source (84 MBq activity at the time of measurement) and a ^{109}Cd radioisotope X-ray and γ-ray source (33 MBq activity at the time of measurement) were accumulated, in turn. The sources were positioned 8 mm (^{55}Fe) and 10 mm (^{109}Cd) above the detector to accumulate spectra.

The test harness containing the packaged detector, preamplifier, and radioisotope radiation source was purged with dry N_2 before being transferred to a TAS Micro MT climatic cabinet for temperature control. The climatic cabinet was also continuously purged with dry N_2 throughout the measurements. The rest of the electronic readout chain (located outside of the climatic cabinet) was not subjected to temperature control. The temperature inside the climatic cabinet was raised to 100 °C, and then decreased in 20 °C steps to -20 °C; spectra were accumulated at each temperature step. The procedure was repeated using each radioisotope radiation source (^{55}Fe radioisotope X-ray and ^{109}Cd radioisotope X-ray and γ-ray sources). The spectra were collected at all of the shaping times, τ, provided by the shaping amplifier (τ = 0.5 μs, 1 μs, 2 μs, 3 μs, 6 μs, and 10 μs) and with 50 V and 100 V potential difference applied across the detector. To ensure that the diamond spectrometer was operating at thermal equilibrium, a 75 minute waiting time was applied after the climatic cabinet reached each temperature before spectra were collected.

The ^{55}Fe radioisotope X-ray source emitted a combination of characteristic Mn Kα (5.9 keV) and Mn Kβ (6.49 keV) X-rays (Schötzig, 2000) and the ^{109}Cd radioisotope X-ray and γ-ray source provided a combination of the five characteristic Ag Kα (21.99 keV and 22.16 keV) and Kβ (24.91 keV, 24.94 keV, and 25.45 keV) (hard) X-rays and an 88.03 keV γ-ray (Xiaolong et al., 2010); the Ag L shell emissions were entirely absorbed by the Be window of the source's capsule. Gaussians that took account of the relative emission ratios and the relative detection efficiency (*QE*) of the diamond detector at the corresponding X-ray photon energies, were fitted to the detected photopeaks to detangle the Mn and Ag Kα and Kβ emissions. Spectrum energy calibration was accomplished using the position of the spectrometer's so called zero energy noise peak and the fitted main photopeak (either the fitted Mn Kα (5.9 keV) or the Ag $K\alpha_1$ (22.16 keV) X-ray photopeak); a linear variation of collected charge with incident X-ray energy on the MCA's charge scale was assumed (see **Section 6.2.3.1**).

The live time for each spectrum accumulated from the ^{55}Fe radioisotope X-ray source was 120 s. A 0.14 mm thick Al attenuator was placed between the ^{55}Fe radioisotope X-ray source and the detector to limit the incident photon flux. The Al attenuated 99 % of the Mn Kα (5.9 keV) photons emitted from the source. A representative Mn Kα (5.9 keV) X-ray count is presented in **Figure 6.7 (a)**. The zero energy noise peak counts have been limited by setting the MCA low energy cut off to ≈ 3.8 keV after the position of the zero energy noise peak was recorded. The energy resolution of the spectrometer (as quantified by the full width at half maximum, (*FWHM)* of the fitted Mn Kα (5.9 keV) photopeak) at the best available shaping time, as a function of temperature for each potential difference applied across the detector is shown in **Figure 6.7**. At $T \geq 80$ °C, the combined ^{55}Fe Mn Kα and Kβ X-ray photopeak was insufficiently separated from the zero energy noise peak and its threshold for accurate Gaussians to be fitted. With 50 V potential difference applied across the detector, the *FWHM* at 5.9 keV improved from 2.93 keV ± 0.08 keV (at 3 μs shaping time) at 60 °C to 2.33 keV ± 0.10 keV (at 2 μs shaping time) at -20 °C. When 100 V potential difference was applied across the detector the *FWHM* at 5.9 keV improved from 2.93 keV ± 0.11 keV (at 3 μs shaping time) at 60 °C to 2.46 keV ± 0.11 keV (at 2 μs shaping time) at -20 °C. The *FWHM* uncertainties quoted are estimated from the uncertainties in fitting the Gaussians to the respective photopeaks. The total number of counts in the Gaussian representing the Mn Kα photopeaks were similar between applied potential differences, shaping times, and temperatures. As an example, with 50 V potential difference applied across the detector, the average count rate for Mn Kα (5.9 keV) X-rays varied between 555 s^{-1} ± 6 s^{-1} (rms error) at 60 °C and 567 s^{-1} ± 6 s^{-1} (rms error) at -20 °C. Here, to calculate *R* (**Equation 4.2**), the

datum was the count rate for Mn Kα (5.9 keV) X-rays and the mean count rate was calculated over the 6 available shaping times.

The live time for the ^{109}Cd X-ray and γ-ray spectra was 90 s; the thickness of the Al attenuator was increased to 1.0 mm. The 1.0 mm of Al attenuated 50 % of the Ag $K\alpha_1$ (22.16 keV) photon flux and 5 % of the ^{109}Cd (88.03 keV) γ-ray flux. A representative accumulated Ag Kα and Kβ spectrum is presented in **Figure 6.7 (b)**. The zero energy noise peak was limited by setting the MCA low energy cut off to ≈ 5.0 keV once its position had been ascertained. A fluorescence peak at ≈ 8.0 keV (Cu Kα = 8.04 keV) from the TO-39 package (Thompson et al., 2009) is also visible. The fitted *FWHM* at 22.16 keV (Ag $K\alpha_1$), at the best available shaping time for each potential difference applied across the detector, as a function of temperature is shown in **Figure 6.9**. With 50 V potential difference applied across the detector, the *FWHM* at 22.16 keV improved from 4.57 keV ± 0.26 keV (1 μs) at 100 °C to 2.70 keV ± 0.18 keV (2 μs) at -20 °C. When 100 V potential difference was applied across the detector, the *FWHM* at 22.16 keV improved from 4.67 keV ± 0.23 keV (1 μs) at 100 °C to 2.85 keV ± 0.19 keV (2 μs) at -20 °C. The total number of counts in the Ag $K\alpha_1$ photopeak were similar between the applied potential differences and shaping times, at $T \leq 60$ °C; at $T > 60$ °C the count rate at 6 μs and 10 μs was significantly larger than the other shaping times available. As an example, with 50 V potential difference applied across the detector the average Ag $K\alpha_1$ (22.16 keV) count rate was 1630 s^{-1} ± 11 s^{-1} (rms error) at 60 °C, whereas at 100 °C the count rate was 1696 counts s^{-1} at 0.5 μs and 2166 counts s^{-1} at 10 μs.

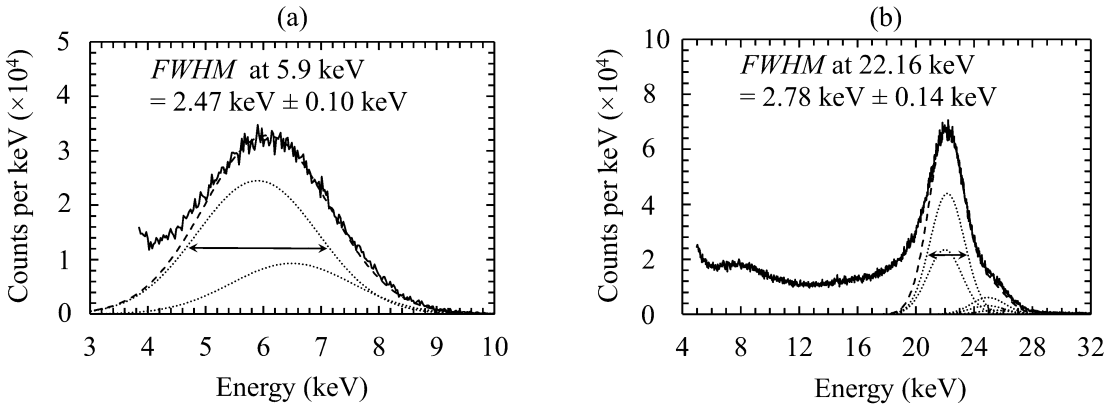

Figure 6.7. (a) ^{55}Fe and (b) ^{109}Cd X-ray spectra collected with the diamond-based spectrometer (solid line) at 20 °C, with +50 V potential difference applied across the detector, and with a shaping time of 2 μs. The dashed lines are fitted Gaussians, dotted lines are the respective Mn and Ag Kα and Kβ emissions. Soft X-rays emitted from the ^{109}Cd (Ag Lα = 3.0 keV, Ag Lβ ≈ 3.2 keV) were entirely absorbed by the Be window of the source's capsule and not detected.

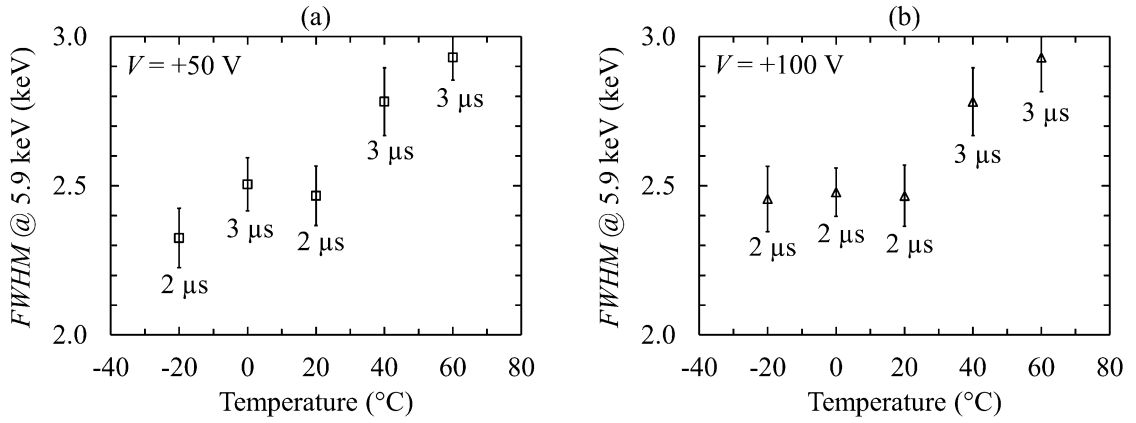

Figure 6.8. The *FWHM* of the fitted Mn Kα (5.9 keV) photopeak, at the best available shaping time, as a function of temperature with (a) 50 V and (b) 100 V potential difference applied across the detector.

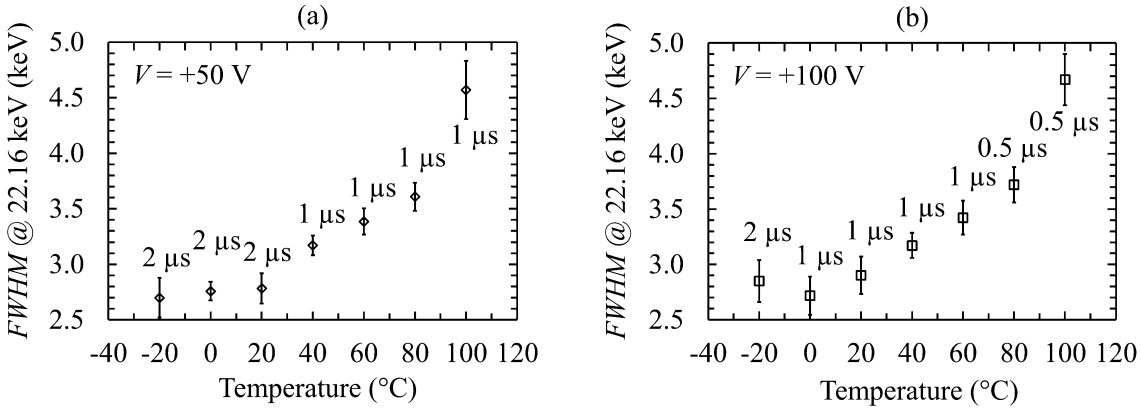

Figure 6.9. *FWHM* of the fitted Ag Kα$_1$ (22.16 keV) photopeak, at the best available shaping time, as a function of temperature with (a) 50 V and (b) 100 V potential difference applied across the detector.

The *FWHM* at 5.9 keV and 22.16 keV did not improve when the applied potential difference across the detector was increased in magnitude. The electric field strength, $E_{detector}$, across the detector was 1 kV cm^{-1} and 2 kV cm^{-1} at 50 V and 100 V applied potential difference, respectively. The drift velocity, v_d, of electron-hole (e-h) pairs produced by photoelectric absorption of X-rays and γ-rays in the detector is constrained by the electric field and inelastic scattering of the charge carriers in the detector. The drift velocity,

$$v_d = \mu_{e,h} E_{detector}, \tag{6.1}$$

is proportional to the carrier mobilities, $\mu_{e,h}$, in the electric field and to the electric field, $E_{detector}$. Work with a CVD SC diamond detector (Pernegger et al., 2005), has shown that at higher electric field strengths (> 1 kV cm^{-1}), the carrier drift velocity deviated from the linear relation of **Equation 6.1**, and reached saturation drift velocity, v_{ds}, at ≈ 8 kV cm^{-1}. An empirical relation that covers both cases is (Pernegger et al., 2005) (Sze and Ng, 2007),

$$v_d = \frac{\mu_0 E_{detector}}{1 + \mu_0 E_{detector}/v_{ds}}, \tag{6.2}$$

where μ_0 is the low field drift mobility. In **Equation 6.2** the only variables are $E_{detector}$ and v_d. When $E_{detector}$ is increased, v_d is reduced. Substituting **Equation 6.1** into **Equation 6.2** (Angelone et al., 2019) gives,

$$\mu_{e,h} = \frac{\mu_0 v_{ds}}{v_{ds} + \mu_0 E_{detector}}, \tag{6.3}$$

which suggested that as $E_{detector}$ is increased, the effective mobility of charge carriers (defined as carrier mobility compensated for space charge in the detector) is reduced. Previously the effective carrier mobility has been shown to reduce with electric field > 2 kV cm^{-1} in a CVD SC diamond detector (Pernegger et al., 2005). Carrier drift velocity saturation and reduced charge carrier mobility associated with large electric field strength in diamond detectors is dominated by optical phonon scattering in the diamond lattice, which in turn depends upon carrier trapping times, charge cloud density, and optical phonon energy (temperature) (Isberg et al., 2002). Charge carrier drift velocity can also be compromised by carrier-carrier scattering in the initial carrier drift in the electric field, more so when a large electric field is applied across the detector (Pernegger et al., 2005). Unlike p-n junction photodiode detectors, the diamond detector is operated in the equivalent of a forward 'bias' mode, although in reality the diamond detector is not biased in the sense that a p-n junction photodiode is biased; as such it is desirable to keep the electric field across the detector as low as possible consistent with stable performance, with high carrier mobility, and where the relationship between drift velocity and electric field is linear. Recently, a CVD SC diamond radiation detector, illuminated by γ-rays from a ^{60}Co radioisotope source and operating in a photocurrent mode, exhibited photocurrent saturation for $E_{detector}$ > 2 kV cm^{-1} at laboratory temperature (Angelone et al., 2019). With the diamond detector reported here, the best spectroscopic resolution of X-rays and γ-rays was achieved when +50 V potential difference (1 kV cm^{-1}) was applied across the detector in the linear charge transport regime where drift velocity and carrier mobility were a maximum.

At each temperature, an additional ^{109}Cd X-ray and γ-ray spectrum was acquired at a single shaping time, with 50 V potential difference applied across the detector, and with a live time limit of four hours. Four hours of live time was sufficient for a statistically meaningful number of ^{109}Cd 88.03 keV γ-rays to be accumulated. The shaping time which provided the best *FWHM* at 22.16 keV in the earlier ^{109}Cd spectra at each temperature was selected for acquisition of the long (four hour) spectra. A representative spectrum collected at 20 °C is presented in **Figure 6.10 (a)** and the *FWHM* of the ^{109}Cd 88.03 keV γ-ray photopeak as a function of temperature are presented in **Figure 6.10 (b)**. In **Figure 6.10 (a)** additional photopeaks (not emitted from the ^{109}Cd radioisotope X-ray and γ-ray source) have been identified at ≈ 8 keV (Cu Kα = 8.04 keV) and ≈ 59 keV (W Kα$_1$ = 59.3 keV) hypothesised to be X-ray fluorescence from the packaging of the detector and the shielding that surrounded the ^{109}Cd radioisotope source, respectively (Thompson et al., 2009). The step at 44 keV was associated with Ag Kα pulse pile-up. The *FWHM* of the ^{109}Cd 88.03 keV γ-ray emission improved from 4.13 keV ± 0.23 keV (at 1 μs) at 100 °C to

2.67 keV ± 0.27 keV (2 μs) at -20 °C. The ^{109}Cd 88.03 keV γ-ray count rate was ≈ 2 counts s^{-1} at all of the temperatures investigated.

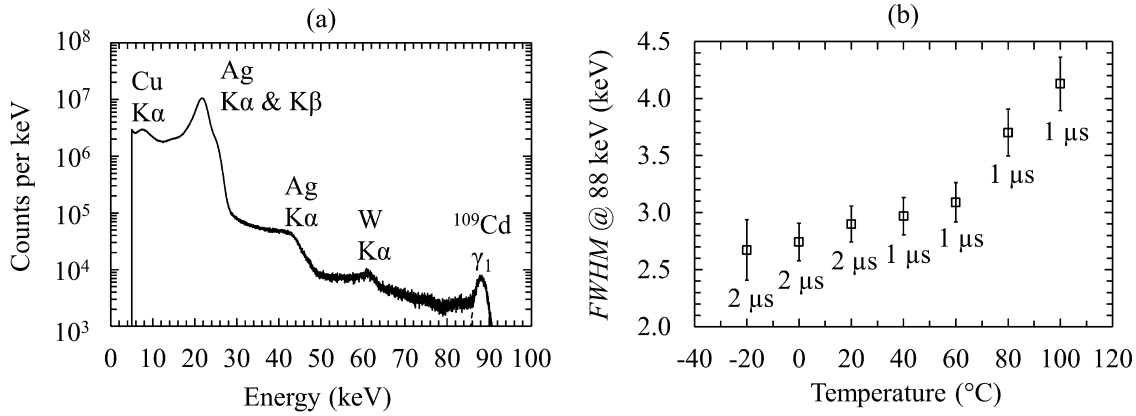

Figure 6.10. (a) A representative ^{109}Cd spectrum acquired at 20 °C with a live time limit of four hours. (b) The *FWHM* of the ^{109}Cd γ_1 (88.03 keV) γ-ray as a function of temperature at the selected shaping times (1 μs at $T \geq 40$ °C; 2 μs at $T < 40$ °C).

6.2.3.1 Linearity of energy response

The MCA channel numbers of the centroids of the Gaussians representing the Mn Kα (5.9 keV) X-ray, Ag Kα_1 (22.16 keV) X-ray, and the ^{109}Cd γ_1 (88.03 keV) γ-ray emissions, along with their corresponding energies, were used to calibrate the spectrometer's energy scale. A line of best fit was calculated, by linear least squares fitting, to investigate the detected charge response as a function of incident X-ray and γ-ray energy on the charge scale of the MCA, between -20 °C ≤ T ≤ 60 °C. The shaping times used were 2 μs at -20 °C ≤ T < 40 °C and 1 μs at 40 °C ≤ T ≤ 60 °C. Separate energy calibrations were required for the two different shaping times and temperatures. A plot of the energy calibrations of the spectrometer at 60 °C and -20 °C is presented in **Figure 6.11 (a)**. The detector exhibited an apparent linear energy response between photon energy, E, and MCA channel number, Y (in analogue-to-digital units (ADU)), at each temperature which was represented by **Equation. 6.4a** and **Equation 6.4b** at 60 °C and -20 °C, respectively,

$$E = (41.2 \pm 0.1)Y - 4.1 \pm 2.8, \quad (6.4a)$$

$$E = (23.3 \pm < 0.05)Y + 52.7 \pm 0.9, \quad (6.4b)$$

The number of MCA ADU encompassing 1 keV of energy changed as a function of temperature. Between 0 °C ≤ T ≤ 60 °C it was 41.2 ADU keV^{-1} ± 0.1 ADU keV^{-1} at 60 °C,

41.8 ADU keV^{-1} ± 0.1 ADU keV^{-1} at 40 °C, and 42.7 ADU keV^{-1} ± 0.1 ADU keV^{-1} at 20 °C. At 0 °C and -20 °C it reduced to 39.1 ADU keV^{-1} ± 0.1 ADU keV^{-1} and 23.3 ADU keV^{-1} ± < 0.05 ADU keV^{-1}, respectively. This is presented in **Figure 6.11 (b)**. The standard deviation, *S*, of the calibrated channel numbers, given by

$$S = \sqrt{\frac{\Sigma\left(y_i - \left(\left(\frac{n\,\Sigma(x_i y_i) - \Sigma x_i \Sigma y_i}{n\,\Sigma {x_i}^2 - (\Sigma x_i)^2}\right)x_i + \frac{\left(\Sigma {x_i}^2 \Sigma y_i - \Sigma x_i \Sigma(x_i y_i)\right)}{n\,\Sigma {x_i}^2 - (\Sigma x_i)^2}\right)\right)^2}{n-2}}, \qquad (6.5)$$

where x_i is the value of the i^{th} energy, y_i is the corresponding MCA channel number in ADU, and n is the number of data points considered (3 in this case: 5.9 keV; 22.16 keV; and 88.03 keV) was 6 ADU and 1 ADU at 60 °C and -20 °C respectively. The estimated uncertainty in the centroid position, Γ, of the 5.9 keV, 22.16 keV, and 88.03 keV emissions used to compute the uncertainty of each photopeak's *FWHM* from Gaussian fittings was 1 ADU ≤ Γ ≤ 3 ADU. Therefore, it was concluded that the spectrometer's charge scale may not have been linear across the full energy range, particularly when the spectrometer was operated at higher temperatures. Great care has been taken to develop and characterise the custom-made preamplifier to ensure that its own response and that of the onwards electronics chain is linear; as such if there was any non-linearity in the charge response it is hypothesised to have arisen from the detector itself.

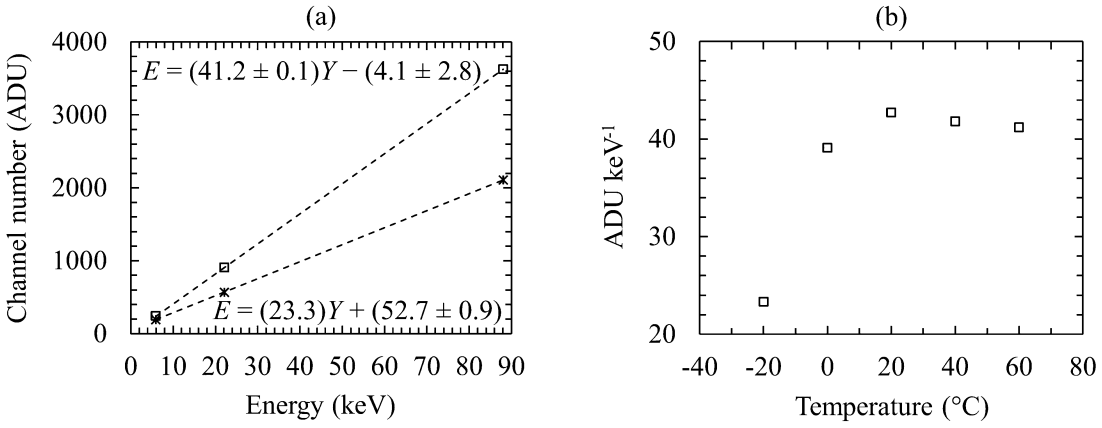

Figure 6.11. (a) The energy response calculated using three X-ray and γ-ray emissions (5.9 keV, 22.16 keV and 88.03 keV) at 60 °C (open squares) and -20 °C (stars). (b) The number of MCA ADU channels encompassing 1 keV of energy for the spectrometer as a function of temperature from -20 °C ≤ T ≤ 60 °C. Error bars are omitted for clarity. Lines are a guide for the eye only.

6.3 Noise analysis

The noise contributions associated with a non-avalanche semiconductor photon counting X-ray and γ-ray detector were previously reviewed in **Chapter 2** and **Section 4.4**. Shaping time variant (series and parallel white noise) and invariant (Fano, incomplete charge collection, 1/*f* series, and dielectric) noise contributions were extracted from the *FWHM* of the Mn Kα (5.9 keV) and the Ag $K\alpha_1$ (22.16 keV) X-ray emissions, as functions of shaping time, by multidimensional least squares fitting. Results of the multidimensional least squares fittings of the Mn Kα and the Ag $K\alpha_1$ X-ray emissions, at different temperatures, with +50 V potential difference applied across the detector are presented in **Figure 6.12** and **Figure 6.13**, respectively. The difference between the multidimensional least squares fitted and the experimentally resolved energies were < 3.3 e^- rms (98 eV *FWHM* at 5.9 keV) and < 6.3 e^- rms (187 eV *FWHM* at 22.16 keV). Fano and 1/*f* series noise were computed and subtracted in quadrature from the combined shaping time invariant noise contributions (Barnett et al., 2012b). The remaining shaping time invariant noise contributions, after subtraction in quadrature, were therefore assumed to be the quadratic sum of dielectric and incomplete charge collection noise.

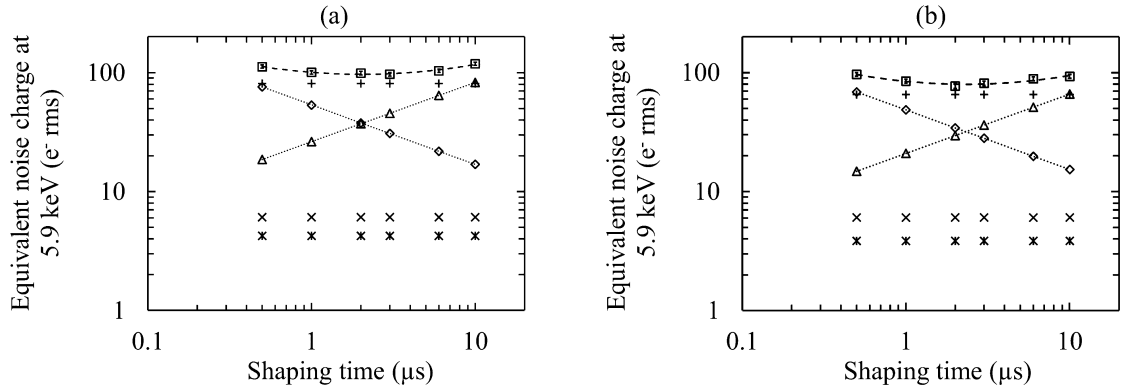

Figure 6.12. Equivalent noise charge at 5.9 keV (Mn Kα) (open squares) as a function of shaping amplifier time constant with +50 V potential difference applied across the detector at (a) 60 °C and (b) -20 °C. The quadratic sum of dielectric and incomplete charge collection noise (crosses), parallel white noise (open triangles), series white noise (open diamonds), Fano noise (× marks), and 1/*f* series noise (stars), are also shown. The dashed lines indicate the multidimensional least squares fittings of the experimental *FWHM*. The dotted lines that link series and parallel white noise are a guide for the eye only.

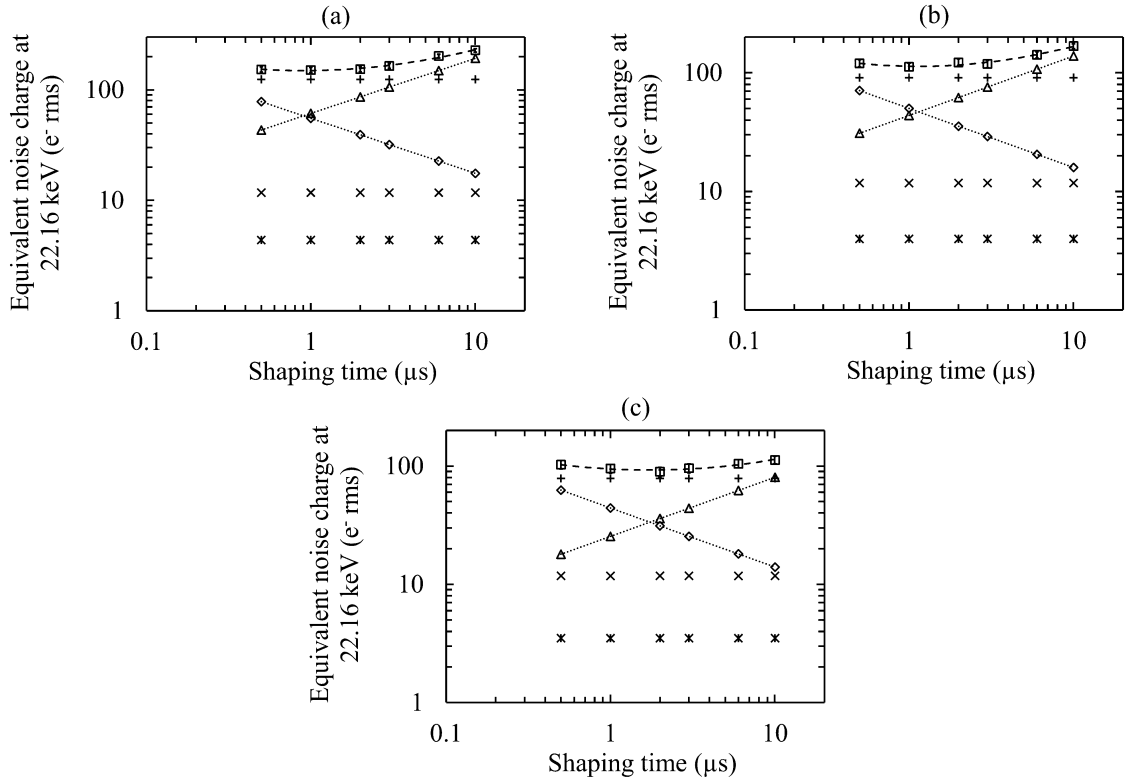

Figure 6.13. Equivalent noise charge at 22.16 keV (Ag $K\alpha_1$) (open squares) as a function of shaping amplifier time constant with +50 V potential difference applied across the detector at (a) 100 °C (b) 60 °C and (c) -20 °C. Quadratic sum of dielectric and incomplete charge collection noise (crosses), parallel white noise (open triangles), series white noise (open diamonds), Fano noise (× marks), and 1/*f* series noise (stars). The dashed lines indicate the multidimensional least squares fittings of the experimental *FWHM*. The dotted lines that link series and parallel white noise are a guide for the eye only.

The Fano noise was calculated assuming a Fano factor of 0.08 (Alig et al., 1980) and an electron-hole pair creation energy of 12.82 eV (Keister et al., 2018). On this basis, the Fano noise was computed to be 6 e^- rms (183 eV *FWHM*) at 5.9 keV (Mn Kα) and 12 e^- rms (355 eV *FWHM*) at 22.16 keV (Ag $K\alpha_1$). Reliable measurements of these parameters as functions of temperature in diamond do not yet exist, as such it has had to be assumed that they are temperature invariant; this is likely to be proven incorrect once reliable measurements are available.

The 1/*f* series noise calculated for each operating temperature and at both X-ray energies (5.9 keV and 22.16 keV) with +50 V potential difference applied across the detector is presented in **Table 6.1**. The 1/*f* series noise was calculated from the noise component inversely proportional to shaping times extracted by linear least square fittings of *FWHM* as a function of shaping times.

The noise component inversely proportional to shaping times (equated to series white noise) was entered into **Equation 2.12** to calculate the total capacitance at the input of the preamplifier, C_T. With C_T computed, **Equation 2.15** was used to calculate the $1/f$ series noise.

Temperature (°C)	$1/f$ series noise at 5.9 keV (e^- rms)	$1/f$ series noise at 22.16 keV (e^- rms)
100	-	4.4 ± 0.9
80	-	4.1 ± 0.9
60	4.2 ± 0.3	4.0 ± 0.8
40	4.0 ± 0.2	3.8 ± 0.4
20	3.1 ± 0.4	3.7 ± 0.4
0	3.7 ± 0.1	2.4 ± 0.6
-20	3.8 ± 0.4	3.5 ± 0.4

Table 6.1. Calculated $1/f$ series noise at the respective spectrometer operating temperature when 5.9 keV and 22.16 keV X-rays were being accumulated with +50 V potential difference applied across the detector.

The noise component inversely proportional to shaping time (series white noise) calculated from the linear least square fittings of the Mn Kα (5.9 keV) and Ag $K\alpha_1$ (22.16 keV) X-ray emissions, accumulated with +50 V potential difference applied across the detector, is presented in **Figure 6.14**. The series white noise is presented as a function of shaping time for temperatures ($0\ °C \leq T \leq 60\ °C$). The series white noise at -20 °C has been omitted from **Figure 6.14** for clarity.

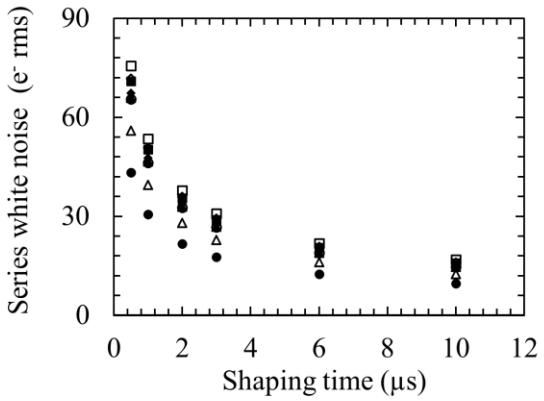

Figure 6.14. The (series white) noise component inversely proportional to shaping time, determined by linear least square fitting of *FWHM* as a function of shaping times for Mn Kα (5.9 keV) X-ray spectra at 60 ° C (open squares), 40 °C (open diamonds), 20 °C (open triangles), 0 °C (open circles), and Ag $K\alpha_1$ (22.16 keV) X-ray spectra at 60 °C (filled squares), 40 °C (filled diamonds), 20 °C (filled triangles), and 0 °C (filled circles) as a function of amplifier shaping time. Error bars have been omitted for clarity.

The noise inversely proportional to shaping time remained independent of energy, within the uncertainties propagated from the linear least square fittings, for all the investigated temperatures, except at $T = 0$ °C. However, the uncertainty of the noise computed at 5.9 keV and 22.16 keV did not include any uncertainty propagated from the *FWHM* of the Mn Kα (5.9 keV) and the Ag $K\alpha_1$ (22.16 keV) emission peaks.

To estimate how *FWHM* uncertainty could affect the noise computation at $T = 0$ °C, linear least square fittings were calculated at the maximum and minimum bounds of *FWHM* uncertainty of the Mn Kα (5.9 keV) and the Ag $K\alpha_1$ (22.16 keV) emission peaks. The results are presented in **Figure 6.15.**

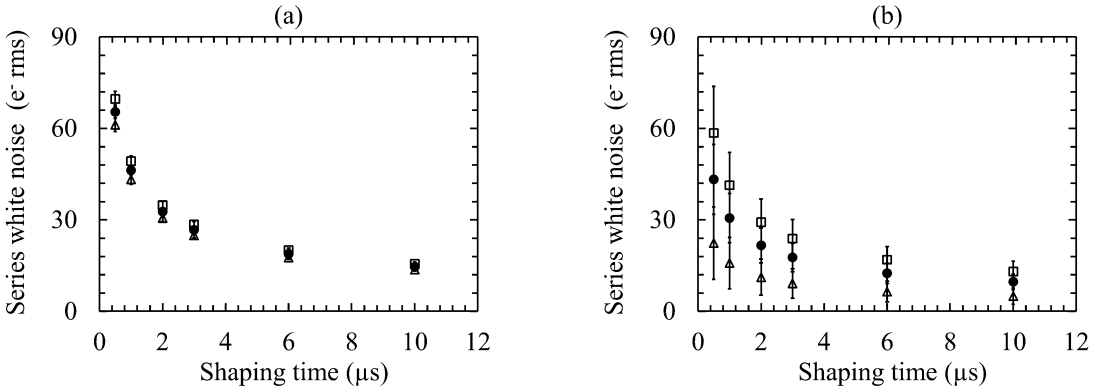

Figure 6.15. The noise inversely proportional to shaping time (equated with series white noise) at T = 0 °C calculated from linear least squares fitting of *FWHM* as a function of shaping time when the spectrometer accumulated (a) Mn Kα and (b) Ag $K\alpha_1$ spectra. The noise inversely proportional to shaping time calculated at the maximum bounds of *FWHM* uncertainty (open squares), minimum bounds of *FWHM* uncertainty (open triangles), and at the median *FWHM* (filled circles). The results were similar at other investigated temperatures where both Mn Kα and Ag $K\alpha_1$ spectra were accumulated.

The additional uncertainties propagated from the uncertainties in *FWHM* were small at 5.9 keV (Mn Kα) cf. 22.16 keV (Ag $K\alpha_1$) (**Figure 6.15 (a)** cf. **Figure 6.15 (b))**. For example, at τ = 0.5 μs, series white noise was 65.5 e⁻ rms $^{+\,6.6}_{-\,6.4}$ e⁻ rms (5.9 keV) and 43.3 e⁻ rms $^{+\,26.7}_{-\,38.5}$ e⁻ rms (22.16 keV). The *FWHM* of the Ag $K\alpha_1$ (22.16 keV) peaks were determined by detangling five combined Ag Kα and Kβ peaks. As such, the uncertainty from fitting Gaussians to the combined Ag Kα and Kβ peaks were larger cf. fitting Gaussians to the Mn Kα and Kβ peaks. At T = 0 °C this could account for the difference in noise inversely proportional to shaping time between the Mn Kα (5.9 keV) and Ag $K\alpha_1$ (22.16 keV) spectra.

The noise component proportional to shaping times (equated to parallel white noise), calculated from the linear least square fittings, also remained independent of the energy (5.9 keV and 22.16 keV), given the uncertainties propagated from the linear least square fittings, at all the investigated temperatures where Mn Kα (5.9 keV) and Ag $K\alpha_1$ (22.16 keV) spectra were accumulated (-20 °C ≤ T ≤ 60 °C), other than at T = 40 °C. To illustrate the differences in this noise at selected temperatures, the noise component proportional to shaping time at T = 60 °C and T = -20 °C, is presented in **Figure 6.16 (a)**; the noise component proportional to shaping time at T = 40 ° is presented in **Figure 6.16 (b)**.

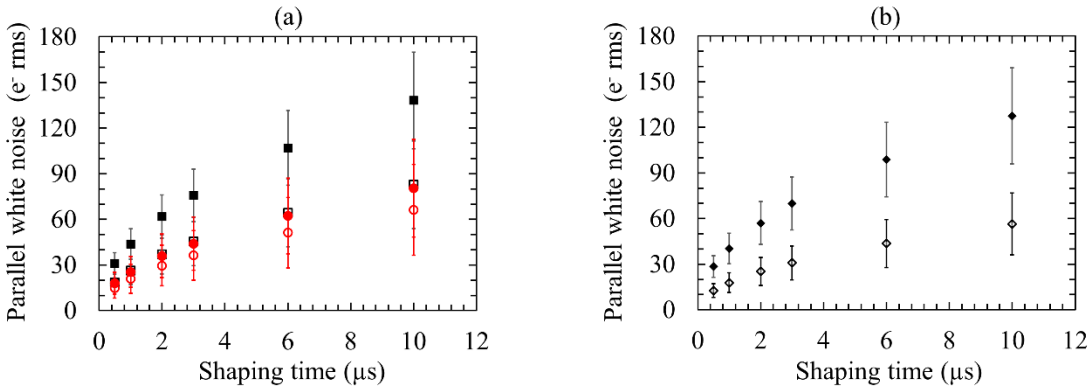

Figure 6.16. The noise component proportional to shaping times (attributed to parallel white noise) when the spectrometer was accumulating (a) Mn Kα (5.9 keV) spectra (open black squares) and Ag $K\alpha_1$ (22.16 keV) spectra (filled black squares) at T = 60 °C and Mn Kα (5.9 keV) spectra (open red circles) and Ag $K\alpha_1$ (22.16 keV) spectra (filled red circles) at T = -20 °C: and (b) Mn Kα (5.9 keV) spectra (open diamonds) and Ag $K\alpha_1$ (22.16 keV) spectra (filled diamonds) at T = 40 °C.

If the noise component proportional to shaping times, extracted from the linear least square fitting of *FWHM* as a function of shaping times can be wholly attributed to parallel white noise **Equation 2.8** can be rearranged and the current flowing in the gate of the input transistor of the preamplifier, I_{JFET}, and the leakage current of the detector, I_D, feeding into the channel of the JFET, can be computed. These calculations of current flowing at the input of the preamplifier (presented in **Table 6.2**) were substantially larger for the Ag $K\alpha_1$ (22.16 keV) spectra cf. the Mn Kα (5.9 keV) spectra. As an example, at T = 40 °C the current flowing at the input of the preamplifier was 27.4 pA ± 3.6 pA (5.9 keV) and 140.7 pA ± 8.7 pA (22.16 keV), respectively. As discussed in **Chapter 3** and **Chapter 4**, if it is assumed that all contributions to current at the input of the preamplifier are independent of each other the current is then equal to $2(I_D + I_{JFET})$ (Bertuccio & Casiraghi, 2003) (Lioliou & Barnett, 2015).

Temperature (°C)	Preamplifier input current when the spectrometer accumulated Mn Kα spectra (pA)	Preamplifier input current when the spectrometer accumulated Ag $K\alpha_1$ spectra (pA)
100	-	323.1 ± 27.4
80	-	273.0 ± 24.4
60	59.5 ± 7.2	165.3 ± 21.2
40	27.4 ± 3.6	140.7 ± 8.7
20	35.8 ± 7.3	92.1 ± 5.8
0	28.3 ± 2.4	47.2 ± 9.1
-20	37.9 ± 7.7	55.9 ± 8.9

Table 6.2. The calculated current flowing at the input of the preamplifier when Mn Kα and Ag $K\alpha_1$ spectra were accumulated by the spectrometer at respective temperatures.

The cause of the difference in the current flowing at the input of the preamplifier when spectra were accumulated at identical temperatures was unknown. The source of the current flowing at the input of the preamplifier is I_D and I_{JFET}, which were expected to be governed by the operating temperature of the spectrometer and the applied electric potential across the detector. However, given that there was a disparity in the count rate between the Mn Kα and Ag $K\alpha_1$ spectra at $T \leq 60$ °C and given that there was a disparity in the count rate of Ag $K\alpha_1$ spectra at different shaping times when the spectrometer was operated at $T > 60$ °C, this result may have rendered the comparison of noise computed from linear least squares fitting at the different energies unjustifiable, particularly so for the noise component proportional to the shaping times.

With +50 V potential difference applied across the detector, the directly measured leakage current of the packaged detector was 0.638 pA ± 0.009 pA at 60 °C and sufficiently small as to be below the noise floor of the femtoammeter at -20 °C (see **Figure 6.1**). When the detector was illuminated by the ^{55}Fe radioisotope X-ray source, the computed total steady state current flowing at the input of the JFET was 59.5 pA ± 7.2 pA at 60 °C and 37.9 pA ± 7.7 pA at -20 °C (see **Table 6.2**). This implied that the JFET's drain-to-gate leakage current was ≈ 30 pA at 60 °C and ≈ 19 pA at -20 °C. When the detector was illuminated by the ^{109}Cd radioisotope X-ray and γ-ray source, the computed total current flowing at the input of the JFET was 165.3 pA ± 21.2 pA (at 60 °C) and 55.9 pA ± 8.9 pA (at -20 °C), thus implying that the JFET's drain-to-gate leakage current was ≈ 83 pA at 60 °C and ≈ 28 pA at -20 °C (see **Table 6.2**).

The possibility that illumination with radiation sources set up a significant steady state current was considered, but is considered unlikely. Configured as it was in this study, the preamplifier

collected charge pulses from the detector onto a feedback capacitor via a low pass filter. The low pass filter fed the steady state currents from detector and the JFET to the JFET's gate. Radiation-induced charge pulses from the detector, after being collected on the feedback capacitor were discharged into the JFET's gate. For radiation induced charge collected onto the feedback capacitor to be a source of steady state parallel white noise, current induced by the radiation interactions in the detector would have to cross the low pass filter.

Considering the spectra obtained and computing the corresponding photocurrents associated with them (i.e. considering all of the charge represented by each spectrum) the corresponding photocurrents were 0.067 pA ± 0.006 pA (rms error) for illumination with the ^{55}Fe radioisotope X-ray source and 1.25 pA ± 0.06 pA (rms error) for illumination with the ^{109}Cd radioisotope X-ray and γ-ray source. Here, the rms error (**Equation 4.2**) was calculated considering the 30 ^{55}Fe radioisotope X-ray spectra and 42 ^{109}Cd radioisotope X-ray and γ-ray spectra obtained. On making the assumption that dead time may be corrected for in the computation of the photocurrent simply by its proportion in each case (which is acknowledged to be an oversimplification in the absolute, but is considered to be an adequate first order estimation for present purposes) then the photocurrent was still likely to be of the same order as that determined from the accumulated spectra. Thus, the photocurrents were insufficient to account for the difference in steady state current seen between the ^{55}Fe radioisotope X-ray source spectra and the ^{109}Cd radioisotope X-ray and γ-ray source spectra, even if they did contribute to it.

The apparent difference in the noise proportional to shaping times (commonly equated to parallel white noise) and hence the steady state current at the preamplifier's input JFET was more likely to be a consequence of the different counting rates (see **Section 6.2.3**) (Gilmore, 2008) (Knoll, 2010). At low count rates, the effects of baseline shift (the amount the baseline of a radiation induced pulse train is depressed below zero in order to pass a CR-RC network in the shaping amplifier) are negligible. However, because the count rate was high when the detector was illuminated with the ^{109}Cd radioisotope X-ray and γ-ray source, baseline shift broadened the Ag Kα and Ag Kβ spectra, particularly so at T > 60 °C and at longer shaping times.

The optimum spectrometer shaping time (where noise components inversely proportional and directly proportional to shaping times are at a minimum) also shifted to a shorter shaping time (Knoll, 2010) when the Ag $K\alpha_1$ (22.16 keV) spectra was accumulated. Baseline shift effects that broadened the Ag $K\alpha_1$ (22.16 keV) X-ray emissions could account for some of the additional computed leakage current at the input of the JFET when the spectrometer was accumulating Ag $K\alpha_1$ spectra cf. Mn Kα spectra. It should also be noted that if the optimum shaping time of an

X-ray or γ-ray spectrometer is moved to short shaping times because of baseline shift, then full charge collection can be compromised which can increase incomplete charge collection noise (if present) (Gilmore, 2008).

The noise component (extracted by linear least squares fitting) that is invariant with shaping time can be equated to the quadratic sum of Fano, 1/*f* series, dielectric, and incomplete charge collection noise. The quadratic sum of dielectric and incomplete charge collection noise, calculated from the linear least squares fittings of *FWHM* as a function of shaping times and after the (quadratic) subtraction of Fano and 1/*f* series noise at each of the investigated temperatures is presented in **Table 6.3**. The reduction of dielectric noise with decreases in temperature have been reported previously for $Al_{0.8}Ga_{0.2}As$ and GaAs photodiodes (Barnett et al., 2012b). To calculate the magnitude of the reduction of the dielectric noise with temperature would require the dielectric dissipation factor of all the materials contributing to the lossy dielectrics at the input of the preamplifier to be known. An estimate of the various dielectric noise contributions with this diamond similarly packaged and installed in a preamplifier of the same type can be found in **Chapter 4**.

Temperature (°C)	Dielectric and ICC noise at 5.9 keV (e^- rms)	Dielectric and ICC noise at 22.16 keV (e^- rms)
100	-	124.0 ± 7.8
80	-	94.5 ± 8.9
60	80.7 ± 3.4	91.1 ± 8.3
40	81.7 ± 1.8	84.8 ± 3.6
20	73.4 ± 3.9	72.9 ± 2.9
0	72.9 ± 1.3	83.8 ± 4.2
-20	65.5 ± 4.6	78.6 ± 4.3

Table 6.3. The calculated sum of dielectric and incomplete charge collection noise at the respective spectrometer operating temperatures when Mn Kα (5.9 keV) and Ag $K\alpha_1$ (22.16 keV) spectra were accumulated with +50 V potential difference applied across the detector.

6.3.1 The presence or absence of incomplete charge collection noise

Dielectric noise is photon energy invariant and incomplete charge collection noise is photon energy dependant (Owens & Peacock, 2004), so by comparing the quadratic sum of dielectric noise and incomplete charge collection noise at two or more energies, an evaluation of the difference in incomplete charge collection noise at two or more energies can be made.

Figure 6.17 shows the additional noise present at 22.16 keV cf. 5.9 keV as a function of temperature. Only those temperatures (-20 °C ≤ T ≤ 60 °C) where the X-ray count rate remained uniform across the available amplifier shaping times have been included in **Figure 6.17**. At T = 20 °C the difference in the quadratic sum of dielectric and incomplete charge collection noise between 22.16 kV and 5.9 keV spectra was less than the errors propagated from the linear least squares fitting. The difference (in quadrature) in the quadratic sum of dielectric and incomplete charge collection noise between 22.16 keV and 5.9 keV X-ray spectra (where present) has been referred to as incomplete charge collection noise. Additional noise was present at all the investigated temperatures and where the count rate remained stable across shaping times, other than at T = 20 °C where extra noise in the spectrometer was absent.

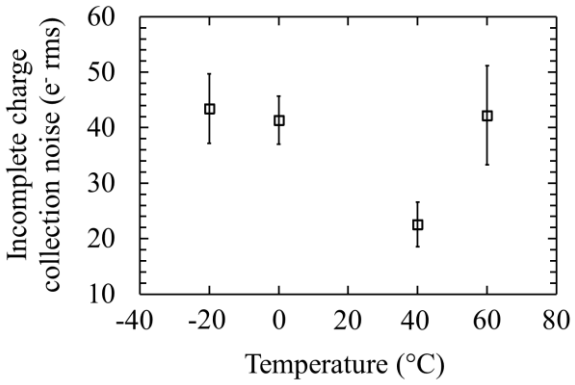

Figure 6.17. The additional noise present when the spectrometer was accumulating Ag $K\alpha_1$ (22.16 keV) cf. Mn Kα (5.9 keV) spectra as a function of temperature. At T = 20 °C additional noise at 22.16 keV cf. 5.9 keV was absent from the spectrometer.

A comparison of the total equivalent noise charge at different energies can be used to qualitatively assess whether incomplete charge collection noise is present in a spectrometer. To make such a comparison the Fano noise was subtracted (in quadrature) from the *FWHM* of the two X-ray emissions and the single γ-ray emission (5.9 keV, 22.16 keV and 88.03 keV) with identical amplifier shaping time constants selected (τ = 2 μs (-20 °C ≤ T ≤ 20 °C); τ = 1 μs (-20 °C < T ≤ 60 °C). This comparison of equivalent noise charge at 5.9 keV, 22.16 keV, and 88.03 keV, as a function of temperature is presented in **Figure 6.18.** At each temperature the equivalent noise charge at each energy was invariant within the uncertainty of fitting Gaussians to the X-ray and γ-ray emissions, except when the spectrometer was collecting an ^{55}Fe X-ray spectrum at T = 20 °C. At T = 20 °C the equivalent noise charge at 5.9 keV (Mn Kα) was 81.5 e^- rms ± 3.3 e^- rms which was less than the equivalent noise charge at 22.16 keV (Ag $K\alpha_1$)

and 88.03 keV (^{109}Cd γ_1), 91.5 e^- rms ± 4.6 e^- rms and 93.1 e^- rms ± 5.2 e^- rms, respectively. However, because the dielectric noise was found to be invariant between Mn Kα (5.9 keV) and Ag $K\alpha_1$ (22.16 keV) spectra (see **Figure 6.17**) the presence or absence of incomplete charge collection noise in the spectrometer could not be determined ultimately.

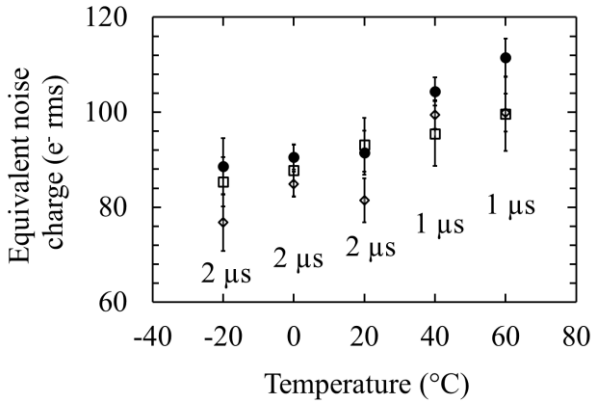

Figure 6.18. Equivalent noise charge in the spectrometer as a function of temperature at 5.9 keV (Mn Kα) (open diamonds), 22.16 keV (Ag $K\alpha_1$) (filled circles), and 88.03 keV (^{109}Cd γ_1) (open squares). The error bars were propagated from the uncertainties in fitting of Gaussians to the X-ray and γ-ray peaks.

6.4 Conclusions

When the detector was illuminated with soft X-rays (from ^{55}Fe), hard X-rays (from ^{109}Cd), and a γ-ray (from ^{109}Cd) at controlled temperatures (-20 °C ≤ T ≤ 100 °C), the best energy resolutions (*FWHM*) were achieved with 50 V (electric field strength 1 keV cm^{-1}) potential difference applied across the detector. The best energy resolution at 5.9 keV (^{55}Fe Mn Kα) was 2.93 keV ± 0.08 keV (at 3 µs shaping time) at 60 °C which improved to 2.33 keV ± 0.10 keV (at 2 µs shaping time) at -20 °C. At T > 60 °C, the combined ^{55}Fe Mn Kα and Kβ photopeak could not be separated from the preamplifier's zero energy noise peak. The best energy resolution at 22.16 keV (^{109}Cd Ag $K\alpha_1$) was 4.57 keV ± 0.26 keV (at 1 µs shaping time) at 100 °C which improved to 2.70 keV ± 0.18 keV (at 2 µs shaping time) at -20 °C. The best energy resolution at 88.03 keV (^{109}Cd γ_1) was 4.13 keV ± 0.23 keV (at 1 µs shaping time) at 100 °C which improved to 2.67 keV ± 0.27 keV (at 2 µs shaping time) at -20 °C.

Shaping time noise analysis conducted using the Mn Kα (5.9 keV) and Ag $K\alpha_1$ (22.16 keV) X-ray peaks was inconclusive with respect to determining whether incomplete charge collection noise degraded the energy resolution of the spectrometer. The shaping time noise analysis also found

more noise equated to parallel white noise present in the spectrometer when ^{109}Cd X-ray spectra were accumulated cf. ^{55}Fe X-ray spectra. The apparent larger parallel white noise component in the former case was in part attributed to an excessive photon count rate in the detector (≈ 1650 s^{-1} in the Gaussian fitted to represent the Ag Kα_1 peak cf. ≈ 560 s^{-1} in the Gaussian fitted to represent the Mn Kα peak) which could have caused baseline shift effects to be present when accumulating ^{109}Cd X-ray spectra. As such it was considered that the additional noise was not additional parallel white noise but stemmed from parasitic effects possibly including baseline shift. At $T > 60$ °C, the count rate within the Ag Kα_1 (22.16 keV) peak appeared to increase as a function of shaping amplifier time constant. The increased count rate was also attributed, in some part, to baseline shift broadening photopeaks at the longer shaping times. A consequence of the apparent larger component of parallel white noise was the spectrometer operating condition shifting to shorter shaping times when ^{109}Cd X-ray spectra were accumulated cf. ^{55}Fe X-ray spectra.

Investigation as to the presence or absence of incomplete charge collection noise in the diamond detector was inconclusive. The different apparent count rates between Mn Kα and Ag Kα_1 spectra and Ag Kα_1 spectra as a function of shaping time at $T > 60$ °C limited the effectiveness of shaping time noise analysis. Revisiting the work with a reduced ^{109}Cd X-ray photon flux incident upon the detector (e.g. achieved through the use of more effective attenuators, or a lower activity radiation source) may elucidate further the origin of the phenomena affecting the spectra accumulated and reported in this chapter.

Chapter 7. Modelling Gd-diamond and Gd-SiC neutron detectors

7.1 Introduction

A custom Monte Carlo (MC) computer model was prepared to simulate thermal neutron absorption and photon and electron emission from natural Gd. The MC code also modelled photon and electron detection in a thick (500 μm) single crystal diamond detector (i.e. the detector investigated in **Chapters 4, 5** and **6**) and a thin (5.15 μm) commercial off the shelf (COTS) 4H-SiC detector (i.e. the detector investigated in **Chapter 3**). An operating temperature of 20 °C was assumed for the simulations, but given that the detectors have already been proven experimentally to work at elevated temperatures operation in high temperature environments is anticipated to be achievable. Having already been investigated in laboratory experiments, the measured responses of the diamond and 4H-SiC detectors to illumination with β^- particles, soft X-rays, and γ-rays was availed as the basis for the detector modelling. The diamond and 4H-SiC detector's quantum detection efficiencies (*QE*) to hard X-rays and γ-rays were relatively low in comparison to their *QE* for electrons, thus making it possible to collect electron spectra which were not overwhelmed by contributions from the γ-rays and X-rays emitted from the Gd. MC simulations affirmed that a photon rejection scheme would not be required to discriminate the electron component of the accumulated spectrum from the photon component of the spectrum, if the detectors were operated as thermal neutron detectors with the Gd converter arrangement as proposed here. The MC code was utilised to determine the optimal thickness of Gd for the efficient detection of a thermal neutron flux. These detectors (radiation hard and spectroscopic) paired with natural Gd, could find utility as robust and compact thermal neutron detectors for nuclear security or space science applications.

Proof of concept portable and direction sensitive thermal neutron detectors that have used thin foils of Gd (25 μm thick and primarily detecting the backward emission of electrons), without energy discrimination, have previously been reported. For example, Si planar detectors of large area (4 cm^2) were used (Schulte & Kesselman, 1999). The Si detectors were also sensitive to the γ-ray emissions from Gd, as such, γ-ray subtraction was required to establish accurate electron counting. In that work, electron energies were not discriminated.

7.2 The capture (absorption) of thermal neutrons with natural Gd

There are seven isotopes present in natural Gd (Z = 64) metal; five of the isotopes are stable and two (^{152}Gd and ^{160}Gd) are quasi-stable (Pritychenko et al., 2006). The probability that a thermal neutron will be captured by the i^{th} Gd isotopes in a natural Gd foil is related to the thermal neutron

capture cross section, σ_i, of each Gd isotope and their relative abundances. The fractional interaction probability, C_i, of each Gd isotope can be expressed as,

$$C_i = \left({\sigma_i f_i} \Big/ {\sum_{i=1}^{i=7} \sigma_i f_i} \right) \tag{7.1}$$

(Harms & McCormack, 1974), where f_i is the respective isotropic abundance. The fractional interaction probabilities of each of the Gd isotopes found in natural Gd were computed, for later use, using **Equation 7.1**; they are presented in **Table 7.1**. Accounting for ^{155}Gd and ^{157}Gd by isotropic abundance, the ^{155}Gd and ^{157}Gd isotopes account for 99.991 % of all thermal neutrons captured, with 81.70 % and 18.30 % captured by ^{157}Gd and ^{155}Gd nuclei, respectively. The other five Gd isotopes account for 0.009 % of the remaining neutron capture reactions and do not significantly contribute to the macroscopic capture of thermal neutrons in natural Gd. For this work the cross section of each Gd isotope was obtained from the Nuclear National Data Centre (NNDC CapGam, N.D.).

Gd isotope (Nucleon number)	**Isotropic abundance f_i (%)**	**Cross section σ_i (b)**	**Fractional interaction C_i (%)**
152	0.2	755 ± 20	0.003
154	2.2	85 ± 12	0.004
155	14.8	60330 ± 500	18.293
156	20.5	1.8 ± 0.7	0.001
157	15.7	254000 ± 815	81.698
158	24.8	2.22 ± 0.1	0.001
160	21.8	1.4 ± 0.3	0.001

Table 7.1. Isotropic abundance of the natural Gd isotopes, respective isotopic cross section to thermal neutrons, and each isotope's fractional interaction expressed as a percentage (NNDC CapGam, N.D.).

When a thermal neutron is captured by a ^{155}Gd or a ^{157}Gd nucleus, an isomeric change to another stable isotope occurs. The nuclear reactions of both isotopes are described by **Equation 7.2** and **Equation 7.3** (Reich, 2012), (Nica, 2017), (Pritychenko et al., 2011),

$$^{155}_{64}\mathrm{Gd} + {}^{1}_{0}\mathrm{n} \rightarrow {}^{156}_{64}\mathrm{Gd}^{*} + \gamma\text{-ray} + \mathrm{e}^{-}; Q = 8536\ \mathrm{keV} \pm 0.07\ \mathrm{keV} \tag{7.2}$$

$$^{157}_{64}\mathrm{Gd} + {}^{1}_{0}\mathrm{n} \rightarrow {}^{158}_{64}\mathrm{Gd}^{*} + \gamma\text{-ray} + \mathrm{e}^{-}; Q = 7937\ \mathrm{keV} \pm 0.06\ \mathrm{keV} \tag{7.3}$$

Where the electrons are internal conversion fast electrons. The total energy, *Q*, shared between the reaction products (electrons and γ-rays) is the difference in mass energy between the initial and resultant Gd nuclei (Das, 2017).

7.2.1 γ-ray emissions from Gd

Upon capture of a thermal neutron, the Gd nucleus enters an excited state, the majority of the excitation energy is subsequently released by the prompt (stochastic) emission of γ-rays as the excited nucleus de-excites to the ground state. For the $^{156}Gd^{*}$ and $^{158}Gd^{*}$ nuclei respectively, there are 1009 and 994 known possible γ-ray energy transitions (Pritychenko et al., 2006) of which 324 ($^{156}Gd^{*}$) and 390 ($^{158}Gd^{*}$) are considered discrete from a continuum, for the purpose of prompt γ-ray activation analysis (Choi et al., 2007). In the case of $^{158}Gd^{*}$, a large part of the 7937 keV ± 0.06 keV of energy is released by a prompt γ-ray cascade of 3.288 photons, on average, for each thermal neutron captured by a ^{157}Gd nucleus (Ralston et al., 2012). For this work, the γ-ray emission energies and the probability of a γ-ray emission was computed using Nuclear Data Sheets supplied by Brookhaven National Laboratory (Reich, 2012) (Nica, 2017).

7.2.2 Internal conversion electrons

Bound atomic electrons (**Equation 7.2** and **Equation 7.3**) are ejected from their atomic shells in competition with the prompt emission of γ-rays from a $^{156}Gd^{*}$ or a $^{158}Gd^{*}$ atomic nucleus. The internal conversion of electrons is a stochastic process governed by the wave function of an atomic nucleus and the wave functions of orbital electrons; those wave functions have a finite probability of overlap (Dumazert et al., 2018). The internal converted electrons are emitted from the lowest energy level transitions of the excited Gd nuclei; as such, they possess the energy of the competing γ-ray minus their atomic shell binding energy. Consequently, internal converted electrons do not exhibit a continuous energy spectrum. Instead, an ejected electron possesses one of nine discrete energies for each of the $^{156}Gd^{*}$ and $^{158}Gd^{*}$ isotopes. The average binding energies of the three innermost electron shells of a Gd atom are presented in **Table 7.2** (Thompson et al., 2009) and the corresponding de-excitation pathways for those γ-rays that compete with ejected electron emissions are presented in **Figure 7.1**.

Electron shell	Average shell binding energy (keV)
K	50.2
L	7.8
M	1.5

Table 7.2. The electron binding energy of the K shell and the average electron binding energy of the L and M electron shells of atomic electrons in Gd atoms (Thompson et al., 2009).

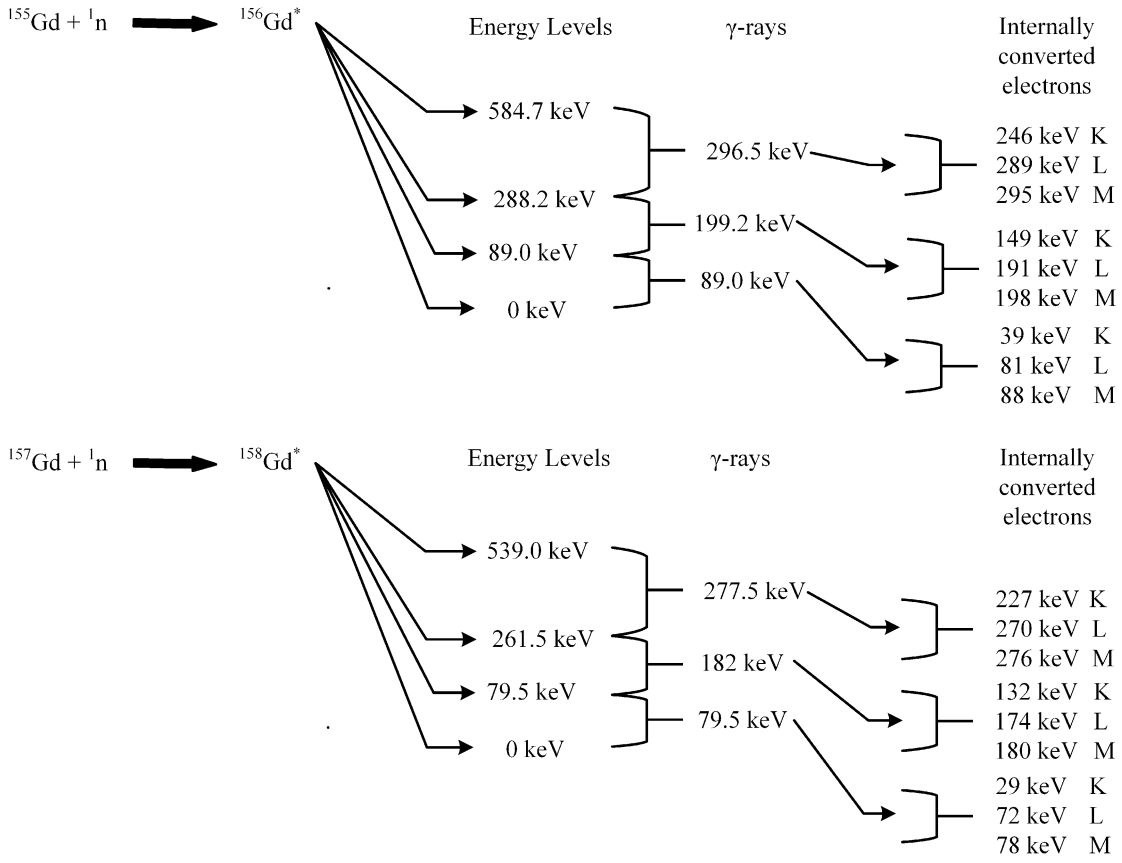

Figure 7.1. The low energy de-excitation pathways of $^{156}Gd^{*}$ and $^{158}Gd^{*}$ after thermal neutron capture by the respective nuclei. The emissions of a γ-ray or an internally converted electron is a competing stochastic process. Figure adapted from Kandlakunta (2014).

The electron conversion cf. γ-ray emission is calculated using the internal conversion coefficient, α, i.e. the ratio of the electron ejection rate to the γ-ray emission rate (Kibédi et al., 2007) (Kibédi et al., 2008). In the case of Gd, the γ-ray emissions that compete with internally converted electrons are the E2 electric quadrupole transitions; the energy levels of the E2 electric quadrupole transitions are also shown in **Figure 7.1** (Harms & McCormack, 1974) (Dumazert et al., 2018). The nuclear energy transition levels of $^{156}Gd^{*}$ and $^{158}Gd^{*}$ that relate to an emitted γ-ray of energy,

E_γ, emitted in competition with internal electron conversion, and the intensity of each γ-ray per neutron captured, I_γ, are presented in **Table 7.3**. The internal conversion coefficients of the ejected electrons were computed using the BrIcc v2.3S conversion coefficient database and calculator (Kibédi et al., 2008) and are included in **Table 7.3**. The total conversion coefficients, α_{tot}, and the conversion coefficients for the respective atomic shells (α_K, α_L, α_M, and α_{N+} (the total coefficient of the N shell and beyond)), are also presented for the $^{156}Gd^*$ and $^{158}Gd^*$ nuclei, respectively. The data tables used to compute the conversion coefficients were the Dirac-Fock computations (BrIccFO); these computations used the 'Frozen Orbitals' approximation, which took account of the effect of the 'hole' in an electron shell left behind by an ejected electron (Kibédi et al., 2008).

	E **(keV)**	***Eγ*** **(keV)**	***Iγ*** **(nc^{-1})**	α_{tot}	α_K	α_L	α_M	α_{N+}
	89	89	0.20900	3.87300	1.55800	1.78600	0.42180	0.10640
$^{156}Gd^*$	288.2	199.2	0.31600	0.22500	0.01565	0.05312	0.01224	0.00314
	584.7	296.5	0.02530	0.06248	0.04768	0.01151	0.00261	0.00007
	79.5	79.5	0.09748	5.93600	2.01800	3.02300	0.71480	0.18000
$^{158}Gd^*$	261.5	182	0.18330	0.30490	0.20580	0.07681	0.01777	0.00455
	539	277.5	0.01128	0.07678	0.05790	0.01468	0.00334	0.00009

Table 7.3. Nuclear excitation energy levels (E), γ-ray emission energies (E_γ), γ-ray intensity per neutron captured (I_γ), and the related internal conversion coefficients, α, for the $^{156}Gd^*$ and $^{158}Gd^*$ nuclei. E_γ and I_γ were obtained from the Nuclear Data Sheets of Nica (2017) and Reich (2012). Conversion coefficients were obtained from the BrIcc v2.3S conversion coefficient database and calculator (Kibédi et al., 2008).

The intensities (probabilities), I_β, of the conversion electrons are given by $I_\beta = I_\gamma \times \alpha$. The intensities (probabilities) of conversion electrons in a natural Gd converter, $I_{\beta\ Na\ Gd}$, are given by $I_{\beta\ Na\ Gd} = I_\beta \times C_i$. The energies, E_β, and intensities of electrons converted per thermal neutron captured in isotopically pure $^{156}Gd^*$ and $^{158}Gd^*$, along with the respective intensities in natural Gd, are presented in **Table 7.4**.

E_β $^{156}Gd^*$ (keV)	I_β (nc^{-1})	$I_{\beta\ Na\ Gd}$ (nc^{-1})	E_β $^{158}Gd^*$ (keV)	I_β (nc^{-1})	$I_{\beta\ Na\ Gd}$ (nc^{-1})
39	0.32562	0.05957	29	0.19671	0.16071
81	0.37327	0.06828	72	0.29468	0.24075
88	0.08816	0.01613	78	0.06968	0.05693
149	0.00495	0.00090	132	0.03772	0.03082
191	0.01679	0.00307	174	0.01408	0.01150
198	0.00387	0.00071	180	0.00326	0.00266
246	0.00121	0.00022	227	0.00065	0.00053
289	0.00029	0.00005	270	0.00017	0.00014
295	0.00007	0.00001	276	0.00004	0.00003
Total yield	0.81421	0.14894	Total yield	0.61699	0.50407

Table 7.4. The energy and intensity of conversion electrons from isotopically pure $^{156}Gd^*$ and $^{158}Gd^*$, and natural Gd.

7.2.3 X-ray fluorescence and Auger electrons

The competing processes of X-ray fluorescence (radiative transitions) or Auger electron emission (non-radiative transitions) will occur whenever an electron is ejected from a Gd atom's electron shell. As explained in **Section 2.2.1.1**, the energy of a characteristic fluorescence X-ray is equal to the difference in binding energy of an ejected electron and the electron that subsequently fills the vacancy left by the ejected electron. The energy and relative intensities of characteristic X-rays emitted from Gd are presented in **Table 7.5**.

Characteristic X-ray	Energy (keV)	Relative intensity
$K\alpha_1$	43	100
$K\alpha_2$	42.3	56
$K\beta_1$	48.7	20
$K\beta_2$	50	7
$K\beta_3$	48.6	10
$L\alpha_1$, $L\alpha_2$	6.1	111
$L\beta_1$	6.7	62
$L\beta_{2,15}$	7.1	21
$L\gamma_1$	7.8	11
$M\alpha_1$	1.2	100

Table 7.5. Characteristic X-rays emitted from a Gd atom as a consequence of electron internal conversion from thermal neutron capture reactions (Thompson et al., 2009). Only the significant characteristic X-rays are shown. An intensity of 100 is assigned to the strongest emission in each of the shells.

The competing Auger electron spectrum is dominated by low energy electrons (4.84 keV for L shell and 0.97 keV for the M shell electron conversions) (Abdushukurov, 2010) and are of short range in Gd (Cerullo et al., 2009). The K shell Auger emission energy is ≈ 35 keV; yields of 0.065 (Krause, 1979) (normalised to the K shell X-ray emission) and 0.079 per neutron captured (Abdushukurov, 2010) have been reported.

7.3 MC model of the thermal neutron capture reaction with Gd

The MC model of photon and electron emissions from natural Gd after thermal neutrons were captured was developed using the CASINO (monte Carlo SImulation of electroN trajectory in sOlids) software package (Drouin et al., 1997) (Hovington et al., 1997) and custom-developed code executed in MATLAB R2020a (MathWorks, 2020). Both software packages were run on a Microsoft Windows 10 computer with an Intel Core i7-8550U CPU and 16 GB of RAM. The model was implemented in two phases. In the first phase the energy and intensity of the reaction products (γ-rays, X-rays, and electrons (via conversion and non-radiative Auger processes)) emitted from a natural Gd converter were determined. In the second phase, the detector response to the reaction products was modelled.

The MC model used inferential statistics to draw conclusions with respect to the transport of thermal neutrons through natural Gd; and, where applicable, the conversion of those thermal neutrons by Gd isotopes. Inferential statistics were also used to model the onward transport of photons and electrons emitted from Gd nuclei and Gd atoms after a nuclear reaction had occurred. Central to the MC model was the random walk initiated by the pseudo random number generator built into MATLAB. The pseudo random numbers generated by MATLAB were compared with the particle emission probabilities (sourced from the evaluated nuclear data sheets ((Reich, 2012) and (Nica, 2017)) to determine the location, emission product, energy of emission product, transport history, attenuation, and absorption of every converted thermal neutron on a particle-by-particle basis.

A flowchart providing an overview of the first phase is presented in **Figure 7.2**; the process is described in more detail in the subsequent sections. The model assumed a thermal neutron energy of 25 meV a priori of the thermal neutron cross sections used in this work. At the start of the simulation, the user was prompted to specify the number of thermal neutrons to be emitted and the thickness of the Gd thermal neutron absorber to be used, up to a maximum thickness of 25 μm. Once the number of thermal neutrons was selected, the simulation, by default, assumed that all the thermal neutrons were emitted towards and normal to the face of the Gd converter. As

explained in **Section 2.2.4**, the macroscopic fraction of thermal neutrons captured by Gd nuclei, $F(z)/F_0$, emitted perpendicular to a natural Gd sheet is

$$F(z)/F_0 = \exp -(N\,\sigma_t\,z), \qquad (7.4)$$

where N is the atomic density of Gd (3.02×10^{22} atoms cm^{-3}) and z is the thickness of the Gd converter. The total macroscopic thermal neutron cross section, σ_t, (48800 b ± 200 b, computed from **Table 7.1**), was pre-set for determining the depth of thermal neutron capture in the Gd. The fraction of thermal neutrons absorbed by Gd up to a depth of 25 μm is presented in **Figure 7.3**. From **Figure 7.3**, 77 % of thermal neutrons incident upon a Gd thermal neutron absorber will have been captured by a Gd nuclei at a depth ≤ 10 μm. The selection of the optimum thickness of Gd is important: a thick Gd thermal neutron converter will allow more thermal neutrons to be captured and consequently more electrons will be emitted (increased thermal neutron capture efficiency); whereas a thin converter will offer the conversion electrons a better opportunity to escape the converter at the cost of fewer thermal neutrons being captured.

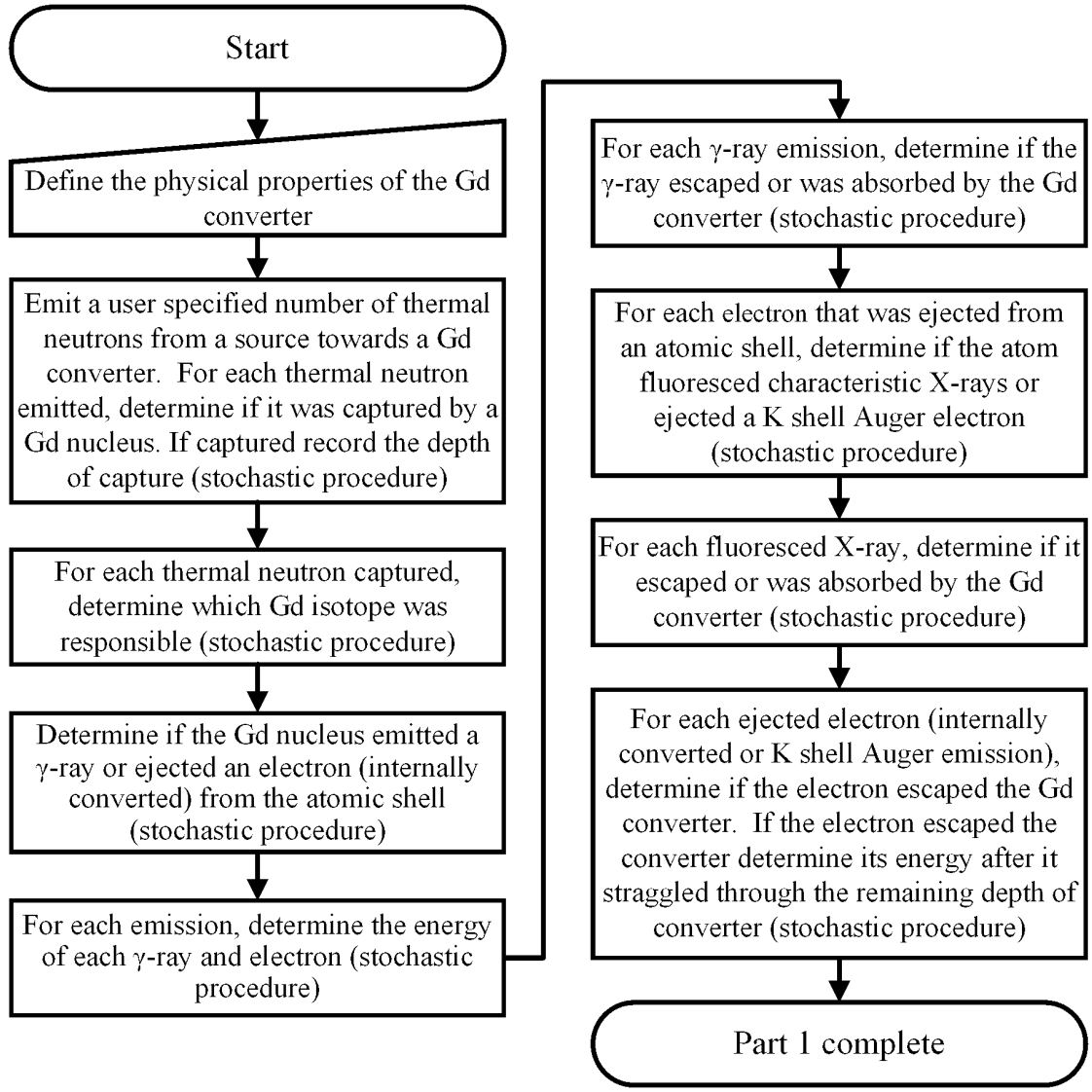

Figure 7.2. Flowchart providing an overview of the first phase of the Monte Carlo model for thermal neutron capture and the emission of reaction products from a natural Gd converter.

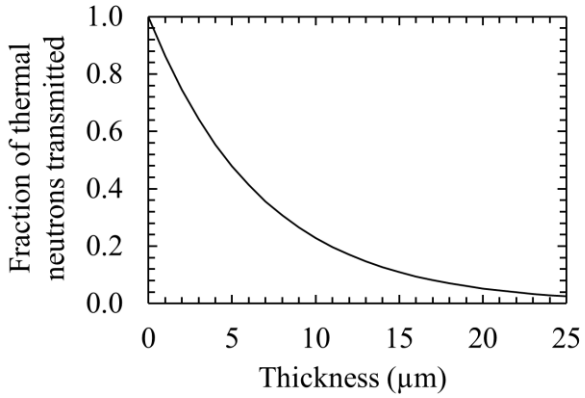

Figure 7.3. Transmissivity of a beam of thermal neutrons through natural Gd as a function of thickness of the Gd converter.

The probabilistic depth of thermal neutron capture by Gd nuclei was computed by rearranging **Equation 7.4** to,

$$z_i = -\frac{1}{N\,\sigma_t}\ln(R_i), \tag{7.5}$$

where z_i is the depth reached by the i^{th} thermal neutron and R_i is a pseudorandom number ($0 < R_i \leq 1$) drawn from a uniform population for the i^{th} thermal neutron. To determine which Gd isotope captured the i^{th} thermal neutron, another pseudorandom number was drawn and compared with the fractional interactions, C_i, (**Table 7.1**) of ^{155}Gd and ^{157}Gd nuclei, respectively. In a similar manner, pseudorandom numbers were drawn to determine, probabilistically, if the i^{th} thermal neutron captured led to the emission of a γ-ray or an electron and to determine the energy of each γ-ray or electron. The γ-ray emission probabilities were computed from the Nuclear Data Sheets of Reich (2012) and Nica (2017) and the electron conversion coefficients (**Table 7.3**) were obtained using BrIcc v2.3S (Kibédi et al., 2008). All possible stochastic γ-ray emission probabilities were modelled, but only γ-rays whose energy was ≤ 300 keV were stored.

The probability that a γ-ray will be emitted from ^{156}Gd* or ^{158}Gd* is 0.727 and 0.717, respectively. The balance of these probabilities is that an internal converted electron will be emitted. The relative probability that an emitted γ-ray will possess an energy ≤ 300 keV is 0.189 and 0.142 for ^{156}Gd* and ^{158}Gd*, respectively. Therefore, the probability that an electron will be emitted is greater than the probability of a ≤ 300 keV γ-ray emission. For ^{156}Gd*, this is 0.273 for an electron and 0.189 for the γ-ray; for ^{158}Gd* this is 0.283 for an electron and 0.142 for the γ-ray.

7.3.1 γ-ray attenuation

The linear attenuation and absorption coefficients for all photon interactions in natural Gd up to an energy of 300 keV are presented in **Figure 7.4** (Berger et al., 2010). The discontinuities at ≈ 8 keV and 50.2 keV are the L and K absorption edges of Gd, respectively. In common with other elements with a large number of electrons (high *Z* atoms), photoelectric absorption remains a significant source of photon scattering up to 300 keV. At the lowest energies, there is a minor Rayleigh elastic scattering contribution and above 150 keV Compton incoherent scattering becomes more significant. However, Compton scattering remains a small component of the total attenuation (scattering) of γ-rays up to 300 keV compared with photoelectric absorption. Pair production in Gd does not occur until a photon's energy exceeds 1 MeV. The total linear attenuation coefficient (coherent and incoherent scattering), μ, for every emitted photon's energy was used to determine if a γ-ray would be attenuated in the depth of Gd that remained, z_{rem}, following the emission of a γ-ray. For this, the Beer-Lambert-Bouger-Law (see **Equation 2.1,** and **Equation 2.2**) for light attenuation was used,

$$I(z_{rem})/\mathrm{I}_0 = \exp - (\mu z_{rem}), \tag{7.6a}$$

where $I(z_{rem})/\mathrm{I}_0$ is the fraction of γ-rays transmitted through the remaining Gd depth, z_{rem}. For the i^{th} emitted γ-ray, **Equation 7.6a** was rearranged to,

$$(z_{rem})_i = -\frac{1}{\mu_i}\ln(R_i), \tag{7.6b}$$

where R_i was another pseudorandom number ($0 < R_i \leq 1$) drawn for the i^{th} γ-ray. The track of each γ-ray was randomised in 4π sr (assuming that emission was randomly distributed into a sphere) and only γ-rays incident on the detector were stored for detector modelling. A histogram of photons emitted from a 10 μm thick Gd converter and incident upon the diamond detector (**Chapter 4, 5** and **6)** is presented in **Figure 7.5**. The events at 43 keV and 49 keV are Gd Kα and Kβ fluorescence X-rays (**Section 7.3.3**). In **Figure 7.5** a significant number of γ-rays are first observed ≥ 80 keV.

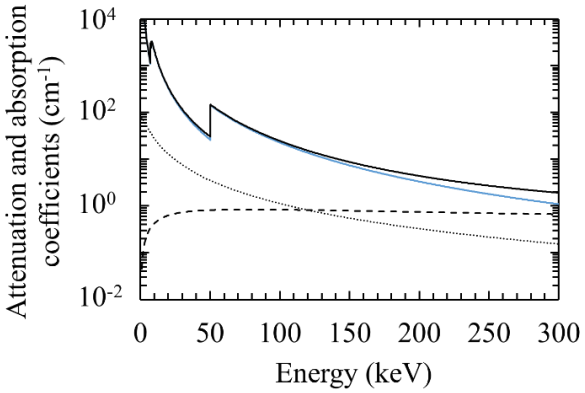

Figure 7.4. The energy dependence of linear attenuation coefficient (black line), linear absorption coefficient (blue line), Rayleigh (coherent) scattering (black dotted line), and Compton (incoherent) scattering (black dashed line) in natural Gd (Berger et al., 2010). Abrupt changes in photon transmissivity occur at the K shell (50.2 keV), L shell (≈ 7.2 keV – 8.4 keV), and M shell (≈ 1.2 keV – 1.9 keV) absorption edges.

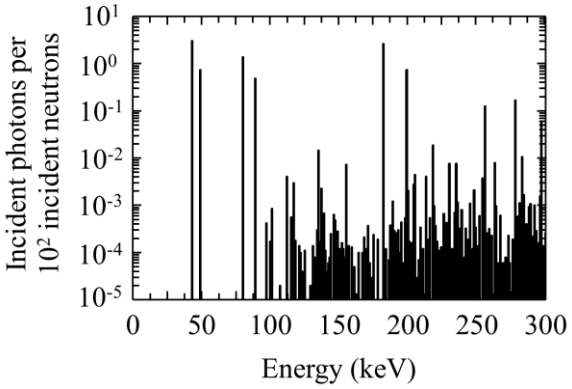

Figure 7.5. The modelled photon spectrum (≤ 300 keV) emitted from a 10 μm thick natural Gd absorber and incident upon the diamond detector. The photon spectrum is presented as the number of photons emitted from the Gd per 100 thermal neutrons incident upon the Gd.

7.3.2 Electron modelling

Unlike photons, electrons follow a tortuous route through matter; moreover, because the mass of a free electron and an orbital electron are equivalent, a large number of path changes are possible. Inelastic scattering events are plentiful and large path deflections can occur, particularly if a free electron scatters off of an atomic nucleus (Knoll, 2010). To determine the energies of the internal conversion electrons that escaped from the Gd absorber, data files (generated using CASINO) of the paths of 10^5 electrons transiting a 25 μm thick Gd foil were employed. For this, 18 data files

(one for each electron energy given in **Table 7.4**) were generated. For each electron energy, the 10^5 trajectories, simulated in CASINO, were separated into separate data packets. Each data packet reflected the history of one electron that initially possessed one of the 18 discrete energies. In total there were 1.8 million separate electron data packets available for selection in this part of the model. For the i^{th} electron emitted from a Gd nucleus, a pseudorandom integer, R_{int}, ($1 \leq R_{int} \leq 10^5$) was drawn from a uniform distribution. The i^{th} R_{int} was then used to select a data packet from the energy set to which the i^{th} electron belonged. The starting depth within the Gd of thermal neutron capture of the n emitted neutrons were previously determined, as was each occurrence of electron emission, as was the energy of the emitted electron. The remaining thickness of Gd (i.e. that through which the electron would have to travel to reach the detector) was calculated for each emitted electron and the selected data packet was used to determine if the i^{th} electron had sufficient energy to escape the absorber. Each electron data packet was randomly rotated in 4π sr to give it an initial direction vector, and the electron's position, determined in the CASINO data packet, was calculated in cartesian coordinates (x, y, and z) to determine if it entered the detector. If the CASINO electron data packet's calculated maximum depth (z coordinate) exceeded the thickness of remaining Gd, the electron was determined to have escaped the Gd convertor; if the electron's calculated x and y coordinates were within the bounded face dimensions of the detector, its remaining energy at the point of escape from the Gd and entry into a detector, as given in the CASINO data packet, was recorded as the energy that electron possessed at the moment it reached the detector. The modelled energy spectrum of electrons ejected from Gd atoms before straggling (i.e. before traveling through Gd) and the energy spectrum of electrons after they straggled through a 10 μm thick Gd absorber, are presented in **Figure 7.6 (a)** and **Figure 7.6 (b)**, respectively. In **Figure 7.6 (a)**, a small number of electrons are shown as having been emitted with an energy of 35 keV; this does not reflect the emission of internal conversion electrons, instead this is the emission of Auger electrons ejected from Gd atoms' L shells, a process competing with Gd K shell X-ray fluorescence (see **Section 7.3.3** and **Section 7.3.4**). In **Figure 7.6 (b)**, the contribution of the Auger emission to the electron spectrum can be observed as the (small) peak between the peaks at 29 keV and 39 keV.

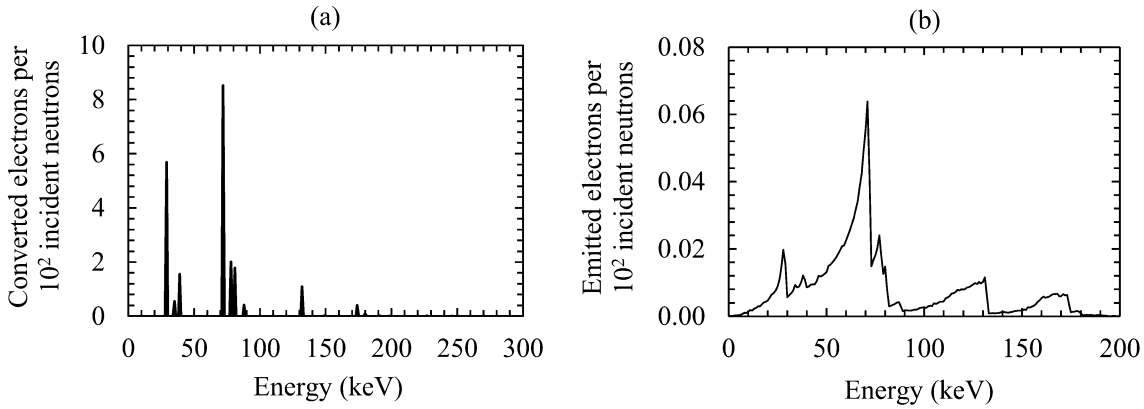

Figure 7.6. The energy spectrum of internal converted and Auger electrons ejected from Gd atoms in a 10 μm thick Gd thermal neutron absorber (a) prior to energy straggling and (b) after straggling through the Gd thickness that remained ahead of a detector. Necessarily, because each neutron had a different interaction position, the starting position of each electron was different, and the thickness of Gd remaining for each electron before the detector was different. The spectrum is presented as the number of electrons emitted per 100 thermal neutrons incident upon the Gd absorber.

To demonstrate the convergence of the MC code, a varying number of thermal neutrons were simulated to be incident on a 10 μm thick Gd thermal neutron absorber. The results of the convergence demonstration are presented in **Figure 7.7**, where 10^5, 10^6, and 10^7 thermal neutrons were simulated as being incident upon the Gd absorber. The electron energy emission specta converged well when the number of thermal neutrons incident on the Gd was increased from 10^5 to 10^6. The uncertainty in the electron emission spectrum then reduced marginally when the number of thermal neutrons was increased to 10^7 from 10^6. The number of thermal neutrons used to produce **Figure 7.6**, and hereafter to investigate the optimum thickness of Gd and the response of the detectors to the emission products, was 10^7.

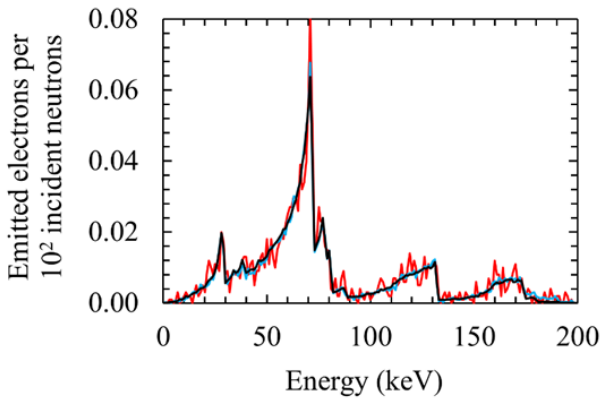

Figure 7.7. The convergence of the electron emission spectrum when 10^5 (red line), 10^6 (blue line), and 10^7 (black line) thermal neutrons were simulated to be incident upon a 10 µm thick natural Gd thermal neutron absorber.

The electron energy spectrum presented in **Figure 7.6 (b)** was compared with similar work in the literature. The data of **Figure 7.6 (b)** is similar to the that of Masaoka et al. (2003) which was produced using MCNP-4C modelling a 5 µm thick natural Gd converter; it is also similar to that reported by Kandlakunta et al. (2013) which was the result of work with SoftWare for Optimization of Radiation Detectors (SWORD) and MCNP-5. However, it should be noted that the MCNP code lacks data libraries that can model the internal converted electron emission following thermal neutron capture (Kandlakunta, 2014). The MCNP transport model of Masaoka et al. (2003) considered an electron distribution up to a maximum energy of 180 keV. A comparison of electron spectra from a 5 µm Gd thermal neutron converter produced using the model reported in this thesis and produced by Masaoka et al. (2003) is presented in **Figure 7.8**. The energy peaks associated with the 29 keV, 39 keV, 72 keV, 78 keV, 88 keV, 132 keV, and 174 keV internal conversion electrons can be identified. The origin of the substantially greater straggling in the spectrum of Masaoka et al. (2003) is unknown as Masaoka et al. did not report how electrons were distributed in the converter. Although it may be inferred from their work that the starting positions of the electrons were uniformly distributed throughout the converter. This may account for the broader energy distribution which suggested that the electrons in the converter were subjected to more energy straggling on average before they escaped from the converter. In contrast, the model presented in this thesis took into account the fact that neutrons are not uniformly captured by the Gd throughout its depth, rather the probabilistic depth of capture was considered on a neutron by neutron basis.

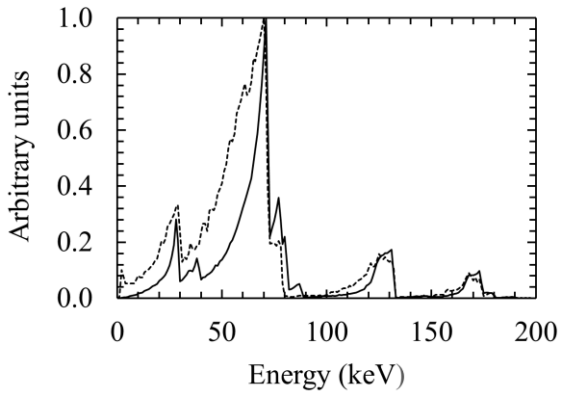

Figure 7.8. Comparison of the electron spectra modelled to be present at the interface between a 5 μm thick Gd converter and the detector as produced using the model reported in this thesis which considered the probabilistic depth of thermal neutron capture (solid line) and that produced by Masaoka et al. (2003) under the apparent assumption that neutrons were uniformly captured throughout the converter (dashed line).

Kandlakunta (Kandlakunta, 2014) used uniform electron distributions in multiple layers of Gd to model the straggled electron emission with MCNP-5. The MCNP-5 model was compared with a SWORD model which included a 200 μm thick (minimum depletion width 100 μm) Si detector. The geometry of the SWORD model was that of an isotropic thermal neutron source, emitting neutrons perpendicular to a 5 μm thick Gd target. The reaction products from thermal neutron capture were detected by the simulated detector mounted at an angle of 45° above the face of the Gd target. This orientation of target and detector collected electrons emitted backwards from the target. The simulation engine chosen for SWORD was GEANT-4 (Novikova et al., 2006).

A comparison between the model presented in this thesis and that of Kandlakunta (2014) is presented in **Figure 7.9**. The 72 keV electron energy peaks in each case are closely comparable, although there are additional counts from straggled electrons surrounding the 29 keV and the 39 keV electron emissions in Kandlakunta's model. The additional counts at 29 keV and 39 keV were thought to be related to the geometry employed in the simulation. In the work of Kandlakunta (2014), the Si detector was positioned to detect electrons emitted backwards from the Gd target which would have resulted in less energy straggling of low energy electrons compared with a forward emission geometry (as considered by the model reported in this thesis) where a greater proportion of the low energy electrons' energy would have been lost on average.

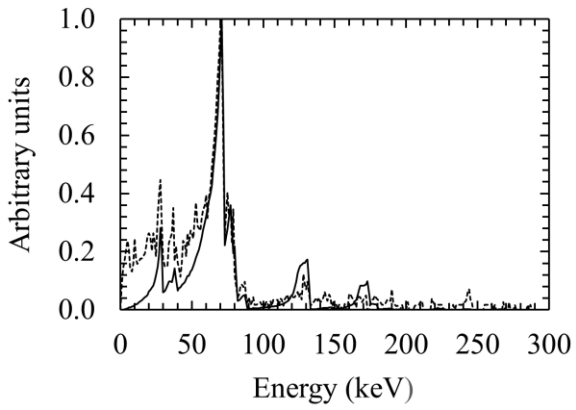

Figure 7.9. Comparison of the electron spectra modelled to be present at the interface between a 5 μm thick Gd converter and the detector as produced using the model reported in this thesis which considered the probabilistic depth of thermal neutron capture (solid line) and that produced by Kandlakunta (2014) (dashed line) using GEANT-4 and SWORD.

As discussed in **Section 7.3,** the thickness of a Gd neutron converter should be optimised to maximise the number of electrons emitted from the Gd (and maximising the transmitted fraction of the energy of each electron) whilst also maximising the number of thermal neutrons captured. As such, the model reported in this thesis was used to investigate the effects of different thicknesses of Gd neutron converter.

The integrated count of electrons emitted from a Gd converter per 100 neutrons incident upon the converter as a function of converter thickness is presented in **Figure 7.10**. The optimum thickness of Gd converter was 4 μm, assuming an arrangement where neutrons are incident on one side of the converter and the detector is located on the other side of the converter (i.e. a forward transmission arrangement). This thickness was in agreement with earlier reported work (Kandlakunta, 2014) (Masaoka et al., 2003) (Pfeifer et al., 2017) (Schulte & Kesselman, 1999).

Given this geometry, the most probable emission from the converter was from electrons which started their track through the Gd with an energy of 72 keV. As such, it is reasonable that it is these electrons which should be targeted for detection, particularly when attempting to detect thermal neutrons in γ-ray rich environments. The number of 72 keV electrons that straggled through the converter and exited such that they would have been incident upon the diamond detector described in **Chapter 4**, **5** and **6** (area of 2.0 mm by 2.0 mm) had it been positioned parallel with, and immediately proximate to, the converter, is presented in **Figure 7.10 (b)**. In order to optimise the detection of mono energetic 72 keV electrons emitted forwards, the converter should be ≈ 0.7 μm thick. The advantage of this optimised thickness will be shown in

Section 7.5. However, as the purpose of this work was to capture the entire electron spectrum and because the natural Gd absorber to be used in future experimental work would likely be from a commercial source, the thickness of converter assumed for the model, unless otherwise noted, was taken to be 10 μm.

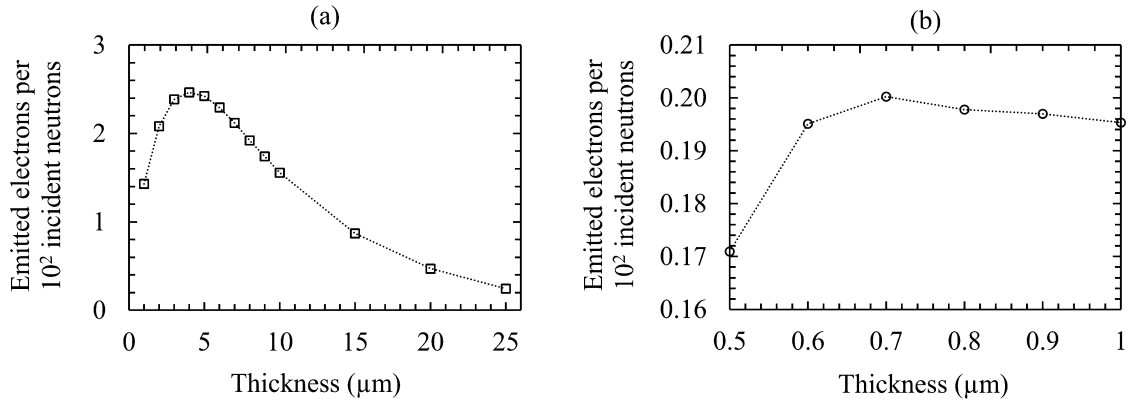

Figure 7.10. The modelled integrated count of electrons incident on the diamond detector per 100 thermal neutrons incident upon a Gd neutron converter as a function of thickness of converter for (a) all electrons and (b) 72 keV electrons. The dotted lines are a guide for the eye.

7.3.3 X-ray modelling

The K shell X-ray fluorescence emissions from Gd were modelled. In **Figure 7.5**, the two prominent K shell X-ray emission lines were at ≈ 43 keV (Gd $K\alpha_1$ = 43.0 keV, Gd $K\alpha_2$ = 42.3 keV) and ≈ 49 keV (Gd $K\beta_1$ = 48.7 keV, Gd $K\beta_2$ = 50.0 keV, Gd $K\beta_3$ = 48.6 keV) (**Table 7.5**). The total K shell fluorescence yield of Gd is 0.935 (Krause, 1979); and the Kα (43 keV) emission probability was calculated to be 0.81 (Thompson et al., 2009). L and M+ shell X-ray fluorescence occurred with low probability and the emitted X-rays were soft (**Table 7.5**), and more likely to be attenuated in the Gd. The electrons ejected from Gd atoms that give rise to K shell X-ray fluorescence are labelled in **Figure 7.1**. If an electron was determined to have been ejected from the K shell two pseudorandom numbers were drawn from uniform populations, R_a and R_b, ($0 < R_a$ and $R_b \leq 1$) if $R_a \leq 0.935$ and $R_b \leq 0.81$ a 43 keV X-ray was recorded as having been emitted. If $R_a \leq 0.935$ and $R_b > 0.81$ a 49 keV X-ray was recorded as having been emitted. The emission direction of each emitted X-ray was randomised into 4π sr and only those X-rays incident upon a detector (i.e. incident towards an area of the sphere projected onto the flat area of the detector) were recorded for onwards modelling of the detector's response to the fluorescence X-rays. The same technique as had been used to determine γ-ray attenuation was used to

determine which emitted X-rays were attenuated in the remaining Gd thickness, and hence absorbed in the Gd or conversely transmitted through it.

7.3.4 Auger electron modelling

Low energy Auger emissions (**Section 7.2.3**) were not simulated because of their short range in Gd and because those electrons that could have straggled out of the Gd would not have been detected if they were below the low energy threshold set for practical real-world spectrometers of the types under consideration ($E \lessapprox 13$ keV at $T = 20$ °C and $E \lessapprox 20$ keV at $T = 80$ °C, see **Chapter 5**). However, Auger electron emission that occurred in competition with K shell X-ray fluorescence was modelled. The K shell Auger yield of Gd was taken as 0.065 (Krause, 1979). An Auger electron ejected in competition with K shell X-ray fluorescence would have had an initial energy equal to the energy of the competing X-ray (the atomic excitation energy) less the binding energy of the ejected Auger electron (≈ 8 keV for Gd L shell). The majority of K shell X-ray fluorescence in Gd occurs at 43 keV and Auger electrons are most likely to be ejected from the L shell so the initial energy of K shell Auger electrons was taken to be 35 keV. The same method as had been used to model internal conversion electrons (**Section 7.3.2**) was used to model this Auger emission. A CASINO data file of 10^5 35 keV electrons simulated interacting with a 25 μm thick Gd foil was generated. Electron paths were separated into data packets and the path and exit energy of each Auger electron from its starting depth in the Gd converter was determined by the random selection of a data packet using the electron modelling procedure described in **Section 7.3.2**. The contribution of Auger electrons to the larger (internal conversion) electron spectrum was negligible; however, K shell Auger emission was included in the model. With this, the first phase of the model, which determined the reaction products emitted from the Gd absorber, was completed.

7.4 Modelling the detectors' responses to electrons and photons

The first phase of the model described in earlier sections, output a spectrum of photons (≤ 300 keV) and electrons emitted from a Gd absorber that would be incident upon the detectors in question (the diamond and COTS 4H-SiC detectors described in **Chapter 3,** and **Chapter 4**, **5** and **6**, respectively). The second phase of the model, an overview of which is presented in **Figure 7.11**, modelled the response of both detectors to the photon and electron emissions. The properties of each type of detector were defined by the user. The required inputs were the detectors' dimensions (length, breadth, and thickness), electron hole pair creation energy (12.82 eV for diamond (Keister et al., 2018); 7.28 eV for 4H-SiC (Chaudhuri et al., 2013)), Fano factor (0.08 for diamond (Alig et al., 1980); 0.128 for 4H-SiC (Chaudhuri et al., 2013)), detector

density, K shell X-ray fluorescence yield, K shell X-ray fluorescence emission probabilities and energies, (Krause, 1979), K shell electron binding energies, (Thompson et al., 2009), and the attention lengths of fluoresced photons in the active layer of the detectors (computed separately using ref. Henke et al. (1993)). A final and optional user input defined the length, breadth, thickness, and densities of the detector contacts and any deadlayers ahead of the detector's active layer. In the second phase of the MC model, the photons and electrons incident upon the detectors were addressed separately (**Figure 7.11**).

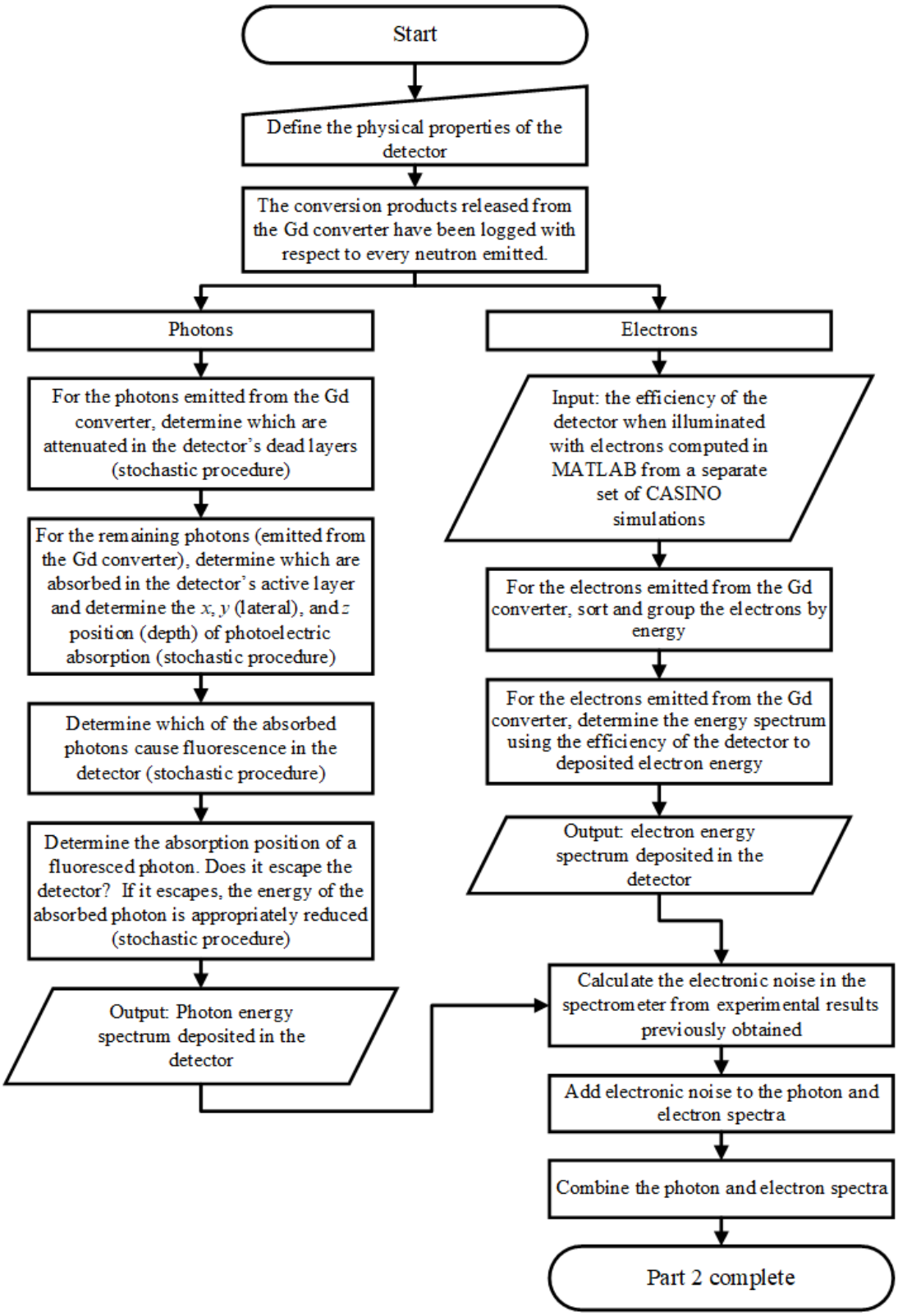

Figure 7.11. Flowchart of the second phase of the MC thermal neutron conversion model; this phase modelled the detectors' responses to the photons and electrons emitted from Gd following the absorption of thermal neutrons.

7.4.1 Photon detection

For the diamond detector, some of the photons emitted from the Gd were absorbed in the detector's electrical contacts and in an inactive deadlayer at the face of the detector immediately adjacent to the front contact. The detector's contacts were 50 nm of Ti overlayed with 200 nm of Ag. The inactive deadlayer was the equivalent of a 4.5 μm thick surface region at the detector's face. Here, electron-hole pairs were unable to move normally under the influence of the applied electrical potential and hence induce charge on the contacts. Accordingly, the photons that were absorbed in the deadlayer were not detected. The 4.5 μm thick deadlayer in the diamond detector had been observed when the detector was operated as part of a β^- particle spectrometer (**Chapter 5**). Similar deadlayers at the contact/detector interface have been reported in other semiconductor radiation detectors (Lioliou et al., 2016). For the COTS 4H-SiC detector, the full epitaxial thickness of the detector (5.15 μm) was active for photoelectric absorption (Zhao et al., 2018) and **Chapter 5**. The detector's front contact comprised a bonding island of negligible surface area when compared with the detector's active area, which was 0.06 mm^2 (Prasai et al., 2012).

User-generated data files of linear attenuation coefficients (Ag, Ti, and diamond) and linear absorption coefficients (diamond and 4H-SiC) from 1 keV to 300 keV, in maximum increments of 0.5 keV were employed. Additional energy steps were included in the linear attenuation and absorption coefficient data files to capture the change of photon transmissivity at the K, L, and M absorption edges, where applicable (Berger et al., 2010).

For the diamond detector, the data files of linear attenuation coefficients were accessed to calculate a total attenuation coefficient, μ_{Ti}, for the i^{th} photon energy emitted from the Gd (**Figure 7.5**). Another pseudorandom number was drawn for the i^{th} photon and **Equation 7.6b** was used (with μ_{Ti} substituted for μ_i) to determine if the i^{th} photon was attenuated prior to entering the active layer of the detector. For every occurrence of photon attenuation in the detector's contact or deadlayer the emitted photon tally was reduced by one. For the COTS 4H-SiC detector, attenuation in the top contact or a deadlayer was not considered as the whole epitaxial width of the detector had previously been shown to be active (see **Section 3.3.2**).

After the stochastic attenuation of photons (if any) in a detector's contact and deadlayer had been determined, photoelectric absorption of the n remaining photons, in the active layer of the detectors were determined. For the i^{th} photon incident on the active layer of a detector, the appropriate linear absorption coefficient, $(\mu_{en})_i$, was found from the linear absorption coefficient data files. Another pseudorandom number was drawn for the i^{th} photon and **Equation 7.6b** was

used (with $(\mu_{en})_i$, substituted for μ_i) to determine if the i^{th} photon was absorbed in the active layer of the detector in question. Such was the quantum detection efficiency (*QE*) of the diamond and COTS 4H-SiC detectors for hard X-rays and γ-rays that most X-rays and γ-rays of high energy passed through the detectors. The *QE* of the detectors to photons ≤ 300 keV are presented in **Figure 7.12**. The discontinuities at 1.8 keV (**Figure 7.12 (b)**) and between 3 keV and 5 keV (**Figure 7.12 (a)**) are the abrupt change in photon transmissivity at the Si K and the Ag and Ti K and L absorption edges.

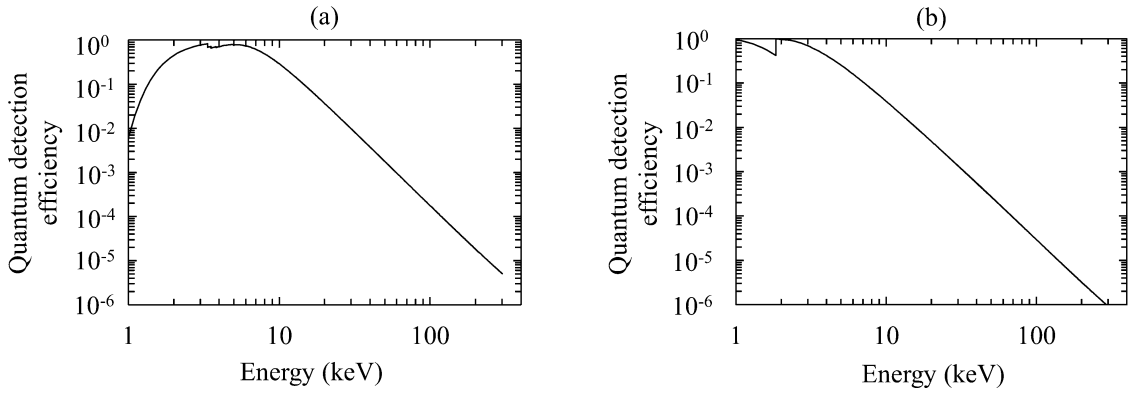

Figure 7.12. The quantum detection efficiency of the (a) diamond; (b) COTS 4H-SiC detector for photoelectric absorption up to 300 keV. The discontinuities at 1.8 keV (COTS 4H-SiC detector) and between 3 keV and 5 keV (diamond detector) are the Si K and the Ag and Ti K and L absorption edges, respectively.

For the X-rays and γ-rays that were absorbed in each detector, the likelihood of K shell fluorescence X-rays escaping from the detectors (and thus producing escape peaks in the spectrum) was modelled. The K shell fluorescence yield of diamond is low (0.003) (Krause, 1979) as is the energy of a fluoresced X-ray (277 eV) (Thompson et al., 2009) so X-ray fluorescence would occur rarely and an escape peak would not be observed. K shell fluorescence X-rays that escaped from the detector would cause there to be a comparatively marginal loss of X-ray energy deposited in the detector which would broaden a detected photopeak with more counts to the low energy side of a photopeak's centroid. To model X-ray fluorescence escape from the COTS 4H-SiC detector, the element (Si or C) that absorbed an X-ray or a γ-ray had to be determined first. Absorption of the i^{th} photon in the COTS 4H-SiC detector was determined by **Equation 7.6b** using the linear absorption coefficient data files for 4H-SiC at the i^{th} photon's energy. The probability that the i^{th} photon was absorbed by a C atom, *P(*C*)*, cf. a Si atom was determined by,

$$P(C) = W_C\, \mu_m(E)_C / \mu_m(E)_{SiC} \qquad (7.7)$$

where W_C is the mass fraction of C in SiC and μ_m are the mass absorption coefficients of C and SiC at the i^{th} photon's energy, respectively (Jenkins et al., 1995). The likelihood that the i^{th} photon was absorbed by a Si atom was simply, $(1 - P(\mathrm{C}))$. The likelihood of K X-ray shell fluorescence from the atom that absorbed the i^{th} photon was determined from the likelihood of photoelectric absorption and the K shell fluorescence yield of each element. The fluorescence yields of C and Si were 0.003 (Krause, 1979) and 0.048 (Brunetti et al., 2004), respectively.

To determine if a fluorescence X-ray escaped a detector, the previously stored coordinates where the i^{th} photon was absorbed were reviewed. The occurrence of fluorescence in the diamond detector was determined by drawing two further pseudorandom numbers (R_1 and R_2) from a uniform population which for fluorescence to occur were required to be: a) $R_1 \leq$ the K shell fluorescence yield (0.003) and then b) $R_2 \leq \mathrm{K}\alpha_1$ yield (0.668), or else c) $R_2 > \mathrm{K}\alpha_1$ yield ($\mathrm{K}\alpha_2$). The occurrence of fluorescence in the COTS 4H-SiC detector was determined similarly. For fluorescence to occur, the pseudorandom numbers were required to be: a) $R_1 \leq$ the K shell fluorescence yield (0.048) and then b) $R_2 \leq \mathrm{K}\alpha$ yield (0.971), or else c) $R_2 > \mathrm{K}\alpha$ yield ($\mathrm{K}\beta$). Si $\mathrm{K}\alpha$ and $\mathrm{K}\beta$ fluorescence X-rays have energies of 1740 eV and 1836 eV, respectively. If fluorescence occurred, the displacement range of the fluoresced photon, $\tilde{\boldsymbol{r}}$, was calculated using another pseudorandom number drawn from a uniform population, the attenuation length ($1/\mu_i$) of the fluoresced photon in diamond (C) and SiC (computed from Henke et al. (1993)), and **Equation 7.6b**. The *x*, *y*, and *z* displacements from the absorption site (**Figure 7.13**) of the i^{th} fluoresced photon were found from **Equation 7.8a**, **Equation 7.8b**, and **Equation 7.8c** where pseudorandom numbers from a uniform population were drawn to factorise the angles $\theta = \pi$ and $\phi = 2\pi$.

$$r_x = |\tilde{\boldsymbol{r}}|\, sin(\theta)\, cos(\phi) \tag{7.8a}$$

$$r_y = |\tilde{\boldsymbol{r}}|\, cos(\theta)\, cos(\phi) \tag{7.8b}$$

$$r_z = |\tilde{\boldsymbol{r}}|\, cos(\theta) \tag{7.8c}$$

If a fluoresced photon escaped the detector (determined by the locality of the i^{th} detected photon's absorption and the fluoresced photon's range) then the energy of the i^{th} detected photon was reduced by 277 eV (C $\mathrm{K}\alpha$ X-ray), 1740 eV (Si $\mathrm{K}\alpha$ X-ray), or 1836 eV (Si $\mathrm{K}\beta$ X-ray).

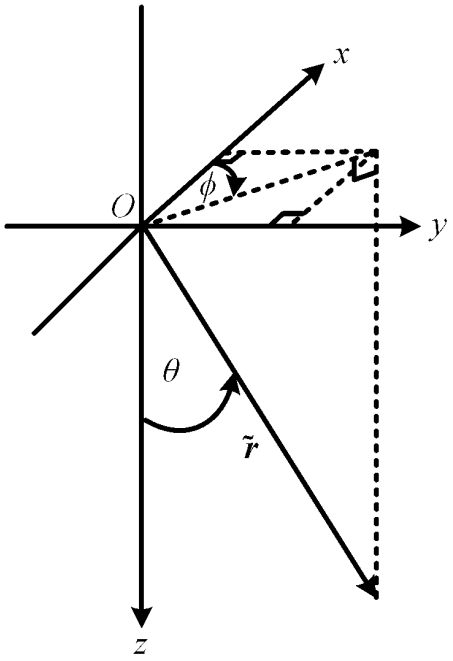

Figure 7.13. Orientation of *x, y,* and *z* displacements of a fluorescence photon in a detector. The origin, *O*, is the site of the original photoelectric absorption.

To complete the photon modelling, Fano noise and electronic noise was added to a detected spectrum. For the *n* detected photons, the standard deviation of the i^{th} photon's normal distribution was calculated using the calculated Fano noise and experimentally determined electronic noise (see **Chapter 3,** and **Chapter 4**). A random number was then drawn from a Gaussian population using the MATLAB 'normrand' function; with the absorbed photon's energy as the mean parameter and the previously calculated standard deviation. The normally distributed energy of the i^{th} photon was then calculated. The modelled photon spectrum emitted from a 10 µm thick Gd absorber (**Figure 7.5**) and subsequently detected by the diamond and the COTS 4H-SiC detectors of **Chapter 3** and **Chapters 4**, **5**, and **6** as predicted to be detected, are presented in **Figure 7.14 (a)** and **Figure 7.14 (b)**. In **Figures 7.14**, the centroid of the detected photopeaks are at 43 keV and 49 keV (X-rays), and 79.5 keV (γ-ray). Beyond 90 keV, there were no significant photon counts in the detectors.

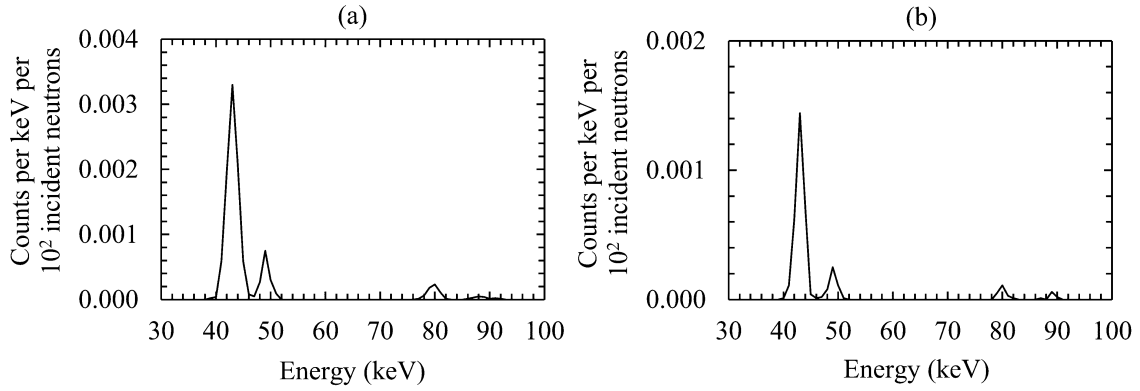

Figure 7.14. The modelled photon spectrum predicted to be detected by the (a) diamond and (b) COTS 4H-SiC detector after thermal neutrons were captured and photons emitted from Gd nuclei in a 10 μm thick absorber. The photon count is presented as the number of photons emitted from the Gd per 100 thermal neutrons incident upon the Gd converter. At this stage, the contributions of internal conversion electrons from the Gd converter are not included.

7.4.1.1 Photon detection verification

In order to provide some verification of the capability of the MC code to accurately model photon detection in the detectors, the model was tested against the experimentally obtained soft X-ray response of the diamond detector when it was illuminated by the ^{55}Fe radioisotope X-ray source (**Chapter 4**) and the diamond detector's experimentally obtained hard X-ray response when it was illuminated by the ^{109}Cd radioisotope X-ray and γ-ray source at T = 20 °C in **Chapter 6**. To test the code, 10^7 photons (≈ 8.8 × 10^6 Mn Kα photons and ≈ 1.2 × 10^6 Mn Kβ photons (Schötzig, 2000) were simulated as emitted from an isotropic ^{55}Fe radioisotope X-ray point source; and 10^8 photons (≈ 1.8 × 10^6 Ag $K\alpha_1$ photons, ≈ 1.0 × 10^6 Ag $K\alpha_2$, ≈ 0.6 × 10^6 Ag Kβ photons, and ≈ 0.1 × 10^6 ^{109}Cd γ_1 (88.03 keV) photons were simulated as emitted from an isotropic ^{109}Cd X-ray and γ-ray point source (Xiaolong et al., 2010). In the simulations both sources were located 1 cm above the centre of the detector. However, it should be noted that the ^{55}Fe radioisotope X-ray source and ^{109}Cd radioisotope X-ray and γ-ray source used in the experiments of **Chapters 3**, **4**, and **6** were a 28.27 mm^2 disc: for the purposes of the model verification this distinction (a disc X-ray/γ-ray source and an isotropic X-ray/γ-ray point source) is inconsequential because the comparison between model and experiment will be made in terms of relative counts not absolute numbers of detected photons. The number of photons emitted from the simulated source and incident upon the face of the detector in this configuration was ≈ 357000 (^{55}Fe) and ≈ 3555360 (^{109}Cd). Of those photons incident upon the detector, ≈ 299000 (^{55}Fe) and ≈ 45900 (^{109}Cd) were counted in the detector. A comparison of the MC modelled and experimentally obtained ^{55}Fe

X-ray and ^{109}Cd X-ray and γ-ray spectra are presented in **Figure 7.14**. In **Figure 7.14 (b)** only the ^{109}Cd Ag Kα and Ag Kβ X-rays are presented, as the ^{109}Cd γ_1 (88.03 keV) γ-rays were emitted and detected with low probability. In the work presented in **Chapter 6**, it took 4 hours to accumulate a statistically meaningful number of ^{109}Cd γ_1 (88.03 keV) γ-rays in the detector and although ^{109}Cd γ_1 (88.03 keV) γ-rays were detected in the modelled spectrum, the number of γ-rays accumulated were few cf. the Ag Kα and Ag Kβ X-rays. For example, of the 117991 ^{109}Cd γ_1 (88.03 keV) γ-rays that entered the detector, only 13 were detected. Computer memory limitations restricted the number of photons ($\lessapprox 10^8$) that could be modelled on a photon by photon basis with each execution of the code. The MC modelled spectra were broadened by the total noise (Fano noise and electronic noise) previously determined from the experimental X-ray spectrum of **Chapter 4**. In **Figure 7.15 (a)**, the experimental ^{55}Fe X-ray spectrum is overlapped by the high energy side tail of the so called 'zero' energy noise peak. It should be noted that zero energy noise was not modelled by the MC code. However, the modelled ^{55}Fe X-ray spectrum and the experimental ^{55}Fe X-ray spectrum exhibited agreement. In **Figure 7.15 (b)**, the modelled Ag Kα and Ag Kβ X-ray spectrum was in reasonable agreement with the experimentally obtained spectrum. The experimental spectrum presented in **Figure 7.15 (b)** shows low energy tailing on the combined Ag Kα and Kβ peak, which may simply be the tailing expected as the counts reduce to the inherent valley which reaches it minimum at ≈ 15 keV, such tailing was not modelled in the simulated spectrum. The modelled Ag Kα and Ag Kβ emission was more resolved than the experimentally accumulated spectrum; it should be noted that this particular photopeak, accumulated at T = 20 °C, was less resolved cf. the combined ^{55}Fe Mn Kα, Kβ experimental photopeak and the ^{109}Cd γ_1 (88.03 keV) experimental photopeak accumulated at the same temperature (see **Section 6.3.1** and **Figure 6.18**).

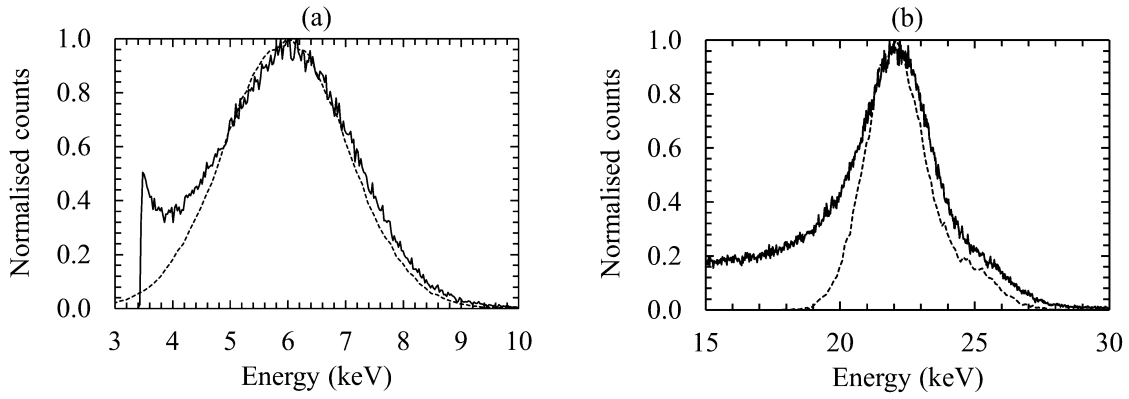

Figure 7.15. The (a) ^{55}Fe X-ray and (b) ^{109}Cd X-ray spectra accumulated by the diamond detector through experiment in **Chapter 4** and **Chapter 6** (at T = 20 °C) (solid lines) and the MC modelled diamond detector's corresponding ^{55}Fe X-ray and ^{109}Cd X-ray spectra (dashed lines). The experimental ^{55}Fe X-ray and the ^{109}Cd X-ray and γ-ray spectra were obtained with shaping time constants of 3 μs and 2 μs, respectively. The ^{109}Cd γ_1 (88.03) keV peak has not been shown in **Figure 7.15 (b)** because of the relatively few 88.03 keV counts accumulated in the experimental spectrum with 90 s of live time or by the model with 10^8 photons emitted from the simulated ^{109}Cd X-ray and γ-ray source.

7.4.2 Electron detection

To model the detected electron spectrum, the *QE* of the detectors were calculated for electrons of energy ≤ 300 keV. For the COTS 4H-SiC detector, 4000 electrons at each energy from 1 keV to 300 keV, in 1 keV steps, were simulated in CASINO as incident upon the detector. For the diamond detector, because of the configuration of the detector's contacts, 4000 electrons were simulated as incident upon the metalized and non-metalized top face in turn (i.e. in total 8000 elections were simulated incident upon the detector at each energy). A total of 1.2 million electrons were simulated for the COTS 4H-SiC detector and 2.4 million electrons were simulated for the diamond detector. The number of electrons was chosen to provide robust counting statistics across the energy range considering the *QE* of the detectors rather than replicate the intensity of any particular electron radiation environment. The *QE* was defined as the fraction of the energy deposited in the detector by electrons incident upon the face of the detector, as a function of energy up to 300 keV, as per the definition used in **Chapter 5**. The *QE* of the detectors as a function of electron energy is presented in **Figure 7.16**. The diamond detector's *QE* at low electron energies was limited by the 4.5 μm deadlayer at the face of the detector; the detector's electron *QE* was zero up to 24 keV. However, for 50 keV electrons the *QE* was 0.63 and for 100 keV electrons the *QE* was 0.91. In contrast, the *QE* of the COTS 4H-SiC detector was high

at low electron energy and rapidly reduced as electron energy increased above ≈ 30 keV. For the COTS 4H-SiC detector, the electron *QE* was 0.94 at 10 keV, 0.41 at 50 keV, and 0.08 at 100 keV.

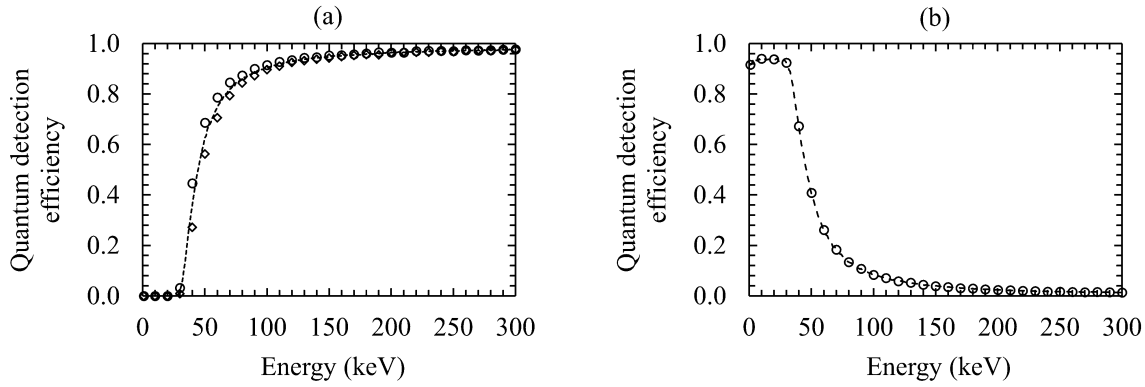

Figure 7.16. The *QE* of the (a) diamond detector's non-metalized face (open circles), metalized face (open diamonds), and the combined *QE* (dashed line) as a function of electron energy with a 4.5 µm deadlayer at the face of the detector and (b) the COTS 4H-SiC detector (open circles).

Both simulations (i.e. the electron spectrum emitted from the Gd and each detector's *QE* determined with CASINO) were combined thus taking account of the *QE* of the detector in each case. For the diamond detector, the adjustment of the emitted electron spectrum was completed separately for the detector's metalized face and non-metalized face, where both configurations included the 4.5 µm deadlayer at the face of the detector. In the final stage, the adjusted detected electron spectra were combined in the appropriate ratio of metalized face (0.49) and non-metalized face (0.51). The combination of emitted spectra and detector *QE* produced a detected electron spectrum without Fano noise and electronic noise for each detector. Electronic noise was added to the spectra by calculating the standard deviation of the i^{th} electron's normal distribution and drawing a random number from a Gaussian population using the MATLAB 'normrand' function, i.e. using the same method as had been used to add noise to the photon spectrum. The modelled electron spectrum predicted to be detected with and without electronic noise (for comparison purposes) is presented as **Figure 7.17**. The electron spectrum detected by the diamond detector in **Figure 7.17 (a)** has been recalibrated to match the photon energy scale of **Figure 7.14 (a)** using the position of the 72 keV and 132 keV electron emissions. The spectrum detected by the COTS 4H-SiC detector in **Figure 7.17 (b)** is not recalibrated and hence does not match the photon energy scale of **Figure 7.14 (b)**. However, peak counts associated with separate electron energies are identified. As the diamond detector was thick (500 µm) with a 4.5 µm dead layer, the majority of electron energy > 50 keV was deposited in the detector and well-defined peaks associated with electron energies > 50 keV are identified. Conversely, the COTS 4H-SiC

detector was thin (5.15 μm), and electrons > 20 keV deposited a fraction of their energy before they exited the detector. The source of the peak electron counts in the COTS 4H-SiC detector were identified by controlled exclusion of electrons of specific energy, emitted from the Gd, and comparing the resultant spectra with a full spectrum (without specific electrons being excluded).

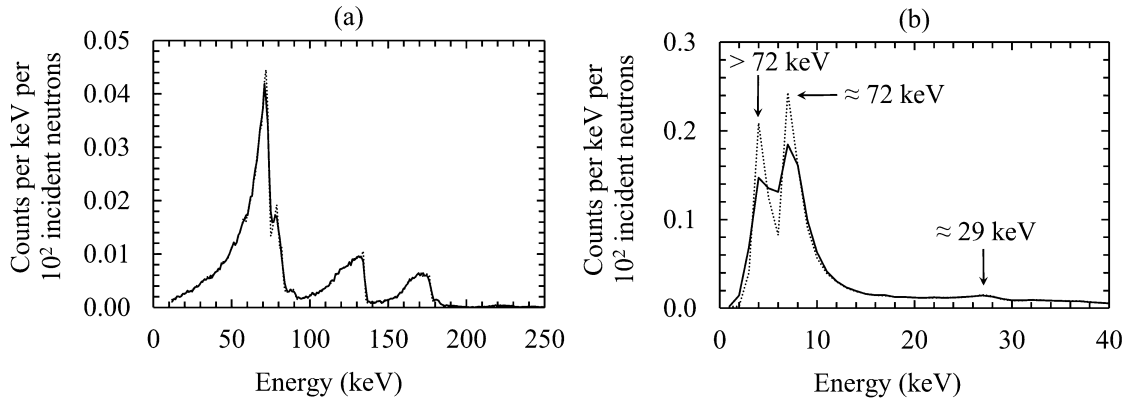

Figure 7.17. The modelled electron spectrum emitted from a 10 μm thick Gd converter and subsequently detected by the (a) diamond and (b) COTS 4H-SiC detector without Fano noise and electronic noise (dashed line) and with Fano and electronic noise (solid line) included. In **Figure 7.17 (b)** the spectrum contributions of electrons originally processing energies of 29 keV, 72 keV, and > 72 keV are labelled.

7.4.2.1 Electron detection verification

To verify the capability of the MC code to accurately model the electron response of the detectors the MC electron code was compared with a previously obtained experimental ^{63}Ni β^- particle spectrum (**Chapter 5**). A comparison of the modelled and a detected ^{63}Ni β^- particle spectrum collected by the diamond detector is presented at **Figure 7.18**. The MC modelled ^{63}Ni β^- particle spectrum showed good agreement with experiment. At low energies ($\lesssim$ 10 keV) the zero energy noise peak (which is not shown) overlapped the experimental ^{63}Ni β^- particle spectrum. Zero energy noise was not modelled in the MC code.

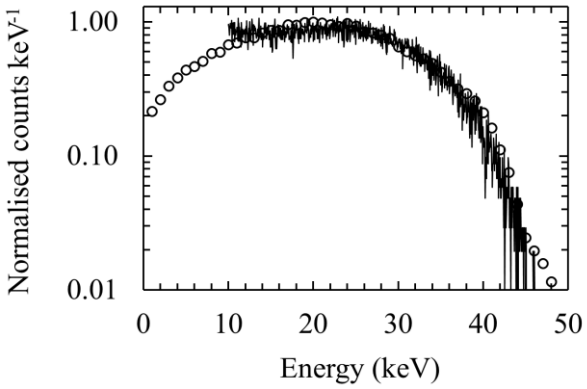

Figure 7.18. The MC modelled (open circles) and an experimentally acquired (black line) ^{63}Ni β^- particle spectrum. The experimental ^{55}Fe X-ray spectrum was obtained at 20 °C with an amplifier shaping time constant of 2 μs.

7.4.3 Electron and photon spectra

Combined photon and electron spectra are presented in **Figure 7.19**. The number of photons detected was one (diamond detector) and two (4H-SiC detector) orders of magnitude fewer than the number of electrons detected. To illustrate the relative impact of photon detection compared with electron detection, the simulated photon component is presented in counts per 10^5 thermal neutrons (secondary vertical axis) for the diamond and the 4H-SiC detector, in **Figure 7.19 (a)** and **(b)** respectively. The minimal impact of the photon component is further emphasised in **Figure 7.19 (c)** and **(d)**, where both components are shown on the same scale. As shown in **Figure 7.19**, the clarities of the electron spectra are unafflicted by X-ray and γ-ray emissions from the Gd absorber being detected in the two detectors investigated.

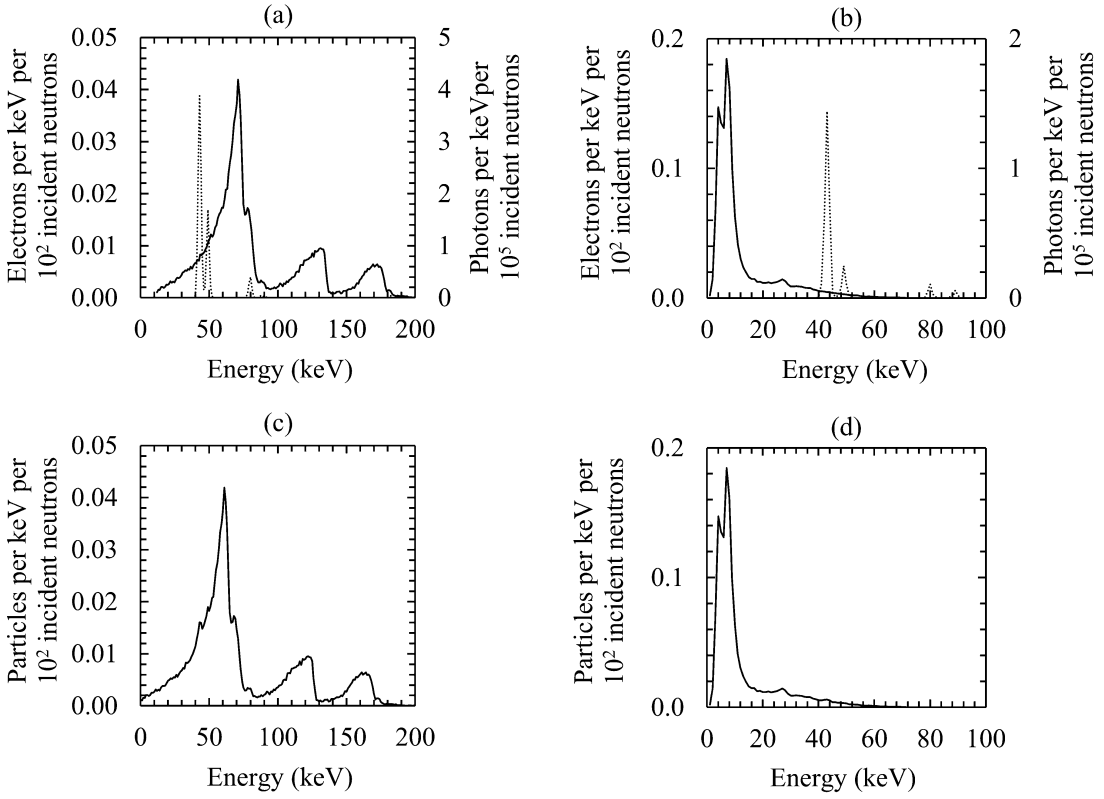

Figure 7.19. The modelled electron (solid line) and photon (dotted line) spectra collected with the (a) diamond and (b) 4H-SiC detector after thermal neutrons were absorbed in a 10 µm layer of Gd. The electron response is presented in counts per keV for 10^2 thermal neutrons incident upon the Gd absorber; the photon spectrum is presented in counts per keV for 10^5 thermal neutrons (right axis in a and b) incident upon the Gd absorber. The combined particle spectra (electrons and photons) collected with the (c) diamond and (d) 4H-SiC detector after thermal neutrons were absorbed in a 10 µm layer of Gd. The effects of Fano noise and electronic noise are included in all spectra predicted by the modelling to be detected.

7.5 Optimised configuration

Work in the previous section considered a Gd converter foil with a thickness of 10 µm as this is a COTS item readily available to the UK market. However, it was proposed in **Section 7.3.2**, that a thin (0.7 µm) Gd neutron absorber would optimise the detected 72 keV electron emission peak height with respect to the number of thermal neutrons incident upon the Gd absorber. The modelled electron emission spectrum from a 0.7 µm thick Gd converter and corresponding electron and photon spectra predicted to be detected using such a converter with the detectors previously described are presented in **Figure 7.20**. The results presented in **Figure 7.20** may be compared with the results presented in **Figure 7.19** and **Figure 7.6 (b)**. In terms of electron

emission from the Gd, the 72 keV electron peak height for a 0.7 μm thick Gd converter was computed and found to be > 3 times greater than for a 10 μm thick Gd converter. Considering other commonly available thicknesses of Gd foil, the 72 keV electron emission peak from a 0.7 μm thick Gd absorber was computed to be > 1.3 times greater than for a 4 μm thick Gd converter. In terms of electron detection with the diamond detector, the detected 72 keV electron emission peak height was computed to be 2.1 times greater with a 0.7 μm thick Gd converter than with a 10 μm thick Gd converter (**Figure 7.20 (b)**); there was no significant improvement in terms of the height of the detected 72 keV electron emissions when a 0.7 μm thick Gd converter was compared with 4 μm thick Gd converter. However, a more resolved electron energy spectrum was collected. Whilst it may seem counterintuitive that a more resolved energy spectrum could result without an improvement in peak height, it should be remembered that because of electron straggling, the detected peaks are, strictly, non-Gaussian, and it should be noted that on average electrons lose less energy straggling through a thinner Gd converter. Also, fewer neutrons are absorbed in a thinner converter and therefore numerically fewer electrons are emitted in the converter.

The higher energy electrons ($\gtrapprox$ 40 keV) emitted from the Gd converter deposited less of their energy in the thin 4H-SiC detector due to the rapid fall in *QE* of the detector above 40 keV cf. the comparatively thicker diamond detector (**Figure 7.20 (c)**). The 29 keV electron emissions were linked with the energy peak at 27 keV in the spectrum predicted to be detected. The *QE* of the 4H-SiC detector at 29 keV was 0.931; on average a 29 keV electron would deposit 28 keV of energy in the detector. For 72 keV electrons, the *QE* of the detector was 0.170; therefore ≈ 12 keV of energy would be deposited. A similar amount of energy, ≈ 11 keV, was deposited by 78 keV and 81 keV electrons (*QE* 0.142 and 0.131, respectively). Electrons possessing greater energy deposited progressively less energy in the detector. Therefore, a proportion of the energy related to the peak centred ≈ 7 keV was attributed to the electrons originally possessing 72 keV ≤ E ≤ 81 keV, before they straggled out of the Gd converter.

The electron spectra for both detectors remained unafflicted by X-ray and γ-ray emissions from the Gd: the photon spectrum was more than two orders of magnitude less than the electron spectrum when the most intense photon (43 keV X-ray) and electron emissions (72 keV conversion electrons) were compared for the diamond detector and three orders of magnitude less for the 4H-SiC detector when the same emissions were compared. The small impact of the photons on the detected spectra is made clear in **Figure 7.20 (d)** and **(e)**, where the photon and electron components of the spectra are presented on the same scale.

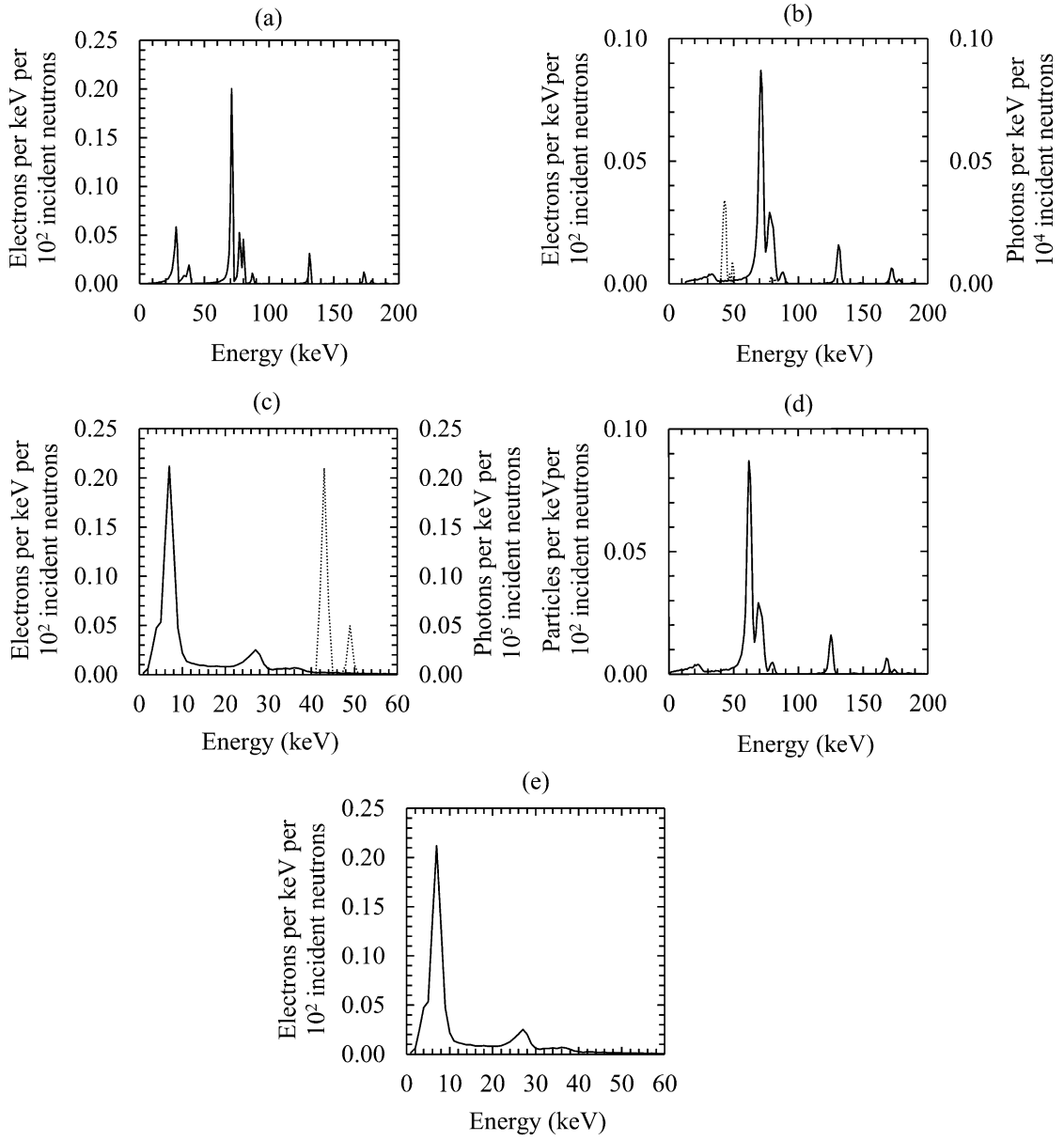

Figure 7.20. The modelled (a) electron emission spectrum after thermal neutron were absorbed in a 0.7 µm layer of Gd. The modelled electron (solid line; left axis in a, b, and e) and photon (dotted line, right axis in b and c) spectra collected with the (b) diamond and (c) 4H-SiC detector after thermal neutrons were absorbed in a 0.7 µm layer of Gd. The electron response is presented in counts per keV for 10^2 thermal neutrons incident upon the Gd absorber; the photon spectrum is presented in counts per keV for 10^4 (right axis in b) and 10^5 thermal neutrons (right axis in c) incident upon the Gd absorber. The combined particle spectra (electrons and photons) collected with the (d) diamond and (e) 4H-SiC detector after thermal neutrons were absorbed in a 0.7 µm

layer of Gd. The effects of Fano noise and electronic noise are included in all spectra predicted by the modelling to be detected.

7.6 Conclusions

The emission of prompt γ-rays, fluorescence X-rays, Auger electrons, and internal conversion electrons from the absorption of thermal neutrons by ^{155}Gd and ^{157}Gd isotopes in natural Gd neutron converter foils has been computer modelled using MC techniques. The responses of the two detectors that were investigated in earlier chapters of this thesis to the emissions from the Gd converter have also been modelled. The detectors' previously reported responses to X-rays, γ-rays, and β^- particles, together with knowledge of the relevant physics involved, was used as the basis for determining the detectors' responses to the photons and electrons emitted from Gd thermal neutron converters. Through the modelling, it was found that the photon component of the emissions from the Gd converters was virtually unimportant in comparison to the electron component of the emissions, when such converters were coupled with the detectors investigated in **Chapters 3**, **4**, **5**, and **6** of this thesis. The only significant numbers of photons detected were the 43 keV and 49 keV Gd K shell X-rays. Although these X-rays were detected, they were shown to be more than two orders of magnitude less significant than the detected 72 keV conversion electron emissions.

The optimum thickness of Gd foil for use as a thermal neutron to electron converter was investigated and found to be ≈ 0.7 μm. It was also shown that a 4 μm thick Gd converter would register the greatest number of electron counts summed over all the emitted electron energies, but that a 0.7 μm converter would produce a more resolved (less broad) 72 keV conversion electron emission spectrum. For the purpose of a future experiment, a 10 μm thickness of Gd (COTS Gd foils of this thickness are readily available) was initially modelled and investigated. This thickness of converter was also shown to be suitable for electron energy discrimination and thus thermal neutron detection when coupled with the detectors investigated in **Chapters 3**, **4**, **5**, and **6** of this thesis. Although the simulations were only conducted assuming an operating temperature of 20 °C, considering that the detectors in question were proven to operate uncooled at substantially higher temperatures (See **Chapters 3**, **5**, and **6**), it is anticipated that the scheme proposed here may also be used for the detection of thermal neutrons in high temperature environments.

Although the modelling reported in this chapter suggests that Gd-diamond and Gd-SiC thermal neutron detectors are highly promising, it should be noted that future experimental work will be required to verify the findings reported in this chapter.

Chapter 8 Summary, conclusions, and future work

8.1 Summary and conclusions

A thin (5.15 μm) low-cost COTS 4H-SiC UV photodiode and a thick (500 μm) CVD SC diamond detector have been investigated for their suitability as uncooled spectroscopic radiation detectors for high temperature (≥ 20 °C) applications.

The COTS 4H-SiC UV photodiode with a 5.15 μm epilayer (**Chapter 3**) was shown to function as an uncooled photon counting spectroscopic X-ray/γ-ray detector across the temperature range, 20 °C ≤ T ≤ 100 °C. The 4H-SiC photodiode, connected to a low noise charge sensitive preamplifier and onwards to a standard readout electronics chain, was operated continuously for 6 days at each of the investigated temperatures. The energy resolution (as defined by the *FWHM* at specific energies) was determined to be 1.66 keV ± 0.15 keV at 5.9 keV and 22.16 keV and 1.83 keV ± 0.15 keV at 59.5 keV when the spectrometer was operated at 20 °C. At the maximum operated temperature (100 °C) the *FWHM* were 2.69 ± 0.25 keV, 2.65 keV ± 0.25 keV, and 3.30 keV ± 0.30 keV, at the same energies. The principal source of noise that broadened the energy resolution at each energy was determined to be the quadratic sum of dielectric and incomplete charge collection noise for T < 80 °C. Parallel white noise was the dominant source of noise when the spectrometer was operated at T ≥ 80 °C when the longest shaping time constant available with the shaping amplifier (10 μs) was selected. After analysis of the experimental data, the presence of incomplete charge collection noise could not be completely discounted. Although it was shown that dielectric sources would contribute the greater part of combined dielectric and incomplete charge collection noise, if incomplete charge collection noise was present.

The X-ray detection capability of the COTS UV photodiode should be considered alongside the capabilities of custom grown 4H-SiC material and other wide bandgap X-ray detectors. Although direct comparisons between studies of different detectors and detector material can be difficult as the energy resolution of a particular spectrometer is often, in first approximation, determined by the noise introduced into the electronics chain when the original radiation induced charge pulse is processed by a preamplifier, rather than the inherent properties of a material (see **Section 2.3.2** and **Section 4.5**). When coupled to the best preamplifier available, with the detector co-located on a common chip with the preamplifier, a custom grown thick (124 μm depleted width) 4H-SiC strip X-ray detector has been operated with an ENC of 11.6 e^- rms (214 eV *FWHM*), measured on a pulser, at room temperature (T = 21 °C) (Puglisi & Bertuccio, 2019). Previously custom made 4H-SiC (20 μm thick epitaxial layer) detectors were reported with more modest energy resolution of 1.3 keV *FWHM* (≈ 76 e^- rms) at 5.9 keV (Mn Kα) when connected to a low noise

charge sensitive preamplifier built on a PCB with the detector packaged separately (Lees et al., 2009). For perspective with some other materials, a GaAs detector array has been reported with an energy resolution of 266 eV *FWHM* (≈ 27 e^- rms) at 5.9 keV (Mn Kα) when operated at room temperature (T = 23 °C) and connected to a feedback resistorless preamplifier (similar in design to the preamplifier used in this thesis) (Owens et al., 2001). The best energy resolution so far reported by an $Al_{0.2}Ga_{0.8}As$ non avalanche X-ray photodiode is 760 eV ± 60 eV *FWHM* (≈ 73 e^- rms ± 6 e^- rms) at 5.9 keV (Whitaker,Lioliou, & Barnett, 2018).

The COTS 4H-SiC detector was not intended for X-ray or γ-ray detection by the manufacturer. Yet it has been shown to be useful for these purposes. As a 4H-SiC based spectrometer, it has been operated successfully for long periods at elevated temperatures (20 °C ≤ T ≤.100 °C); it was operated almost continually for a month in a high temperature environment whilst ^{241}Am (59.5 keV) γ-rays were accumulated at each temperature over 6 days. In addition, it was found that it could operate without significant photopeak noise broadening from small leakage current instabilities.

The ready availability, cost effectiveness, and the ease with which the UV photodiode could be repurposed as a robust temperature tolerant X-ray and γ-ray detector makes this detector a readymade option for low-cost space or industrial applications (see **Chapter 8**). However, if the acquisition of finely energy resolved spectra was required or if a project or application had a generous instrumentation budget, a bespoke, purpose grown, wide bandgap detector – for example one made from GaAs, would be expected to be selected over the COTS 4H-SiC photodiode, for a temperature tolerant photon counting spectrometer.

A custom made, 500 μm thick electronic grade CVD SC diamond detector was investigated as an uncooled temperature tolerant (-20 °C ≤ T ≤ 100 °C) photon counting spectroscopic X-ray and γ-ray detector. The custom diamond detector was configured as a metal-diamond-metal device by sputtering Ti/Ag contacts onto the face of the detector. The maximum leakage current of the packaged detector, at an applied electric field strength of 2 kV cm^{-1}, was 40.6 pA ± 0.2 pA at 100 °C. At 20 °C, the measured leakage current was negligible and at lower temperatures the leakage current could not be reliably measured with the equipment used. When the leakage current attributed to the device's packaging was subtracted from the total leakage current of the packaged detector, the maximum recorded leakage current of the detector itself was 1.64 pA ± 0.57 pA at 100 °C and 0.11 pA ± 0.02 pA at 60 °C (electric field strength of 2 kV cm^{-1}). At T < 60 °C, the leakage current of the detector could not be measured as it was below the noise floor of the Keysight B2980 femtoammeter used in the work. Assuming the leakage current was

entirely constrained to the volume between the electrical contacts of the detector, the maximum leakage current density was calculated to be 83.7 pA cm^{-2} ± 29.0 pA cm^{-2} at 100 °C and 5.38 pA cm^{-2} ± 1.08 pA cm^{-2} at 60 °C. At 100 °C, the diamond detector's leakage current (i.e. with the leakage current of the package subtracted) reduced as a function of time and reach a steady state (within the uncertainty of the equipment used) after 20 minutes. The same reduction of leakage current was not observed at lower temperatures. Shallow trap activation, where the shallow trap population was gradually emptied, was suggested as the mechanism for the reduction of leakage current.

Using the diamond detector, soft X-ray spectra (< 10 keV) were accumulated; this work was the first report of soft X-ray spectroscopy with a diamond detector. A custom low noise charge sensitive preamplifier (CSP) with a standard onwards readout electronics chain comprised of a shaping amplifier, multichannel analyser, and personal computer was used to accumulate X-ray spectra at temperatures, -20 °C ≤ T ≤ 100 °C. The best energy resolution (*FWHM*) was achieved when 50 V potential difference (electric field strength = 1 keV cm^{-1}) was applied across the detector. ^{55}Fe Mn Kα (5.9 keV) and Kα (6.49 keV) X-rays were detected and counted at temperatures < 80 °C; at higher temperatures electronic noise prevented their detection. The *FWHM* at 5.9 keV was 2.93 keV ± 0.08 keV (at 3 μs shaping time) at 60 °C which improved to 2.33 keV ± 0.10 keV (2 μs shaping time) at -20 °C. The detector was also investigated with higher energy X-rays and γ-rays using a ^{109}Cd radioisotope X-ray and γ-ray source. The *FWHM* at 22.16 keV (^{109}Cd Ag $K\alpha_1$) was 4.57 keV ± 0.26 keV (at 1 μs shaping time) at 100 °C which improved to 2.70 keV ± 0.18 keV (2 μs shaping time) at -20 °C. The *FWHM* at 88.03 keV (^{109}Cd γ_1) was 4.13 keV ± 0.23 keV (at 1 μs shaping time) at 100 °C and 2.67 keV ± 0.27 keV (2 μs shaping time) at -20 °C.

Shaping time noise analysis determined that the dominant source of noise, when the diamond detector was illuminated by the ^{55}Fe radioisotope X-ray source, was dielectric noise for all but the shortest shaping amplifier time constant (0.5 μs) available. Here, series white noise, driven by the capacitance at the input of the preamplifier and the short shaping time constant, was the dominant noise source. Incomplete charge collection noise was absent when the diamond detector was operated at 20 °C, congruent with the count rate being unchanged when the potential difference across the detector was increased. Noise analysis of the spectra collected when the detector was illuminated with the ^{109}Cd radioisotope X-ray and γ-ray source determined that parallel white noise dominated over the quadratic sum of dielectric and incomplete charge collection noise as the shaping amplifier time constant was lengthened, particularly at high temperatures (> 60 °C). When the detector was illuminated with the ^{109}Cd radioisotope X-ray and

γ-ray source, the count rate was high (≈ 1650 s^{-1} in the Gaussian fitted to represent the Ag $K\alpha_1$ peak). At $T > 60$ °C, the count rate of within this peak increased as a function of shaping amplifier time constant. Some of the increased count rate was attributed to baseline shift (or other parasitic effects) broadening photopeaks at the longer shaping times. A consequence of the high count rate was a reduction in the optimum shaping time cf. the shaping time used when the diamond detector was illuminated by the ^{55}Fe radioisotope X-ray source.

An analysis of the lossy dielectrics of the detector's packaging, the electronic components that comprised the CSP, and the diamond detector itself indicated that the modest energy resolution of the diamond-based spectrometer was more a consequence of the detector's packaging, the packaging of the first transistor of the preamplifier, and the interconnection of the detector and transistor, rather than the detector itself, although the large electron-hole pair creation energy in diamond placed extraordinary demands upon the readout electronics. The packaging of the diamond detector was estimated to have contributed 50 e^- rms (1.5 keV *FWHM* at 5.9 keV) of dielectric noise.

The diamond detector was investigated for its utility as a high temperature tolerant particle counting electron (β^- particle) spectrometer. This was the first report of an energy calibrated spectroscopic β^- particle diamond detector capable of detecting low energy ($\lessapprox$ 50 keV) electrons, and the first time β^- particle spectra had been accumulated at high temperature (> 20 °C) with a diamond detector. The spectrometer was demonstrated to be operable at temperatures -20 °C ≤ T ≤ 80 °C. The detector was illuminated using a ^{63}Ni radioisotope β^- particle source. At 100 °C, the detector polarised and the morphology of the accumulated ^{63}Ni β^- particle spectra evolved as a function of time. Shallow traps in the bandgap of the material were proposed as the mechanism for the polarisation. At 100 °C, intrinsic charge was thought to have filled traps at a faster rate than trap depopulation could occur, thus causing space charge to build and the electric field across the detector to be disrupted.

Monte Carlo computer simulations were used to calibrate the energy scale of the β^- particle spectra accumulated at $T \leq 80$ °C. Through these simulations, it was determined that there was a 4.5 μm deadlayer in the diamond material at the top metal-diamond interface.

The diamond detector had good *QE* for β^- particles (*QE* = 0.79 at 66 keV). Despite the polarisation at 100 °C, CVD SC diamond was shown to be a promising material for solid state electron spectrometers in high temperature (≤ 80 °C, and possibly hotter if the polarisation-limited operation at 100 °C could be eliminated).

Following the experimental investigation of both the 4H-SiC and CVD SC diamond detectors, custom Monte Carlo computer code was developed to model the detectors' responses as thermal neutron detectors when coupled with thin (≤ 25 μm) natural Gd foils. Gd converts thermal neutrons to X-ray, γ-ray, and electron emissions which can be detected by the detectors. The Monte Carlo computer simulations determined that 0.7 μm of Gd converter was the optimal thickness to detect thermal neutrons by the targeted detection of the most intense internal conversion electron emission (72 keV).

The experimentally characterised responses of the COTS 4H-SiC detector and the CVD SC diamond detectors to X-rays, γ-rays, and β^- particles were used to model their response to the neutron interaction products from Gd converters. The Monte Carlo modelling suggested that both detectors could detect a conversion electron energy spectrum from neutron interactions with Gd converters without a significant number of X-rays and γ-rays obscuring the electron spectrum. When a 10 μm layer of Gd was modelled as the neutron converter, the number of photons detected, in terms of the height of the most intense photon emission cf. the most intense conversion electron emission, was one (diamond) and two (4H-SiC) orders of magnitude less than the number of electrons detected. When a 0.7 μm layer of Gd was modelled as the neutron converter the number of photons detected were two and three orders of magnitude less than the number of electrons detected.

The high *QE* for electrons (0.91 at 100 keV) of the diamond detector resulted in relatively straightforward electron spectra from the Gd converter (electron emission energies were identified by virtue of the majority of an electron's energy (> 50 keV) being deposited in the detector, on average). The lower electron *QE* of the 4H-SiC detector (0.08 at 100 keV) made the interpretation of the accumulated electron energy spectrum less straightforward. An electron, on average, deposited a small fraction of its energy in the 4H-SiC detector at $E_{electron} > 50$ keV ($QE \leq 0.41$). This meant that a 72 keV electron deposited only 9 keV of its energy, on average, in the 4H-SiC detector. Nevertheless, the accumulated electron energy spectrum detector could be interpreted and the spectral contribution from discrete electron energies could be identified.

Research suggested that the 4H-SiC and CVD SC diamond radiation detectors are likely to be useful devices for the detection of neutrons in high temperature environments (≤ 80 °C) when coupled with Gd neutron converters.

8.2 Future work

The work reported in this thesis has substantially advanced the state of the art for COTS 4H-SiC and CVD SC diamond radiation detectors, particularly for the detection of X-rays, γ-rays, β^-

particles and electrons, and thermal neutrons, in high temperature > 20 °C environments. However, there is still much future work which could be addressed with the detectors.

When the COTS 4H-SiC and CVD SC diamond-based spectrometers were operated at their optimum available shaping amplifier time constants, dielectric noise was a key factor limiting the achievable energy resolutions. This electronic component of noise could be reduced by reducing the capacitances (and their associated dielectric dissipation factors) acting at with the gate of the input JFET of the charge sensitive preamplifier. In part, this may be achieved through the use of a bare die JFET co-located on a low noise (high resistivity, low dielectric dissipation factor) package together with the detector; the detector would be directly wire bonded to the gate of the JFET (Bertuccio et al., 1993) (Bertuccio et al., 1994). It is also known that the conductive (typically Au or Ag loaded) epoxy used in die attach can be a significant source of dielectric noise (Barnett, 2021); consequently, trials should be undertaken to establish the lowest noise epoxy suitable for use. An alternative to epoxy die attach is Au ball bump bonding; this would eliminate entirely the need for epoxy, which will always be dielectrically lossy by virtue of its inherent nature. A hybrid integrated circuit could also be created with the transistor and detector connected either by conductive epoxy gold ball bump bonding or conductive epoxy; in such an arrangement the JFET should be located beneath the detector in order to minimise the transistor's radiation exposure. However, the performance of the 2N4416A JFETs employed as the input transistors in the preamplifiers used in the research reported in this thesis vary significantly on a transistor to transistor basis, even for transistors from the same manufacturing batch. As such, before a transistor can be selected for use, an extensive characterisation campaign is required to investigate a typically large (~10 – ~100) number of JFETs in order to select a 'good' candidate and establish its optimal biasing characteristics. This process is substantially more difficult if bare die (cf. packaged) transistors are used (Barnett, 2021). Furthermore, a detector which is quasi-permanently connected (e.g. by wire bond) or permanently connected (e.g. by bump bonding) cannot be electrically characterised separately from the JFET to which it is attached, once the connection has been made. As such, the practical challenges of integrating the detector with the first transistor of the preamplifier are substantial.

A future avenue of research towards reducing the electronic noise associated with the spectrometers reported in this thesis would be to investigate the possible benefits of the use of low noise (low dielectric dissipation factor) printed circuit board (PCB) material for the charge sensitive preamplifier. Whilst FR-4 (Edwards & Steer, 2016) PCBs were used for the preamplifiers employed throughout the work in this thesis, PCB materials with lower dielectric

dissipation factors are COTS components (e.g. RT/duroid 5880 (Rogers Corporation, N.D.)). The use of such PCB material may further reduce the dielectric noise at the input of the preamplifier.

It should also be noted that in each case reported here, the charge sensitive preamplifier, which employed Si components, was operated at the same temperature as the detector. If the first transistor of the preamplifier, a Si JFET, was replaced with a SiC JFET of the same design, parallel white noise would be reduced and the energy resolution would be improved (Lioliou & Barnett, 2015). The practical development of SiC JFETs suitable for radiation spectroscopy readout electronics has not received a great deal of attention to date, although its importance is widely appreciated within the relevant communities. Given the substantial progress made in SiC transistors for power electronics in recent years, the time for SiC spectrometer readout electronics maybe close to hand.

Investigation as to the presence or absence of incomplete charge collection noise in the diamond detector at $T > 60$ °C was inconclusive (see **Chapter 6**). Substantial changes in the apparent count rate as a function of shaping time (see **Section 6.2.3**) limited the effectiveness of shaping time noise analysis when comparing the spectrometer's *FWHM* at 22.16 keV with that at 5.9 keV. Revising the work of **Chapter 6** with a reduced photon flux incident upon the detector (e.g. achieved through the use of more effective attenuators, or a lower activity radiation source) may be valuable. Investigation of the spectrometer using an apparatus similar to that employed by (Lioliou & Barnett, 2017), in that case a current controllable Mo target X-ray tube which was used to fluoresce interchangeable high purity X-ray calibration foils to provide a multitude of well-defined characteristic X-ray lines, may further enable investigation of the relevant phenomena by virtue of providing ready control of both photon flux and photon energy.

The polarisation phenomena that was observed in **Chapter 5** when the diamond detector was operated at $T > 80$ °C should examined further. Additional ^{63}Ni β^- particle spectra collected with smaller temperature steps (≤ 5 °C per step) between $80\ °C \leq T \leq 100\ °C$ are required to identify the onset of temperature dependant polarisation. In addition, the responsivity of the diamond detector for ultraviolet / vacuum ultraviolet photons should be investigated to verify the thickness of the deadlayer at the face of the detector, thus employing a technique analogous to that employed at longer wavelengths for other detectors (Lioliou et al., 2015) (Lioliou et al., 2016).

The Monte Carlo simulations reported in **Chapter 7** should be experimentally verified by characterising both detectors (each coupled with Gd foils of various thickness) under the illumination of thermal neutrons from a suitable neutron source (e.g. a properly neutron moderated AmBe radioisotope neutron source). This would confirm or refute the results of the

modelling, potentially provide proof-of-concept for a low-cost high temperature tolerant thermal neutron detector made with entirely COTS components (thanks to the 4H-SiC detector) as well as Gd-diamond thermal neutron detectors, and provide impetus for future refinements or extension of the Monte Carlo code.

Furthermore, whilst the research reported in this thesis has concentrated on the high temperature operation of the 4H-SiC and diamond detectors, another key and often touted (though rarely properly verified) characteristic of devices made from these materials is their radiation hardness (Bertuccio et al., 2013) (Sellin & Vaitkus, 2006) (Lees et al., 2009) (Hodgson et al., 2017) (Radulović et al., 2020) (Coutinho et al., 2021). Thorough investigations of the changes (if any) in characteristics of the detectors as functions of absorbed radiation dose are also warranted in future; such research should investigate the changes in electrical and radiation detection characteristics of the detectors as functions of dose from a variety of radiation types (e.g. electrons, α particles, neutrons, protons, heavy ions), energies, and exposure profiles (e.g. prolonged moderate exposures; abrupt intense exposures). The effect of operating temperature on the radiation damage and its persistence should also be investigated. Such radiation damage investigations would help establish the likely lifetimes of detectors in intense radiation environments and may provide important signposting of ways in which the radiation hardness of the detectors could be improved.

References

Abdushukurov, D. A., 2010, *'Gadolinium Foils as Converters of Thermal Neutrons in Detectors of Nuclear Radiation'*, Nova Science Publishers Inc., New York, USA.

Ahmed, N. A., 2015, *'Physics and Engineering of Radiation Detection*, First edition, Academic Press Inc., London, UK.

Alexopoulos, A., Artuso, M., Bachmair, F., Bani, L., Bartosik, M., Beacham, J., Beck, H., Bellini, V., Belyaev, V., Bentele, B., Bergonzo, P., Bes, A., Brom, J.-M., Bruzzi, M., Chiodini, G., Chren, D., Cindro, V., Claus, D., Collot, J., Cumalat, J., Dabrowski, A., D'Alessandro, R., Dauvergne, D., de Boer, W., Dick, S., Dorfer, C., Dunser, M., Eigen, G., Eremin, V., Forneris, J., Gallin-Martel, L., Gallin-Martel, M. L., Gan, K. K., Gastal, M., Giroletti, C., Goffe, M., Goldstein, J., Golubev, A., Gorisek, A., Grigoriev, E., Grosse-Knetter, J., Grummer, A., Guthoff, M., Hiti, B., Hits, D., Hoeferkamp, M., Hofmann, T., Hosslet, J., Hostachy, J.-Y., Hugging, F., Hutton, C., Janssen, J., Kagan, H., Kanxheri, K., Kasieczka, G., Kass, R., Kis, M., Kramberger, G., Kuleshov, S., Lacoste, A., Lagomarsino, S., Giudice, A. Lo, Lukosi, E., Maazouzi, C., Mandic, I., Marino, A., Mathieu, C., Menichelli, M., Mikuz, M., Morozzi, A., Moss, J., Mountain, R., Murphy, S., Muskinja, M., Oh, A., Olivero, P., Passeri, D., Pernegger, H., Perrino, R., Picollo, F., Pomorski, M., Potenza, R., Quadt, A., Rarbi, F., Re, A., Reichmann, M., Riley, G., Roe, S., Sanz, D., Scaringella, M., Schaefer, D., Schmidt, C., Schioppa, E., Schnetzer, S., Sciortino, S., Scorzoni, A., Seidel, S., Servoli, L., Smith, D. S., Sopko, B., Sopko, V., Spagnolo, S., Spanier, S., Stenson, K., Stone, R., Stugu, B., Sutera, C., Traeger, M., Tromson, D., Trischuk, W., Tuve, C., Velthuis, J., Venturi, N., Vittone, E., Wagner, S., Wallny, R., Wang, J. C., Weingarten, J., Weiss, C., Wermes, N., Yamouni, M., Zalieckas, J., and Zavrtanik, M., 2018, *'Development of Diamond Tracking Detectors for High Luminosity Experiments at the LHC, HL-LHC and Beyond'*, RD 42 2018 LHCC Status Report.

Alig, R. C., Bloom, S., and Struck, C. W., 1980, *'Scattering by ionization and phonon emission in semiconductors'*, Physical Review B, Vol. 22, No. 12, pp. 5565–5582.

Amptec, N.D., *'XR-100SDD Data Sheet'*, AMPTEC Inc, Bedford, MA, USA.

Angelone, M., Cesaroni, S., Loreti, S., Pagano, G., and Pillon, M., 2019, *'High temperature response of a single crystal CVD diamond detector operated in current mode'*, Nuclear Instruments and Methods in Physics Research Section A, Vol. 943, pp. 162493–162501.

References

Angelone, M., Fonnesu, N., Pillon, M., Prestopino, G., Sarto, F., Milani, E., Marinelli, M., Verona, C., and Verona-Rinati, G., 2012, *'Spectrometric Performances of Monocrystalline Artificial Diamond Detectors Operated at High Temperature'*, IEEE Transactions on Nuclear Science, Vol. 59, No. 5, pp. 2416–2423.

Barnett, A. M., Bassford, D. J., Lees, J. E., Ng, J. S., Tan, C. H., and David, J. P. R., 2010, *'Temperature dependence of AlGaAs soft X-ray detectors'*, Nuclear Instruments and Methods in Physics Research Section A, Vol. 621, No. 1–3, pp. 453–455.

Barnett, A. M., Lees, J. E., and Bassford, D. J., 2013, *'Temperature dependence of the average electron-hole pair creation energy in $Al_{0.8}Ga_{0.2}As$'*, Applied Physics Letters, Vol. 102, No. 18, Art. No. 181119.

Barnett, A. M., Lees, J. E., Bassford, D. J., and Ng, J. S., 2012a, *'Determination of the electron-hole pair creation energy in $Al_{0.8}Ga_{0.2}As$'*, Journal of Instrumentation, Vol. 7, No. 6, Art. No. 06016.

Barnett, A. M., Lees, J. E., Bassford, D. J., and Ng, J. S., 2012b, *'A varied shaping time noise analysis of $Al_{0.8}Ga_{0.2}As$ and GaAs soft X-ray photodiodes coupled to a low-noise charge sensitive preamplifier'*, Nuclear Instruments and Methods in Physics Research Section A, Vol. 673, pp. 10-15.

Barnett, A. M., Lees, J. E., Bassford, D. J., Ng, J. S., Tan, C. H., Babazadeh, N., and Gomes, R. B., 2011, *'The spectral resolution of high temperature GaAs photon counting soft X-ray photodiodes'*, Nuclear Instruments and Methods in Physics Research Section A, Vol. 654, No. 1, pp. 336–339.

Barnett, A. M., Lioliou, G., and Ng, J. S., 2015, *'Characterization of room temperature AlGaAs soft X-ray mesa photodiodes'*, Nuclear Instruments and Methods in Physics Research Section A, Vol. 774, pp. 29–33.

Barnett, A. M., 2021, personal communication, 26 October.

Bau, X. J., Schlesinger, T. E., and James, R. B., 1995, *'Chapter 4: Electrical properties of mercuric iodide'*, in: '*Semiconductors for Room Temperature Nuclear Detector Applications'*, First edition, Willardson, W. R. K., Beer, A. C., and Webster, E. R. (eds), Semiconductors and Semimetals, Volume 43, Academic Press Ltd., London, U.K.

References

BenMoussa, A., Giordanengo, B., Gissot, S., Dammasch, I. E., Dominique, M., Hochedez, J.-F., Soltani, A., Bourzgui, N., Saito, T., Schühle, U., Gottwald, A., Kroth, U., and Jones, A. R., 2015, *'Degradation assessment of LYRA after 5 years on orbit - Technology Demonstration'*, Experimental Astronomy, Vol. 39, No. 1, pp. 29–43.

Berger, M. J., Hubbell, J. H., Seltzer, S. M., Chang, J., Coursey, J. S., Sukumar, R., Zucker, D. S., and Olsen, K., 2010, *'XCOM: Photon Cross Sections Database'*, National Institute of Standards and Technology, Gaithersburg, MD., USA.

Bergonzo, P., Tromson, D., Descamps, C., Hamrita, H., Mer, C., Tranchant, N., and Nesladek, M., 2007, *'Improving diamond detectors: A device case'*, Diamond and Related Materials, Vol. 16, pp. 1038–1043.

Bertuccio, G., 2005, *'Prospect for energy resolving X-ray imaging with compound semiconductor pixel detectors'*, Nuclear Instruments and Methods in Physics Research Section A, Vol. 546, No. 1–2, pp. 232–241.

Bertuccio, G., Caccia, S., Puglisi, D., and Macera, D., 2011, *'Advances in silicon carbide X-ray detectors'*, Nuclear Instruments and Methods in Physics Research Section A, Vol. 652, No. 1, pp. 193–196.

Bertuccio, G. and Casiraghi, R., 2003, *'Study of silicon carbide for X-ray detection and spectroscopy'*, IEEE Transactions on Nuclear Science, Vol. 50, No. 1, pp. 175–185.

Bertuccio, G., Casiraghi, R., Cetronio, A., Lanzieri, C., and Nava, F., 2004, *'Silicon carbide for high resolution X-ray detectors operating up to 100°C'*, Nuclear Instruments and Methods in Physics Research Section A, Vol. 522, No. 3, pp. 413–419.

Bertuccio, G., Casiraghi, R., and Nava, F., 2001, *'Epitaxial silicon carbide for X-ray detection',* IEEE Transactions on Nuclear Science, Vol. 48, No. 2, pp. 232–233.

Bertuccio, G. and Maiocchi, D., 2002, *'Electron-hole pair generation energy in gallium arsenide by x and γ photons'*, Journal of Applied Physics, Vol. 92, No. 3, pp. 1248–1255.

Bertuccio, G., Puglisi, D., Torrisi, L., and Lanzieri, C., 2013, *'Silicon carbide detector for laser-generated plasma radiation'*, Applied Surface Science, Vol. 272, pp. 128–131.

Bertuccio, G. and Pullia, A., 1993, *'A method for the determination of the noise parameters in preamplifying systems for semiconductor radiation detectors'*, Review of Scientific Instruments, Vol. 64, No. 11, pp. 3294–3298.

References

Bertuccio, G., Pullia, A., and De Geronimo, G., 1996, *'Criteria of choice of the front-end transistor for low-noise preamplification of detector signals at sub-microsecond shaping times for X- and γ-ray spectroscopy'*, Nuclear Instruments and Methods in Physics Research Section A, Vol. 380, No. 1, pp. 301–307.

Bertuccio, G., Rehak, P., and Xi, D., 1993, *'A novel charge sensitive preamplifier without the feedback resistor'*, Nuclear Instruments and Methods in Physics Research Section A, Vol. 326, No. 1, pp. 71–76.

Bertuccio, G., Rehak, P., and Xi, D., 1994, *'Low noise charge sensitive preamplifier DC stabilised without a physical resistor'*, US 1994/005347231A.

Blank, T. V., Goldberg, Y. A., and Konstantinov, O. V., 2003, *'Temperature dependence of the performance of ultraviolet detectors'*, Nuclear Instruments and Methods in Physics Research Section A, Vol. 509, No. 1–3, pp. 109–117.

Bludau, W., Onton, A., and Heinke, W., 1974, *'Temperature dependence of the band gap of silicon'*, Journal of Applied Physics, Vol. 45, No. 4, pp. 1846–1848.

Boyle, W. S. and Smith, G. E., 1970, *'Charge Coupled Semiconductor Devices'*, Bell System Technical Journal, Vol. 49, No. 4, pp. 587–593.

Brunetti, A., Sanchez del Rio, M., Golosio, B., Simionovici, A., and Somogyi, A., 2004, *'A library for X-ray–matter interaction cross sections for X-ray fluorescence applications'*, Spectrochimica Acta Part B: Atomic Spectroscopy, Vol. 59, No. 10–11.

Bruzzi, M., Lagomarsino, S., Nava, F., and Sciortino, S., 2003, *'Characterisation of epitaxial SiC Schottky barriers as particle detectors'*, Diamond and Related Materials, Vol. 12, No. 3–7, pp. 1205–1208.

Bruzzi, M., Menichelli, D., Sciortino, S., and Lombardi, L., 2002, *'Deep levels and trapping mechanisms in chemical vapor deposited diamond'*, Journal of Applied Physics, Vol. 91, No. 9, pp. 5765–5774.

Butera, S., Lioliou, G., Krysa, A. B., and Barnett, A. M., 2017, *'InGaP (GaInP) mesa p-i-n photodiodes for X-ray photon counting spectroscopy'*, Scientific Reports, Vol. 7, No. 1, pp. 1–8.

Butera, S., Lioliou, G., Krysa, A. B., and Barnett, A. M., 2018, *'Measurement of the electron–hole pair creation energy in $Al_{0.52}In_{0.48}P$ using X-ray radiation'*, Nuclear Instruments and Methods in Physics Research Section A, Vol. 879, pp. 64–68.

References

Butera, S., Lioliou, G., Zhao, S., Whitaker, M. D. C., Krysa, A. B., and Barnett, A. M., 2019, *'InGaP electron spectrometer for high temperature environments'*, Scientific Reports, Vol. 9, No. 1, Art. No. 11096.

Casnati, E., Tartari, A., and Baraldi, C., 1982, *'An empirical approach to K-shell ionisation cross section by electrons'*, Journal of Physics B: Atomic and Molecular Physics, Vol. 15, No. 1, Art. No. 155.

Cerullo, N., Bufalino, D., and Daquino, G., 2009, *'Progress in the use of gadolinium for NCT'*, Applied Radiation and Isotopes, Vol. 67, No. 7–8, pp. S157–S160.

Chaudhuri, S. K., Zavalla, K. J., and Mandal, K. C., 2013, *'Experimental determination of electron-hole pair creation energy in 4H-SiC epitaxial layer: An absolute calibration approach'*, Applied Physics Letters, Vol. 102, No. 3, Art. No. 31109.

Cheong, J. S., Ong, J. S. L., Ng, J. S., Krysa, A. B., and David, J. P. R., 2014, *'$Al_{0.52}In_{0.48}P$ SAM-APD as a blue-green detector'*, IEEE Journal of Selected Topics in Quantum Electronics, Vol. 20, No. 6, pp. 142–146.

Choi, H. D., Firestone, R. B., Lindstrom, R. M., Molnar, G. L., Mughabghab, S. F., Paviotti-Coruera, R., Revay, Z., Trkov, A., Zerkin, V., and Zhou, C., 2007, '*Database of Prompt Gamma Rays from Slow Neutron Capture for Elemental Analysis'*, Vienna, Austria.

Chu, S. Y. F., Ekström, L. P. and Firestone, R. B., 1996. '*WWW Table of Radioactive Isotopes'* [Online]. Available at http://nucleardata.nuclear.lu.se/nucleardata/toi/ (Accessed 29 April 2020).

Chynoweth, A. G., 1952, *'Conductivity Crystal Counters'*, American Journal of Physics, Vol. 20, No. 4, pp. 218–226.

Clark, C. D., Dean, P. J., and Harris, P. V., 1964, *'Intrinsic edge absorption in diamond'*, Proceedings of the Royal Society of London, Vol. 277, No. 1370, pp. 312–329.

Clarke, R. H., J Dunster, C. H., K Guskova, L. A., Jacobi, M. W., Li, N. D., Liniecki, T. J., B Meinhold, L. C., Mettler, U. F., Shigematsu, A. L., Silini, H. G., K Sinclair, I. W., Lindell, B. B., Z Morgan, S. K., and S Taylor, A. L., 1991, *'1990 Recommendations of the International Commission on Radiological Protection'* Vol. 21, No.1−3, Pergamon Press, Oxford, U.K.

References

Coutinho, J., Torres, V. J. B., Capan, I., Brodar, T., Ereš, Z., Bernat, R., Radulović, V., Ambrožič, K., Snoj, L., Pastuović, Ž., Sarbutt, A., Ohshima, T., Yamazaki, Y. and Makino, T., 2021, *'Silicon carbide diodes for neutron detection'*, Nuclear Instruments and Methods in Physics Research Section A, Vol. 986, Art. No. 164793

Cromer, D. T. and Liberman, D., 1970, *'Relativistic Calculation of Anomalous Scattering Factors for X Rays'*, The Journal of Chemical Physics, Vol. 53, No. 5, pp. 1891–1898.

Das, P. K., 2017, *'Measurement of Relative Intensity of the Discrete γ Rays From the Thermal Neutron Capture Reaction Gd(n,γ) Using ANNRI Detector (JPARC)'*, Okayama University, Japan.

Denecke, B., 1987, *'Measurement of the 59.5-keV gamma-ray emission probability in the decay of ^{241}Am with a 4π-CsI(T1) - sandwich spectrometer'*, International Journal of Radiation Applications and Instrumentation, Vol. 38, No. 10, pp. 823–830.

Drouin, D., Hovington, P., and Gauvin, R., 1997, *'CASINO: A new monte carlo code in C language for electron beam interactions-part II: Tabulated values of the Mott cross section'*, Scanning, Vol. 19, No. 1, pp. 20–28.

Dueñas, J. A., de la Torre Pérez, J., Martín Sánchez, A., and Martel, I., 2014, *'Diamond detector for alpha-particle spectrometry'*, Applied Radiation and Isotopes, Vol. 90, pp. 177–180.

Dumazert, J., Coulon, R., Lecomte, Q., Bertrand, G. H. V., and Hamel, M., 2018, *'Gadolinium for neutron detection in current nuclear instrumentation research: A review'*, Nuclear Instruments and Methods in Physics Research Section A, Vol. 882, pp. 53–68.

Edwards, A. J., Bruinsma, M., Burchat, P., Kagan, H., Kass, R., Kirkby, D., Petersen, B. A., and Pulliam, T., 2005, *'Radiation monitoring with CVD diamonds in BABAR'*, Nuclear Instruments and Methods in Physics Research Section A, Vol. 552, No. 1–2, pp. 176–182.

Edwards, T. C. and Steer, M. B., 2016, *Foundations of Microchip Circuit Design*, Fourth Edition, John Wiley and Sons Ltd., Chichester, U.K.

Element Six (N.D.) Element Six Ltd, Ascot, UK.

Erjun, B. and Junde, H., 2001, *'Nuclear Data Sheets 92'*, National Nuclear Data Centre, Brookhaven National Laboratory, USA.

Ewan, G. T., 1979, *'The solid ionization chamber'*, Nuclear Instruments and Methods in Physics Research Section A, Vol. 162, No. 1–3, pp. 75–92.

Fano, U., 1947, *'Ionization Yield of Radiations. II. The Fluctuations of the Number of Ions'*, American Physical Society, Vol. 72, No. 1, pp. 26–29.

Fraser, G. W., 1989, '*X-ray detectors in astronomy'*, Cambridge University Press, Cambridge, UK.

Gatti, E., Manfredi, P. F., Sampietro, M., and Speziali, V., 1990, *'Suboptimal filtering of 1/f-noise in detector charge measurements'*, Nuclear Instruments and Methods in Physics Research Section A, Vol. 297, No. 3, pp. 467–478.

Gatti, E. and Rehak, P., 1984, *'Semiconductor drift chamber — An application of a novel charge transport scheme'*, Nuclear Instruments and Methods in Physics Research Section A, Vol. 225, No. 3, pp. 608–614.

Geiger, H. and Müller, W., 1928, *'Elektronenzählrohr zur Messung schwächster Aktivitäten" (Electron counting tube for the measurement of the weakest radioactivities)'*, Die Naturwissenschaften (The Sciences), Vol. 16, No. 31, pp. 617–618.

Gilmore, G. R., 2008, *Practical Gamma-ray Spectrometry*, Second edition, John Wiley and Sons Ltd., Chichester, UK.

Girolami, M., Allegrini, P., Conte, G., Trucchi, D. M., Ralchenko, V. G., and Salvatori, S., 2012, *'Diamond Detectors for UV and X-Ray Source Imaging'*, IEEE Electron Device Letters, Vol. 33, No. 2, pp. 224–226.

Glesius, F. L. and Kniss, T. A., 1988, *'He3 neutron detectors for hostile environments'*, IEEE Transactions on Nuclear Science, Vol. 35, No. 1, pp. 867–871.

Goldsten, J. O., Rhodes, E. A., Boynton, W. V., Feldman, W. C., Lawrence, D. J., Trombka, J. I., Smith, D. M., Evans, L. G., White, J., Madden, N. W., Berg, P. C., Murphy, G. A., Gurnee, R. S., Strohbehn, K., Williams, B. D., Schaefer, E. D., Monaco, C. A., Cork, C. P., Eckels, J. D., Miller, W. O., Burks, M. T., Hagler, L. B., DeTeresa, S. J., and Witte, M. C., 2007, '*The MESSENGER mission to Mercury'*, Domingue, D. L. and Russell, C. T. (eds.), Springer Science and Business Media LLC., New York, USA.

Grivickas, V., Linnros, J., Grivickas, P., and Galeckas, A., 1999, *'Band edge absorption, carrier recombination and transport measurements in 4H-SiC epilayers'*, Materials Science and Engineering B, Vol. 61–62, pp. 197–201.

Guerrero, M. J., Tromson, D., Descamps, C., and Bergonzo, P., 2006, *'Recent improvements on the use of CVD diamond ionisation chambers for radiotherapy applications'*, Diamond and Related Materials, Vol. 15, No. 4–8, pp. 811–814.

Hall, D. J. and Holland, A., 2010, *'Space radiation environment effects on X-ray CCD background'*, Nuclear Instruments and Methods in Physics Research Section A, Vol. 612, No. 2, pp. 320–327.

Han, S., Wagner, R. S., and Gullikson, E., 1996, *'Response of diamond photoconductors to soft x ray in the spectral range 125 Å to 240 Å'*, Nuclear Instruments and Methods in Physics Research Section A, Vol. 380, No. 1–2, pp. 205–208.

Hansen, H. H., 1983, *'Measurement of the beta-ray spectra of ^{90}Sr-^{90}Y'*, The International Journal Of Applied Radiation And Isotopes, Vol. 34, No. 8, pp. 1241–1247.

Hansson, C. C. T., Owens, A., and Biezen, J. V. D., 2014, *'X-ray, γ-ray and neutron detector development for future space instrumentation'*, Acta Astronautica, Vol. 93, pp. 121–128.

Harms, A. A. and McCormack, G., 1974, *'Isotopic conversion in gadolinium-exposure neutron imaging'*, Nuclear Instruments and Methods, Vol. 118, No. 2, pp. 583–587.

Harris G. L., 1995, *'Properties of Silicon Carbide'*, INSPEC, the Institution of Electrical Engineers, London, UK.

Henke, B. L., Gullikson, E. M., and Davis, J. C., 1993, *'X-Ray Interactions: Photoabsorption, Scattering, Transmission, and Reflection at E = 50-30,000 eV, Z = 1-92'*, Atomic Data and Nuclear Data Tables, Vol. 54, No. 2, pp. 181–342.

Hewlett Packard, 1979, *'Hewlett Packard 4275A LCR Meter: Operating Manual'*, Hewlett Packard, Tokyo, Japan.

Hodgson, M., Lohstroh, A., Sellin, P., and Thomas, D., 2017, *'Characterization of silicon carbide and diamond detectors for neutron applications'*, Measurement Science and Technology, Vol. 28, No. 10, Art. No. 105501.

Hofstadter, R., 1949, *'The detection of gamma-rays with thallium-activated sodium iodide crystals'*, Physical Review, Vol. 75, No. 5, pp. 796–810.

Hovington, P., Drouin, D., Gauvin, R., Joy, D. C., and Evans, N., 1997, *'CASINO: A new monte Carlo code in C language for electron beam interactions-part III: Stopping power at low energies'*, Scanning, Vol. 19, No. 1, pp. 29–35.

References

Hubbell, J. H., 1999, *'Review of photon interaction cross section data in the medical and biological context'*, Physics in Medicine and Biology, Vol. 44, No. 1, pp. R1–R22.

Ihantola, S., Tengblad, O., Toivonen, H., Peräjärvi, K., Csome, C., Borg, J., Paepen, J., Tagziria, H., and Gattinesi, P., 2018, '*European Reference Network for Critical Infrastructure Protection: Radiological and Nuclear Threats to Critical Infrastructure Thematic Group: Novel detection technologies for nuclear security'* Publications Office of the European Union, Luxembourg.

Isberg, J., Hammersberg, J., Johansson, E., Twitchen, D. J., and Whitehead, A. J., 2002, *'High Carrier Mobility in Single-Crystal Plasma-Deposited Diamond'*, Scientific Reports, Vol. 297, pp. 1670–1673.

Ivanov, P. A., and Chelnokov, V. E., 1992 *'Recent developments in SiC single-crystal electronics'*, Semiconductor Science and Technology, Vol. 7 pp. 863 880.

Ivanov, A. M., Strokan, N. B., and Lebedev, A. A., 2012, *'Radiation resistance of wide-gap materials as exemplified by SiC nuclear radiation detectors'*, Technical Physics, Vol. 57, No. 4, pp. 556–560.

Jenkins, R., Gould, R. W., and Gedcke, D., 1995, '*Quantitive X-ray Spectrometry'*, Second Edition, Marcel Dekker Inc., New York, USA.

Joy, D. C. and Luo, S., 1989, *'An empirical stopping power relationship for low-energy electrons'*, Scanning, Vol. 11, No. 4, pp. 176–180.

Kandlakunta, P., 2014, *'Gamma Rays Rejection in a Gadolinium based Semiconductor Neutron Detector'*, Ohio State University, USA.

Kandlakunta, P., Cao, L. R., and Mulligan, P., 2013, *'Measurement of internal conversion electrons from Gd neutron capture'*, Nuclear Instruments and Methods in Physics Research Section A, Vol. 705, pp. 36–41.

Keister, J. W., Cibik, L., Schreiber, S., and Krumrey, M., 2018, *'Characterization of a quadrant diamond transmission X-ray detector including a precise determination of the mean electron-hole pair creation energy'*, Journal of Synchrotron Radiation, Vol. 25, No. 2, pp. 407–412.

Kemmer, J. and Lutz, G., 1987, *'New detector concepts'*, Nuclear Instruments and Methods in Physics Research Section A, Vol. 253, No. 3, pp. 365–377.

References

Kennedy, S. A. and Kelloway, S. J., 2021, *'Heavy Metals in Archaeological Soils: The Application of Portable X-Ray Fluorescence (pXRF) Spectroscopy for Assessing Risk to Human Health at Industrial Sites'*, Advances in Archaeological Practice, Vol. 9, No. 2, pp. 145–159.

Kibédi, T., Burrows, T. W., Trzhaskovskaya, M. B., Davidson, P. M., and Nestor, C. W., 2008, *'Evaluation of theoretical conversion coefficients using BrIcc'*, Nuclear Instruments and Methods in Physics Research Section A, Vol. 589, No. 2, pp. 202–229.

Kibédi, T., Burrows, T. W., Trzhaskovskaya, M. B., Nestor, C. W., and Davidson, P. M., 2007, *'Internal conversion coefficients - How good are they now?'*, ND 2007, Les Ulis, France, EDP Sciences, pp. 57–60.

Klein, C. A., 1968, *'Bandgap Dependence and Related Features of Radiation Ionization Energies in Semiconductors'*, Journal of Applied Physics, Vol. 39, No. 4, pp. 2029–2038.

Knoll, G. F., 2010, *'Radiation detection and measurement'*, John Wiley and Sons Ltd., Hoboken, NJ, USA.

Kouzes, R. T., 2009, '*The ^{3}He Supply Problem'*, Pacific Northwest National Laboratory Report 18388, Richland, WA, USA.

Kouzes, R. T., Ely, J. H., Erikson, L. E., Kernan, W. J., Lintereur, A. T., Siciliano, E. R., Stephens, D. L., Stromswold, D. C., Van Ginhoven, R. M., and Woodring, M. L., 2010, *'Neutron detection alternatives to ^{3}He for national security applications'*, Nuclear Instruments and Methods in Physics Research Section A, Vol. 623, No. 3, pp. 1035–1045.

Koyama, K., Tsunemi, H., Dotani, T., Bautz, M. W., Hayashida, K., Tsuru, T. G., Matsumoto, H., Ogawara, Y., Ricker, G. R., Doty, J., Kissel, S. E., Foster, R., Nakajima, H., Yamaguchi, H., Mori, H., Sakano, M., Hamaguchi, K., Nishiuchi, M., Miyata, E., Torii, K., Namiki, M., Katsuda, S., Matsuura, D., Miyauchi, T., Anabuki, N., Tawa, N., Ozaki, M., Murakami, H., Maeda, Y., Ichikawa, Y., Prigozhin, G. Y., Boughan, E. A., LaMarr, B., Miller, E. D., Burke, B. E., Gregory, J. A., Pillsbury, A., Bamba, A., Hiraga, J. S., Senda, A., Katayama, H., Kitamoto, S., Tsujimoto, M., Kohmura, T., Tsuboi, Y., and Awaki, H., 2007, *'X-Ray Imaging Spectrometer (XIS) on Board Suzaku'*, Publications of the Astronomical Society of Japan, Vol. 59, No. sp1, pp. S23–S33.

Krause, M. O., 1979, *'Atomic radiative and radiationless yields for K and L shells'*, Journal of Physical and Chemical Reference Data, Vol. 8, pp. 307–327.

Krumrey, M. K. and Scholze, F., 2004, *'High-accuracy x-ray detector calibration at PTB'*, High-Energy Detectors in Astronomy, Vol. 5501, pp. 277–285.

References

Kumar, Amit., Kumar, Arvind., Topkar, A., and Das, D., 2017, *'Prototyping and performance study of a single crystal diamond detector for operation at high temperatures'*, Nuclear Instruments and Methods in Physics Research Section A, Vol. 858, pp. 12–17.

Kuo, C. P., Vong, S. K., Cohen, R. M., and Stringfellow, G. B., 1998, *'Effect of mismatch strain on band gap in III-V semiconductors'*, Journal of Applied Physics, Vol. 57, No. 12, pp. 5428-5432.

Lees, J. E., Bassford, D. J., Bunce, E. J., Sims, M. R., and Horsfall, A. B. (2009) *'Silicon carbide X-ray detectors for planetary exploration'*, Nuclear Instruments and Methods in Physics Research Section A, Vol. 604, No. 1–2, pp. 174–176.

Lees, J. E., Bassford, D. J., Fraser, G. W., Horsfall, A. B., Vassilevski, K. V., Wright, N. G., and Owens, A. (2007) *'Semi-transparent SiC Schottky diodes for X-ray spectroscopy'*, Nuclear Instruments and Methods in Physics Research Section A, Vol. 578, No. 1, pp. 226–234.

Lees, J. E., Bassford, D J., and Barnett, A. M., 2016, *'Lubricant analysis using X-ray fluorescence'*, US 2016/0202194A1.

Lefeuvre, G. ,2020, email communication, 13 January.

Liaugaudas, G., Dargis, D., Kwasnicki, P., Arvinte, R., Zielinski, M., and Jarašiunas, K., 2015, *'Determination of carrier lifetime and diffusion length in Al-doped 4H-SiC epilayers by time-resolved optical techniques'*, Journal of Physics D: Applied Physics, Vol. 48, No. 2, Art. No. 025103.

Lioliou, G. and Barnett, A. M., 2015, *'Electronic noise in charge sensitive preamplifiers for X-ray spectroscopy and the benefits of a SiC input JFET'*, Nuclear Instruments and Methods in Physics Research Section A, Vol. 801, pp. 63–72.

Lioliou, G., Chan, H. K., Gohil, T., Vassilevski, K. V., Wright, N. G., Horsfall, A. B., and Barnett, A. M. (2016) *'4H-SiC Schottky diode arrays for X-ray detection'*, Nuclear Instruments and Methods in Physics Research Section A, Vol. 840, pp. 145–152.

Lioliou, G. and Barnett, A. M., 2017, *'Prototype GaAs X-ray detector and preamplifier electronics for a deep seabed mineral XRF spectrometer'*, X-Ray Spectrometry, Vol. 47, No. 3, pp. 201–214.

References

Lioliou, G., Butera, S., Zhao, S., Whitaker, M. D. C., and Barnett, A. M., 2018, *'GaAs Spectrometer for Planetary Electron Spectroscopy'*, Journal of Geophysical Research: Space Physics, Vol. 123, No. 9, pp. 7568–7580.

Lioliou, G., Lefeuvre, G., and Barnett, A. M., 2021, *'High temperature (≤ 160 °C) X-ray and β- particle diamond detector'*, Nuclear Instruments and Methods in Physics Research Section A, Vol. 991, Art. No. 165025.

Lioliou, G., Mazzillo, M. C., Sciuto, A., and Barnett, A. M., 2015, *'Electrical and ultraviolet characterization of 4H-SiC Schottky photodiodes'*, Optics Express, Vol. 23, No. 17, pp. 21657−21670.

Lioliou, G., Meng, X., Ng, J. S., and Barnett, A. M., 2016, *'Characterization of gallium arsenide X-ray mesa p-i-n photodiodes at room temperature'*, Nuclear Instruments and Methods in Physics Research Section A, Vol. 813, pp. 1–9.

Lioliou, G., Whitaker, M. D. C., Butera, S., and Barnett, A. M., 2021, *'Repurposing a low-cost commercial Si photodiode as a detector for X-ray and γ-ray spectroscopy at temperatures up to 80 °C'*, Nuclear Instruments and Methods in Physics Research Section A, Vol. 1010, Art No. 165543.

Liu, Y., Tang, X., Xu, Z., Hong, L., Wang, H., Liu, M., and Chen, D., 2015, *'Influences of planar source thickness on betavoltaics with different semiconductors'*, Journal of Radioanalytical and Nuclear Chemistry, Vol. 304, No. 2, pp. 517–525.

Loctite, 2014, *'Loctite Ablesik 2902 Technical Data Sheet'*, Anderlechtstraat 33, 1620 Drogenbos, Belgium.

Lohstroh, A., Sellin, P. J., Boroumand, F., and Morse, J., 2007, *'High gain observed in X-ray induced currents in synthetic single crystal diamonds'*, Physica Status Solidi (a), Vol. 204, No. 9, pp. 3011–3016.

Lohstroh, A., Sellin, P. J., Wang, S. G., Davies, A. W., and Parkin, J. M., 2007, *'Mapping of polarization and detrapping effects in synthetic single crystal chemical vapor deposited diamond by ion beam induced charge imaging'*, Journal of Applied Physics, Vol. 101, No. 6, Art. No. 063711.

Lowe, B. G. and Sareen, R. A., 2007, *'A measurement of the electron-hole pair creation energy and the Fano factor in silicon for 5.9 keV X-rays and their temperature dependence in the range 80-270 K'*, Nuclear Instruments and Methods in Physics Research Section A, Vol. 576, No. 2–3, pp. 367–370.

Lowe, B. G. and Sareen, R. A., 2014, '*Semiconductor X-ray Detectors'*, Taylor and Francis Group LLC., Boca Raton, FL, USA.

Lutz, G., Porro, M., Aschauer, S., Wölfel, S., and Strüder, L., 2016, *'The DEPFET Sensor-Amplifier Structure: A Method to Beat 1/f Noise and Reach Sub-Electron Noise in Pixel Detectors'*, Sensors, Vol. 16, No. 5, Art. No. 608.

Madelung, O., 1982, '*Physics of Group IV Elements and III-V Compounds'*, Springer-Verlag, Berlin, Germany.

Manfredotti, C., Apostolo, G., Fizzotti, F., Lo Giudice, A., Morando, M., Pignolo, R., Polesello, P., Truccato, M., Vittone, E., and Nastasi, U., 1998, *'CVD diamond tips as X-ray detectors'*, Diamond and Related Materials, Vol. 7, No. 2–5, pp. 523–527.

Manfredotti, C., Fizzotti, F., Polesello, P., Vittone, E., and Wang, F., 1996, *'A Study of Polycrystalline CVD Diamond by Nuclear Techniques'*, Physica Status Solidi (a), Vol. 154, No. 1, pp. 327–350.

Masaoka, S., Nakamura, T., Yamagishi, H., and Soyama, K., 2003, *'Optimization of a micro-strip gas chamber as a two-dimensional neutron detector using gadolinium converter'*, Nuclear Instruments and Methods in Physics Research Section A, Vol. 513, No. 3, pp. 538–549.

MATLAB, 2020, Version 9.8.0.15385580 (R2010a) Update 6, Natick, Massachusetts: The MathWorks.

McKenzie, J. M., 1979, *'Development of the semiconductor radiation detector'*, Nuclear Instruments and Methods in Physics Research Section A, Vol. 162, No. 1–3, pp. 49–73.

Metcalfe, A., Fern, G. R., Hobson, P. R., Smith, D. R., Lefeuvre, G., and Saenger, R., 2017, *'Diamond based detectors for high temperature, high radiation environments'*, Journal of Instrumentation, Vol. 12, No. 1, Art. No. C01066.

Miller, G. L., Gidson, W. M., and Donovan, P. F., 1962, *'Semiconductor Particle Detectors'*, Annual Review of Nuclear Science, Vol. 12, No. 1, pp. 189–220.

References

Moll, M., 2006, *'Radiation tolerant semiconductor sensors for tracking detectors'*, Nuclear Instruments and Methods in Physics Research Section A, Vol. 565, No. 1, pp. 202–211.

Nava, F., Vanni, P., Bruzzi, M., Lagomarsino, S., Sciortino, S., Wagner, G., and Lanzieri, C., 2004, *'Minimum ionizing and alpha particles detectors based on epitaxial semiconductor silicon carbide'*, IEEE Transactions on Nuclear Science, Vol. 51, No. 1, pp. 238–244.

Nica, N., 2017, *'Nuclear Data Sheets for A=158'*, Nuclear Data Sheets, Vol. 141, pp. 1–326.

Novikova, E. I., Strickman, M. S., Gwon, C., Phlips, B. F., Wulf, E. A., Fitzgerald, C., Waters, L. S., and Johns, R. C., 2006, *'Designing SWORD-SoftWare for optimization of radiation detectors'*, IEEE Nuclear Science Symposium Conference Record, Vol. 1, pp. 607–612.

Owens, A., 2012, '*Compound Semiconductor Radiation Detectors'*, Taylor & Francis Group LLC., Boca Raton, FL, USA.

Owens, A., Bavdaz, M., Peacock, A., Poelaert, A., Andersson, H., Nenonen, S., Sipila, H., Tröger, L., and Bertuccio, G., 2001, *'High resolution X-ray spectroscopy using GaAs arrays'*, Journal of Applied Physics, Vol. 90, No. 10, pp. 5376–5381.

Owens, A. and Peacock, A., 2004, *'Compound semiconductor radiation detectors'*, Nuclear Instruments and Methods in Physics Research Section A, Vol. 531, No. 1, pp. 18–37.

Park, J., Park, S. H., Shin, H., Kim, H., Kim, J., Lee, S. W., Lee, S. K., and Kim, Y. K., 2014, *'Effect of metal electrode on characteristics of gamma-irradiated silicon carbide detector'*, Journal of Nuclear Science and Technology, Vol. 51, No. 4, pp. 482–486.

Pernegger, H., Roe, S., Weilhammer, P., Eremin, V., Frais-Kölbl, H., Griesmayer, E., Kagan, H., Schnetzer, S., Stone, R., Trischuk, W., Twitchen, D., and Whitehead, A., 2005, *'Charge-carrier properties in synthetic single-crystal diamond measured with the transient-current technique'*, Journal of Applied Physics, Vol. 97, No. 7, Art. No. 073704.

Pfeifer, K. B., Achyuthan, K. E., Allen, M., Denton, M. L. B., Siegal, M. P., and Manginell, R. P., 2017, *'Microfabrication of a gadolinium-derived solid-state sensor for thermal neutrons'*, Journal of Radiation Research, Vol. 58, No. 4, pp. 464–473.

Pietropaolo, A., Angelone, M., Bedogni, R., Colonna, N., Hurd, A. J., Khaplanov, A., Murtas, F., Pillon, M., Piscitelli, F., Schooneveld, E. M., and Zeitelhack, K., 2020, *'Neutron detection techniques from μeV to GeV'*, Physics Reports, Vol. 875, pp. 1–65.

Pilotti, R., Angelone, M., Loreti, S., Pagano, G., Pillon, M., Sarto, F., Marinel-Li, M., Milani, E., Prestopino, G., Verona, C., and Verona-Rinati, G., 2015, *'High Temperature Performances of CVD Single Crystal Diamond Detectors'*, Vol. 1, 1st EPS Conference on Plasma Diagnostics, Frascati, Italy.

Pomorski, M., Berdermann, E., Caragheorgheopol, A., Ciobanu, M., Kiš, M., Martemiyanov, A., Nebel, C., and Moritz, P., 2006, *'Development of single-crystal CVD-diamond detectors for spectroscopy and timing'*, Physica Status Solidi (a), Vol. 203, No. 12, pp. 3152–3160.

Prasai, D., John, W., Weixelbaum, L., Krüger, O., Wagner, G., Sperfeld, P., Nowy, S., Friedrich, D., Winter, S., and Weiss, T., 2012, *'Highly reliable silicon carbide photodiodes for visible-blind ultraviolet detector applications'*, Journal of Materials Research, Vol. 28, No. 1, pp. 33–37.

Press, W. H., Teukolsky, S. A., Vetterling, W. T., and Flannery, B. P., 1986, '*Numerical Recipes'*, Cambridge University Press, Cambridge, UK.

Pritychenko, B., Běták, E., Kellett, M. A., Singh, B., and Totans, J., 2011, *'The Nuclear Science References (NSR) database and Web Retrieval System'*, Nuclear Instruments and Methods in Physics Research Section A, Vol. 640, No. 1, pp. 213–218.

Pritychenko, B., Sonzogni, A. A., Winchell, D. F., Zerkin, V. V., Arcilla, R., Burrows, T. W., Dunford, C. L., Herman, M. W., McLane, V., Obložinský, P., Sanborn, Y., and Tuli, J. K., 2006, *'Nuclear reaction and structure data services of the national nuclear data center'*, Annals of Nuclear Energy, Vol. 33, No. 4, pp. 390–399.

Prosvirin, D. V., Amosov, V. N., Krasil'Nikov, A. V., and Gvozdeva, N. M., 2004, *'A dosimeter for on-line dose rate monitoring based on a natural diamond detector'*, Instruments and Experimental Techniques, Vol. 47, No. 5, pp. 675–677.

Puglisi, D. and Bertuccio, G., 2019, *'Silicon Carbide Microstrip Radiation Detectors'*, Micromachines, Vol. 10, No. 12, pp. 835–847.

Radulović, V., Yamazaki, Y., Pastuović, Ž., Sarbutt, A., Ambrožič, K., Bernat, R., Ereš, Z., Coutinho, J., Ohshima, T., Capan, I., and Snoj, L., 2020, *'Silicon carbide neutron detector testing at the JSI TRIGA reactor for enhanced border and port security'*, Nuclear Instruments and Methods in Physics Research Section A, Vol. 972, Art. No. 164122.

Ralston, J., Kandlakunta, P., and Cao, L., 2012, *'Electron emission following ^{157}Gd neutron capture'*, Transactions of the American Nuclear Society, pp. 313–314.

References

Ramo, S., 1939, *'Currents Induced by Electron Motion'*, Proceedings of the IRE, Vol. 27, No. 9, pp. 584–585.

Reich, C. W., 2012, *'Nuclear Data Sheets for A = 156'*, Nuclear Data Sheets, Vol. 113, No. 11, pp. 2537–2840.

Rieder, R., Gellert, R., Brückner, J., Klingelhöfer, G., Dreibus, G., Yen, A., and Squyres, S. W., 2003, *'The new Athena alpha particle X-ray spectrometer for the Mars Exploration Rovers'*, Journal of Geophysical Research: Planets, Vol. 108, E12. Art. No. 8066.

Rinard, P., 1991, *'Neutron interactions with matter'*, in '*Passive Non-destructive Assay of Nuclear Materials'*, Reilly, D., Ensslin, N., and Smith, H. (eds.), Regulatory Research, US Nuclear Regulatory Commission, Washington, DC, pp. 357–377.

Rogalla, M., Runge, K., and Söldner-Rembold, A., 1999, *'Particle detectors based on semi-insulating silicon carbide'*, Nuclear Physics B - Proceedings Supplements, Vol. 78, No. 1–3, pp. 516–520.

Rogers Corporation, N.D., www.rogerscorp.com *'Product Selector Guide'* [Online], (Accessed 19 October 2021).

Ruggieri, D. J., 1972, *'Microchannel plate imaging detectors'*, IEEE Transactions on Nuclear Science, Vol. 19, No. 3, pp. 74–84.

Rutherford, E. and Geiger, H., 1908, *'An electrical method of counting the number of α-particles from radio-active substances'*, Proceedings of the Royal Society of London, Vol. 81, No. 546, pp. 141–161.

Saxena, A. K., 1981, *'Non-Γ Deep Levels and the Conduction Band Structure of* $Ga_{1-x}Al_xAs$ *Alloys'*, Physica Status Solidi (b), Vol. 105, No. 2, pp. 777–787.

Schirru, F., Kisielewicz, K., Nowak, T., and Marczewska, B., 2010, '*Single crystal diamond detector for radiotherapy'*, Journal of Physics D, Vol. 43, No. 26, Art. No. 265101.

Schirru, F., Lohstroh, A., Jayawardena, K. D. G. I., Henley, S. J., and Sellin, P. J., 2013, *'X-ray induced photocurrent characteristics of CVD diamond detectors with different carbon electrodes'*, Journal of Instrumentation - 13th Topical Seminar on Innovative Particle and radiation Detectors, Vol. 8, No. 12, Art. No, C12046.

Schmid, G. J., Koch, J. A., Lerche, R. A., and Moran, M. J., 2004, *'A neutron sensor based on single crystal CVD diamond'*, Nuclear Instruments and Methods in Physics Research Section A, Vol. 527, No. 3, pp. 554–561.

Schott, 2014, *'Schott Technical Glasses, Physical and Technical Properties catalogue'*, Hattenbergstrasse 10, 55122 Mainz, Germany.

Schötzig, U., 2000, *'Half-life and X-ray emission probabilities of ^{55}Fe'*, Applied Radiation and Isotopes, Vol. 53, No. 3, pp. 469–472.

Schulte, R. L. and Kesselman, M., 1999, *'Development of a portable directional thermal neutron detection system for nuclear monitoring'*, Nuclear Instruments and Methods in Physics Research Section A, Vol. 422, No. 1–3, pp. 852–857.

Sellin, P. J. and Vaitkus, J., 2006, *'New materials for radiation hard semiconductor dectectors'*, Nuclear Instruments and Methods in Physics Research Section A, Vol. 557, No. 2, pp. 479–489.

Shive, J. N., 1953, *'The Properties of Germanium Phototransistors'*, Journal of the Optical Society of America, Vol. 43, Issue 4, pp. 239-244.

Shockley, W., 1938, *'Currents to Conductors Induced by a Moving Point Charge'*, Journal of Applied Physics, Vol. 9, No. 10, pp. 635–636.

Siffert, P., Berger, J., Scharager, C., Cornet, A., Stuck, R., Bell, R. O., Serreze, H. B., and Wald, F. V., 1976, *'Polarization in Cadmium Telluride Nuclear Radiation Detectors'*, IEEE Transactions on Nuclear Science, Vol. 23, No. 1, pp. 159–170.

Siliconix, V., 2001, 'Vishay Siliconix 2N4416/2N4416A/SST4416 N-Channel Silicon Junction Field-Effect Transistor', Document Number: 70242 S-04028 Rev. F.

Skidmore, M. S., Ambrosi, R. M., and Simon, H., 2009, *'Hybrid X-ray and γ-ray spectrometer for in-situ planetary science missions'*, Nuclear Instruments and Methods in Physics Research, Section A, Vol. 604, No. 3, pp. 592–603.

Space Exploration Technologies Corp., N.D., https://www.spacex.com/vehicles/falcon-9/ *'SpaceX - Falcon 9'* [Online]. (Accessed 31 August 2021).

Spear, K. E. and Dismukes, J. P., 1994, '*Synthetic diamond: emerging CVD science and technology'*, John Wiley and Sons Ltd., New York, USA.

Spieler, H., 2005, '*Semiconductor Detector Systems'*, Oxford University Press, Oxford, UK.

Strüder, L., Meidinger, N., Stotter, D., Kemmer, J., Lechner, P., Leutenegger, P., Soltau, H., Eggert, F., Rohde, M., and Schulein, T., 1999, *'High-resolution X-ray spectroscopy close to room temperature'*, Microscopy and Microanalysis, Vol. 4, No. 6, pp. 622–631.

Sweeting, M. N. and Underwood, C. I., 2014, '*Spacecraft Systems Engineering'*, Fourth Edition, Fortescue, P., Swinerd, G., and Stark, J. (eds), John Wiley and Sons Ltd, Chichester, UK.

Sze, S. M. and Ng, K. K. (2007) '*Physics of semiconductor devices'*, John Wiley and Sons Ltd., Hoboken, NJ, USA.

Tartoni, N., Angelone, M., Pillon, M., Almaviva, S., Marinelli, M., Milani, E., Prestopino, G., Verona, C., Rinati, G. V., and Roberts, M. A., 2009, *'X-ray detection by using CVD single crystal diamond detector'*, IEEE Transactions on Nuclear Science, Vol. 56, No. 3, pp. 849–852.

Tchouaso, M. T., Kasiwattanawut, H., and Prelas, M. A., 2018, *'Energy response of diamond sensor to beta radiation'*, Applied Radiation and Isotopes, Vol. 139, pp. 66–69.

Thompson, A., Lindau, I., Attwood, D., Liu, Y., Gullikson, E., Pianetta, P., Howells, M., Robinson, A., Kim, K., Scofield, J., Kirz, J., Underwood, J., Kortright, J., Williams, G., and Winick, H., 2009, '*Center for X-ray Optics, X-ray Data Booklet'*, Lawrence Berkeley National Laboratory, Berkeley, CA, USA.

Tosi, G., Torresin, A., Agosteo, S., Foglio Para, A., Sanqiust, V., Zeni, L., and Silari, M., 1991, *'Neutron Measurements Around Medical Electron Accelerators By Active And Passive Detection Techniques'*, Medical Physics, Vol. 18, No. 1, pp. 54–60.

Trombka, J. I., Nittler, L. R., Starr, R. D., Evans, L. G., Mccoy, T. J., Boynton, W. V., Burbine, T. H., Brückner, J., Gorenstein, P., Squyres, S. W., Reedy, R. C., Goldsten, J. O., Lim, L., Hurley, K., Clark, P. E., Floyd, S. R., Mcclanahan, T. P., Mccartney, E., Branscomb, J., Bhangoo, J. S., Mikheeva, I., and Murphy, M. E., 2001, *'The NEAR-Shoemaker x-ray/gamma-ray spectrometer experiment: Overview and lessons learned'*, Meteoritics & Planetary Science, Vol. 36, No. 12, pp. 1605–1616.

Tromson, D., Bergonzo, P., Brambilla, A., Mer, C., Foulon, F., and Amosov, V. N., 2000, *'Thermally stimulated current investigations on diamond X-ray detectors'*, Journal of Applied Physics, Vol. 87, No. 7, pp. 3360–3364.

References

Tsubota, M., Kaneko, J. H., Miyazaki, D., Shimaoka, T., Ueno, K., Tadokoro, T., Chayahara, A., Watanabe, H., Kato, Y., Shikata, S., and Kuwabara, H., 2015, *'High-temperature characteristics of charge collection efficiency using single CVD diamond detectors'*, Nuclear Instruments and Methods in Physics Research Section A, Vol. 789, pp. 50–56.

Van Heerden, P. J. and Milatz, J. M. W., 1950, *'The crystal counter a new apparatus in nuclear physics for the investigation of β⁻ and y-RAYS. Part II'*, Physica, Vol. 16, No. 6, pp. 517–527.

Vasilescu, G., 2005, '*Electronic Noise and Interfering Signals - Principles and Applications'*, Springer-Verlag, Berlin, Germany.

Verma, H. R., 2017, *'Measurements of M and L X-ray energies and relative intensities emanating from ^{241}Am source'*, Applied Radiation and Isotopes, Vol. 122, pp. 41–46.

Whitaker, M. D. C., Lioliou, G., Krysa, A. B., and Barnett, A. M., 2020, *'$Al_{0.6}Ga_{0.4}As$ X-ray avalanche photodiodes for spectroscopy'*, Semiconductor Science and Technology, Vol. 35, No. 9, Art No. 095026.

Whitaker, M. D. C., Butera, S., Lioliou, G., and Barnett, A. M., 2017, *'Temperature dependence of $Al_{0.2}Ga_{0.8}As$ X-ray photodiodes for X-ray spectroscopy'*, Journal of Applied Physics, Vol. 122, Art No. 3.

Whitaker, M. D. C., Butera, S., Lioliou, G., Krysa, A. B., and Barnett, A. M., 2021, *'A prototype AlInP electron spectrometer'*, Planetary and Space Science, Vol. 205, Art. No. 105284.

Whitaker, M. D. C., Zhao, S., Lioliou, G., Butera, S., and Barnett, A. M., 2020, *'AlGaAs two by two pixel detector for electron spectroscopy in space environments'*, Nuclear Instruments and Methods in Physics Research Section A, Vol. 951, Art. No. 163039.

Whitaker, M. D. C., Lioliou, G., and Barnett, A. M., 2018, *'$Al_{0.2}Ga_{0.8}As$ 2 × 2 square pixel X-ray photodiode array'*, Nuclear Instruments and Methods in Physics Research Section A, Vol. 899, pp. 106–114.

Wiącek, P. and Dąbrowski, W., 2016, *'Low dose radiation damage effects in silicon strip detectors'*, Journal of Instrumentation, Vol. 11, No. 11, Art. No. C11015.

Weitzel, C. E., Palmour J. W., Carter, C. H., Moore, K., Nordquist, K. J., Allen, S., Thero, C., and Bhatnagar, M., 1996, *'Silicon Carbide High-Power Devices*' Transactions on Electron Devices, Vol 43, No. 10, pp. 1732-1739.

References

Williams-Thorpe, O., 2008, *'Portable X-ray Fluorescence Spectrometry: Capabilities for In Situ Analysis'*, Potts, P. J. and West, M. (eds), Royal Society of Chemistry, Cambridge, UK.

Xiaolong, H., Shenggui, Y., and Chunsheng, D., 2010, *'Evaluation of the decay data of ^{109}Cd'*, Nuclear Instruments and Methods in Physics Research Section A, Vol. 621, pp. 443–446.

Zhang, F., He, Z., Knoll, G. F., Wehe, D. K., and Berry, J. E., 2005, *'3-D position sensitive CdZnTe spectrometer performance using third generation VAS/TAT readout electronics'*, IEEE Transactions on Nuclear Science, Vol. 52, No. 5, pp. 2009–2016.

Zhao, S., Gohil, T., Lioliou, G., and Barnett, A. M., 2016, *'Soft X-ray detection and photon counting spectroscopy with commercial 4H-SiC Schottky photodiodes'*, Nuclear Instruments and Methods in Physics Research Section A, Vol. 830, pp. 1–5.

Zhao, S., Lioliou, G., and Barnett, A. M., 2017, *'Temperature dependence of commercial 4H-SiC UV Schottky photodiodes for X-ray detection and spectroscopy'*, Nuclear Instruments and Methods in Physics Research Section A, Vol. 859, pp. 76–82.

Zhao, S., Lioliou, G., Butera, S., Whitaker, M. D. C., and Barnett, A. M., 2018, *'Electron spectroscopy with a commercial 4H-SiC photodiode'*, Nuclear Instruments and Methods in Physics Research Section A, Vol. 910, pp. 35–40.

Zhao, S, Lioliou, G., and Barnett, A. M., 2018b, *'X-ray spectrometer with a low-cost SiC photodiode'*, Nuclear Instruments and Methods in Physics Research Section A, Vol. 887, pp. 138–143.

Zheng, Y., Ye, H., Thornton, R., Knott, T., Ochalski, T. J., Wang, J., Liu, J., Wei, J., Chen, L., Cumont, A., Zhang, R., and Li, C., 2020, *'Subsurface cleavage of diamond after high-speed three-dimensional dynamic friction polishing'*, Diamond and Related Materials, Vol. 101, pp. 107600−10